Computational Study of Vaccination Strategies to Change B Cell Immunodominance

by

Leerang Yang

B.S. in Chemical Engineering

Columbia University in the City of New York (2016)

Submitted to the Department of Chemical Engineering
in partial fulfillment of the requirements for the degree of

Doctor of Philosophy

at the

Massachusetts Institute of Technology

February 2024

Author .....
Leerang Yang
Department of Chemical Engineering
October 6th, 2023

Certified by .....
Arup K. Chakraborty
John M. Deutch Institute Professor

Accepted by .....
Hadley D. Sikes
Professor
Graduate Officer

Computational Study of Vaccination Strategies to Change B cell Immunodominance

by

Leerang Yang

Submitted to the Department of Chemical Engineering on 6 October 2023, in partial fulfillment of the requirements for the degree of

Doctor of Philosophy in Chemical Engineering

Abstract

B cell Immunodominance refers to the phenomenon where B cells that target certain epitopes of a pathogen are preferentially selected among the B cells that potentially target diverse epitopes presented on a pathogenic protein. This phenomenon presents a challenge in the development of vaccines against mutable viruses like HIV, influenza, and SARS-CoV-2 which rapidly modify the immunodominant epitopes and render existing antibodies ineffective. Moreover, as the immune system preferentially targets immunodominant epitopes, functionally important and conserved epitopes are less targeted, which poses a barrier to the generation of broadly neutralizing antibodies.

Computational modeling offers a valuable tool for understanding how immunodominance arises from the stochastic and dynamic processes of immune response. By simulating the systemic interactions between B cells, helper T cells, antibodies, and antigens, we can gain insights into the underlying mechanisms of immunodominance, thereby informing more effective vaccine design strategies. In this thesis, computational models are developed to investigate strategies for modulating B cell immunodominance in vaccinations. Experimental data from collaboration are used to validate model findings.

The first project investigates engineered influenza immunogens designed to elicit cross-reactive B cells targeting the receptor-binding site. A computational model reveals that the efficacy of an immunogen in eliciting cross-reactive antibodies depends on interactions between B cell antigen engagement and T cell-mediated selection within germinal centers. The second project addresses the enhanced efficacy of a third dose of SARS-CoV-2 vaccines against the Omicron variant. Through computational models and human vaccination data, we find that a third dose significantly boosts neutralizing antibody responses by targeting less-mutated, subdominant epitopes. This is facilitated by pre-existing antibodies from earlier doses, which improve antigen availability and partially mask immunodominant epitopes. The third project seeks to optimize 'slow delivery' immunization schemes. Our mathematical models, developed in collaboration with experimentalists, propose a practical way to optimize vaccine delivery kinetics for superior T follicular helper cell and antigen-specific germinal center B cell responses.

Thesis Supervisor: Arup K. Chakraborty
Title: John M. Deutch Institute Professor

Acknowledgements

I am deeply grateful to those who guided my development as a researcher. Reflecting upon the past five years, I am pleasantly surprised by how much I have learned about the process of conducting research and amused by how little I understood about it when I started. My advisor, Arup, has patiently led me through this journey. I am deeply influenced and inspired by Arup's endless enthusiasm for science and striving for excellence and rigor. Arup has been a caring and sincere mentor and was always generous with his time. While I have faced my share of difficult times in grad school and many times felt like I was hitting a wall, I never felt that I was alone in it. Arup allowed me to be independent and explore my ideas but also provided feedback and guidance that I needed to grow. I also want to thank my thesis committee members, Prof. Dane Wittrup and Prof. Mehran Kardar, for their encouragements and insights over the years that helped me stay on track. I also learned a lot from Dr. Assaf Amitai, who was a postdoc in our group when I first joined. A large part of how I define and approach problems comes from the training I got in my early years from Assaf.

I am fortunate to have collaborated with scientists from various places. The works presented in this thesis would not have been possible without them. I want to specifically acknowledge Tim Caradonna, Sachin Bhagchandani, and Vinci Wang who led the experiments that complemented my computational works. I want to also thank Prof. Aaron Schmidt, Prof. Darrell Irvine, and Prof. Michel Nussenzweig who were their PIs and facilitated these fruitful collaborations.

All the past and present members of the Chakraborty Group have helped me in many ways. The collaborations, inspirations, and emotional support I have received from them have been invaluable. I want to especially thank Pradeep Natarajan, who was not only a labmate but also my roommate of three years, best friend, and a best man at my wedding. Our countless conversations about both science and life will forever be cherished. I want to also thank Matt Van Beek specifically for his direct research contribution. I thank Federica Ferretti, Eric Wang, Rose Yin, Eric Wang, Pranav Murugan, Deepti Kannan, Saeed Mahdisoltani, Andriy Goychuk, Sam Melton, Raman Ganti, Allen Lin, Krishna Shrinivas, Dariusz Murakowski, Julia Doelger, Kayla Sprenger, and Ang Gao for the comraderies over the years. I also thank Michelle Antunes who was a wonderful lab admin and is a good friend.

I want to thank all the amazing friends I have found in MIT and Boston. They have been the pillars that supported me. I feel very lucky to leave MIT with so many cherished memories – pizza nights with Chris and Jackie, camping trips with Allen and Noelle, many potluck dinners and barbecues with Minju, Hyunhee, Hao-Wei, Marc, TJ, Keith, Luke, Lauren, Elvin, Billy, and Pradeep, ski trips with Tanguy, Juliette, Aileen, Angie, and Elisa.

My family's unconditional love, understanding and support have meant everything for me. My father, Sichun Yang, my mother, Busim Kim, and my sister, Harang Yang may be across the globe in South Korea, but I feel their presence in my life every day. It is my parents who taught me the importance of diligence and persistence. They always encouraged me to pursue things that are meaningful. I am grateful for that.

My wife, Grace, has seen every little one of my struggles and victories in grad school. More times than not, it was her love, support, and kindness that allowed me to bounce back from setbacks. She made the past five years the happiest of my life, and I am excited for what awaits us next. I am truly grateful for her extraordinary presence in my life.

Table of Contents

List of Figures

Chapter 2

experiments. All fractions were calculated after combining B cells from 1,000 independent stochastic simulations. See also **Figure 2-S3**.

Figure 2-5. Potential mechanism of how T cell selection stringency affects expansion and evolution of RBS-directed B cells. 44
(A) Selection probability of the RBS-directed B cell precursor at GC initiation as a function of T cell help stringency. **(B)** Average number of unique mutations that occur in a GC in the first 5 days which increase the affinities of RBS-directed B cells towards multiple rsHA components. In panels A and B, the effects of T cell selection stringency are opposite for immunizations with the cocktail and chimera. **(C-F)** Positive selection probabilities of unique RBS-directed B cell mutants in day 5 GCs, simulated under either stringent T cell selection (**C** and **E**) or permissive T cell selection (**D** and **F**) conditions after immunization with either the chimera (**C** and **D**) or the cocktail (**E** and **F**). The mutants are classified based on how many rsHA components they can bind (from one to three).

Supplemental Figure 2-S1. Related to Figure 2-2. Antigen capture by B cells. 52
(A) Examples of antigen-BCR clustering in immunological synapses from the simulations of antigen capture. The simulation shows that after the chimera immunization, a strain-specific B cell binds to most of the antigen molecules in the synapse, but cannot form multivalent antigen-BCR clusters. After the cocktail immunization, it binds to only the cognate molecules but forms multivalent antigen-BCR clusters. A cross-reactive B cell bind to most antigen molecules in the synapse and form multivalent antigen-BCR clusters after immunization with either of the immunogens. **(B)** Clustering of Ag molecules when the number of Ag molecules in the immunological synapse is varied and the number of BCRs is ratio between them is 1. The fraction of Ag molecules that exist in clusters of at least 3 Ag molecules is shown. The data is from 30 simulations of immunological synapse between an FDC presenting the chimera immunogen and a cross-reactive B cell that binds all three rsHA components with the affinities of -14.8 k_BT. **(C-D)** Amount of antigen captured as a function of Ag-BCR binding affinity when the numbers of Ag and BCR molecules in the immunological synapse are varied.

Figure 2-S2. Related to Figure 2-3. Effect of antigen design on selection by T cells. 53
(A-B) Pairwise comparison of computationally predicted helper T cell epitopes in rabbit serum albumin and human serum albumin. Each axis corresponds to the ranks of the top 20 percentile predicted 15-mer T cell epitopes. (A) Number of conserved residues in pairwise comparisons of the 9-mer cores of the predicted epitopes. (B) Number of conserved residues in pairwise comparisons of the P2, P5, P7 and P8 residues of the 9-mer cores.

Figure 2-S3. Related to Figure 2-4. Evolution of RBS-directed B cells in Germinal Centers. 54
(A) Fraction of GCs from 1000 simulations that contain at least one RBS-directed B cell. When selection by T cells is permissive, RBS-directed B cells survive in most GCs after immunization with the cocktail, while they slowly become extinct in an increasing number of GCs after immunization with the chimera. When selection is stringent, RBS-directed B cells rapidly become extinct in many GCs after immunization with the cocktail. They survive in most GCs after immunization with the chimeric antigen for the first several days, then, since affinity increases quickly and the advantage of cross-reactivity decreases in late GCs, some GCs lose the RBS-directed B cells. **(B-C)** The fraction of GC B cells that are RBS-directed when the parameters ρ and P_{max} are changed, showing the same qualitative trend as the main result in Figure 4. (B) ρ is 0.4, instead of 0.7. (C) P_{max} is 1, instead of 0.6. **(D-E)** Heterogeneities among 1000 GC simulations on day 9, when T cell selection is stringent (x = 1.5), resulting from stochasticity in evolution. (D) Histogram of the fraction of GC B cells that belong to the single most dominant clonal lineage. The GCs show varying degrees of homogenization. (E) Histogram of the highest and lowest affinity of the B cells that are concurrently positively selected on day 9 from each GC. There is a ~10 fold affinity difference among positively selected B cells within the same GCs, which is represented by the difference between the two peaks. Across all the GCs, B cells with an even wider range of affinities are concurrently positively selected.

Chapter 3

shown is from a single simulation of 200 GCs. **(D-F)** Cross-reactivity of memory B cells derived from GCs and EGCs. The areas of the markers scale with the number of cells that have identical affinities. (D) GC at 1m after Vax 1, (E) EGC after Vax 2, (F) GC at 5m after Vax 2. Only a very small number of subdominant memory cells are generated after Vax 1, and they undergo limited expansion in EGC after Vax 2. In contrast, diverse subdominant B cells are produced in Vax 2 GCs, some of which have high affinities towards the variant.

Number of memory B cells derived from GCs at 1 month after Vax 1 and 5 months after Vax 2 that target dominant and subdominant epitopes, when various simulations parameters are changed. **(A)** The reference antigen concentration, C_0, is varied. Decreasing C_0 makes B cells easily activated even when the antigen concentration is small. The quantitative difference between the number of subdominant memory cells after Vax 2 and Vax 1 is largest when C_0 is large; that is, when the importance of antigen concentration is high. However, the qualitative trend that more subdominant B cells are generated after Vax 2 is robust across ~2 orders of magnitude variation in C_0. **(B-C)** Parameters that characterize the affinity distribution of naïve B cells are varied. E_1^h and dE_{12} are varied in (B), p and dE_{12} are varied in (C). For some parameter values, especially small dE_{12} and large p, some subdominant memory cells develop after Vax 1. However, for all parameter values, the number of subdominant B cells greatly increases after Vax 2, showing the robustness of our findings. **(D)** Parameter K, which controls the stringency of selection, is varied. Both after Vax 1 and Vax 2, more subdominant B cells develop when selection is permissive (small value of K). For all values of K tested, the number of subdominant B cells greatly increases after Vax 2 compared to Vax 1. **(E)** An alternative model of antigen capture is used, and the parameter H is varied. With this model, the amount of antigen captured by B cells saturates if the product of B cell affinity and antigen concentration is much greater than H. The original model is equivalent to infinite H. The qualitative finding is robust to changes in the model. Quantitatively, slightly more subdominant B cells develop after Vax 2 but not after Vax 1 when H is small because selection becomes permissive when antigen concentration is high. **(F)** p_1, the fraction of positively selected GC B cells that exit GC, and p_2, the fraction of such cells that become plasma cells, are varied. Left panel) If p_2 increases, GC-derived B cells contribute more to the antibody titer at long times after Vax 2. This makes the antibody dynamics not consistent with clinically observed behavior where the antibody titers decay over time after Vax 2. Middle panel) If p_1 increases, the ratio between GC-derived memory cells and EGC-derived memory cells changes, and the total number of memory cells increase over time. Right panel) The qualitative finding of the study is highly robust to changes in p_1 and p_2. Only a relatively narrow range of p_1 and p_2 values will be consistent with clinically observed dynamics of antibody titer and memory cell numbers, and these uncertainties will not affect the general findings of the study.

(A) Number of memory B cells derived from GCs at 5 months after Vax 2 that target dominant and subdominant epitopes, when different fractions of pre-existing memory cells generated from Vax 1 GCs were allowed to re-enter Vax 2 GCs. **(B)** Fraction of memory cells derived from Vax 2 GC that are descendants of memory cells generated from Vax 1 and re-entered Vax 2 GC, as a function of the highest affinity of such re-activated memory cells. Each GC is represented by a blue dot (n=2000). The black curve shows the mean values. The fraction of pre-existing memory cells allowed to re-enter the secondary GCs is 0.04.

(A) Number of memory B cells from simulated data that have identical sequences, shown in the order of most to least expanded sequences. A few sequences dominate the Vax 2 EGC-derived memory cells. In contrast, diverse sequences of similar sizes make up the Vax 2 GC-derived memory cells. The result is from a single simulation of 200 GCs. **(B)** Sensitivity and precision of our method for finding EGC-derived B cells tested on simulated data while assuming varying numbers of sequences were sampled. The statistics calculated with Bayesian inference and with a Monte Carlo method agree well. When only a small number of sequences are sampled, the sensitivity will be low, but the precision will be high. This is likely the case for the clinical data; however, since the actual number of memory B cells in vaccinated humans will be different from the simulated data, the quantitative numbers can be different. Sensitivity is defined as (TP/TP+FN), and precision is defined as (TP/TP+FP). TP: True Positive (EGC B cell labeled as EGC), FN: False Negative (EGC B cell labeled as GC), FP: False Positive (GC B cell labeled as EGC).

Chapter 4

lymph node DC antigen uptake and activation. C57BL/6J mice (*n*=3 animals/group) were immunized with 10 μg Cy5 dye-labled-N332-GT2 trimer and 5 μg SMNP adjuvant according to the dosing schemes shown in (**G),** and DCs in draining lymph nodes were analyzed by flow cytometry on days indicated by arrows. Shown are number of DCs (**H**)**,** representative histograms of trimer antigen fluorescence and CD86 expression by $CD11c^+$ DCs (**I**)**,** and number of $trimer^+CD86^+$ DC counts over time for bolus, 2-ED, and 7-ED immunization regimens (**J**).

Figure 4-4. *In Silico* modeling predicts increased intact antigen accumulation on FDCs for extended dosing compared to bolus immunization.....129

(**A**) Schematic showing antigen fates considered in the computational model. (**B**) *In silico* prediction of the levels of free antigen in lymph nodes over time in an intact ("soluble native") or degraded ("soluble non-native") state, and amounts of native and non-native antigen captured on FDCs in the form of immune complexes ("IC") over time. The antigen amounts are normalized to the total antigen dose in immunization. (**C**) Antibody titers predicted by the *in silico* model for bolus, 2-ED, and 7-ED immunization regimens. In the simulation, antibody titers are defined as the concentration of antibodies weighted by their affinities, reflecting their capabilities to bind to the antigen. (**D**) Comparison of predicted antigen amounts accumulated on FDCs after the final shot from each dosing scheme, normalized to the total antigen dose in immunization. (**E**) Model prediction for the number of GC B cells over time. (**F, G**) Model prediction for the number of native antigen-binding (i.e. $trimer^+$) GC B cells over time (**F**) and frequency of $trimer^+$ GC B cells at day 21 (**G**) from bolus, 2-ED, and 7-ED immunization schemes. The results reported are mean values from 10 independent stochastic simulations of the lymph node. ****, $p < 0.0001$; by one-way ANOVA with Tukey's multiple comparison post test.

Figure 4-5. Two-dose extended prime immunization enables antigen capture of the second shot on FDCs 132

(**A-B**) Groups of C57Bl/6 mice (n=3 animals/group) were immunized by bolus, 2-ED, or 7-ED regimens as in Fig. 3G followed by collection of lymph nodes for imaging at 48 h after bolus or after the last injection of 2-ED and 7-ED regimens. FDC networks were labeled *in situ* by s.c. injection of anti-CD35 antibody 16h before tissue collection. Collected tissues were clarified and imaged intact by confocal microscopy; shown are maximum intensity projections from z-stacks through FDC clusters (Scale bars, 150 μm), (**A**). Alternatively**,** lymph node sections were stained for FDCs (CD35; blue) and then analyzed by confocal microscopy (Scale bars, 300 μm) to detect co-localization with Cy5-labeled N332-GT2 (pink), (**B**). (**C-E**) Flow cytometry analysis of LN cells (*n*=3 pools/group, with each pool containing six LNs from 3 mice) isolated 48 hr after the final injection following immunization with fluorescently labeled N332-GT2 (10 ug) and SMNP (5 ug) using either bolus, 2-ED, or 7-ED dosing regimens. Shown are representative histograms of antigen intensities among LN cells (**C**)**,** frequencies of trimer+ FDCs (**D**)**,** and the mean trimer fluorescence intensity among $trimer^+$ FDCs (**E**) for the indicated immunization conditions. Shown are data from one independent experiment for each immunization series. ****, $p < 0.0001$; ***, $p < 0.001$; **, $p < 0.01$; *, $p < 0.05$; ns, not significant; by one-way ANOVA with Dunnett's multiple comparison post test compared to bolus immunization.

Figure 4-6. Extending the duration of antigen delivery during the second dose of 2-ED vaccination increases native antigen capture on FDCs and antigen-specific GC responses.....134

(**A-I**) Computational modeling of GC responses elicited by 2-ED dosing administered as two bolus doses vs. a bolus on day 0 and a prolonged antigen delivery at day 7 ("dose 2 extended"). (**A**) Schematic of 2-ED vs. "dose 2 extended" vaccination regimens. (**B, C**) Amounts of free and immune-complexed native or degraded ("non-native") antigen in the LN over time (**B**) and serum antibody titers recognizing native vs. non-native antigen (**C**) for the "dose 2 extended" regimen. (**D-F**) *In silico* prediction of antigen captured on FDCs (**D**), total GC B cells at day 21 (**E**), and frequency of trimer-binding GC B cells at day 21 (**F**) for bolus, 2-ED, and "dose 2 extended" vaccination regimens. (**G-I**) *In silico* prediction of proportions of intact vs. degraded antigen captured by FDCs (**G**), total number of GC B cells (**H**), and the fraction of GC B cells that are native vs. non-native antigen-binding (**I**) at day 21 as a function of the duration of antigen release used in "dose 2 extended" vaccination. (**J-O**) Experimental testing of "dose 2 extended" immunizations using alum-anchored immunogens. (**J**) Schematic demonstrating anchoring trimer immunogen onto alum via phosphoserine linkers (Alum-pSer). (**K-O**) C57Bl/6J mice (*n*=5 animals/group) were immunized with 10 μg MD39 trimer (either soluble bound to 50 μg alum) and 5 μg SMNP adjuvant as in Fig. 3G. Shown are the numbers of GC B cells (**K**) and Tfh cells (**L**), representative histograms of trimer staining of GC B cells (**M**), frequencies of trimer-binding GC B cells (**N**), and

the number of trimer-binding GC B cells (**O**)**,** for the different dosing regimens determined by flow cytometry at day 14. Shown are data from one representative of two independent experiments for each immunization series. ****, $p < 0.0001$; ***, $p < 0.001$; **, $p < 0.01$; *, $p < 0.05$; ns, not significant; by one-way ANOVA with Dunnett's multiple comparison post test compared to bolus immunization.

List of Tables

Chapter 2

Chapter 3

Chapter 4

Chapter 1.

Introduction

1.1. Challenges of vaccination against highly mutable viruses

Vaccination is a remarkably simple but effective solution to one of humanity's most lethal health challenges: the infectious diseases. It leverages our body's inherent ability to form immune memory to prepare us for future threats. Once exposed to a pathogen, the adaptive immune system undergoes a learning phase where antibodies and memory cells that specifically recognize that pathogen are generated and expanded. Vaccines mimic this natural process by introducing a modified form of the pathogen to the body that induces immune memory without causing the actual disease. When the body encounters the actual pathogen later, the immune system rapidly responds to neutralize the threat. The success of vaccinations has eradicated smallpox and dramatically reduced the incidence of lethal diseases like polio and measles. For these pathogens that have low rates of mutations, a single vaccine can provide lifelong immunity.

However, many viruses employ various strategies to evade our immune defense, which present a complex challenge for vaccine development. Influenza and HIV are prime examples. These viruses are highly mutable, which enables them to rapidly evade the pre-existing immune responses formed by vaccination. In the case of influenza, seasonal vaccines must be reformulated and administered each year to match the circulating strains. Even then, mismatch between the predicted vaccine strain and the dominant circulating strain occur frequently. For HIV, the extremely high mutability has prevented the development of an effective vaccine despite decades of dedicated research[1].

A complementary strategy that a virus may use to evade immunity is to deceive the immune system into targeting sites that are not crucial for the virus's functionality. For example, HIV viral proteins decay rapidly, and the immune responses are often directed toward non-native epitopes that are not present in the functional native virions[2,3]. HIV, influenza, and SARS-CoV-2 are all adept at hindering the development of antibodies that can neutralize multiple strains of the virus. Broadly neutralizing antibodies that target functional and difficult-to-mutate sites on the viral proteins have been observed for these viruses, but they are exceedingly difficult to reliably induce through vaccination.

The consequences of failing to vaccinate effectively against these viruses are enormous, from loss of human lives to economic burden. For example, the waves of new mutants extended the COVID-19 pandemic for over two years after the vaccine became available, leading to millions of deaths and substantial economic loss[4]. HIV has resulted in approximately 40 million deaths and continues to infect over a million people each year[5].

While vaccines have been successful in combating many infectious diseases, the challenges of vaccinating against more difficult viruses like influenza, HIV, and SARS-CoV-2 remain significant. Therefore, novel approaches to vaccination that can overcome these challenges are critical for global public health.

1.2. Adaptive immune system and affinity maturation

The hallmarks of adaptive immune system are the targeted specificity and memory. Unlike the innate immune system that offers fast but non-specific protection, adaptive immune system develops a highly specific response over several weeks to months upon the initial encounter with a pathogen. This process also results in the formation of immune memory that confers a specific and fast response when the same pathogen is encountered in the future.

One of the key cell types involved in the adaptive immune response is the B cell, which is responsible for the production of antibodies. B cells originate in the bone marrow and express surface B cell receptors (BCRs) which can bind to specific antigens, such as pathogenic proteins and polysaccharides. Staggering diversity of unique BCRs exist among the naïve B cells in the body due to the process of V(D)J recombination. While this repertoire of B cells typically provides many good candidates for any given pathogen, it is also unlikely to find highly specific B cells for an almost infinite array of antigens from the finite number of B cells in the body.

Therefore, upon encounter of a pathogen, the process of affinity maturation is initiated in secondary lymphoid organs like the lymph nodes and spleen. In these sites, antigen-presenting cells such as the follicular dendritic cells (FDCs) display antigen molecules on the surface for several weeks, protect them from degradation by proteases, and present to B cells. During the affinity maturation, cycles of mutation and selection refine the binding affinities of B cells. Naïve B cells that can bind to the given antigen with relatively high affinity are activated. The activated B cells enter the germinal center and undergo rapid cycles of somatic hypermutation in the BCR sequences, altering their

binding affinities to the antigen. The B cells with higher affinity for the antigen have increased capacity of internalizing antigen from the FDCs and are more likely to undergo positive selection.

Another type of cell that plays a major role in this process is the T cell. Within the germinal centers, a specialized subset of T cells, known as the follicular helper T (Tfh) cells, interact with GC B cells. The Tfh cells selectively provide survival and proliferation signals to the GC B cells that present highest amounts of peptide-Major Histocompatibility Complex (pMHC) complexes. This interaction ensures that B cells with high binding affinities towards the antigen will preferentially expand and continue to mutate.

During the process of affinity maturation, B cells continuously differentiate into memory cells and plasma cells. Memory cells serve as a long-term immune reservoir that can quickly respond upon re-encounter with the same or similar antigen in the future. Plasma cells produce large amounts of antibodies that are released into bloodstream and lymphatic system.

1.3. B cell immunodominance

During the evolutionary process in affinity maturation, B cells with high affinities undergo clonal expansion, while those that fail to get positively selected undergo apoptosis. A germinal center is initiated by 100-200 distinct founder B cells, but over time the diversity is lost[6]. For example, when mice are immunized with germline-targeting antigen that bind with high affinity to a small fraction ($\sim$1 in 10^6) of naïve B cells, the descendants of these B cells dominated GCs by day 20[7]. The rate at which diversity is stochastic and may also depend on factors such as the distribution of germline-endowed affinities, mutational landscape, and stringency of selection[6–9].

B cell immunodominance refers to the phenomenon where certain epitopes on an antigen preferentially elicit a stronger B cell response than others. Understanding the B cell immunodominance has emerged as an important challenge, especially in the context of mutable viruses like influenza, SARS-CoV-2, and HIV. These viruses, with the ability to rapidly mutate many of their epitopes, present a unique challenge for vaccine development.

For instance, the influenza virus has five canonical antigenic sites on its head domain (Ca1, Ca2, Cb, Sa, and Sb) which are highly immunodominant and highly variable[10]. These antigenic sites are most frequently targeted during natural infection and vaccination, but quickly undergo antigenic drift to allow the virus to escape neutralization from host immunity. This focus on the

immunodominant sites can overshadow and limit the antibody response to other epitopes that might offer longer-lasting protection, such as the receptor binding site (RBS) or the conserved stalk domain. Similarly, with SARS-CoV-2, despite the presence of numerous B cell epitopes on the receptor-binding domain (RBD) of the spike protein, certain regions have been observed to be both immunodominant and more mutable than others[11]. HIV is currently the most virus to vaccinate against. It is not only extremely mutable, but also has inherently unstable envelope glycoprotein (Env) trimer that rapidly degrades in vivo. When the unstable trimer breaks down, it reveals non-native epitopes, also referred to as neoepitopes. These regions are not typically exposed on the functional, fusion-competent viral trimer. However, they can be highly immunogenic, meaning they elicit strong immune responses. As a result, the immune system often produces antibodies against these neoepitopes rather than against the native regions that might confer broad neutralizing protection[2].

Recognizing and understanding immunodominance have profound implications for vaccine design. Traditional vaccination strategies often lead to strong responses against mutable or non-neutralizing regions of a virus. To combat mutable and difficult viruses effectively, it will be beneficial to divert the immune response from these immunodominant but less protective regions to more conserved and functionally relevant areas. By engineering vaccines that can change B cell immunodominance, it will be possible to guide the immune system to target these conserved regions, resulting in broader and more durable protection.

1.4. Thesis Outline

In this thesis, we present three projects that address the problems of B cell immunodominance outlined above. The thesis integrates materials from two first-authored publications by the author and one co-first-authored manuscript currently in development. Chapter 2 and 3 are reproductions of reference[12] and reference[13], respectively, with minor modifications in formatting. Chapter 4 is a reproduction of a manuscript currently in submission for review.

In Chapter 2, we develop computational model to explore how the designs of immunogens interact with GC biology to establish or subvert immunodominance. We focus on two designed influenza immunogens aimed at eliciting B cells to target the receptor-binding site with cross-reactivity across multiple strains. These immunogens were designed by collaborators and tested in mice. Our computational analysis combined with the experimental observation indicates that an

immunogen's ability to elicit cross-reactive antibody production hinges on the interplay between B cell antigen engagement and T cell-driven selection within germinal centers.

In Chapter 3, we explore how repeated immunization can relax B cell immunodominance hierarchy to elicit increased subdominant responses towards conserved epitopes. This project was motivated by the observation that the third dose of SARS-CoV-2 mRNA vaccine, containing the original Wuhan strain, elicited much higher neutralizing antibody titer against the highly mutated Omicron variant. Using computational model and clinical antibody data, we propose that the antigen presentation dynamics play a key role in modulating immunodominance hierarchy.

In Chapter 4, we explore how "extended priming" can amplify humoral immune response. Specifically, we investigate its ability to induce superior response targeting native antigens during immunization with HIV Env trimers, which is typically subdominant compared to non-native epitopes. Using an iteration of mathematical models and immunization experiments in mice, we introduce a practical strategy for vaccine delivery, ensuring better T follicular helper cell and antigen-specific germinal center B cell reactions.

1.5. Statements on Collaboration

The three projects presented in this thesis benefited from fruitful collaborations with experimental collaborators.

The work on modeling the B cell response to designed influenza immunogens in Chapter 2 was carried out in collaboration with Dr. Tim Caradonna who was a graduate student in Aaron Schmidt Group at Harvard. Dr. Caradonna led the experimental efforts for synthesizing and characterizing immunogens, and obtaining mice immunization data obtained that was used to corroborate the insights from the model.

The work on modeling the response to SARS-CoV-2 vaccination in Chapter 3 was carried out in collaboration with Dr. Matthew Van Beek who was a graduate student in the Chakraborty Group. This work also benefited from collaboration with experimental researchers from The Rockefeller University, led by Dr. Zijun (Vinci) Wang from Michel Nussenzweig Group. They performed the measurements of monoclonal antibody IC50 values against SARS-CoV-2 viruses that were used to validate the model predictions.

The work on modeling the immune response to slow delivery of antigen in Chapter 4 was carried out in collaboration with Dr. Sachin Bhagchandani who was a graduate student in Darrell Irvine Group at MIT. He led the experimental work of mice immunizations and characterizations of their responses. Iterations of experiments and modeling enabled the progress described in this work.

1.6. Chapter 1 References

1. Burton, D.R. (2019). Advancing an HIV vaccine; advancing vaccinology. Nat Rev Immunol *19*, 77–78. 10.1038/s41577-018-0103-6.

2. Hu, J.K., Crampton, J.C., Cupo, A., Ketas, T., Gils, M.J. van, Sliepen, K., Taeye, S.W. de, Sok, D., Ozorowski, G., Deresa, I., et al. (2015). Murine Antibody Responses to Cleaved Soluble HIV-1 Envelope Trimers Are Highly Restricted in Specificity. J Virol *89*, 10383–10398. 10.1128/jvi.01653-15.

3. Aung, A., Cui, A., Maiorino, L., Amini, A.P., Gregory, J.R., Bukenya, M., Zhang, Y., Lee, H., Cottrell, C.A., Morgan, D.M., et al. (2023). Low protease activity in B cell follicles promotes retention of intact antigens after immunization. Science *379*, eabn8934. 10.1126/science.abn8934.

4. Yang, J., Vaghela, S., Yarnoff, B., Boisvilliers, S.D., Fusco, M.D., Wiemken, T.L., Kyaw, M.H., McLaughlin, J.M., and Nguyen, J.L. (2023). Estimated global public health and economic impact of COVID-19 vaccines in the pre-omicron era using real-world empirical data. Expert Rev. Vaccines *22*, 54–65. 10.1080/14760584.2023.2157817.

5. Bekker, L.-G., Beyrer, C., Mgodi, N., Lewin, S.R., Delany-Moretlwe, S., Taiwo, B., Masters, M.C., and Lazarus, J.V. (2023). HIV infection. Nat. Rev. Dis. Prim. *9*, 42. 10.1038/s41572-023-00452-3.

6. Tas, J.M.J., Mesin, L., Pasqual, G., Targ, S., Jacobsen, J.T., Mano, Y.M., Chen, C.S., Weill, J.-C., Reynaud, C.-A., Browne, E.P., et al. (2016). Visualizing antibody affinity maturation in germinal centers. Science *351*, 1048–1054. 10.1126/science.aad3439.

7. Abbott, R.K., Lee, J.H., Menis, S., Skog, P., Rossi, M., Ota, T., Kulp, D.W., Bhullar, D., Kalyuzhniy, O., Havenar-Daughton, C., et al. (2018). Precursor Frequency and Affinity Determine B Cell Competitive Fitness in Germinal Centers, Tested with Germline-Targeting HIV Vaccine Immunogens. Immunity *48*, 133-146.e6. 10.1016/j.immuni.2017.11.023.

8. Victora, G.D., and Wilson, P.C. (2015). Germinal Center Selection and the Antibody Response to Influenza. Cell *163*, 545–548. 10.1016/j.cell.2015.10.004.

9. Amitai, A., Mesin, L., Victora, G.D., Kardar, M., and Chakraborty, A.K. (2017). A Population Dynamics Model for Clonal Diversity in a Germinal Center. Front. Microbiol. *8*, 1693. 10.3389/fmicb.2017.01693.

10. Angeletti, D., Gibbs, J.S., Angel, M., Kosik, I., Hickman, H.D., Frank, G.M., Das, S.R., Wheatley, A.K., Prabhakaran, M., Leggat, D.J., et al. (2017). Defining B cell immunodominance to viruses. Nat. Immunol. *18*, 456–463. 10.1038/ni.3680.

11. Andreano, E., Paciello, I., Pierleoni, G., Piccini, G., Abbiento, V., Antonelli, G., Pileri, P., Manganaro, N., Pantano, E., Maccari, G., et al. (2023). B cell analyses after SARS-CoV-2 mRNA third vaccination reveals a hybrid immunity like antibody response. Nat. Commun. *14*, 53. 10.1038/s41467-022-35781-6.

12. Yang, L., Caradonna, T.M., Schmidt, A.G., and Chakraborty, A.K. (2022). Mechanisms that promote the evolution of cross-reactive antibodies upon vaccination with designed influenza immunogens. Cell Rep. *42*, 112160. 10.1016/j.celrep.2023.112160.

13. Yang, L., Beek, M.V., Wang, Z., Muecksch, F., Canis, M., Hatziioannou, T., Bieniasz, P.D., Nussenzweig, M.C., and Chakraborty, A.K. (2022). Antigen presentation dynamics shape the antibody response to variants like SARS-CoV-2 Omicron after multiple vaccinations with the original strain. Cell Rep. *42*, 112256. 10.1016/j.celrep.2023.112256.

Chapter 2.

Mechanisms that promote the evolution of cross-reactive antibodies upon vaccination with designed influenza immunogens

2.1. Summary

Immunogens that elicit broadly neutralizing antibodies targeting the conserved receptor-binding site (RBS) on influenza hemagglutinin may serve as candidates for a universal influenza vaccine. Here, we develop a computational model to interrogate antibody evolution by affinity maturation after immunization with two types of immunogens: a heterotrimeric 'chimera' hemagglutinin that is enriched for the RBS epitope relative to other B cell epitopes, and a cocktail composed of three non-epitope-enriched homotrimers of the monomers that comprise the chimera. Experiments in mice (Caradonna et al.) find that the chimera outperforms the cocktail for eliciting RBS-directed antibodies. We show that this result follows from an interplay between how B cells engage these antigens and interact with diverse helper T cells, and requires T cell-mediated selection of germinal center B cells to be a stringent constraint. Our results shed light on antibody evolution and highlight how immunogen design and T cells modulate vaccination outcomes.

2.2. Introduction

The mutability of viruses like human immunodeficiency virus (HIV) and influenza poses a major public health challenge. No effective vaccine is available for HIV, and seasonal variation of influenza requires annual vaccine reformulation. Additionally, the severe acute respiratory syndrome coronavirus 2 (SARS-CoV-2) is rapidly evolving variants that reduce the efficacy of current vaccines, thus raising the possibility that booster shots may be required periodically[1,2]. Developing vaccines that can induce broadly neutralizing antibodies (bnAbs) against highly mutable pathogens could address these challenges. BnAbs can neutralize diverse mutant strains by targeting relatively conserved regions on viral surface-exposed proteins. Although bnAbs for both HIV[3–5] and influenza[6–8] have been identified, their natural development is typically rare and delayed.[9,10] Therefore, significant efforts are devoted to designing immunogens[11–13] or vaccination regimens[14,15] that may elicit bnAbs with the ultimate goal of creating so-called "universal" vaccines. The complexity of this

challenge has also motivated several theoretical and computational studies focused on the mechanisms underlying bnAb evolution.[16–26]

Upon natural infection or vaccination, antibodies are elicited through a Darwinian evolutionary process called affinity maturation.[27] Naive B cells that express a B cell receptor (BCR) with sufficiently high affinity for an antigen, such as a viral protein, can seed germinal centers (GCs). GC B cells multiply and diversify their BCRs through somatic hypermutation, and subsequently interact with the antigen presented on follicular dendritic cells (FDCs). GC B cells internalize varying amounts of antigen based on the binding affinity of their BCRs to the cognate antigen and then display peptides derived from the antigen complexed with class II MHC molecules (pMHC complexes) on their surfaces.[28] These B cells compete to interact with helper T cells. Productive interactions result in a positive selection that leads to proliferation and mutation, while failure to obtain sufficient help signal triggers B cell apoptosis. Many rounds of mutation and selection ensue, resulting in a progressive increase in B cell binding affinity; some B cells differentiate into memory B cells and plasma cells that produce antibodies.[29]

BnAb evolution is rare upon natural infection for at least two reasons. First, the frequency of germline B cell precursors that target conserved epitopes is low.[30] Many germline B cells that target highly variable regions on the antigen can co-seed GCs and ultimately outcompete rare B cells that recognize the conserved epitope during affinity maturation.[31] Second, the conserved epitope-directed B cell precursors may acquire "specializing" mutations and lose their breadth of coverage during affinity maturation.[16,32,33] Specialization can occur if the BCR binding footprint is larger than the exposed conserved region on the antigen epitope, which is true for both HIV and influenza RBS epitopes.[32,34] In this case, the BCR can develop strong interactions not with the conserved residues but with the variable residues surrounding them. Therefore, an engineered immunogen that selectively enriches rare B cell precursors for the conserved epitope and also guides them to acquire mutations that promote high breadth is necessary for eliciting bnAbs.

Here, we develop a computational model to study the mechanisms that influence the evolution of influenza RBS-directed B cells during affinity maturation. Toward this goal, we study the relative efficacy of RBS-directed B cell evolution upon vaccination with two different types of designed immunogens.[35] Both immunogens are "resurfaced" hemagglutinin (rsHA) immunogens, where the RBS epitope of H1 A/Solomon Islands/03/2006 (H1 SI-06) is grafted onto antigenically distinct H3, H4, and H14 hemagglutinin (HA) head scaffolds (**Fig. 2-1A**) [36]. The first type of immunogen is an rsHA trimeric 'chimera', a cystine-stabilized rsH3-rsH4-rsH14 heterotrimer each presenting the same H1

SI-06 RBS epitope; due to the antigenic distance between the H3, H4, and H14 scaffolds, the RBS epitope is enriched relative to all other epitopes.[37] The second type is a cocktail of non-epitope-enriched homotrimers of each rsHA; this cocktail contains the same rsHA monomers as the chimera but as homotrimers rather than a single heterotrimer.

Caradonna et al. report that immunization with the chimera and cocktail immunogens in mice both elicit cross-reactive RBS-directed B cells, but the chimera qualitatively outperforms the cocktail[35]. Our computational results reveal the mechanism underlying this result. By studying these complex immunogens, we show how the outcome of GC processes is determined by the interplay of multiple factors: how B cells engage with these immunogens and internalize antigen, the diversity of helper T cells that GC B cells can interact with, and the stringency of helper T cell-mediated selection. We find that upon immunization with the cocktail of homotrimers, only the cross-reactive B cells can interact with T cells of diverse specificities, while the strain-specific B cells must rely on a restricted set of helper T cells. In contrast, upon immunization with the chimeric heterotrimer, both cross-reactive and strain-specific B cells can interact with T cells of diverse specificities. So, intuition may lead us to the conclusion that immunization with the cocktail of homotrimers should perform better than the chimeric heterotrimer at promoting the evolution of cross-reactive B cells. The experiments show that the opposite is true. This is because, upon immunization with the chimera, the cross-reactive B cells internalize far more antigen than the strain-specific B cells in the early GCs, while these two types of B cells internalize similar amounts of antigen upon immunization with the cocktail. We show that the chimera performs better as a result of more effective antigen internalization coupled with helper T cells stringently discriminating between B cells based on the amount of pMHC displayed.

Previously, Gitlin et al. showed that T cell help is a stringent constraint on the selection of GC B cells,[38] while another study suggested that this was not so.[39] Our finding that T cell help must be a stringent constraint on B cell evolution in the GC helps resolve this debate. Furthermore, these data highlight the importance of immunogen design and helper T cells in determining vaccination outcomes and suggest that modulating these effects is necessary to elicit influenza RBS-directed B cells with breadth.

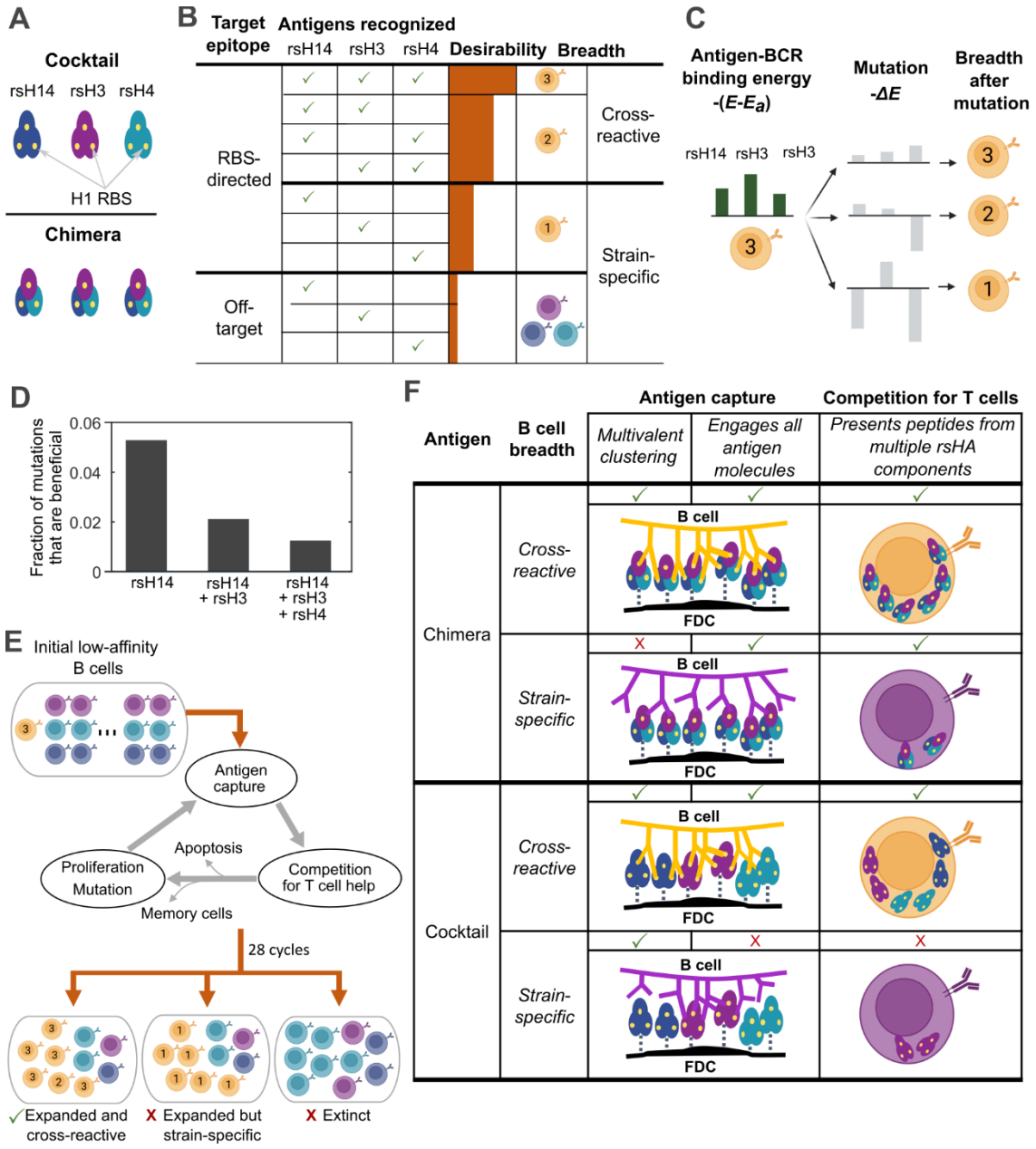

Figure 2-1. Schematics of the study design. (A) Schematic of the two rsHA immunogen designs: the cocktail of three rsHA homotrimers, and the heterotrimeric 'chimera'. **(B)** Classifications of the GC B cells based on their target epitopes as RBS-directed or off-target, and based on their breadths as cross-reactive or strain-specific; an RBS-directed B cell can bind three, two, or one of the rsHA components and an off-target B cell can only bind one of the three components. **(C)** Schematics of how a mutation can alter the breadth of an RBS-directed B cell. **(D)** Fraction of affinity-changing mutations in the simulations that are beneficial for one or two specific rsHA components, or all three. Interchanging the specific rsHA components referred to in the panel yields the same result. **(E)** Schematics of the affinity maturation simulation, and three general possible outcomes of the GCs. The most desirable outcome is that the rare RBS-directed B cells are expanded, and the descending B cells are cross-reactive. **(F)** Schematics that summarize how the designs of the two immunogens affect the abilities of cross-reactive and strain-specific B cells to capture antigen and compete for T cell help.

2.3. Results

2.3.1. Model development

Overview of the model

We simulate GC reactions induced by either the cocktail or the chimera immunogens, described above and in Caradonna et al.[35] The GC B cells that bind to these antigens are classified as either "RBS-directed" or "off-target". The three HA scaffolds are antigenically distinct; the sequence homologies between the rsHA components are ~58.4% (rsH3-rsH4), ~60.5% (rsH3-rsH14), and ~72.5% (rsH4-rsH14). These values are comparable to or lower than the HA sequence homology of ~70.8% between a pandemic influenza strain and a previous strain (H1N1 A/California/4/2009 and H1N1 A/Solomon Islands/3/2006), and are much lower than the typical sequence homology resulting from antigenic drift (*e.g.,* ~95.4% between H1N1 A/New Caledonia/20/1999 and H1N1 A/Solomon Islands/3/2006). Therefore, while it may not be impossible for off-target B cells to develop cross-reactivity towards multiple rsHA components, such cases are likely very rare. In our model, we assume an off-target B cell is always strain-specific and can only target one of the rsHA components (**Fig. 2-1B**).

An RBS-directed B cell can potentially target all three components because of the similarities of the resurfaced RBS regions. However, because the grafted RBS is smaller than the typical footprint of a BCR, we account for the fact that RBS-directed B cells must contact peripheral residues that are variable. Thus, different RBS-directed B cells may have different breadths in our model, as summarized in **Fig. 2-1B**. A mutation changes the binding free energies of an RBS-directed B cell for the three rsHA components differently (**Fig. 2-1C**). These changes are drawn from a positively correlated probability distribution to account for the similarities of the RBS regions. Yet, some mutations will be beneficial for binding to one or two rsHA components and deleterious for the others (**Fig. 2-1D**). As affinity maturation progresses, the affinities of an RBS-directed B cell for the three components can vary and even fall below the recognition threshold for some components.

Fig. 2-1E describes the process that occurs in germinal centers. Because off-target germline B cells outnumber the RBS-directed germline B cells,[32,40] we seed each GC with 99 off-target B cells and 1 RBS-directed B cell, making the total founder number representative of GCs in mice.[41] Each off-target B cell is randomly designated a single rsHA target at the beginning of the simulation. To model the GC dynamics in mice, founder B cells divide four times without mutation, and then, the competitive phase of affinity maturation lasts for 28 cycles, or ~14 days.[29,42] These B cells undergo

cycles of antigen capture and competition for T cell help. In each cycle, B cells that fail positive selection are subsequently removed from the GC via apoptosis. Additionally, ~10 % of positively selected B cells stochastically differentiate into memory and plasma cells and exit the GC. The remaining positively selected B cells divide twice,[43] and one daughter cell mutates in each division.[44]

In this study, we ask how the design of an immunogen affects its ability to expand the RBS-directed B cells in GCs and to shepherd them to acquire mutations that confer cross-reactivity. Undesirable alternative outcomes are that RBS-directed B cells become outcompeted by off-target B cells, or that they become strain-specific by acquiring specializing mutations (**Fig. 2-1E**). The chimera and cocktail immunogens give advantages to cross-reactive B cells over strain-specific B cells in different ways during the antigen capture and T cell help steps, as summarized in **Fig. 2-1F**. The chimera antigen presented on the FDC during the antigen capture step can form multivalent clusters with cross-reactive B cells but not with strain-specific B cells. This is because a cross-reactive RBS-directed B cell can bind to a single chimera molecule with up to three BCRs, but a strain-specific B cell can bind to a single chimera molecule with, at most, one BCR. Then, during the competition for T cell help, both cross-reactive and strain-specific B cells that capture the chimera can present peptides from all three rsHA components (**Fig. 2-1F**).

In contrast, after cocktail immunization, both cross-reactive B cells and strain-specific B cells can engage a single antigen trimer with multiple BCRs, and thus form multivalent clusters between BCRs and antigen molecules. However, the strain-specific B cells can only recognize a third of the total antigen molecules. Then, during the competition for T cell help, only the cross-reactive B cells present peptides from multiple rsHA components, while strain-specific B cells only present the peptides from the single component that they target (**Fig. 2-1F**).

Initial condition and mutation of B cells

The initial free energy of binding (or affinity) is set to be E_a for the target rsHA component for the off-target B cells. For simplicity, the RBS-directed precursors are assumed to initially bind all three components with affinity, E_a. The absolute value of E_a does not affect the results because all other free energies are scaled to this reference. We choose E_a = -13.8 k_BT, where k_B is the Boltzmann constant and T is the temperature (~300 K), because it corresponds to a dissociation coefficient, K_d, of 1 μM, which is approximately the threshold for naive B cell activation.[45]

A mutation is either fatal, silent, or affinity-changing with probabilities of 0.3, 0.5, and 0.2, respectively.[46] The PINT database shows that affinity changes of protein-protein interfaces upon mutations are more likely to decrease than to increase the binding affinity.[47] We describe this data using a shifted log-normal distribution; for an off-target B cell, i, the free energy change due to mutation is given by:

$$\Delta E_i = e^{\mu+\sigma Y} - \delta \qquad (1)$$

where Y is a standard normal random variable, and μ, σ, and δ are parameters chosen so that about 5% of the mutations are beneficial.[16,18]

For RBS-directed B cells, a mutation changes the binding affinities towards the rsHA components differently. However, the marginal distribution of affinity change towards any one component should be equivalent to that of an off-target B cell mutation. To model this, we draw three random numbers $\bar{y} = [y_1, y_2, y_3]$, one for each component, from a multivariate Gaussian distribution with the mean of zero and the covariance matrix of Λ, as follows:

$$\bar{y} \sim \frac{\exp\left(-\frac{1}{2}\bar{y}^T\Lambda^{-1}\bar{y}\right)}{\sqrt{(2\pi)^3|\Lambda|}} \qquad (2)$$

where $\Lambda = \begin{bmatrix} 1 & \rho & \rho \\ \rho & 1 & \rho \\ \rho & \rho & 1 \end{bmatrix}$. Choosing the correlation, ρ, to be smaller than 1 allows us to study the effects of the mutations that make B cells specialize to a subset of rsHA components. For a given RBS-directed B cell, i, each sampled number, y_j, corresponding to the rsHA component, j, is then converted to the free energy change due to mutation, ΔE_{ij}, for this variant analogous to Eq. 1 as follows:

$$\Delta E_{ij} = e^{\mu+\sigma y_j} - \delta \qquad (3)$$

We chose $\rho = 0.7$; we have also carried out calculations with $\rho = 0.4$ and the qualitative findings are not affected by this change. In Eq. 2, by using symmetric Λ, we treat the antigenic differences between the RBS epitopes of the three rsHA components to be equidistant. Since the RBS is grafted on to the scaffold, the variations among the RBS epitopes should be smaller than the differences between the scaffolds, and not directly correlated to them. For simplicity, and because the qualitative findings of the study do not depend on changing ρ, we use the same value for each pair.

Antigen capture by B cells

GC B cells extract antigens from the surfaces of FDCs using mechanical pulling forces.[28,48] The B cell synapse interacting with an FDC is modeled as a 2-dimensional circle divided into lattice points occupied by antigen molecules and BCRs.[49,50] BCRs and antigen molecules are initially randomly distributed on the lattice. The lattice spacing is 10 nm, which is of the same order as the collision radius of BCR and ligand.[50] During the clustering phase, BCR and antigen molecules diffuse freely and attempt to bind when they are within one lattice point (see METHODS for details). The probability of success is:

$$p_{on} = 1 - \mathrm{e}^{-q_{on}\Delta t} \cdot [E_{ij} \leq E_a] \tag{4}$$

where the Iverson bracket sets the minimum affinity required for binding to be E_a, which is equal to the initial B cell affinity, and

$$q_{on} = q_{on}^0 n_{arm} n_{ep} \tag{1}$$

represents the steric factor. This factor is determined by n_{arm}, the number of free BCR arms (between 0 and 2); n_{ep}, the number of free cognate BCR epitopes on the antigen (between 0 and 3); and the basal rate q_{on}^0= 10 s^{-1}. With $\Delta t = 5 \times 10^{-4}$ s, which is the characteristic time scale of diffusion over the lattice, this basal rate results in the successful binding probability of $p_{on} = 5 \times 10^{-3}$. This number approximately accounts for the entropic penalty of aligning two molecules.

An established antigen-BCR bond (labeled, *i* below) breaks with probability,

$$p_i^{off} = 1 - \mathrm{e}^{-k_i^{off}\Delta t} \tag{6}$$

where k_i^{off} is its off-rate. Assuming the activation barrier for bond formation is negligible compared to the binding free energy, the off-rate is related to binding free energy by:

$$k_i^{off} = k_0^{off}\, e^{E_{ij}/k_B T}\,. \tag{7}$$

where E_{ij} is the binding free energy of BCR, *i*, for antigen, *j*, and k_0^{off} = 10^6 s^{-1}.[45]

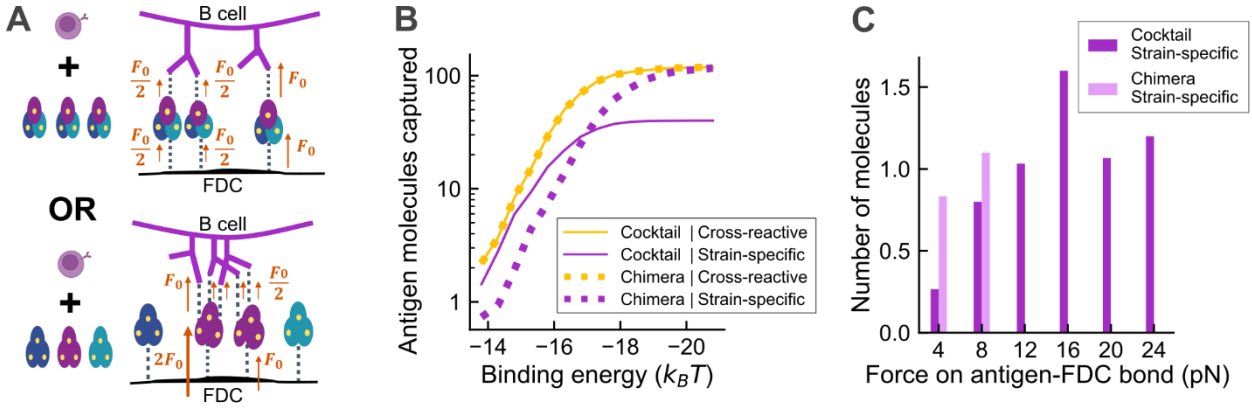

Figure 2-2. Effect of immunogen design on antigen capture by B cells. (A) Schematics of the force-based antigen extraction by a strain-specific B cell. For the chimera, the only two possible configurations of antigen and BCR interactions are shown. For the cocktail, an example among many possible configurations of BCR-antigen clusters is shown. For the heterotrimeric chimera, one antigen molecule can be bound by only one BCR, so the pulling force on the antigen-FDC bond is always equal to the pulling force on the antigen-BCR bond. For the homotrimer molecules in the cocktail, multiple BCRs can pull on the same cognate antigen molecule so that greater force accumulates on the antigen-FDC bond. **(B)** Amount of antigen captured as a function of antigen-BCR binding affinity. For the cross-reactive B cell, when the binding affinity towards all three rsHA components is equal is shown. **(C)** Histogram of the forces on antigen-FDC bonds when either the cocktail or the chimera antigen molecules are extracted by a strain-specific B cell of low affinity (-14.8 k_BT). Panels **B** and **C** were constructed by taking the mean value from 30 simulations. See also **Fig. 2-S1.**

Our simulations result in the formation of antigen-BCR clusters, dependent on the cross-reactivity of the B cell and the design of the antigen. The clustering is followed by antigen internalization through mechanical pulling. We assume that antigen molecules are tethered to the FDC membrane with a binding free energy of -19 k_BT, which makes antigen capture most sensitive to affinity change in K_d of 1 – 0.01 μM range, but affinity ceiling is reached when K_d << 1 nM.[45] A pulling force of 8 pN is applied to each BCR,[28] which is transferred to the antigen-BCR bonds and the antigen-FDC bonds,[51] as schematically shown in **Fig. 2-2A**. If a BCR is bound to 2 antigen molecules, the force is divided equally by the two arms of the BCR. For a given antigen molecule, the force applied to its antigen-FDC bond is the sum of forces applied by all the BCR arms bound to it. The off-rates of both antigen-FDC and antigen-BCR bonds increase with the applied force[52]:

$$k_F^{off} = k^{off} \times \exp\left(\frac{x_b F}{k_B T}\right) \quad (8)$$

where k_F^{off} is the off-rate under force, F is the force and x_b is the bond length, taken to be 1 nm.[53] When an antigen-BCR bond breaks, the BCR goes into a refractory state, which prevents instant rebinding with the same antigen.[53] The duration is taken to be 0.1 s, which is much greater than the antigen diffusion timescale of 5×10^{-4} s (see METHODS). At the end of each time step, any BCR or antigen-BCR cluster that is not connected to the FDC is internalized.

2.3.2. Antigen capture depends on immunogen design and cross-reactivity of B cells

Fig. 2-2B shows the total amount of antigen captured as a function of BCR binding affinity for cross-reactive and strain-specific B cells, capturing the cocktail or the chimera immunogen. Notably, neither immunogen design is better at conferring an advantage to RBS-directed B cells in capturing antigens across the entire affinity range. At low affinity, representative of the early GC, the advantage of cross-reactive B cells over strain-specific B cells is greater for the chimera. At high affinity, the opposite is true.

At low affinity, antigen availability is not limiting, and the amount of antigen captured is largely determined by the forces imposed on the antigen-FDC bonds by the BCRs bound to the antigen molecules. A strain-specific B cell can engage a homotrimeric antigen in the cocktail with multiple BCRs, but not the chimera (**Fig. 2-1F and 2-S1A**). Therefore, the forces on the antigen-FDC bonds are typically higher for the homotrimeric antigen bound by strain-specific B cells compared to the chimera bound by such cells. This point is illustrated quantitatively using results from our simulations. At the low B cell affinity of -14.8 k_BT, successful extraction of homotrimers in the cocktail frequently results from high forces on antigen-FDC bonds (**Fig. 2-2C**), enabled by clustering of antigens and BCRs. When multiple BCRs pull on the same antigen, the force on the antigen-FDC bond is greater than the force on each of the antigen-BCR bonds (**Fig. 2-2A**), so the off-rate of the former is relatively increased. The maximum possible force of 24 pN is realized when three BCRs are bound to one antigen, each contributing 8 pN of force. Using Eq. 8, the off-rate for the antigen-FDC bond increases by ~300-fold if an antigen is bound by three BCRs, while the off-rate for each antigen-BCR bond increases by ~7-fold. For the strain-specific B cells capturing the chimera, however, the force on the antigen-FDC bond is always equal to the force on a single antigen-BCR bond because only one

BCR can bind to an antigen (**Fig. 2-2A**). Thus, the pulling forces do not increase the relative off-rate of the antigen-FDC bond compared the antigen-BCR bonds. This is why low-affinity strain-specific B cells internalize smaller amounts of the heterotrimeric antigen than homotrimeric antigen (**Fig. 2-2B**). For both types of immunogens, cross-reactive RBS-directed B cells can bind an antigen molecule with multiple BCRs (**Fig. 2-1F** and **Fig. 2-S1B**). So, at low affinity, these cells capture a larger amount of antigen relative to strain-specific B cells for the chimera and a similar amount of antigen for the cocktail (**Fig. 2-2B**).

For high BCR affinity, the cross-reactive B cells capture more antigen than the strain-specific B cells do when interacting with the cocktail of homotrimers (**Fig. 2-2B**). Beyond a certain affinity, the amount of antigen captured plateaus for the cocktail; this plateau corresponds to the B cell binding affinity approaching the antigen-FDC bond energy of -19 k_BT. As a result, B cells capture most of the cognate antigens they encounter (**Fig. 2-2B**). Consequently, antigen availability becomes a limiting factor, and cross-reactive B cells are favored because they can bind all antigens while strain-specific B cells only recognize about a third of the antigen molecules presented in the cocktail. For the chimera, however, all antigen molecules can be internalized successfully even with monomeric bonds at very high affinity, so the advantage of cross-reactive B cells is small.

The results of antigen capture shown were obtained from simulations with 120 BCRs and 120 antigen molecules in the immune synapse. The multivalent antigen-BCR clustering behaviors are well manifested at this number (**Fig. 2-S1B**). Changing these numbers does not change the qualitative trends of antigen capture (**Figs. 2-S1C, 2-S1D**), because they are the results of qualitative differences in the ways B cells and antigens engage based on their types, as described above.

2.3.3. Cross-reactive B cells evolve more readily upon immunization with the chimera if T cell help is a stringent constraint for the positive selection of GC B cells

After antigen capture, B cells compete for positive selection by helper T cells by presenting the T cell epitopes that are derived from the internalized antigen. The homotrimeric cocktail allows only cross-reactive B cells to capture diverse rsHA components, while the nature of the chimeric design allows both cross-reactive and strain-specific B cells to internalize all three components (**Fig. 2-3A**). Thus, after immunization with the chimera, all B cells will compete for diverse T cells and the differences in competitive advantages will be based on the amounts of antigen captured. However, if the T cell epitopes contained in each rsHA variant are distinct sets, then upon immunization with the

cocktail, only the cross-reactive B cells can interact with diverse T cells while strain-specific B cells can only interact with a subset of the T cells (**Fig. 2-3A**). This is because each T cell is specific for its epitope, and a single mutation within a TCR epitope or flanking sites can abrogate recognition.[54–57]

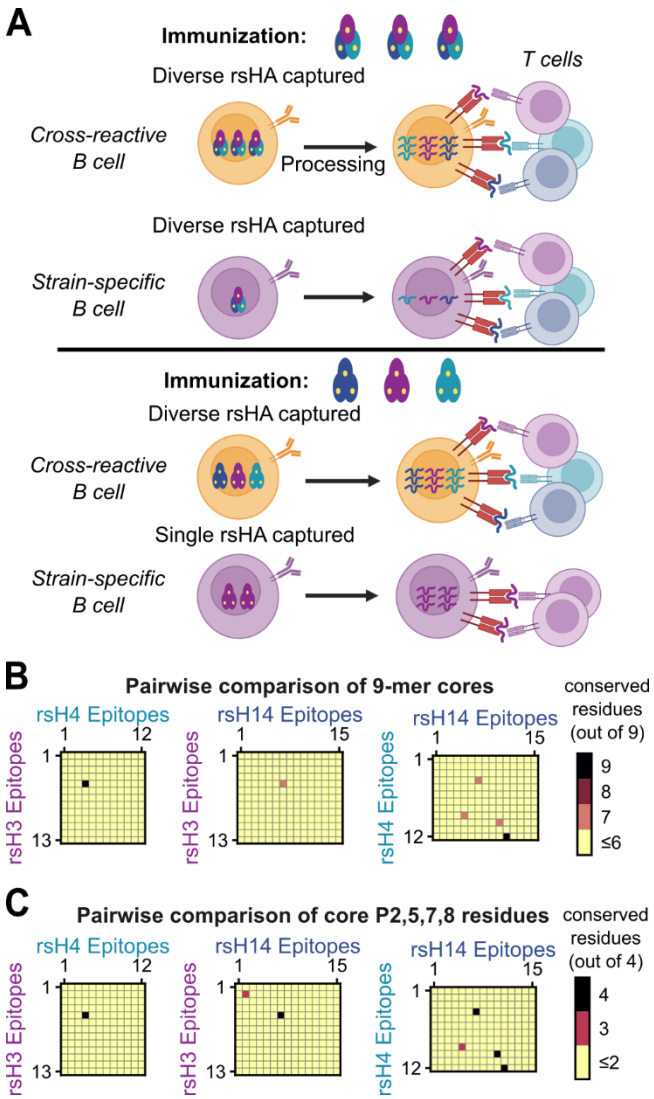

Figure 2-3. Effect of immunogen design on selection by T cells. (A) Schematics showing the differences between how cross-reactive and strain-specific B cells interact with helper T cells. For immunization with the chimera, both strain-specific and cross-reactive B cells present pMHCs from all three rsHA components, but the cross-reactive B cells capture much more antigen. For the cocktail immunization, only the cross-reactive RBS-directed B cells present pMHCs derived from multiple rsHA components, but the amount of antigen captured is not sufficiently different. **(B-C)** Pairwise comparison of computationally predicted helper T cell epitopes in the rsHA components. Each axis corresponds to the ranks of the top 20 percentile predicted 15-mer T cell epitopes, derived from the three rsHA components. (**B**) Number of conserved residues in pairwise comparisons of the 9-mer cores of the predicted epitopes. (**C**) Number of conserved residues in pairwise comparisons of the P2, P5, P7 and P8 residues of the 9-mer cores. See also **Table 2-S1**, **Figure 2-S2**.

The rsHA components use antigenically distinct scaffolds derived from different subtypes, which results in large antigenic distances between the overall proteins (except for the RBS epitope). The large antigenic distance between the scaffolds raises the possibility that the components in the cocktail carry distinct T cell epitopes.

We used the Immune Epitope Database and Analysis Resource (IEDB) MHCII binding prediction tool to analyze the predicted T cell epitopes in the H3, H4, and H14 rsHA components (**Table 2-S1**).[58–62] Mice immunized with the cocktail or the chimera immunogens were mixed 129/Sv and C57BL/6 mice. Therefore, we used the I-A^b MHC allele to ask whether the T cell epitopes contained in the three HA components were distinct. None of the predicted 15-mer peptides that ranked in the top 20 percentile against randomly generated peptides were fully conserved in two different variants. When we relaxed the comparison criteria to just the 9-mer cores, still only two pairs were conserved in two different variants (**Fig. 2-3B**). We further focused on the identity of just P2, 5, 7, and 8 of the cores, which are the most likely TCR-contacting residues for the I-A^b haplotype.[63] Still, only five pairs were conserved in all pairwise comparisons (**Fig. 2-3C**). In mice with I-A^b haplotype, B cells that capture rabbit serum albumin and human serum albumin (76% sequence homology) do not compete with each other due to mutations in T cell epitopes.[64] For this rabbit and human serum albumin, we found 3 pairs of conserved 9-mer cores and 3 pairs of conserved peptides 2, 5, 7, and 8 in both proteins, which is comparable to the resurfaced HA components (**Fig. 2-S2**). Therefore, we conclude that the components of the cocktail likely contain distinct T cell epitopes. We account for this feature in our simulations by keeping track of which antigens a B cell internalizes, and partitioning helper T cells into three distinct groups based on their specificity for epitopes derived from each of the rsHA components. The number of T cells in each group is the same.

T cells make numerous short contacts with diverse B cells.[65] For each contact, there is a small chance of it being a productive encounter, which increases with the amount of peptide presented.[66] It is conjectured that positive selection likely requires several productive encounters.[67] Therefore, the amount of help a B cell receives will increase with the number of encounters with cognate T cells, which is determined by the types of pMHC it presents, the number of cognate T cells, and the number of competing B cells. Therefore, we represent the probability of positive selection of a B cell i as follows:

$$P_i = P_{max}\,\frac{\sum_k \left(\frac{T_k}{N_{B,k}}\right)\cdot\left(\frac{A_{ki}}{\langle A_k\rangle}\right)^{\chi}}{1+\sum_k \left(\frac{T_k}{N_{B,k}}\right)\cdot\left(\frac{A_{ki}}{\langle A_k\rangle}\right)^{\chi}} \qquad (9)$$

where A_{ki} is the amount of the HA component k internalized by the B cell i; $\langle A_k\rangle$ is the mean amount of HA component k internalized by the B cells that recognize this component; $N_{B,k}$ is the number of

such B cells; and T_k is the number of T cells that target the epitopes from the HA component k, which we assume to be equal for all variants. The maximum probability of selection, P_{max}, accounts for the fact that GC B cells are inherently apoptotic irrespective of BCR affinity.[68] We can consider P_{max} to be the chance of avoiding the default fate of apoptosis: $1 - P_{apoptosis}$. We chose $P_{max} = 0.6$ as it results in good correspondence between the timescales of our model results and experiments; other values were also tested, and the qualitative result does not change.

An important feature of the model is the exponent χ; larger values of it imply T cell help depends more stringently on the amount of pMHC presented. If χ is less than 1, small differences (e.g., 2-fold) in pMHC displayed on two B cells would have a relatively small effect on selection outcome, whereas if χ is greater than 1, such small differences would likely lead to the selection of the B cell that displays more pMHC.

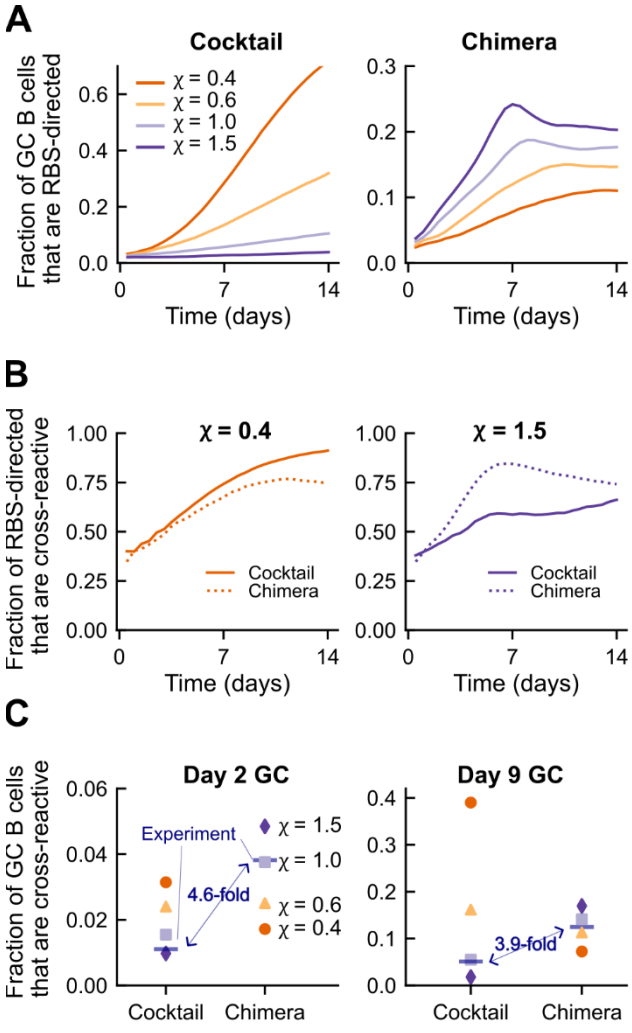

Figure 2-4. Model predictions and experimental results for the expansion and evolution of cross-reactive B cells upon immunization with the cocktail or the chimera immunogen. (A) Fraction of GC B cells that are RBS-directed as a function of time in the simulations. Changing the stringency of T cell selection have opposite effects for immunization with the chimera or the cocktail immunogen. **(B)** Fraction of RBS-directed B cells that are cross-reactive. When selection by T cells is permissive ($\chi < 1$), the cocktail outperforms the chimera for evolving cross-reactive B cells. The opposite is true for stringent selection ($\chi \geq 1$). **(C)** Fraction of GC B cells that are RBS-directed and cross-reactive in early and late GCs. Model predictions for varying levels of T cell selection stringency are compared with the results of mice immunization experiments. All fractions were calculated after combining B cells from 1,000 independent stochastic simulations. See also **Fig. 2-S3**.

Fig. 2-4A shows predictions of our model upon immunization with the chimeric and cocktail immunogens for the temporal evolution of the fraction of GC B cells that evolve from the initial RBS-directed B cell precursors; i.e., B cells that have acquired higher binding affinities than the precursors. A striking feature of these results is that, for immunization with the chimera immunogen, the evolution of RBS-directed B cells becomes increasingly more efficient as T cell selection becomes more stringent (larger values of χ); but for immunization with the cocktail immunogen, the opposite is true. **Fig. 2-4B** shows the fraction of evolved RBS-directed B cells that are cross-reactive towards at least two rsHA components in the immunogens. A low value indicates that RBS-directed B cells tend to specialize to only one component. Our model predicts that cross-reactive mutants evolve more readily upon immunization with the cocktail when T cell help is permissive, but with the chimera when T cell help is stringent. The cocktail improves in selecting cross-reactive B cells in late GC if T cell help is stringent, because of the advantages in antigen capture at high affinity (**Fig. 2-2B**). However, by day 14 only a small fraction (12 % for x = 1.5) of the simulated GCs still have any RBS-directed B cell (**Fig. 2-S3A**). So, our model predicts that cross-reactive RBS-directed B cells will evolve more readily upon immunization with the chimera compared to the cocktail if T cell help is a stringent constraint for the positive selection of B cells. **Fig. 2-S3B** and **2-S3C** show that this qualitative trend is not changed when ρ is changed to 0.4 or when P_{max} is changed to 1.

In **Fig. 2-4C**, we compare the model predictions with the experimental findings by Caradonna et al. for the fraction B cells that are RBS-directed and cross-reactive in early and late GCs after immunization with either type of immunogen.[35] This data represents the combined objectives of expanding rare RBS-directed B cells (**Fig. 2-4A**) and shepherding them to accumulate cross-reactive mutations (**Fig. 2-4B**). We assume days 8 and 15 post-immunization in experiments correspond to days 2 and 9 of GC, since GC initiation typically takes about 6 days.[69] While Caradonna et al. report the value as a fraction of all IgG^+ GC B cells, because our model does not consider background GC B cells that do not bind to any rsHA, we only consider the B cells that bind to at least one rsHA component from the experimental data. The qualitative trends in the data are not affected by the background B cells.

The experiments show a qualitatively higher frequency of cross-reactive RBS-directed B cells in GCs on both day 8 and day 15 after immunization with the chimera.[35] These experimental results are consistent with our predictions when T cell help is stringent but not when it is permissive. The model predicts that, if the T cell help is stringent ($\chi \geq 1$), a higher fraction of GC B cells will be RBS-directed and cross-reactive after immunization with the chimera than with the cocktail (**Fig. 2-4C**). If χ = 1,

3.8% of B cells in day 2 GCs are RBS-directed and cross-reactive after chimera immunization and 1.5% after the cocktail immunization. On day 9, the numbers are 14% for the chimera and 5.5% for the cocktail. In contrast, if T cell help is permissive (χ < 1), the cocktail favors the evolution of cross-reactive B cells. For example, if χ = 0.4, 3.1% of B cells in day 2 GCs are RBS-directed and cross-reactive after cocktail immunization and 1.7% after the chimera immunization; the same trend is true at day 9 (39% for the cocktail and 7.2% for the chimera). We emphasize that what is important is not the precise numbers noted above, but that the qualitative trend of which type of immunogen promotes the evolution of RBS-directed cross-reactive antibodies is opposite for stringent versus permissive selection by helper T cells. The model predictions have the same trend as the experimental data when T cell help is a stringent constraint. Therefore, we conclude that T cell help stringently depends on pMHC density. We also note that even under the most stringent selection tested (χ = 1.5), stochasticity in evolution allows for clonal heterogeneities inside individual GCs (**Fig. 2-S3D**)[41] and broad affinity distribution of B cells both within and across GCs (**Fig. 2-S3E**),[40] consistent with previous findings in the literature.

2.3.4. Mechanism for why T cell selection stringency promotes cross-reactive B cell evolution for the chimera immunogen, but not the cocktail

Events that occur in the early GC are critically important for the RBS-directed precursors as they are few in number and could be easily extinguished due to stochastic effects. For the chimera immunogen, cross-reactive RBS-directed B cells can bind to the antigen multivalently while strain-specific B cells cannot, so the former can capture significantly more antigen than the latter in the early stages of the GC reaction (**Fig. 2-2**). Thus, to promote the evolution of RBS-directed B cells, their principal advantage over off-target B cells (more antigen captured) must be amplified by the selection force. This advantage is amplified if positive selection by helper T cells discriminates stringently based on the amount of captured antigen, as this favors the selection of the cross-reactive B cells. Indeed, our simulation results show that the probability that RBS-directed precursors are positively selected in the early GC grows with the value of χ upon immunization with the chimera (**Fig. 2-5A**). If RBS-directed B cells are more readily positively selected in the early GC, they multiply more and thus have a higher chance of acquiring the rare mutations that confer breadth. Such an effect of an early advantage affecting future fate has been observed in evolving asexual populations.[70]

Consistent with this expectation, simulation results under stringent T cell selection show that upon immunization with the chimera, rare mutations that confer breadth are quickly found in the population (**Fig. 2-5B**). The resulting cross-reactive cells are then selected for and proliferate because they have a large advantage in antigen capture, which translates to a high probability of selection by T cells (**Fig. 2-5C**).

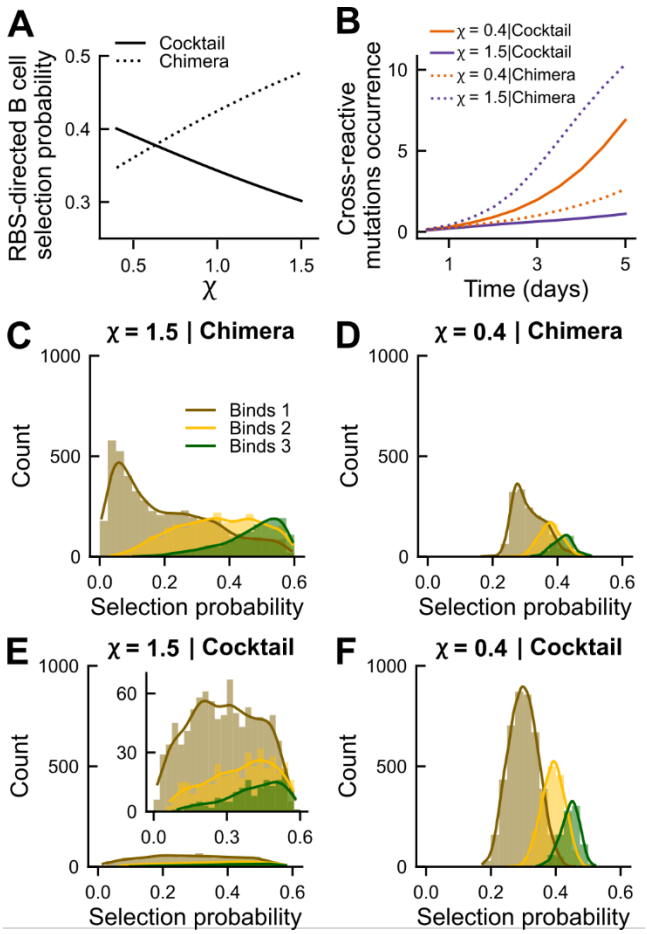

Figure 2-5. Potential mechanism of how T cell selection stringency affects expansion and evolution of RBS-directed B cells. (A) Selection probability of the RBS-directed B cell precursor at GC initiation as a function of T cell help stringency. **(B)** Average number of unique mutations that occur in a GC in the first 5 days which increase the affinities of RBS-directed B cells towards multiple rsHA components. In panels A and B, the effects of T cell selection stringency are opposite for immunizations with the cocktail and chimera. **(C-F)** Positive selection probabilities of unique RBS-directed B cell mutants in day 5 GCs, simulated under either stringent T cell selection (**C** and **E**) or permissive T cell selection (**D** and **F**) conditions after immunization with either the chimera (**C** and **D**) or the cocktail (**E** and **F**). The mutants are classified based on how many rsHA components they can bind (from one to three).

Specializing mutations occur frequently for RBS-directed B cells, but such mutations result in a loss of cross-reactivity and this inhibits antigen capture. When selection is stringent, this disadvantage in the amount of antigen captured is magnified during selection. In early GCs (day 5), when selection is stringent ($\chi = 1.5$), the median selection probability of the RBS-directed B cells that bind all three rsHA components and that of the B cells that bind only one are 0.49 and 0.17, respectively (**Fig. 2-5C**). When selection is permissive ($\chi = 0.4$), the corresponding values are 0.40 and 0.30 (**Fig. 2-5D**). Therefore, while mutations generate strain-specific RBS-directed B cells in both cases, these mutated B cells are more heavily disfavored when selection is stringent. These reasons

promote cross-reactive B cell evolution upon immunization with the chimera if T cell selection is a stringent constraint.

For immunization with the cocktail immunogens, the difference in the amounts of antigen captured by low-affinity cross-reactive and strain-specific B cells is small in the early GC when antigen is not limiting (**Fig. 2-2B**). Therefore, increasing the stringency of how positive selection probability depends on the amount of antigen captured will not favor the cross-reactive B cells. The predominant difference between the cross-reactive and strain-specific B cells in the early GC is that only the former can capture diverse types of rsHA components so it can be positively selected by T cells with diverse epitope specificities, while the latter seeks help from only a part of the repertoire of helper T cells. Cross-reactive B cells are promoted if this difference helps them during T cell selection. If selection stringency is permissive, each encounter with a cognate helper T cell will give a similar chance of receiving positive selection signals. Cross-reactive B cells will encounter cognate T cells more frequently by capturing diverse epitopes, and despite the lower pMHC density of each epitope, the total probability of receiving help will be greater than strain-specific B cells that capture a similar total amount of antigen. Mathematical analysis of Eq. 9 (see METHODS) shows that this is true when $\chi < 1$. Consistent with this analysis, our simulation results show that the selection probability of RBS-directed precursor in the early GC increases with decreasing χ (**Fig. 2-5A**). The enhanced early selection probability allows RBS-directed B cells to more readily evolve future cross-reactive mutations (**Fig. 2-5B**). The cross-reactive mutants have a distinct advantage over strain-specific mutants when selection is permissive and therefore selectively accumulate, but not when selection is stringent (**Fig. 2-5E-F**). This is because, for less stringent selection, the ability of cross-reactive B cells to get positively selected by interacting with diverse T cells is amplified.

2.4. Discussions

Eliciting bnAbs is a necessary step towards a universal influenza vaccine that confers protection against seasonal variants and pandemic-causing novel strains. Influenza RBS is a promising target for bnAbs, but germline B cell precursors that target the RBS are rare relative to off-target sites,[32] and affinity-matured RBS-directed B cells often have low breadth because they strongly interact with the variable residues within their footprints.[37,71] Thus, vaccination strategies to amplify the rare RBS-directed B cell precursors and shepherd their mutation pathways toward high breadth are required. Here, we study the evolution of cross-reactive B cells that target the conserved HA RBS upon

immunization with either a heterotrimeric RBS-enriched chimera or a cocktail of three homotrimeric rsHAs.[35] Toward this end, we developed a computational model of affinity maturation upon vaccination with the chimera and cocktail immunogens. Our analyses of the pertinent processes and simulation results (**Figs. 1-5**) provide mechanistic insights into the factors that influence antibody repertoire development upon vaccination with different types of immunogens.

We identify two important variables: the valency with which the antigen is bound to BCR, and the diversity of antigens captured by B cells. If cross-reactive B cells engage antigen multivalently, and strain-specific B cells cannot, as is true for the chimera (**Fig. 2-2**), then stringent selection of GC B cells by helper T cells promotes cross-reactive B cell evolution (**Figs. 4** and **5**). If the diversity of antigens captured is the principal difference between cross-reactive and strain-specific B cells, as is true for the cocktail (**Figs. 2 and 3**), then selection stringency must be permissive to promote the evolution of cross-reactive B cells (**Figs. 4** and **5**). Because cross-reactive B cells are more enriched in mice immunized with the chimera immunogen, we conclude that the positive selection of B cells by helper T cells is a stringent constraint during GC reactions. Thus, our studies provide fundamental mechanistic insights on the role of T cell help during affinity maturation,[39–41,43,72] which will help improve vaccine design.

Our result suggests that one promising future direction would be to further optimize antigen valency using nanoparticles and epitope enrichment, to maximize the difference between the antigen capture capabilities of cross-reactive and strain-specific B cells. Furthermore, we show that stringent selection by T cells will maximize the efficacy of such immunogens. Many nanoparticle-based immunogens that aim to optimize antigen capture by cross-reactive B cells have large non-native protein cores[13,73–75], which can contain many highly immunogenic helper T cell epitopes[76]. Yet, the understanding of how this addition might affect the selection by helper T cells and the efficacy of the designed immunogens is currently lacking. Our study highlights the need for a better understanding of this relationship.

Alternatively, our model predicts that if T cell selection is permissive, a cocktail of antigens with distinct T cell epitopes can be highly effective at eliciting cross-reactive B cells. There is evidence that some T follicular helper cells are of higher “quality” than others, that is, they can maintain a greater GC B cell/T follicular helper cell ratio.[77,78] This observation suggests that such helper T cells may have more frequent productive encounters with B cells while being less stringent regarding the amounts of pMHC presented by the B cells, consistent with permissive selection in our model. This hypothesis can be tested by combining adoptive transfer of T cells and graded delivery of peptides to GC B cells.[38]

Alternatively, it has been suggested that upregulating key surface adhesion molecules on T cells such as SAP and SLAM may make them more potent helpers.[79] Such a method has been successfully demonstrated for dendritic cells and macrophages[80] and could be applied to T cells to study its effect on selection stringency. Finally, we can ask whether increasing the total number of T cells affects the stringency of selection by the individual T cells, which can be tested by the adoptive transfer of different numbers of T cells. The answer will depend on the mechanisms of selection by the T cells. Testing these hypotheses to further improve our computational model and immunogen designs will shed light on basic questions in immunology and vaccine design.

Our results are generalizable for other epitope targets. First, when amplification of rare B cells that target a conserved epitope is the goal, and second, when a selective accumulation of mutations that confer high breadth is needed. However, it will be also necessary to consider the constraints of the specific target. For example, for HIV CD4 binding site bnAbs, germline-targeting immunogens are usually first used to amplify the rare germline precursors[81]. The approaches presented in this study can be applied for shepherding the mutations required for these precursor B cells to evolve into bnAbs. This is because strain-specific variable residues shield the CD4 binding site, making the exposed conserved target smaller than typical BCR footprints[34]. For the stem epitope of influenza, the shepherding step may not be as important because the conserved region is large[82]. However, the steric hindrance for B cells to bind to this target is also a critical consideration for an effective immunogen design[83]. Thus, an interesting future direction may be to study how the design principles outlined by our study can be incorporated with other design constraints specific to various targets of bnAbs.

2.5. Methods Details

Affinity maturation simulation algorithm

As described in section **2.3.1. Model development**, we simulate in-silico germinal centers in which B cells capture antigen and then compete for help by T cells in each cycle, for 28 cycles. The stochastic GC simulation is repeated 1,000 times. We keep track of the following quantities: the number of GC B cells that target each epitope (rsH3, rsH4, or rsH14 off-target B cells or RBS-directed B cells), the binding affinities of the GC B cells, the mutations that are carried by the RBS-directed B cells, and the probabilities of positive selection of RBS-directed B cells at each round. For reporting

the RBS-directed B cell fractions (see Figure 4), all B cells from the 1,000 GCs are first pooled together, and then the fraction is calculated.

The amounts and types of antigens captured by the B cells are determined by simulating the immunological synapse between the B cell and the FDC. BCRs first cluster with antigens, then internalize them by applying force (see sections **2.3.1. Model development** and **2.3.2. Antigen capture depends on immunogen design and cross-reactivity of B cells**). Then, the probability of positive selection by T cells is determined based on the amount and diversity of the antigens captured by the B cell, relative to other competing B cells (see Eq. 9 and the associated description in the text). We provide further detail and analyses of these steps below.

Simulation of antigen capture

The immunological synapse is modeled as a circle of radius 0.5 μm divided up into lattice points with an interval of 10 nm that can be occupied by the antigens and BCRs. No two homotypic molecules are allowed on the same lattice site, but a BCR and an antigen molecule can occupy the same site. To begin the simulation, 120 BCRs and 120 antigen molecules are randomly distributed on the lattice sites. During the clustering phase, BCR and antigen molecules diffuse freely. In each time step, each molecule randomly chooses one of the four neighboring sites, then moves to it with the probability of,

$$p_{move} = \frac{4D\Delta t}{l^2} \qquad (10)$$

where $D = 5 \times 10^4\ nm^2 s^{-1}$ is the diffusion constant for both antigen and BCR[50] and $l = 10\ nm$ is the lattice size. For clusters of BCRs and antigens, only those containing up to 3 molecules are allowed to diffuse and the diffusion coefficient is reduced to D/M where M is the number of molecules in a cluster.[84] The move is completed if the new sites are not blocked for the diffusing molecules. If any of the new sites are already occupied or are outside the boundary of the immunological synapse, the move is not accepted and the simulation continues to the next step.

When the distance between a BCR and an antigen molecule is either 0 or 1 lattice site, they can form a bond, as described in the text. When several free epitopes on the antigen molecules are recognized by the BCR, one is randomly chosen upon binding. The sizes of clusters stabilize within a few seconds of simulation time (data not shown), so we simulate the clustering phase for 10 seconds.

When the extraction phase begins, BCRs and any antigen molecules bound to them stop diffusing, but free antigen molecules still diffuse. A pulling force is applied to each BCR, which affects the antigen extraction as described in the text (see Equations 6-8). The simulation terminates once all BCRs are internalized, and the number and types of internalized antigen molecules are calculated.

The simulation of antigen capture is computationally intensive, so repeating it for thousands of B cells for each round of affinity maturation is impractical. Therefore, we first run the antigen capture simulations to determine the mapping between the binding affinities of a B cell and the amount of antigen it captures, then use this mapping to quickly determine how much antigen each B cell captures during the affinity maturation simulations. To obtain the mapping for a strain-specific B cell, we run 30 independent simulations of antigen capture for each value of binding affinity between -13.8 and $-20.8\,k_BT$ with an interval of $0.5\,k_BT$. The mean amount of antigen captured is determined at each point. This affinity range covers the limits of B cell affinities relevant in our affinity maturation simulation. The amount of antigen captured by a B cell is determined from standard linear interpolation using the two nearest points to its binding affinity. For the RBS-directed B cells, we run the antigen capture simulations for a set of grid points on a three-dimensional grid, where each axis corresponds to the binding affinity towards one rsHA component, ranging between -13.8 and $-20.8\,k_BT$ with an interval of $0.5\,k_BT$. The amount of antigen captured by a given B cell is obtained from a standard trilinear interpolation using the eight nearest points.

Selection by T cells

The text describes how the probability of positive selection by T cells depends on both the amount and the diversity of the captured antigens (see Equation 9). Here, we provide a mathematical analysis of why immunization with the cocktail antigen favors cross-reactive B cells in the early GC when T cell help is permissive, but not when it is stringent (see Figure 4).

The low-affinity RBS-directed B cell precursor and off-target B cells capture similar amounts of total antigen. For simplicity, let us assume that the amounts of antigen captured are equal. That is, $A_1 + A_2 + A_3 = A_{1,off}$ where $A_1, A_2, A_3 > 0$ are the amounts of the three variants captured by an RBS-directed B cell, and $A_{1,off}$ is the amount captured by an off-target B cell that, without loss of generality, is assumed to target only the first variant.

Eq. 9 is a monotonically increasing function of the numerator $\sum_k \left(\frac{T_k}{N_{B,k}}\right) \cdot \left(\frac{A_{ki}}{\langle A_k \rangle}\right)^x$. Therefore, to understand how the positive selection probability of the RBS-directed B cell compares with that of the off-target B cell, we will compare q_{RBS}, defined as $\sum_k \left(\frac{T_k}{N_{B,k}}\right) \cdot \left(\frac{A_{ki}}{\langle A_k \rangle}\right)^x$ and q_{off}, defined as $\left(\frac{T_1}{N_{B,1}}\right)\left(\frac{A_{1,off}}{\langle A_1 \rangle}\right)^x$.

In our model, we assume that equal numbers of T cells target the epitopes from each of the three rsHA variants. That is, $T_1 = T_2 = T_3$. Also, each off-target B cell is randomly assigned the target variant with equal probability. Since there is a relatively large number of founder B cells (99 off-target B cells), we can approximate that the number of B cells that capture each variant are equal, i.e. $N_{B,1} = N_{B,2} = N_{B,3}$.

Also, the mean amount of antigen k internalized by B cells that recognize antigen k, $\langle A_k \rangle$, is equal for all k at the beginning of the GC because all B cells have the same affinity. Since GCs contain thousands of B cells, this equality also holds well due to symmetry even when B cells begin to mutate, at least in early GCs. Taken together, the following equality holds.

$$\frac{q_{RBS}}{q_{off}} = \frac{\left(\frac{T_1}{N_{B,1}}\right)\left(\frac{A_1}{\langle A_1 \rangle}\right)^x + \left(\frac{T_2}{N_{B,2}}\right)\left(\frac{A_2}{\langle A_2 \rangle}\right)^x + \left(\frac{T_3}{N_{B,3}}\right)\left(\frac{A_3}{\langle A_3 \rangle}\right)^x}{\left(\frac{T_1}{N_{B,1}}\right)\left(\frac{A_{1,off}}{\langle A_1 \rangle}\right)^x} = \frac{A_1^x + A_2^x + A_3^x}{A_{1,off}^x} = \frac{A_1^x + A_2^x + A_3^x}{(A_1 + A_2 + A_3)^x}$$

To show that the RBS-directed B cells are favored for positive selection when T cell help is permissive, we will prove the following inequality:

$$A_1^x + A_2^x + A_3^x > (A_1 + A_2 + A_3)^x \quad if\ 0 < x < 1$$

Consider the function $f(a_1, a_2, a_3) = a_1^x + a_2^x + a_3^x - (a_1 + a_2 + a_3)^x$ defined for positive real numbers a_1, a_2, a_3. The partial derivatives are always positive if $0 < x < 1$:

$$\frac{\partial f}{\partial a_i} = x a_i^{x-1} - x(a_1 + a_2 + a_3)^{x-1} > 0 \ \ for\ i = 1,2,3$$

because $a_i < a_1 + a_2 + a_3$ and $x - 1 < 0$.

Assume that there exists $A_1, A_2, A_3 > 0$ such that $f(A_1, A_2, A_3) = s \leq 0$. Then, for any a_1, a_2, a_3 such that $a_1 \in (0, A_1)$, $a_2 \in (0, A_2), a_3 \in (0, A_3)$, the following inequality must be true:

$$f(a_1, a_2, a_3) < f(A_1, A_2, A_3) = s \leq 0$$

However, f is a continuous function and $\lim_{a_1 \to 0, a_2 \to 0, a_3 \to 0} f(a_1, a_2, a_3) = 0$. Therefore, there must exist $\delta > 0$ such that

$$|f(a_1, a_2, a_3) - 0| < |s| \quad for\ all\ a_1, a_2, a_3 \in (0, \delta)$$

which is contradictory.

Therefore, $q_{RBS} > q_{off}$ when $x < 1$, and by simple extension, $\frac{p_{max} q_{RBS}}{1+q_{RBS}} > \frac{p_{max} q_{off}}{1+q_{off}}$. That is, despite capturing the same amount of antigen, the RBS-directed B cell has a higher probability of positive selection because of capturing diverse T cell epitopes. By similar analysis, it can be shown that when $x > 1$ the opposite is true, and the RBS-directed B cells have a lower probability of positive selection.

T cell epitope prediction and comparison

T cell epitopes in the rsH3, rsH4, and rsH14 antigens (Fig. 2-3) as well as in the rabbit serum albumin and human serum albumin (Fig. 2-S2) are predicted with IEDB MHCII binding prediction tool. For the comparison of rabbit serum albumin and human serum albumin, we excluded the peptides whose 9-mer core sequences were also found in mouse serum albumin, since such peptides would not be immunogenic in mice.[64] The following settings are used: Prediction Method – IEDB recommended 2.22; Select species/locus – mouse, H-2-I; Select MHC allele – H2-I-A^b; Select length – 15. The predicted peptides are sorted by the percentile rank given by the IEDB tool, and the peptides in the top 20 percentile are chosen for the pairwise comparisons of the epitopes in different variants. This value corresponds to roughly ~3000 nM predicted half-maximal inhibitory concentration (IC50) value. We choose this cutoff to be comprehensive because most immunogenic MHC II T cell epitopes have an IC50 value under 1,000 nM.[85] The 9-mer cores associated with the peptides, predicted by the smm_align method, are then used for the pairwise comparisons.

2.6. Supplemental Figures and Tables

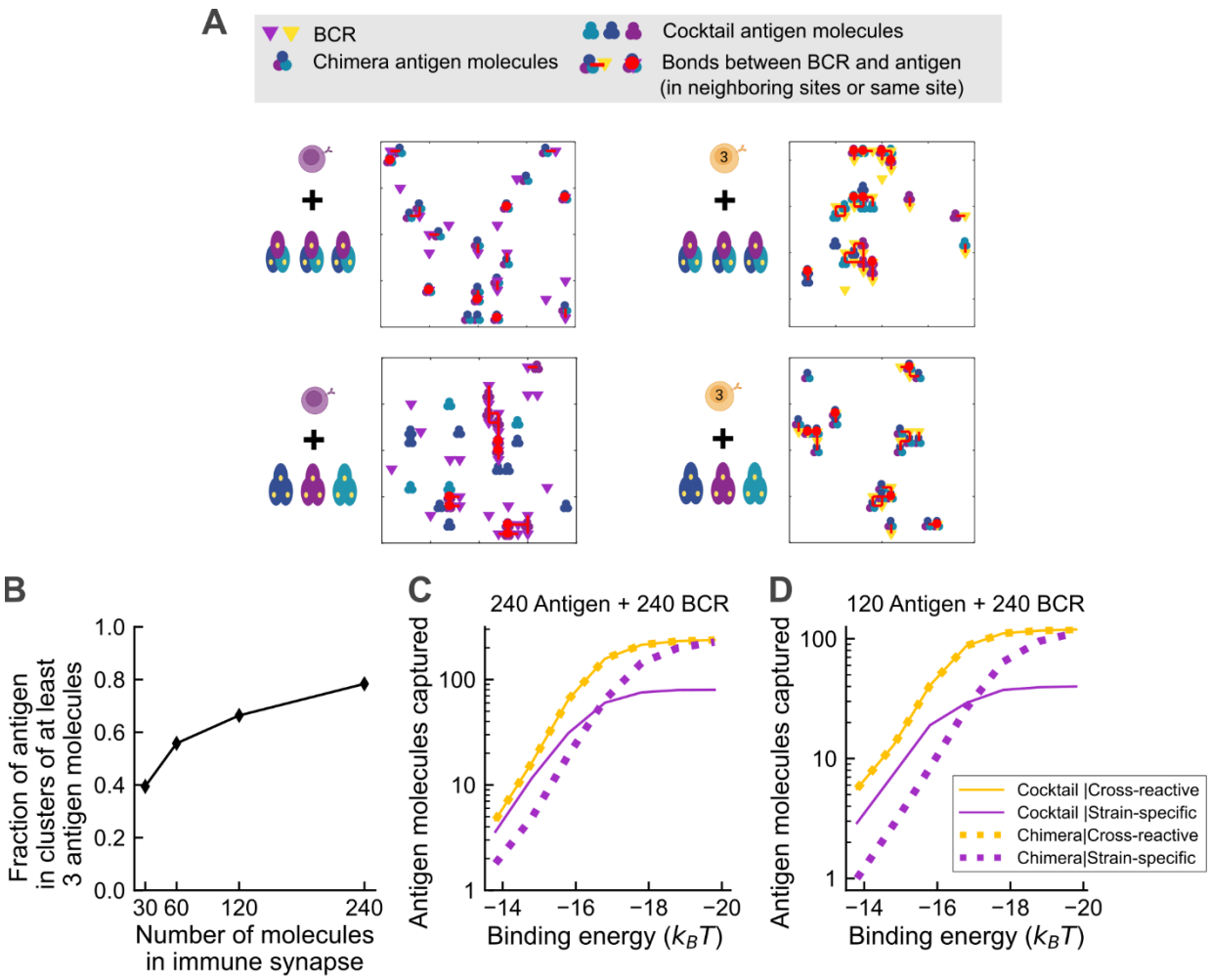

Figure 2-S1. Related to Figure 2-2. Antigen capture by B cells. **(A)** Examples of antigen-BCR clustering in immunological synapses from the simulations of antigen capture. The simulation shows that after the chimera immunization, a strain-specific B cell binds to most of the antigen molecules in the synapse, but cannot form multivalent antigen-BCR clusters. After the cocktail immunization, it binds to only the cognate molecules but forms multivalent antigen-BCR clusters. A cross-reactive B cell bind to most antigen molecules in the synapse and form multivalent antigen-BCR clusters after immunization with either of the immunogens. **(B)** Clustering of Ag molecules when the number of Ag molecules in the immunological synapse is varied and the number of BCRs is ratio between them is 1. The fraction of Ag molecules that exist in clusters of at least 3 Ag molecules is shown. The data is from 30 simulations of immunological synapse between an FDC presenting the chimera immunogen and a cross-reactive B cell that binds all three rsHA components with the affinities of -14.8 k_BT. **(C-D)** Amount of antigen captured as a function of Ag-BCR binding affinity when the numbers of Ag and BCR molecules in the immunological synapse are varied.

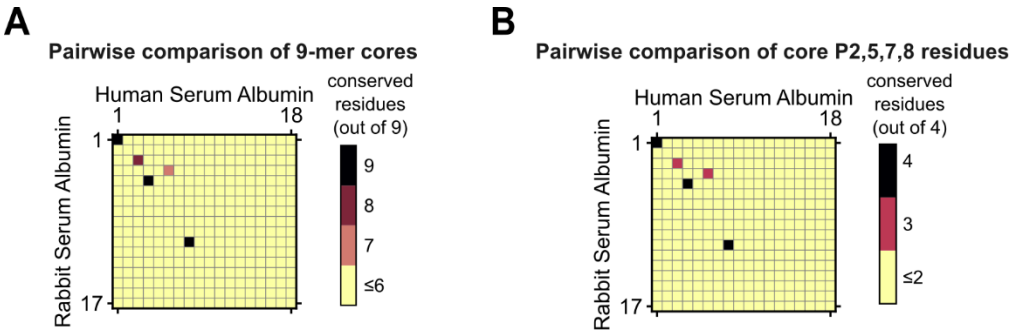

Figure 2-S2. Related to Figure 2-3. Effect of antigen design on selection by T cells. (A-B) Pairwise comparison of computationally predicted helper T cell epitopes in rabbit serum albumin and human serum albumin. Each axis corresponds to the ranks of the top 20 percentile predicted 15-mer T cell epitopes. (A) Number of conserved residues in pairwise comparisons of the 9-mer cores of the predicted epitopes. (B) Number of conserved residues in pairwise comparisons of the P2, P5, P7 and P8 residues of the 9-mer cores.

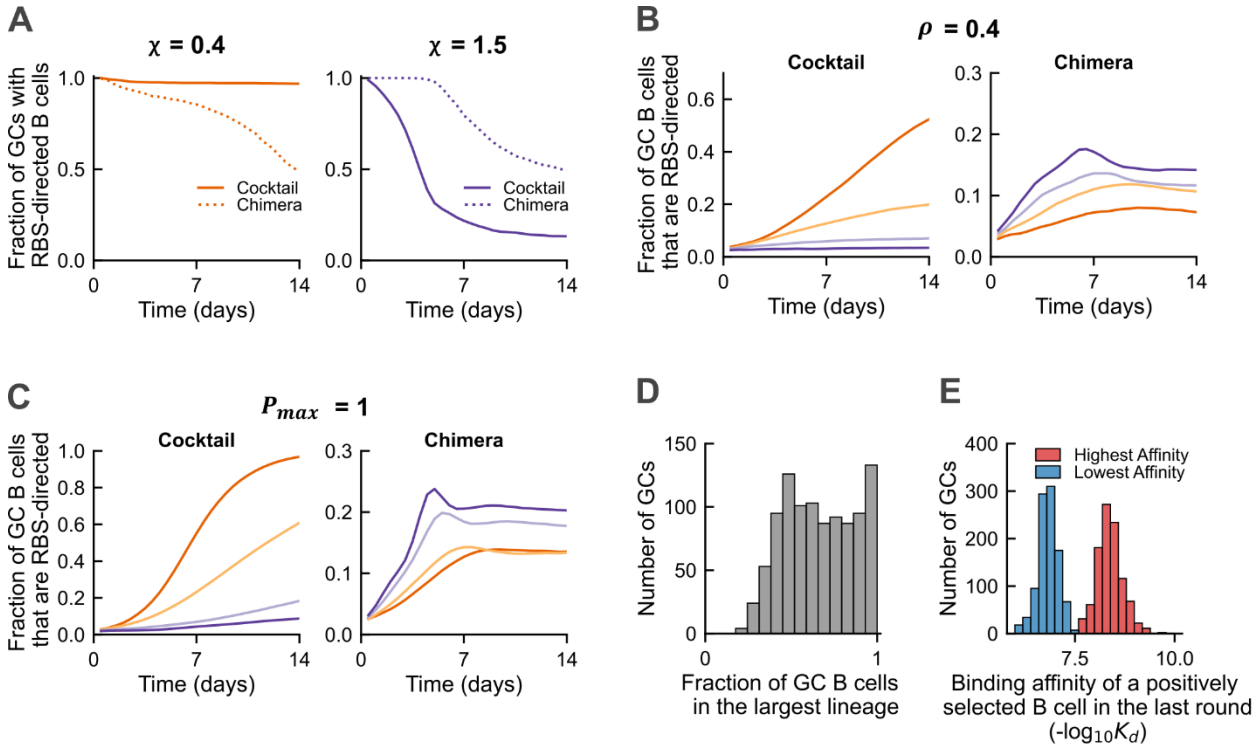

Figure 2-S3. Related to Figure 2-4. Evolution of RBS-directed B cells in Germinal Centers. (A) Fraction of GCs from 1000 simulations that contain at least one RBS-directed B cell. When selection by T cells is permissive, RBS-directed B cells survive in most GCs after immunization with the cocktail, while they slowly become extinct in an increasing number of GCs after immunization with the chimera. When selection is stringent, RBS-directed B cells rapidly become extinct in many GCs after immunization with the cocktail. They survive in most GCs after immunization with the chimeric antigen for the first several days, then, since affinity increases quickly and the advantage of cross-reactivity decreases in late GCs, some GCs lose the RBS-directed B cells. **(B-C)** The fraction of GC B cells that are RBS-directed when the parameters ρ and P_{max} are changed, showing the same qualitative trend as the main result in Figure 4. (B) ρ is 0.4, instead of 0.7. (C) P_{max} is 1, instead of 0.6. **(D-E)** Heterogeneities among 1000 GC simulations on day 9, when T cell selection is stringent (x = 1.5), resulting from stochasticity in evolution. (D) Histogram of the fraction of GC B cells that belong to the single most dominant clonal lineage. The GCs show varying degrees of homogenization. (E) Histogram of the highest and lowest affinity of the B cells that are concurrently positively selected on day 9 from each GC. There is a ~10 fold affinity difference among positively selected B cells within the same GCs, which is represented by the difference between the two peaks. Across all the GCs, B cells with an even wider range of affinities are concurrently positively selected.

Table 2-S1. Related to Figure 2-2. MHC II Binding T Cell Epitopes Predicted by Computational Tools. The 15-mer epitopes are grouped based on the 9-mer cores. Peptides in top 20 percentile rank are shown, corresponding to roughly 3000 nM predicted half maximal inhibitory concentration (IC50) value. The prediction was made by MHCII binding prediction tool using IEDB recommended 2.22 method, for the mouse MHC H2-IAb allele.

rsH3			rsH4			rsH14		
Core	**Peptide**	**Rank**	**Core**	**Peptide**	**Rank**	**Core**	**Peptide**	**Rank**
FNWTGVTQN	NNESFNWTGVTQNGV	1.6	FQWSTVTQN	IAEEFQWSTVTQNGV	2.8	FTWNGVTVD	IAEQFTWNGVTVDGV	5.85
	NESFNWTGVTQNGVS	1.65		FIAEEFQWSTVTQNG	2.9		AEQFTWNGVTVDGVS	6.15
	ESFNWTGVTQNGVSA	1.7		AEEFQWSTVTQNGVS	3.1		EQFTWNGVTVDGVSA	6.4
	FNNESFNWTGVTQNG	1.7		EEFQWSTVTQNGVSA	3.2		FIAEQFTWNGVTVDG	7.1
	SFNWTGVTQNGVSAS	3.4		EFQWSTVTQNGVSAS	4.25		QFTWNGVTVDGVSAS	9.9
	FNWTGVTQNGVSASC	4.9	EEFQWSTVT	EFIAEEFQWSTVTQN	3	EQFTWNGVT	EFIAEQFTWNGVTVD	7.05
ESFNWTGVT	EFNNESFNWTGVTQN	1.8	VSASCSRAN	TQNGVSASCSRANVS	3.35	YVKQGSLML	CPKYVKQGSLMLATG	9.75
ITPNGSIPN	KSECITPNGSIPNDK	6.75		QNGVSASCSRANVSD	3.75		NCPKYVKQGSLMLAT	10.4
	CKSECITPNGSIPND	8.2		VTQNGVSASCSRANV	4.15		PKYVKQGSLMLATGG	10.9
	SECITPNGSIPNDKP	8.25		NGVSASCSRANVSDF	4.5		KYVKQGSLMLATGGA	15.5
	ECITPNGSIPNDKPF	9.25		GVSASCSRANVSDFF	9.05		GNCPKYVKQGSLMLA	15.8
	CITPNGSIPNDKPFQ	13.7		VSASCSRANVSDFFN	13		YVKQGSLMLATGGAG	19.5
	ITPNGSIPNDKPFQN	16	VTQNGVSAS	TVTQNGVSASCSRAN	4.05	KNGLYGPIN	TGKNGLYGPINVTKE	10.2
YASLRSLVA	DVPDYASLRSLVASS	6.8		FQWSTVTQNGVSASC	5.45		LTGKNGLYGPINVTK	14
	VPDYASLRSLVASSG	6.8		STVTQNGVSASCSRA	7.3		WLTGKNGLYGPINVT	16.5
	YDVPDYASLRSLVAS	7.2		WSTVTQNGVSASCSR	8.55	YLWGVHHPS	VRLYLWGVHHPSNIG	10.5
	PDYASLRSLVASSGT	7.3		QWSTVTQNGVSASCS	9.85		RLYLWGVHHPSNIGD	11.1
	YASLRSLVASSGTLE	9.3	LNTAVPIGS	STILNTAVPIGSCVS	8.7		YVRLYLWGVHHPSNI	11.4
	DYASLRSLVASSGTL	9.4	AVPIGSCVS	TILNTAVPIGSCVSK	9.25		LYLWGVHHPSNIGDQ	14
VTQNGVSAS	WTGVTQNGVSASCSR	8.05		ILNTAVPIGSCVSKC	11.5		YLWGVHHPSNIGDQR	16.3
	TGVTQNGVSASCSRR	8.1		LNTAVPIGSCVSKCH	13.5		SYVRLYLWGVHHPSN	17.5
	NWTGVTQNGVSASCS	9.25	WGVHHPPNI	ARLYIWGVHHPPNIG	9.3	YGPINVTKE	GKNGLYGPINVTKEN	11.9
	GVTQNGVSASCSRRS	12.6		RLYIWGVHHPPNIGD	10.4		KNGLYGPINVTKENT	12.7
	VTQNGVSASCSRRSS	14.5		LYIWGVHHPPNIGDQ	11.6		NGLYGPINVTKENTG	19.5
SECITPNGS	KCKSECITPNGSIPN	8.15		YIWGVHHPPNIGDQR	13.4	VTVDGVSAS	FTWNGVTVDGVSASC	14
PDYASLRSL	PYDVPDYASLRSLVA	8.55	TILNTAVPI	QKKSTILNTAVPIGS	11	FNSIGNLIA	IIFNSIGNLIAPRGH	15.5
KNGLYPALN	TGKNGLYPALNVTMP	8.85		KSTILNTAVPIGSCV	11.7		SIIFNSIGNLIAPRG	15.5
	LTGKNGLYPALNVTM	9.8		KKSTILNTAVPIGSC	11.9		DSIIFNSIGNLIAPR	16
	WLTGKNGLYPALNVT	11		SQKKSTILNTAVPIG	15		GDSIIFNSIGNLIAP	16.5
GLYPALNVT	GKNGLYPALNVTMPN	10.6	YIWGVHHPP	YARLYIWGVHHPPNI	13.5	SIIFNSIGN	PGDSIIFNSIGNLIA	16.5
	KNGLYPALNVTMPNK	10.8	IFIERPTAV	EWDIFIERPTAVDTC	15.5	VFIERPTAM	TWDVFIERPTAMDTC	16.5
YPALNVTMP	NGLYPALNVTMPNKE	11		WDIFIERPTAVDTCY	16		TTWDVFIERPTAMDT	17
LNVTMPNKE	GLYPALNVTMPNKEQ	12.5		AEWDIFIERPTAVDT	16.5		WDVFIERPTAMDTCY	17.5
	LYPALNVTMPNKEQF	18		GAEWDIFIERPTAVD	17.5		DTTWDVFIERPTAMD	18.5
SLVASSGTL	ASLRSLVASSGTLEF	15.5	KKSTILNTA	NSQKKSTILNTAVPI	17	YQSLRSILA	PDYQSLRSILASSGS	17
	SLRSLVASSGTLEFN	17.5	YQSLRSILA	DVPDYQSLRSILANN	17.5		DVPDYQSLRSILASS	17.5
	LRSLVASSGTLEFNN	19		FDVPDYQSLRSILAN	17.5		VPDYQSLRSILASSG	17.5
FKIRSGKSS	RGYFKIRSGKSSIMR	17.5		VPDYQSLRSILANNG	17.5		FDVPDYQSLRSILAS	18
	PRGYFKIRSGKSSIM	18		PDYQSLRSILANNGK	19		DYQSLRSILASSGSL	18.5
	GYFKIRSGKSSIMRS	19.5				IYWTLVNPG	ISIYWTLVNPGDSII	17.5
							SIYWTLVNPGDSIIF	19.5
						RLYLWGVHH	GSYVRLYLWGVHHPS	18.6
						SILASSGSL	QSLRSILASSGSLEF	19
							YQSLRSILASSGSLE	19
						KYVKQGSLM	IGNCPKYVKQGSLML	19.4

2.7. Chapter 2 References

1. Zhou, D., Dejnirattisai, W., Supasa, P., Liu, C., Mentzer, A.J., Ginn, H.M., Zhao, Y., Duyvesteyn, H.M.E., Tuekprakhon, A., Nutalai, R., et al. (2021). Evidence of escape of SARS-CoV-2 variant B.1.351 from natural and vaccine-induced sera. Cell. *184*, 2348-2361.e6. 10.1016/j.cell.2021.02.037.

2. Cao, Y., Wang, J., Jian, F., Xiao, T., Song, W., Yisimayi, A., Huang, W., Li, Q., Wang, P., An, R., et al. (2021). Omicron escapes the majority of existing SARS-CoV-2 neutralizing antibodies. Nature. *602,* 657-663 10.1038/s41586-021-04385-3.

3. Hraber, P., Seaman, M.S., Bailer, R.T., Mascola, J.R., Montefiori, D.C., and Korber, B.T. (2014). Prevalence of broadly neutralizing antibody responses during chronic HIV-1 infection. AIDS *28*, 163–169. 10.1097/QAD.0000000000000106.

4. Simek, M.D., Rida, W., Priddy, F.H., Pung, P., Carrow, E., Laufer, D.S., Lehrman, J.K., Boaz, M., Tarragona-fiol, T., Miiro, G., et al. (2009). Human Immunodeficiency Virus Type 1 Elite Neutralizers: Individuals with Broad and Potent Neutralizing Activity Identified by Using a High-Throughput Neutralization Assay together with an Analytical Selection Algorithm. J. Virol. *83*, 7337–7348. 10.1128/JVI.00110-09.

5. Burton, D.R., Pyati, J., Koduri, R., Sharp, S.J., Thornton, G.B., Parren, P.W.H., Sawyer, L.S.W., Hendry, R.M., Dunlop, N., Nara, P.L., et al. (1994). Efficient Neutralization of Primary Isolates of HIV-1 by a Recombinant Human Monoclonal Antibody. Science *266*, 1024–1027. 10.1126/science.7973652.

6. Corti, D., Suguitan, A.L., Pinna, D., Silacci, C., Fernandez-Rodriguez, B.M., Vanzetta, F., Santos, C., Luke, C.J., Torres-Velez, F.J., Temperton, N.J., et al. (2010). Heterosubtypic neutralizing antibodies are produced by individuals immunized with a seasonal influenza vaccine. J. Clin. Investig. *120*, 1663–1673. 10.1172/JCI41902.

7. Wrammert, J., Koutsonanos, D., Li, G., Edupuganti, S., Sui, J., Morrissey, M., Mccausland, M., Skountzou, I., Hornig, M., Lipkin, W.I., et al. (2011). Broadly cross-reactive antibodies dominate the human B cell response against 2009 pandemic H1N1 influenza virus infection. J. Exp. Med. *208*, 181–193. 10.1084/jem.20101352.

8. Whittle, J.R.R., Zhang, R., Khurana, S., King, L.R., Manischewitz, J., Golding, H., Dormitzer, P.R., Haynes, B.F., Walter, E.B., Moody, M.A., et al. (2011). Broadly neutralizing human antibody that recognizes the receptor-binding pocket of influenza virus hemagglutinin. Proc. Natl. Acad. Sci. U.S.A. *108*, 14216–14221. 10.1073/pnas.1111497108.

9. Stamatatos, L., Morris, L., Burton, D.R., and Mascola, J.R. (2009). Neutralizing antibodies generated during natural hiv-1 infection: Good news for an hiv-1 vaccine? Nat. Med. *15*, 866–870. 10.1038/nm.1949.

10. Sui, J., Sheehan, J., Hwang, W.C., Bankston, L.A., Burchett, S.K., Huang, C.Y., Liddington, R.C., Beigel, J.H., and Marasco, W.A. (2011). Wide prevalence of heterosubtypic broadly neutralizing human anti-influenza a antibodies. Clin. Infect. Dis. *52*, 1003–1009. 10.1093/cid/cir121.

11. Jardine, J.G., Ota, T., Sok, D., Pauthner, M., Kulp, D.W., Kalyuzhniy, O., Skog, P.D., Thinnes, T.C., Bhullar, D., Briney, B., et al. (2015). Priming a broadly neutralizing antibody response to HIV-1 using a germline-targeting immunogen. Science *349*, 156–161. 10.1126/science.aac5894.

12. Steichen, J.M., Lin, Y.C., Havenar-Daughton, C., Pecetta, S., Ozorowski, G., Willis, J.R., Toy, L., Sok, D., Liguori, A., Kratochvil, S., et al. (2019). A generalized HIV vaccine design strategy for priming of broadly neutralizing antibody responses. Science *366*. 10.1126/science.aax4380.

13. Kanekiyo, M., Joyce, M.G., Gillespie, R.A., Gallagher, J.R., Andrews, S.F., Yassine, H.M., Wheatley, A.K., Fisher, B.E., Ambrozak, D.R., Creanga, A., et al. (2019). Mosaic nanoparticle display of diverse influenza virus hemagglutinins elicits broad B cell responses. Nat. Immunol. *20*. 10.1038/s41590-018-0305-x.

14. Escolano, A., Steichen, J.M., Dosenovic, P., Kulp, D.W., Golijanin, J., Sok, D., Freund, N.T., Gitlin, A.D., Oliveira, T., Araki, T., et al. (2016). Sequential Immunization Elicits Broadly Neutralizing Anti-HIV-1 Antibodies in Ig Knockin Mice. Cell *166*, 1445-1458.e12. 10.1016/j.cell.2016.07.030.

15. Torrents de la Peña, A., de Taeye, S.W., Sliepen, K., LaBranche, C.C., Burger, J.A., Schermer, E.E., Montefiori, D.C., Moore, J.P., Klasse, P.J., and Sanders, R.W. (2018). Immunogenicity in Rabbits of HIV-1 SOSIP Trimers from Clades A, B, and C, Given Individually, Sequentially, or in Combination. J. Virol. *92*, e01957-17. 10.1128/jvi.01957-17.

16. Wang, S., Mata-Fink, J., Kriegsman, B., Hanson, M., Irvine, D.J., Eisen, H.N., Burton, D.R., Wittrup, K.D., Kardar, M., and Chakraborty, A.K. (2015). Manipulating the selection forces during affinity maturation to generate cross-reactive HIV antibodies. Cell *160*, 785–797. 10.1016/j.cell.2015.01.027.

17. Shaffer, J.S., Moore, P.L., Kardar, M., and Chakraborty, A.K. (2016). Optimal immunization cocktails can promote induction of broadly neutralizing Abs against highly mutable pathogens. Proc. Natl. Acad. Sci. U.S.A. *113*, E7039–E7048. 10.1073/pnas.1614940113.

18. Sprenger, K.G., Louveau, J.E., Murugan, P.M., and Chakraborty, A.K. (2020). Optimizing immunization protocols to elicit broadly neutralizing antibodies. Proc. Natl. Acad. Sci. U.S.A. *117*, 20077–20087. 10.1073/PNAS.1919329117.

19. Meyer-Hermann, M. (2019). Injection of Antibodies against Immunodominant Epitopes Tunes Germinal Centers to Generate Broadly Neutralizing Antibodies. Cell Rep. *29*, 1066-1073.e5. 10.1016/j.celrep.2019.09.058.

20. Childs, L.M., Baskerville, E.B., and Cobey, S. (2015). Trade-offs in antibody repertoires to complex antigens. *Philos. Trans. R. Soc*. B: Biol. Sci. *370*, 1–10. 10.1098/rstb.2014.0245.

21. Murugan, R., Buchauer, L., Triller, G., Kreschel, C., Costa, G., Martí, G.P., Imkeller, K., Busse, C.E., Chakravarty, S., Kim Lee Sim, B., et al. (2018). Clonal selection drives protective memory B cell responses in controlled human malaria infection. Sci. Immunol. *3*. 10.1126/sciimmunol.aap8029.

22. Luo, S., and Perelson, A.S. (2015). Competitive exclusion by autologous antibodies can prevent broad HIV-1 antibodies from arising. Proc. Natl. Acad. Sci. U.S.A. *112*, 11654–11659. 10.1073/pnas.1505207112.

23. Ganti, R.S., and Chakraborty, A.K. (2021). Mechanisms underlying vaccination protocols that may optimally elicit broadly neutralizing antibodies against highly mutable pathogens. Phys. Rev. E *103*, 1–17. 10.1103/physreve.103.052408.

24. Sachdeva, V., Husain, K., Sheng, J., Wang, S., and Murugan, A. (2020). Tuning environmental timescales to evolve and maintain generalists. Proc. Natl. Acad. Sci. U.S.A. *117*, 12693–12699. 10.1073/pnas.1914586117.

25. de Boer, R.J., and Perelson, A.S. (2017). How Germinal Centers Evolve Broadly Neutralizing Antibodies: the Breadth of the Follicular Helper T Cell Response. J. Virol. *91*, 1–23.

26. Nourmohammad, A., Otwinowski, J., and Plotkin, J.B. (2016). Host-Pathogen Coevolution and the Emergence of Broadly Neutralizing Antibodies in Chronic Infections. PLoS Genet. *12*. 10.1371/journal.pgen.1006171.

27. Victora, G.D., and Nussenzweig, M.C. (2012). Germinal Centers. Annu. Rev. Immunol. *30*, 429–457. 10.1146/annurev-immunol-020711-075032.

28. Nowosad, C.R., Spillane, K.M., and Tolar, P. (2016). Germinal center B cells recognize antigen through a specialized immune synapse architecture. Nat. Immunol. *17*, 870–877. 10.1038/ni.3458.

29. Victora, G.D., Schwickert, T.A., Fooksman, D.R., Kamphorst, A.O., Meyer-Hermann, M., Dustin, M.L., and Nussenzweig, M.C. (2010). Germinal center dynamics revealed by multiphoton microscopy with a photoactivatable fluorescent reporter. Cell *143*, 592–605. 10.1016/j.cell.2010.10.032.

30. Jardine, J.G., Kulp, D.W., Havenar-Daughton, C., Sarkar, A., Briney, B., Sok, D., Sesterhenn, F., Ereño-Orbea, J., Kalyuzhniy, O., Deresa, I., et al. (2016). HIV-1 broadly neutralizing antibody precursor B cells revealed by germline-targeting immunogen. Science *351*, 1458 LP – 1463. 10.1126/science.aad9195.

31. Pantophlet, R., Wilson, I.A., and Burton, D.R. (2003). Hyperglycosylated Mutants of Human Immunodeficiency Virus (HIV) Type 1 Monomeric gp120 as Novel Antigens for HIV Vaccine Design. J. Virol. *77*, 5889–5901. 10.1128/jvi.77.10.5889-5901.2003.

32. Schmidt, A.G., Therkelsen, M.D., Stewart, S., Kepler, T.B., Liao, H.X., Moody, M.A., Haynes, B.F., and Harrison, S.C. (2015). Viral receptor-binding site antibodies with diverse germline origins. Cell *161*, 1026–1034. 10.1016/j.cell.2015.04.028.

33. Wu, N.C., Grande, G., Turner, H.L., Ward, A.B., Xie, J., Lerner, R.A., and Wilson, I.A. (2017). In vitro evolution of an influenza broadly neutralizing antibody is modulated by hemagglutinin receptor specificity. Nat. Commun. *8*, 1–12. 10.1038/ncomms15371.

34. Kwong, P.D., Doyle, M.L., Casper, D.J., Cicala, C., Leavitt, S.A., Majeed, S., Steenbeke, T.D., Venturi, M., Chaiken, I., Fung, M., et al. (2002). HIV-1 evades antibody-mediated neutralization through conformational masking of receptor-binding sites. Nature 2002 420:6916 *420*, 678–682. 10.1038/nature01188.

35. Caradonna, T.M., Windsor, I.W., Roffler, A.A., Song, S., Watanabe, A., Kelsoe, G., Kuraoka, M., and Schmidt, A.G. (2022). An epitope-enriched immunogen increases site targeting in germinal centers. bioRxiv, 2022.12.01.518697. 10.1101/2022.12.01.518697.

36. Bajic, G., Maron, M.J., Caradonna, T.M., Tian, M., Mermelstein, A., Fera, D., Kelsoe, G., Kuraoka, M., and Schmidt, A.G. (2020). Structure-Guided Molecular Grafting of a Complex Broadly Neutralizing Viral Epitope. ACS Infect. Dis. *6*, 1182–1191. 10.1021/acsinfecdis.0c00008.

37. Caradonna, T.M., Ronsard, L., Yousif, A.S., Windsor, I.W., Hecht, R., Bracamonte-Moreno, T., Roffler, A.A., Maron, M.J., Maurer, D.P., Feldman, J., et al. (2022). An epitope-enriched immunogen expands responses to a conserved viral site. Cell Rep. *41*, 111628. 10.1016/J.CELREP.2022.111628.

38. Gitlin, A.D., Shulman, Z., and Nussenzweig, M.C. (2014). Clonal selection in the germinal centre by regulated proliferation and hypermutation. Nature *509*, 637–640. 10.1038/nature13300.

39. Yeh, C.H., Nojima, T., Kuraoka, M., and Kelsoe, G. (2018). Germinal center entry not selection of B cells is controlled by peptide-MHCII complex density. Nat. Commun. *9*. 10.1038/s41467-018-03382-x.

40. Kuraoka, M., Schmidt, A.G., Nojima, T., Feng, F., Watanabe, A., Kitamura, D., Harrison, S.C., Kepler, T.B., and Kelsoe, G. (2016). Complex Antigens Drive Permissive Clonal Selection in Germinal Centers. Immunity *44*, 542–552. 10.1016/j.immuni.2016.02.010.

41. Tas, J.M.J., Mesin, L., Pasqual, G., Targ, S., Jacobsen, J.T., Mano, Y.M., Chen, C.S., Weill, J.C., Reynaud, C.A., Browne, E.P., et al. (2016). Visualizing antibody affinity maturation in germinal centers. Science *351*, 1048–1054. 10.1126/science.aad3439.

42. Meyer-Hermann, M., Mohr, E., Pelletier, N., Zhang, Y., Victora, G.D., and Toellner, K.M. (2012). A theory of germinal center b cell selection, division, and exit. Cell Rep. *2*, 162–174. 10.1016/j.celrep.2012.05.010.

43. Mesin, L., Ersching, J., and Victora, G.D. (2016). Germinal Center B Cell Dynamics. Immunity *45*, 471–482. 10.1016/j.immuni.2016.09.001.

44. Sablitzky, F., Wildner, G., and Rajewsky, K. (1985). Somatic mutation and clonal expansion of B cells in an antigen-driven immune response. EMBO J *4*, 345–350. 10.1002/j.1460-2075.1985.tb03635.x.

45. Batista, F.D., and Neuberger, M.S. (1998). Affinity dependence of the B cell response to antigen: A threshold, a ceiling, and the importance of off-rate. Immunity *8*, 751–759. 10.1016/S1074-7613(00)80580-4.

46. Zhang, J., and Shakhnovich, E.I. (2010). Optimality of mutation and selection in germinal centers. PLoS Comput. Biol. *6*, 1–9. 10.1371/journal.pcbi.1000800.

47. Kumar, M.D.S., and Gromiha, M.M. (2006). PINT : Protein – protein Interactions Thermodynamic Database. Nucleic Acids Res. *34*, 195–198. 10.1093/nar/gkj017.

48. Nakanski, E., Lee, W.-Y., Mistry, B., Casal, A., Molloy, J.E., and Tolar, P. (2013). B Cells Use Mechanical Energy to Discriminate Antigen Affinities. Science, 1587–1590.

49. Tsourkas, P.K., Baumgarth, N., Simon, S.I., and Raychaudhuri, S. (2007). Mechanisms of B-cell synapse formation predicted by Monte Carlo simulation. Biophys. J. *92*, 4196–4208. 10.1529/biophysj.106.094995.

50. Fleire, S.J., Goldman, J.P., Carrasco, Y.R., Weber, M., Bray, D., and Batista, F.D. (2006). B cell ligand discrimination through a spreading and contraction response. Science *312*, 738–741. 10.1126/science.1123940.

51. Amitai, A., Chakraborty, A.K., and Kardar, M. (2018). The low spike density of HIV may have evolved because of the effects of T helper cell depletion on affinity maturation. PLoS Comput. Biol. *14*, e1006408. 10.1371/journal.pcbi.1006408.

52. Bell, G.I. (1978). Models for the specific adhesion of cells to cells. Science *200*, 618–627. 10.1126/science.347575.

53. Erdmann, T., and Schwarz, U.S. (2004). Stochastic dynamics of adhesion clusters under shared constant force and with rebinding. J. Chem. Phys. *121*, 8997–9017. 10.1063/1.1805496.

54. Huseby, E.S., Crawford, F., White, J., Marrack, P., and Kappler, J.W. (2006). Interface-disrupting amino acids establish specificity between T cell receptors and complexes of major histocompatibility complex and peptide. Nat. Immunol. *7*, 1191–1199. 10.1038/ni1401.

55. Birnbaum, M.E., Mendoza, J.L., Sethi, D.K., Dong, S., Glanville, J., Dobbins, J., Davis, M.M., Wucherpfennig, K.W., and Garcia, K.C. (2014). Deconstructing the Peptide-MHC Specificity of T Cell Recognition. Cell, 1073–1087. 10.1016/j.cell.2014.03.047.

56. Carson, R.T., Vignali, K.M., Woodland, D.L., and Vignali, D.A.A. (1997). T cell receptor recognition of MHC class II-bound peptide flanking residues enhances immunogenicity and results in altered TCR V region usage. Immunity *7*, 387–399. 10.1016/S1074-7613(00)80360-X.

57. Huseby, E.S., White, J., Crawford, F., Vass, T., Becker, D., Pinilla, C., Marrack, P., and Kappler, J.W. (2005). How the T cell repertoire becomes peptide and MHC specific. Cell *122*, 247–260. 10.1016/j.cell.2005.05.013.

58. Wang, P., Sidney, J., Kim, Y., Sette, A., Lund, O., Nielsen, M., and Peters, B. (2010). Peptide binding predictions for HLA DR, DP and DQ molecules. BMC Bioinform. *11*, 568. 10.1186/1471-2105-11-568.

59. Wang, P., Sidney, J., Dow, C., Mothé, B., Sette, A., and Peters, B. (2008). A Systematic Assessment of MHC Class II Peptide Binding Predictions and Evaluation of a Consensus Approach. PLoS Comput. Biol. *4*, e1000048.

60. Jensen, K.K., Andreatta, M., Marcatili, P., Buus, S., Greenbaum, J.A., Yan, Z., Sette, A., Peters, B., and Nielsen, M. (2018). Improved methods for predicting peptide binding affinity to MHC class II molecules. Immunology *154*, 394–406. https://doi.org/10.1111/imm.12889.

61. Nielsen, M., Lundegaard, C., and Lund, O. (2007). Prediction of MHC class II binding affinity using SMM-align, a novel stabilization matrix alignment method. BMC Bioinform. *8*, 238. 10.1186/1471-2105-8-238.

62. Nielsen, M., and Lund, O. (2009). NN-align. An artificial neural network-based alignment algorithm for MHC class II peptide binding prediction. BMC Bioinform. *10*, 296. 10.1186/1471-2105-10-296.

63. Nelson, R.W., Beisang, D., Tubo, N.J., Dileepan, T., Wiesner, D.L., Nielsen, K., Wüthrich, M., Klein, B.S., Kotov, D.I., Spanier, J.A., et al. (2015). T Cell Receptor Cross-Reactivity between Similar Foreign and Self Peptides Influences Naive Cell Population Size and Autoimmunity. Immunity *42*, 95–107. 10.1016/j.immuni.2014.12.022.

64. Woodruff, M.C., Kim, E.H., Luo, W., and Pulendran, B. (2018). B Cell Competition for Restricted T Cell Help Suppresses Rare-Epitope Responses. Cell Rep. *25*, 321-327.e3. 10.1016/j.celrep.2018.09.029.

65. Allen, C.D.C., Okada, T., and Cyster, J.G. (2007). Germinal-Center Organization and Cellular Dynamics. Immunity *27*, 190–202. 10.1016/j.immuni.2007.07.009.

66. Shulman, Z., Gitlin, A.D., Weinstein, J.S., Lainez, B., Esplugues, E., Flavell, R.A., Craft, J.E., and Nussenzweig, M.C. (2014). Dynamic signaling by T follicular helper cells during germinal center B cell selection. Science *345*.

67. Dustin, M.L. (2014). Review What Counts in the Immunological Synapse? Mol. Cell *54*, 255–262. 10.1016/j.molcel.2014.04.001.

68. Mayer, C.T., Gazumyan, A., Kara, E.E., Gitlin, A.D., Golijanin, J., Viant, C., Pai, J., Oliveira, T.Y., Wang, Q., Escolano, A., et al. (2017). The microanatomic segregation of selection by apoptosis in the germinal center. Science *358*, 0–9. 10.1126/science.aao2602.

69. Jacob, J., Kassir, R., and Kelsoe, G. (1991). In situ studies of the primary immune response to (4-hydroxy-3-nitrophenyl)acetyl. I. The architecture and dynamics of responding cell populations. J. Exp. Med. *173*, 1165–1175. 10.1084/jem.173.5.1165.

70. Nguyen Ba, A.N., Cvijović, I., Rojas Echenique, J.I., Lawrence, K.R., Rego-Costa, A., Liu, X., Levy, S.F., and Desai, M.M. (2019). High-resolution lineage tracking reveals travelling wave of adaptation in laboratory yeast. Nature *575*, 494–499. 10.1038/s41586-019-1749-3.

71. Zost, S.J., Lee, J., Gumina, M.E., Wilson, P.C., Bloom, J.D., and Hensley Correspondence, S.E. (2019). Identification of Antibodies Targeting the H3N2 Hemagglutinin Receptor Binding Site following Vaccination of Humans. Cell Rep. *29*, 4460-4470.e8. 10.1016/j.celrep.2019.11.084.

72. Finney, J., Yeh, C.H., Kelsoe, G., and Kuraoka, M. (2018). Germinal center responses to complex antigens. Immunol. Rev. *284*, 42–50. 10.1111/imr.12661.

73. Cohen, A.A., Gnanapragasam, P.N.P., Lee, Y.E., Hoffman, P.R., Ou, S., Kakutani, L.M., Keeffe, J.R., Wu, H.-J., Howarth, M., West, A.P., et al. (2021). Mosaic nanoparticles elicit cross-reactive immune responses to zoonotic coronaviruses in mice. Science *371*, 735–741. 10.1126/science.abf6840.

74. Yassine, H.M., Boyington, J.C., Mctamney, P.M., Wei, C., Kanekiyo, M., Kong, W., Gallagher, J.R., Wang, L., Zhang, Y., Joyce, M.G., et al. (2015). Hemagglutinin-stem nanoparticles generate heterosubtypic influenza protection. Nat. Med. *21*, 1065–1073. 10.1038/nm.3927.

75. Kanekiyo, M., Wei, C., Yassine, H.M., Mctamney, P.M., Boyington, J.C., Whittle, J.R.R., Rao, S.S., Kong, W., Wang, L., and Nabel, G.J. (2013). Self-assembling influenza nanoparticle vaccines elicit broadly neutralizing H1N1 antibodies. Nature *498*, 102–106. 10.1038/nature12202.

76. Nelson, S.A., Richards, K.A., Glover, M.A., Chaves, F.A., Crank, M.C., Graham, B.S., Kanekiyo, M., and Sant, A.J. (2022). CD4 T cell epitope abundance in ferritin core potentiates responses to hemagglutinin nanoparticle vaccines. NPJ Vaccines *7*, 124. 10.1038/s41541-022-00547-0.

77. Locci, M., Havenar-Daughton, C., Landais, E., Wu, J., Kroenke, M.A., Arlehamn, C.L., Su, L.F., Cubas, R., Davis, M.M., Sette, A., et al. (2013). Human circulating PD-1+CXCR3-CXCR5+ memory Tfh cells are highly functional and correlate with broadly neutralizing HIV antibody responses. Immunity *39*, 758–769. 10.1016/j.immuni.2013.08.031.

78. Havenar-daughton, C., Lee, J.H., and Crotty, S. (2017). Tfh cells and HIV bnAbs , an immunodominance model of the HIV neutralizing antibody generation problem. Immunol. Rev. *275*, 49–61. 10.1111/imr.12512.

79. Hu, J., Havenar-Daughton, C., and Crotty, S. (2013). Modulation of SAP dependent T:B cell interactions as a strategy to improve vaccination. Curr. Opin. Virol. *3*, 363–370. 10.1016/j.coviro.2013.05.015.

80. Aldhamen, Y.A., Appledorn, D.M., Seregin, S.S., Liu, C.J., Schuldt, N.J., Godbehere, S., and Amalfitano, A. (2011). Expression of the SLAM Family of Receptors Adapter EAT-2 as a Novel Strategy for Enhancing Beneficial Immune Responses to Vaccine Antigens. J. Immunol. *186*, 722–732. 10.4049/JIMMUNOL.1002105.

81. Jardine, J., Julien, J.P., Menis, S., Ota, T., Kalyuzhniy, O., McGuire, A., Sok, D., Huang, P.S., MacPherson, S., Jones, M., et al. (2013). Rational HIV immunogen design to target specific germline B cell receptors. Science *340*, 711–716. 10.1126/science.1234150.

82. Ekiert, D.C., Bhabha, G., Elsliger, M.A., Friesen, R.H.E., Jongeneelen, M., Throsby, M., Goudsmit, J., and Wilson, I.A. (2009). Antibody recognition of a highly conserved influenza virus epitope. Science *324*, 246–251. 10.1126/science.1171491

83. Amitai, A., Sangesland, M., Barnes, R.M., Rohrer, D., Lonberg, N., Lingwood, D., and Chakraborty, A.K. (2020). Defining and Manipulating B Cell Immunodominance Hierarchies to Elicit Broadly Neutralizing Antibody Responses against Influenza Virus. Cell Syst. *11*, 573-588.e9. 10.1016/j.cels.2020.09.005.

84. Meakin, P. (1984). Diffusion-limited aggregation in three dimensions: Results from a new cluster-cluster aggregation model. J. Colloid. Interface. Sci. *102*, 491–504. 10.1016/0021-9797(84)90252-2.

85. Southwood, S., Sidney, J., Kondo, A., del Guercio, M.F., Appella, E., Hoffman, S., Kubo, R.T., Chesnut, R.W., Grey, H.M., and Sette, A. (1998). Several common HLA-DR types share largely overlapping peptide binding repertoires. J. Immuno.l *160*, 3363–3373.

Chapter 3.

Antigen presentation dynamics shape the response to emergent variants like SARS-CoV-2 Omicron strain after multiple vaccinations with wild type strain

3.1. Summary

The Omicron variant of SARS-CoV-2 is not effectively neutralized by most antibodies elicited by two doses of mRNA vaccines, but a third dose increases anti-Omicron neutralizing antibodies. We reveal mechanisms underlying this observation by combining computational modeling with data from vaccinated humans. After the first dose, limited antigen availability in germinal centers (GCs) results in a response dominated by B cells that target immunodominant epitopes that are mutated in an Omicron-like variant. After the second dose, these memory cells expand and differentiate into plasma cells that secrete antibodies that are thus ineffective for such variants. However, these pre-existing antigen-specific antibodies transport antigen efficiently to secondary GCs. They also partially mask immunodominant epitopes. Enhanced antigen availability and epitope masking in secondary GCs together result in generation of memory B cells that target subdominant epitopes that are less mutated in Omicron. The third dose expands these cells and boosts anti-variant neutralizing antibodies.

3.2. Introduction

The emergence of viral mutants that escape from vaccine-imprinted immune memory is a major challenge for the development of vaccines against highly mutable viruses. In less than two years since effective vaccines became available, several SARS-CoV-2 variants of concern have emerged and spread. The Omicron (BA.1) variant harbors 32 mutations in the spike protein that enables it to escape from the majority of known monoclonal antibodies.[1–3] Individuals vaccinated with two doses of mRNA vaccines encoding the spike protein of the original Wuhan strain have much lower neutralizing antibody titers against Omicron compared to the original strain. However, a third dose (booster) of the same vaccine significantly increases protection against Omicron.[4–7]

After the booster, the peak neutralization titer increased roughly 3-fold against the wildtype (WT) Wuhan strain compared to the peak value after the second dose, but increased 20-30 fold against

Omicron.[8–11] Thus, the booster shot increased the breadth of the resulting neutralizing antibodies in addition to restoring antibody titers that waned over time. The increase in breadth after the third dose has been attributed to the rise of antibodies targeting diverse epitopes in the receptor-binding domain (RBD), some of which are relatively conserved between the Wuhan and Omicron strains.[8,12]

Many immunodominant epitopes on the SARS-CoV-2 spike protein lie in the ACE2 binding interface region.[8,9,13,14] Several human germline heavy chain genes exhibit high affinities for these epitopes.[15] Antibodies that develop from these germlines are highly enriched in responses to both infection[16] and two doses of mRNA vaccination.[17] The Omicron variant is highly mutated in the epitopes targeted by these antibodies, and therefore it can effectively evade the immune response generated after two doses of mRNA vaccines.[9]

Some of the Omicron-neutralizing antibodies that develop after the third vaccine dose must target relatively conserved epitopes. These antibodies must be subdominant because they are not present in large titer after the second vaccine dose. Immunodominance during interclonal competition of germinal center (GC) B cells is not well-understood. It is thought to be shaped by a combination of factors that include the frequency and affinity of naïve B cells,[18–21] antigen availability in the lymph node,[22,23] re-activation of pre-existing memory B cells[20,24] and epitope masking by pre-existing antibodies.[25–30]

In this paper, we study the mechanisms that underlie how repeated doses of the vaccine that encodes for Wuhan strain's spike change the immunodominance hierarchy of the resulting antibody response. We first developed an *in-silico* model that integrates the processes that occur in GCs with the expansion and differentiation of memory B cells outside the GC (extra germinal centers or EGCs). We explicitly consider antigen presentation dynamics in lymph nodes after the first and subsequent shots of homologous vaccines. Our results show that antigen availability on follicular dendritic cells (FDCs) in GCs differs markedly between the first and second shots, and this difference plays a key role in the diversity of memory B cells generated. Limited antigen availability in GCs after the first shot results in a memory response restricted to B cells that target immunodominant epitopes, which are heavily mutated in an Omicron-like strain. In secondary GCs seeded after the second dose, higher levels of antigen are available on FDCs because antibodies generated after the first dose enable effective antigen transport to FDCs. The increased antigen availability leads to an increase in memory B cells that target subdominant epitopes that are relatively conserved in an Omicron-like strain.

We also investigate the role of epitope masking by circulating antibodies in secondary GCs. These antibodies are mainly derived from memory cells generated after the first dose and can block the

dominant epitopes more effectively than subdominant epitopes. By incorporating experimental data on epitope mapping of serum antibodies, our *in silico* results show that considering the degree of overlap between RBD epitopes is important to understand the role of epitope masking in polyclonal response to vaccines.

In response to the third dose, the existing memory B cells that target subdominant epitopes expand and differentiate into plasma cells, leading to production of antibodies that confer better protection against emergent variants. These predictions from the *in-silico* model are consistent with our analyses of new and existing data obtained from individuals vaccinated with three shots of mRNA vaccines. Taken together, our results show that antigen availability on FDCs and epitope masking are two distinct factors that affect affinity maturation in secondary GCs. Clinically observed changes in immunodominance hierarchy upon receiving the third shot of COVID mRNA vaccines cannot be explained by accounting for only one of these effects. These insights shed new light on fundamental aspects of the nature of the recall response that are directly relevant to vaccine design. Our results also explain several recent observations linking different vaccine regimens to protection from Omicron.[31,32]

3.3. Results

3.3.1 Model Development

Our model incorporates four main aspects of the B cell and antibody responses: (i) antigen presentation on FDCs, (ii) activation of naive B cells and entry into GCs, (iii) affinity maturation in GCs and export of memory and plasma cells, and (iv) expansion of memory B cells and differentiation into plasma cells in EGCs (**Fig. 3-1**). A set of differential equations that extends a previous study[33] models antigen capture and transport. Stochastic agent-based models are used to simulate GC and EGC processes.[20,24,34] We consider four general classes of B cells: naive B cells, GC B cells, memory B cells, and plasma cells. At each incremental time step in the simulations, the probabilities of actions such as activation, selection, proliferation, mutation, differentiation, and apoptosis are calculated for the B cells, and these actions are then executed accordingly. 200 separate GCs are simultaneously simulated to mimic a secondary lymphoid organ.[35] The simulation is repeated 10 times for each vaccine dose. The average quantities thus calculated could be considered to be the typical population-level response. Descriptions of the computational model and the simulation algorithm are outlined below (see **METHODS** for further details of the model; **Tables 3-S1** and **3-S2** for parameters used

and **Table 3-S3** for detailed simulation algorithm). Parameter sensitivity analysis was performed for several key parameters, while the values for the other parameters were chosen to be consistent with experimental observations, as described in **Table 3-S2**.

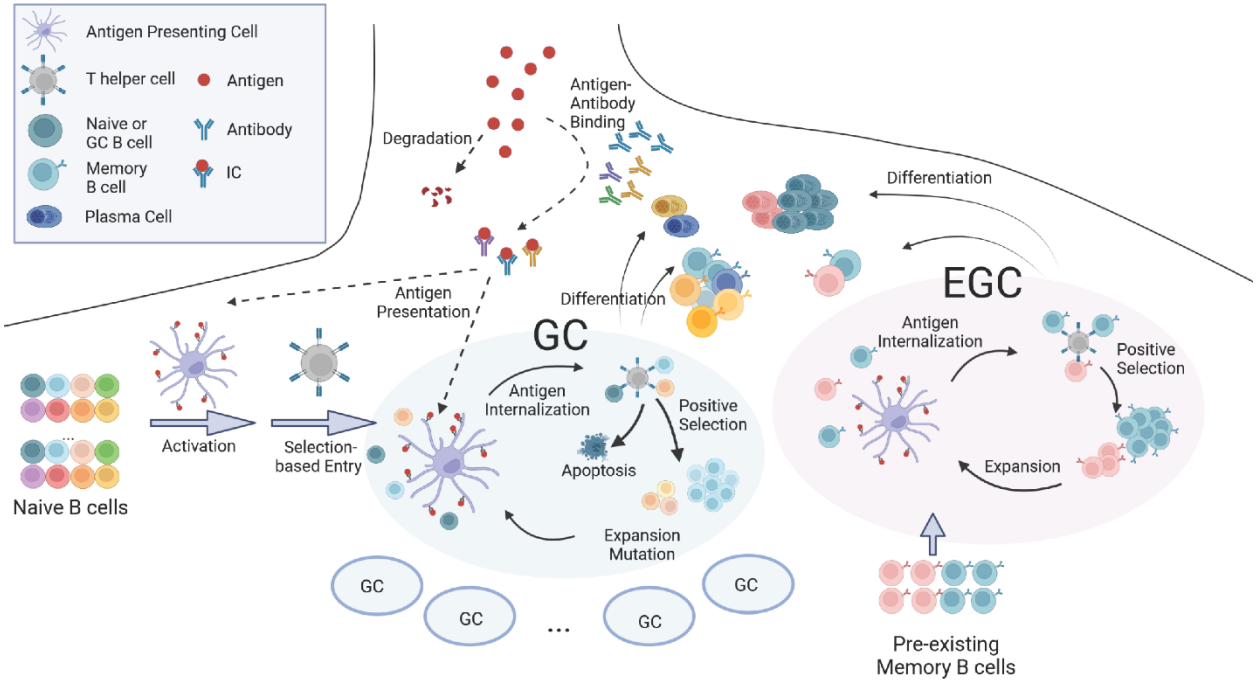

Figure 3-1. Schematic depiction of the In-Silico Model. The model integrates antigen presentation dynamics with processes in GCs and EGCs. Circulating antibodies help present antigen on FDCs. GC entry, GC B cell selection, replication and mutation, and differentiation of GC B cells into memory and plasma cells are considered. In the EGC, pre-existing memory cells undergo selection, proliferation, and differentiation without mutations. See also Figure 3-S1. The figure was created with Biorender software.

Model for antigen presentation

Although mRNA vaccines induce antigen production *in-vivo*, the protein production rate decreases rapidly and exponentially.[36] So we model vaccination as injection of a bolus of antigen.[33] Soluble and immune complex (IC) forms of the antigen rapidly reach dynamic equilibrium, with their relative amounts determined by the pre-existing antibody concentrations and equilibrium constants for antibody-antigen binding. The soluble antigen decays quickly but ICs are transported to FDCs where they decay with a much longer half-life. Upon immunization with a new antigen, small numbers of low-affinity circulating IgM antibodies are available to bind antigen. For subsequent

immunizations, higher affinity antibodies generated by earlier GC/EGC processes are available to form ICs. The differential equations that describe IC formation and antigen presentation are coupled to the agent-based simulation of GC and EGC processes (parameters used, **Table 3-S1**; simulation methods in **METHODS**).

Model for naive B cells and WT and variant strains

We model the distribution of germline-endowed affinities of naive B cells as an exponential distribution between K_d = 10^{-6} M and 10^{-8} M, where K_d is the dissociation constant. This is because a minimum affinity of about K_d = 10^{-6} M is required for activation,[37] and rare naive B cells with ~100-fold higher affinities can be found for antigens like SARS-CoV-2.[38,39] In our coarse-grained model, we group the few dominant epitopes on an antigen into a single "dominant" epitope and group the subdominant epitopes into a single "subdominant" epitope. The "dominant" epitope is targeted by a greater number of naive B cells and their affinities exhibit a longer high-affinity tail compared to the "subdominant" epitope (**Fig. 3-S1A; METHODS, Eqs. 2-5; parameters in Table 3-S2**).

Most immunodominant neutralizing epitopes on the SARS-CoV-2 spike protein are highly mutated in the Omicron variant (compared to WT),[2] while some subdominant epitopes are relatively conserved.[40] It has been suggested that mutations in the Omicron variant emerged to escape from immune pressure.[41] Therefore, in our model, the dominant epitope is less conserved. Each B cell has different affinities for the WT and the variant because the initial affinity and the effects of the mutations depend on the antigen (**Fig. 3-S1B, METHODS, Eqs. 6-7**). The effect of mutations on binding affinities for the WT and the variant are drawn from correlated log-normal distributions so that ~5% of affinity-affecting mutations are beneficial for each strain and most mutations are deleterious (**Fig. 3-S1C**).[42,43] The level of correlation between the WT and variant distributions determines the fraction of mutations that will be beneficial for binding to both strains (**Fig. 3-S1D**). We chose parameters so that about 72% and 19% of beneficial mutations increase affinities towards both strains for B cells that target subdominant and dominant epitopes, respectively. Our qualitative results are robust to changes in these parameters within reasonable ranges. Details of the simulation methods are in **METHODS**.

Model for germinal center entry of naive B cells

Naive B cells continuously enter 200 GCs after activation and selection.[44,45] At each time step, naive B cells internalize different amounts of antigen based on their binding affinity for the WT antigen and its availability.[24,37,46] Then, they stochastically get activated and compete for T helper

cells for survival signals that allow GC entry.[47–49] The probabilities for these entry events are determined by the amounts of internalized antigen (**METHODS**, Eqs. 10-13). The effect of memory B cell participation in GCs is studied by varying the fraction of pre-existing memory B cells added to the pool of naive B cells.

Selection stringency is an important factor in shaping B cell competition dynamics and thus the diversity of the response.[50] We studied the effects of changing the level of selection stringency and alternative models for antigen internalization to test the robustness of our qualitative results (**METHODS**, Eqs. 10 and 14).

Model for affinity maturation in germinal centers

For positive selection, GC B cells require activation by antigen capture[51,52] followed by selection by T helper cells.[53] In our model, GC B cells internalize antigen and are stochastically activated in the same way as the naive B cells. To model the competition for limited amount of T cell help, the birth rate of an activated GC B cell is determined by two factors: the amount of antigen it has captured relative to the average amount captured by all activated GC B cells, and the ratio between the number of T helper cells and activated B cells (**METHODS**, Eqs. 15-16). The number of T cells at a given time point is determined by a model that recapitulates a clinical observation in SARS-CoV-2 vaccinated subjects (**METHODS**, Eq. 17).[54] All GC B cells also stochastically undergo apoptosis with a constant death rate (**METHODS**, Eq. 18).[55] The use of birth-death model implicitly treats the cyclical migration between the light and dark zones. Many previous studies have used similar models and shown that they recapitulate the qualitative aspects of GC dynamics.[20,43,56–58] In our model, GC B cells that receive a stronger selection signal from T helper cells will statistically undergo greater number of birth events in a given time. Therefore, our model is qualitatively consistent with experimental findings, which shows that GC B cells that receive stronger selection signals proliferate a greater number of times in one cycle.[59]

With a probability, p_1, each positively selected B cell exits the GC. It can differentiate into a plasma cell with probability p_2, or become a memory cell. As discussed later, we studied varying p_1 and p_2. The remaining positively selected cells proliferate once. During a birth event, one of the two daughter cells mutates.[60] A mutation leads to apoptosis (probability 0.3), no affinity change (probability 0.5), or a change in the mutation state of a randomly selected residue (probability 0.2).[43] Details of the simulation methods are in **METHODS**.

Model for extra germinal center processes

Upon the second and third vaccination, an EGC response develops. EGCs select and expand pre-existing memory B cells without introducing mutations.[61] The number of memory B cells peaked 1 week after the second dose in vaccinated subjects.[54] Thus, although some memory B cells may continue to be generated in EGCs, in the simulation we terminate the EGC after 6 days. The selection process is identical to that in the GCs, except that the number of T cells is assumed to be equal to the peak value to account for the fast kinetics of the EGC. Proliferating cells in the EGC are assumed to differentiate into plasma cells with a high probability of 0.6, consistent with the observation that ~60% of newly proliferating memory cells are short-lived plasma cells.[62]

3.3.2. Limited antigen availability after the first vaccine dose leads mostly to memory B cells that are descendants of naive B cells with high germline-endowed affinities for dominant epitopes

Our simulations show that after the first vaccine dose (Vax 1) only a small amount of antigen gets deposited and retained on FDCs (**Fig. 3-2A**). This is because soluble antigen decays rapidly and IgM antibodies with relatively low affinity for the new antigen form immune complexes. These results are consistent with images of antigen retention on FDCs in mouse and monkey lymph nodes after a first vaccine dose.[22,33,63] In the first week after immunization, many naive B cells are activated and about 70 distinct cells enter each simulated GC (**Fig. 3-S2A**), a result consistent with observations in mice.[33,64]

Given the low antigen availability, the probability of low-affinity GC B cells capturing enough antigen to become activated and receive survival signals from T helper cells is low, consistent with experimental observations.[37,51] Consequently, B cells in early GCs with low germline affinities have a low frequency of proliferation. GC B cells also develop deleterious mutations more frequently than beneficial ones,[42] which further reduces their chance of being positively selected. Since the default for GC B cells is to undergo apoptosis,[55] in many simulated GCs the B cell population begins to decline, which makes it even more unlikely that beneficial affinity-increasing mutations will evolve. Thus, many GCs eventually collapse (**Fig. 3-2B**). In some GCs, however, B cells with high affinity evolve through mutations, and they can continue to proliferate, affinity mature and generate memory B cells despite low antigen availability. We find that ~75% of these memory B cells generated after Vax 1 originate from B cells with high germline affinities ($-logK_d \geq 7$) even though they make up a small

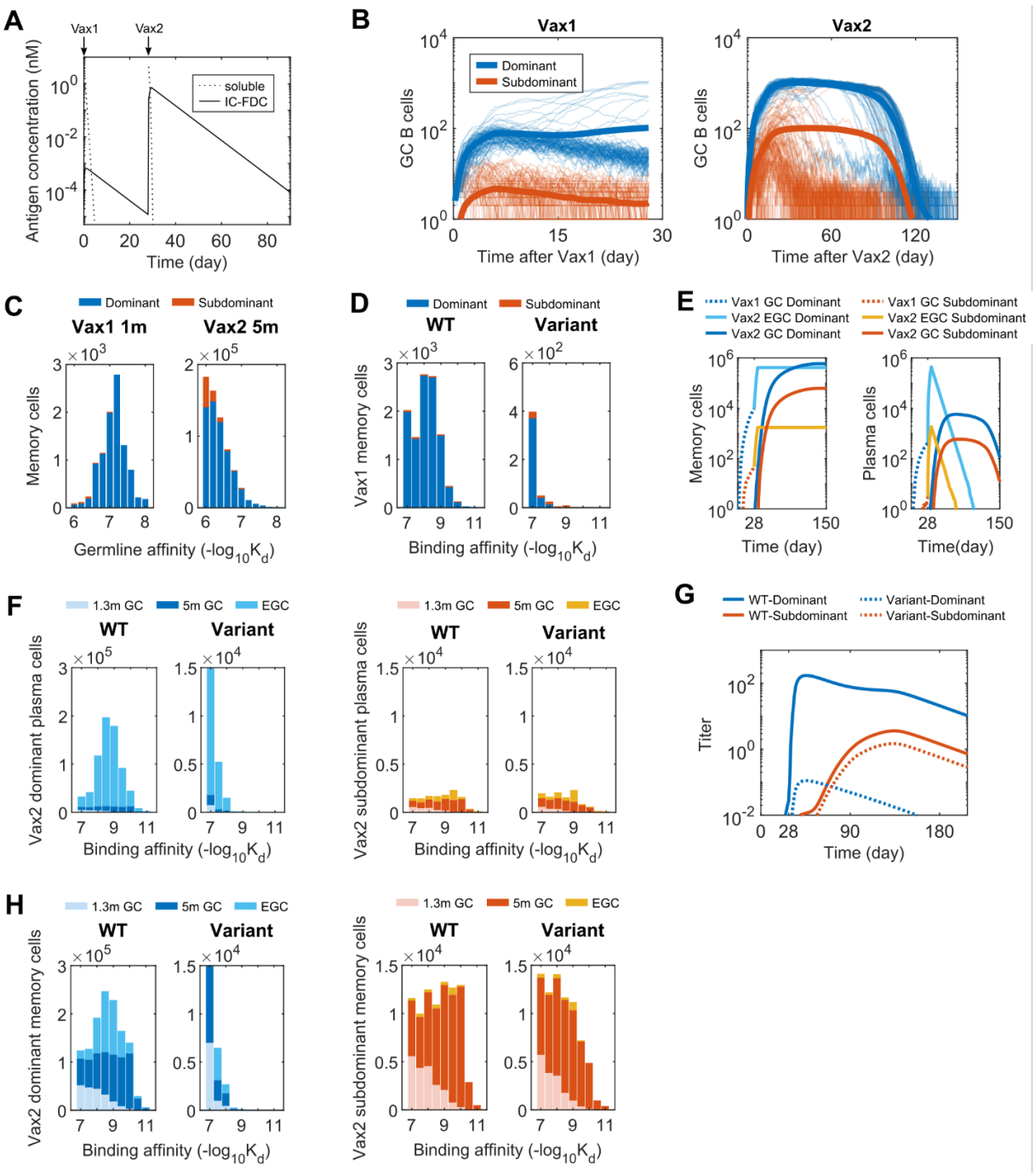

Figure 3-2. B cell and Antibody Responses after Vax 1 and Vax 2. (**A**) Concentrations of soluble antigen and immune complexes on FDCs. Vax 1 was administered on day 0 and Vax 2 on day 28. (**B**) Number of GC B cells that target dominant and subdominant epitopes after Vax 1 (Left panel) and Vax 2 (Right panel). 10 independent simulations of 200 GCs were performed for each case, and the bold curves show the mean values per GC. The other curves represent individual dynamic trajectories in 100 randomly selected GCs. (**C**) Histograms showing the distribution of WT-binding affinities of the germline B cell ancestors of GC-derived memory cells at 1m after Vax 1 (Left panel) and 5m after Vax 2 (Right panel). (**D**) Histograms showing the distribution of binding affinities of memory B cells against the WT and the variant at 1m after Vax 1. (**E**) Number

of memory cells (Left panel) and plasma cells (Right panel) from GCs and EGCs after Vax 1 and Vax 2. Memory cells generated from Vax1 are expanded in the EGC and differentiate into plasma cells. New memory B cells and plasma cells are also generated from Vax 2 GCs. The plasma cells are short-lived and decay at a constant rate. (**F**) Histograms showing the distribution of binding affinities of plasma cells for the dominant (left panels) and subdominant (right panels) epitopes of the WT and the variant strains after Vax 2. GC-derived cells at 1.3m and 5m after vaccination and EGC-derived cells are shown. EGCs only last for six days, so no plasma cells are generated between 1.3m and 5m. Since plasma cells are short-lived, the data for a given time point shows all cells generated until that time. (**G**) Antibody titers after Vax 1 and Vax 2 that target the dominant and subdominant epitopes of the WT and the variant strains. Titers are calculated as the antibody concentrations divided by K_d. (**H**) Histograms showing the distribution of binding affinities of memory cells for the dominant (left panels) and subdominant (right panels) epitopes of the WT and the variant strains after Vax 2. All histograms show distributions in terms of numbers of cells from 200 GCs, averaged over 10 simulations. See also Figure 3-S2 to S4.

fraction (~0.06%) of naïve B cells (**Fig. 3-2C**). High germline affinities are critical because they allow the B cells to proliferate frequently in the early GC, enabling them to acquire rare beneficial mutations. These cells predominantly target dominant epitopes (**Figs. 3-2B and 3-2C**). The genetic diversity in GCs is also limited as a small number of high affinity B cells quickly dominate (**Fig. 3-S2B**).[65,66] Thus, the memory response after Vax 1 is dominated by a small number of expanded clones (**Fig. 3-S2C**), consistent with data from vaccinated humans.[17] Since these B cells target immunodominant epitopes that are highly mutated in the variant, they exhibit limited cross-reactivity (**Figs. 3-2D and 3-S2D**).

Many observed neutralizing class 1/2 antibodies against WT SARS-CoV-2 that target dominant epitopes differ by only one or two mutations from the corresponding germline ancestors.[15,67–69] Our results suggest that this is because the GC response after Vax 1 is dominated by a few expanded clones that originate from naive B cells characterized by relatively high germline affinity for the dominant epitopes. One or two mutations are sufficient for these B cells to successfully mature in GCs.

We chose a particular set of parameters (**Table 3-S2**) to obtain the results shown in the main text, but we tested the robustness of this finding by varying the following key simulation parameters: the parameter that determines the relative importance of antigen availability for positive selection of GC B cells; parameters that characterize the naïve B cell repertoire and stringency of affinity-based selection. Our qualitative findings are robust across a wide range of these parameter values (**Fig. 3-S3A-D**). Our results are also robust to using an alternative model for the selection of GC B cells (**METHODS** Eq. 14, Fig. 3-S3E).

3.3.3. Expansion and differentiation of existing memory B cells that target dominant epitopes control the antibody response after the second dose, while increased antigen availability in secondary GCs elicits memory B cells that target subdominant epitopes

After the second vaccine dose (Vax 2), the memory and plasma cell responses are determined by processes that occur in newly formed secondary GCs and in EGC compartments. Our choice of simulation parameters that characterize the relative numbers of plasma and memory cells that exit from the GCs and EGCs was informed by data from mice and humans (see the section on model). These data suggest that many short-lived plasma cells are rapidly produced in EGCs which then quickly decay, while GCs produce a relatively small number of plasma cells over longer times.[8,54,70] The number of EGC and GC-derived memory B cells appear to be of similar orders of magnitude since the numbers of RBD-targeting memory cells are similar between ~1 month and ~5 months after Vax 2.[8,54] Our qualitative results are robust to parameter variations over wide ranges (**Figs. 3-S3A-S3F**).

Since EGCs select and expand the memory B cells generated in response to Vax 1 in an affinity-dependent manner (**Fig. 3-2E**), most of the plasma cells that differentiate from them target the dominant epitopes and have low cross-reactivity to the variant (**Fig. 3-2F, 3-S2D-E**). Therefore, the WT antibody titer rapidly increases but not the variant titer (**Fig. 3-2G**). The number of plasma cells derived from secondary GCs is small compared to EGC-derived plasma cells (**Fig. 3-2E-F**) and has a limited contribution to the overall antibody titer after Vax 2, an observation consistent with original antigenic sin.[71] That is, the antibody response to secondary immunization is dominated by the recall of previously generated responses.

After Vax 2, soluble antigen rapidly forms ICs with pre-existing high-affinity antibodies before it decays to low levels (**Fig. 3-2A**). Thus, we find a large difference in antigen availability after primary and secondary immunization, consistent with lymph node imaging of rhesus macaques.[63] In the first week after immunization, a similar number of B cells join the GCs as in Vax 1 (**Fig. 3-S2A**). The high amounts of antigen available on FDCs now allow lower affinity B cells that target subdominant epitopes to internalize antigen, proliferate, acquire beneficial mutations and compete with higher affinity cells for survival signals from helper T cells. Unlike Vax 1 GCs, this effect prevents secondary GC B cells from being completely dominated by high-affinity B cells that target dominant epitopes (**Figs. 3-2B, 3-S2B**), and diverse memory B cells exit from the GCs (**Fig. 3-S2C**). Since low-affinity naive B cells are much more common, they often ultimately outcompete the rare high-affinity naive B cells to take over GCs (**Fig. 3-2C**). Only ~7% of memory B cells descend from naive cells with high affinities after Vax 2 ($-logK_d \geq -7$), in contrast to ~75% after Vax 1. By 5 months after Vax 2, large numbers of GC-derived memory B cells are produced, and they have higher affinities towards WT than the EGC-derived clones because of affinity maturation over time (**Fig. 3-2H**). Notably, by 5m after Vax 2, some subdominant epitope-targeting memory B cells also develop high affinities towards the variant (**Fig. 3-2H, Fig. 3-S2F**).

We also studied the role of memory B cell re-entry into secondary GCs. We added different fractions of existing memory B cells to the naive B cell pool after Vax 2. We find that more memory B cell re-entry into GCs decreases the output of memory B cells that target subdominant epitopes (**Fig. 3-S4A**). This is because most of the existing memory cells target dominant epitopes, and high-affinity memory B cells have a high chance of dominating the GC once they enter (**Fig. 3-S4B**). These findings suggest that limiting memory B cell re-entry into the secondary GCs promotes the generation of memory B cells that target subdominant epitopes, and may be a mechanism that evolved to confer protection against future variants that may emerge.[27,72] Similar effects could result from alternative mechanisms such as the early export of predominantly low-affinity GC B cells as memory cells.[73]

3.3.4. Memory B cells generated in GCs after the second dose are expanded and differentiated in EGCs after the third vaccine dose to drive improved variant neutralization

After the third vaccine dose (Vax 3), existing memory B cells expand in the EGC and differentiate into plasma cells. A number of high-affinity memory B cells generated after Vax 2 target subdominant epitopes that are relatively conserved between the WT and variant strains (**Fig. 3-2H**). These cells differentiate into plasma cells with high affinity for the variant (**Fig. 3-3A**). Thus, the antibody titer against the variant increases after Vax 3 (**Fig. 3-3B**). The fold-change in titer from 1.3 months post Vax 2 to 1 month post Vax 3 is greater for the variant than for the WT, consistent with serum responses in vaccinated humans.[8,10] The breakdown of antibody titers based on epitope specificity shows that the variant-binding titer is driven by the subdominant epitope-targeting antibodies, while the WT-binding titer is still driven by the dominant epitope-targeting antibodies (**Fig. 3-3B**). The greater fold-change in variant-binding titer is therefore explained by the large increase in the number of subdominant memory B cells that emerge from Vax 2 GCs compared to that from Vax 1 GCs. Note that our results showing that neutralizing antibodies for the variant after Vax 3 are drawn from the existing memory pool after Vax 2 are consistent with clinical data showing that antibody sequences that neutralize Omicron after the third dose were present in the memory compartment after the second dose.[8]

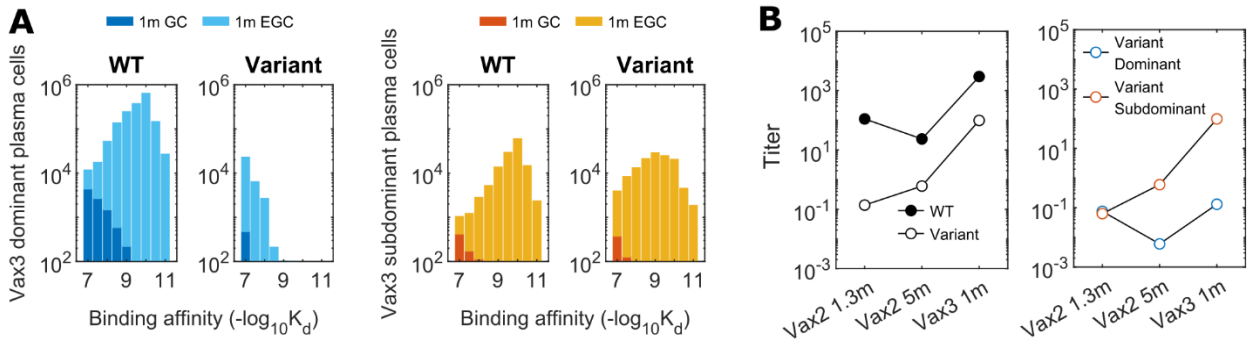

Figure 3-3. B cell and antibody responses after Vax 3. (A) Histograms showing the distribution of binding affinities of plasma cells targeting the dominant and subdominant epitopes of the WT and variant strains 1m after Vax3. Almost all of the plasma cells at this point are derived from the EGC. A substantial response to the subdominant epitope of the variant emerges. All histograms show distributions in terms of numbers of cells from 200 GCs, averaged over 10 simulations. (B) Comparison of antibody titers against the WT and the variant (left panel) and the epitope-specificity of the variant-targeting antibodies (right panel) at 1.3m after Vax 2, 5m after Vax 2, and 1m after Vax 3. The titer for antibodies targeting the subdominant epitope of the variant increases monotonically after 1.3m post Vax 2 because it has a very low value at early times. Titers are calculated as the antibody concentrations divided by K_d.

3.3.5. Analysis of sera from vaccinated humans is consistent with in-silico predictions

We explored the veracity of our *in-silico* predictions by analyzing data on sera obtained from individuals vaccinated with COVID-19 mRNA vaccines. Muecksh et al. sampled B cells from 5 uninfected individuals after the first, second, and third doses of the Moderna or Pfizer-BioNTech vaccines.[8] The samples were collected an average of 2.5 weeks, 1.3 and 5 months, and 1 month after the first, second and third doses, respectively. We grouped sequences of 1370 B cells into clonal families and constructed a phylogenetic tree for each clonal family using Matlab's seqlinkage function. If a phylogenetic tree contained two or more identical IGH sequences at the same time point or at different time points, we assumed that these clones were expanded in EGCs. The basis for this method is that EGCs expand memory cells with little to no mutations (**Fig. 3-S5A**). This method is conservative as there is a low rate of mutation in EGCs.[62] For this reason and because of under-sampling, we can identify only a small fraction of EGC-derived B cells. However, when tested against simulated data, we found the precision of our method for identifying EGC clones to be very high. From the simulation data in Figs. 3-2 and 3-3, we randomly sampled B cells from different time points as was done in experiments. We then applied the method described above, and found our identification method has a sensitivity of ~0.3 and a precision of ~0.9 for finding the EGC B cells (**Fig. 3-S5B**). Bayesian analysis agrees with these estimates (**METHODS**, **Fig. 3-S5B**). Sequences that were not EGC-derived were considered to be derived from GCs. Thus, we classified the sequences of B cells

obtained after Vax 2 and Vax 3 as either EGC-derived or GC-derived. The GC-derived cells were further classified as clones if clonally related sequences were observed and otherwise as singlets.

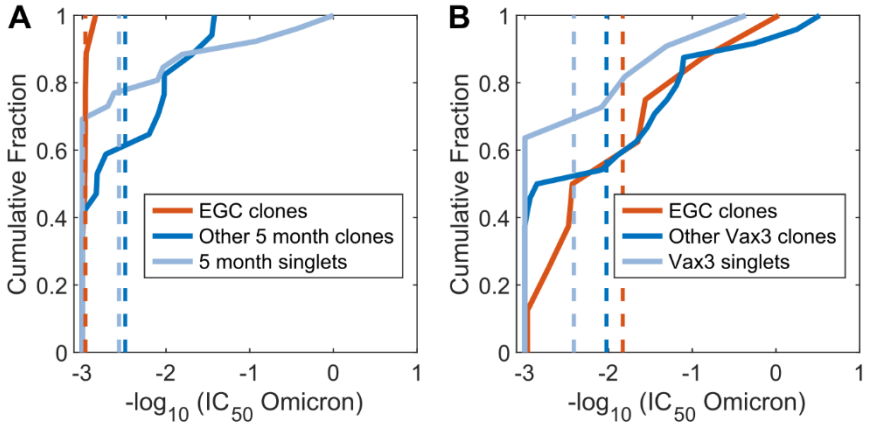

Figure 3-4. Omicron neutralization potency of monoclonal antibodies that are inferred to originate in EGCs and GCs, derived from vaccinated humans. (**A**) The cumulative distributions of omicron neutralization titers (IC_{50}) of B cells and their antibodies sampled after Vax 2. Based on the sequence analysis (see text), the B cells have been classified as those identified to be derived from EGCs (red curves), other clonal families (blue curves), or singlets (light blue curves). Dashed lines indicate mean values. Because the EGCs are short-lived and the distributions were identical, EGC B cells collected 5 months after Vax 2 were combined with EGC B cells collected 1.3 months after Vax 2. (**B**) Similar data as in panel A for cells sampled 1m after Vax 3. A statistical comparison of the distributions shown in Panels A and B is noted in the text. See also Figure 3-S5.

To test the *in-silico* results against clinical data, we determined the neutralization activity of antibodies derived from the sequences classified as EGC-derived and GC-derived. We combined existing data[8] with new measurements of neutralization activities for some of the sequences that our analyses identified as EGC-derived. The new measurements were carried out using the methods described before.[8,74,75] The neutralization activities (IC_{50}) of 112 antibodies derived from B cells were measured against the Omicron RBD. Nine EGC-derived B cells were identified from samples collected after Vax 2. Other B cells sampled 5 months after Vax 2 were labeled as GC-derived clonal families or singlets. The EGC-derived clones have a much higher IC_{50} than the likely GC-derived clones or singlets in terms of the mean and the maximum (**Fig. 3-4A**), indicating their low potency. The geometric mean of the GC-derived clones and singlets is 341 ng/mL which is much lower than the 919 ng/ml for EGC clones (p=0.00027). This result agrees with the *in-silico* prediction that GC-derived B cells exhibit better omicron neutralization titers than the EGC-derived B cells after Vax 2 (**Fig. 3-2H, Fig. 3-S2E,F**). We note that five of the nine EGC-derived B cells after Vax 2 also did not neutralize the WT (**Table 3-S4**).

8 EGC-derived B cells were identified after Vax 3. Fig. 3-4B shows that the IC_{50} of EGC clones improved from a geometric mean of 919 ng/mL after Vax 2 to 68 ng/mL after Vax 3 (p=0.0035, **METHODS**). Comparing Figs. 3-4A and 3-4B shows that the geometric mean of IC_{50} values for EGC-derived antibodies after Vax 3 is more similar to the GC-derived ones after Vax 2 (341ng/ml) than the EGC-derived clones after Vax 2 (919 ng/ml). This is consistent with our *in-silico* predictions (**Fig. 3-3A and Fig. 3-2H**), which show that the EGCs formed after Vax 3 expand the subdominant and cross-reactive memory B cells generated after Vax 2.

3.3.6. Epitope masking by polyclonal antibodies amplifies the increase in subdominant responses, but increased antigen availability plays a key role

Circulating antibodies can mask their corresponding epitopes, promoting the evolution of GC B cells that target other epitopes. Several experiments show that injection of high-affinity monoclonal antibodies along with the immunogen in mice[25–28] and humans[29] abrogates de-novo affinity maturation to the target epitopes. However, while some studies have also observed enhanced subdominant response upon repeated vaccinations in animals, the role of epitope masking by vaccine-induced polyclonal antibodies in this response is less conclusive.[26,28] It has been speculated that masking of dominant epitopes by circulating antibodies may drive the diversity increase of memory B cells upon repeated mRNA vaccinations.[8,76,77] By combining mathematical modeling with available clinical observations, we aimed to clearly understand the effects of epitope masking in the context of SARS-CoV-2 vaccination in humans.

Given the reported serum RBD-targeting antibody concentrations and affinities after mRNA vaccination,[78,79] the extent to which antibodies mask their corresponding epitopes can be calculated assuming dynamic equilibrium.[80] Such a calculation suggests that epitope masking will not be important after Vax 1 because of low antibody titer, but by 2 weeks after Vax 2, antibodies will mask ~99% of the epitopes (**Fig. 3-S6A**). If the dominant and subdominant epitopes do not overlap, then epitope masking selectively lowers the effective dominant epitope concentrations by ~100-fold. In our simulations, this causes subdominant B cells to monopolize the secondary GC response (**Fig. 3-S6B-C**), consistent with the observations in experimental studies that used monoclonal antibodies to block immunodominant epitopes.

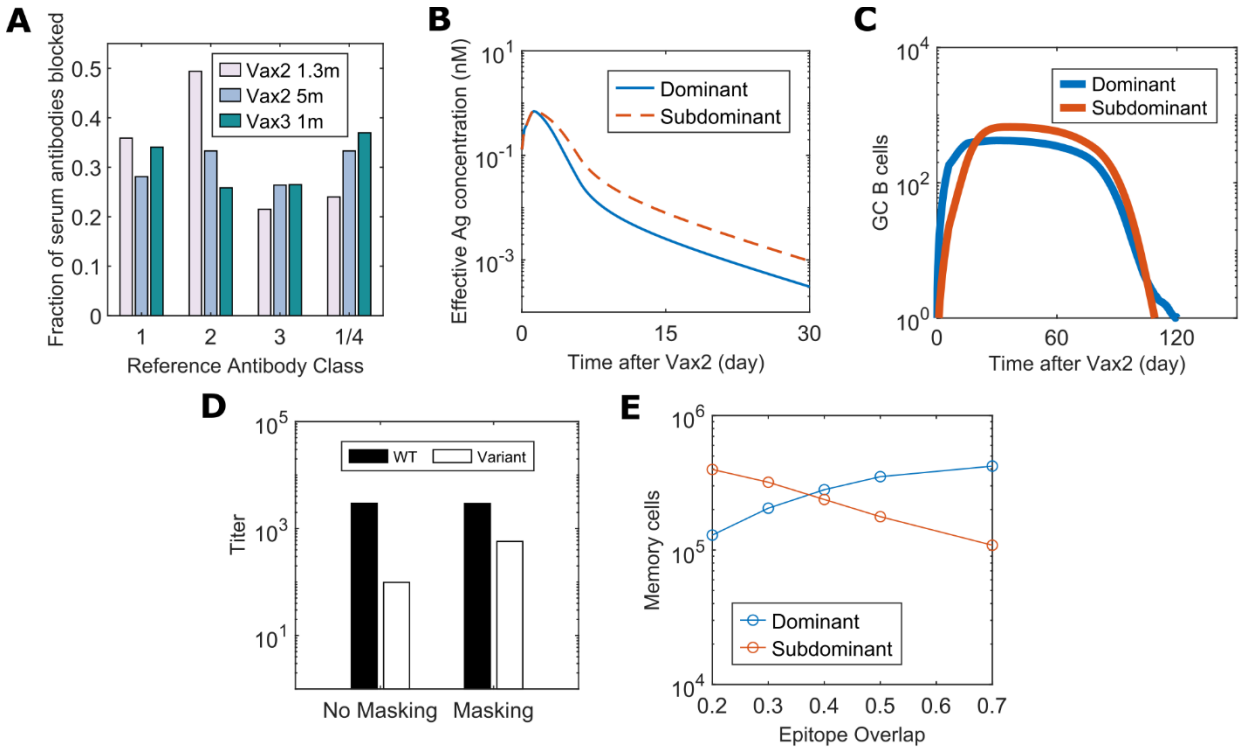

Figure 3-5. Role of epitope masking on immunodominance hierarchy. (**A**) Fraction of antibodies derived from human serum responses that blocked the binding of four reference antibodies (class 1, 2, 3, and 1/4) that target different regions of the SARS-CoV-2 RBD. Data from Muecksch et al. were reanalyzed [8]. (**B**) Epitope-dependent effective antigen concentrations when there is epitope masking with 30% of epitope overlapping. (**C**) Number of GC B cells that target dominant and subdominant epitopes after Vax 2 with 30% epitope overlap. (**D**) Comparison of antibody titers at 1m after Vax 3 between simulations with no epitope masking ("No Masking") and epitope masking with 30% of epitope overlap ("Masking"). Titers are calculated as the antibody concentrations divided by K_d. (**E**) Number of dominant and subdominant memory B cells at 5m Vax 2 when the degree of epitope overlap is varied in simulations. See also Figure 3-S6.

However, antibodies developed after mRNA vaccination are highly polyclonal and target many overlapping epitopes. Class 1 and 2 antibodies that dominate early neutralizing antibody responses bind to the ACE2 binding motif.[2,81] Class 3 and 4 neutralizing antibodies target relatively conserved peripheries of the RBD and are subdominant.[2,8] Yet, reanalysis of data from Muecksch et al.[8] shows that each of the reference class 1, 2, 3, and 1/4 neutralizing antibodies interfere with 20-50% of the polyclonal antibodies across all time points (**Fig. 3-5A**). These data suggest that serum polyclonal antibodies will likely partially block both dominant and subdominant epitopes due to overlap between epitopes.

Therefore, we studied an epitope masking model where a fraction of antibodies targeting dominant epitopes can also block subdominant epitopes, and *vice versa*. When this fraction (epitope overlap) is 30%, the antigen availability advantage for subdominant B cells is relatively small (**Fig.**

3-5B). But even this moderate effect amplifies the subdominant B cell response from the secondary GCs (**Fig. 3-5C**). Compared to the case without epitope masking, the antibody titer for the variant further increases after Vax 3, without much difference in the WT titer (**Fig. 3-5D**). Thus, our model suggests that epitope masking from polyclonal responses can enhance targeting of subdominant epitopes that moderately overlap with immunodominant epitopes. Thus, epitope masking likely plays a significant role in the observed increase in class 3 and 4 neutralizing antibodies (that bind to the RBD periphery) after Vax 3.[8]

However, well-conserved, but subdominant, epitopes also exist on the ACE2 binding motif that are targeted by class 1 and 2 antibodies, and antibodies that target these epitopes can neutralize Omicron well.[40] These subdominant epitopes overlap significantly with the epitopes targeted by immunodominant class 1 and 2 antibodies because antibody footprints typically cover most of the ACE-2 binding motif.[81,82] Our calculations show that the promotion of subdominant epitope-targeting by epitope masking decreases with an increase in the degree of overlap between dominant and subdominant epitopes (**Fig. 3-5E**). Thus, if epitope masking was the only mechanism underlying increased Omicron neutralization after Vax 3, Omicron-neutralizing subdominant class 1 and 2 antibodies should be rare. However, analysis of 43 Omicron-neutralizing antibodies isolated from humans after Vax 3 showed that 63% of them were class 1/2 antibodies.[83] These antibodies were derived mostly from subdominant germlines that were rarely observed 1.3m after Vax 2, but they became more prevalent after Vax 3 and were significantly mutated.[83] These observations suggest their development in secondary GCs. Meanwhile, class 1/2 antibodies derived from immunodominant germlines dominated the early antibody response after Vax 2, as expected.[83] Since these immunodominant antibodies likely also significantly mask the epitopes targeted by subdominant class 1/2 antibodies, epitope masking alone cannot explain the rise of the latter in secondary GCs. Increased antigen availability on FDCs after Vax 2 (see earlier sections) likely plays a key role in promoting their emergence.

3.4. Discussions

We studied the effects of repeated immunization with a WT vaccine on antibody responses to a highly mutated variant, such as the Omicron strain of SARS-CoV-2. Our findings shed new light on fundamental aspects of the humoral immune response, and can guide the design of vaccination strategies that aim to elicit broadly protective responses against mutable viruses.

After Vax 1, the limited antigen availability during GC reactions strongly promotes the dominance of the B cells that have high germline affinity or can acquire high affinity via a small number of mutations (**Fig. 3-2D**). Such B cells likely target the immunodominant epitopes that are highly mutated in the variant. Upon receiving Vax 2, memory B cells generated by GCs after Vax 1 are rapidly expanded and they differentiate into plasma cells that secrete antibodies (**Fig. 3-2E-F**). Thus, the antibodies produced after Vax 2 largely target immunodominant epitopes, and so Omicron neutralizing titers are low (**Fig. 3-2G**). These *in-silico* results are consistent with data showing the dominant antibodies produced after the first two doses have few mutations[8].

After Vax 2, higher amounts of antigen are displayed on FDCs. This increased antigen availability allows memory B cells that target subdominant epitopes to emerge despite their lower germline affinities (**Fig. 3-2B-C**). These epitopes are relatively conserved between the WT and Omicron strains. After Vax 3, these memory B cells are expanded in EGCs, resulting in increased Omicron neutralizing antibody titers (**Fig. 3-3B**). This is consistent with data showing that the Omicron-neutralizing antibodies present after Vax 3 existed in the memory pool after Vax 2[8]. Importantly, our *in-silico* predictions are consistent with our analyses of sequence and neutralization data that we obtained from vaccinated individuals (**Fig. 3-4**).

In addition to the effects of increased antigen availability, epitope masking in secondary GCs can further promote B cell response against the subdominant epitopes. However, the effects of epitope masking in the context of vaccine-induced polyclonal responses in humans is more complex than in past studies using monoclonal antibodies in mice[25–28] since the overlap between epitopes targeted by polyclonal antibodies must be considered. Our in silico model incorporates the analysis of serum antibody epitope mapping data. Our findings indicate that epitope masking is likely to enhance the class 3 and 4 B cell response in secondary GCs, but the observation of Omicron-neutralizing subdominant class 1 and 2 antibodies in large numbers after Vax 3 [83] cannot be explained only by epitope masking. Instead, this observation suggests that increased antigen availability on FDCs and epitope masking work together to promote the emergence of subdominant responses upon boosting.

Regev-Yochay et al. reported that a fourth dose of an mRNA vaccine restored the antibody titer against Omicron to a level similar to the peak response after Vax 3, but unlike Vax 3 it did not further boost the titer compared to the previous dose.[32] Results from our model are consistent with this finding (**Fig. 3-6**). The mechanistic explanation is that GCs formed after Vax 3 do not benefit further from increased antigen availability compared to the GCs formed after Vax 2. Moreover, antibodies that target subdominant epitopes are available in higher titers soon after Vax 3 and they can mask

these epitopes. Therefore, masking immunodominant epitopes confers less of an advantage to the subdominant B cells in GCs formed after Vax 3 compared to those formed after Vax 2. Thus, similar or fewer subdominant GC B cells develop after Vax 3. However, overall antibody titer after the fourth dose is still similar to Vax 3 because both GC and EGC-derived memory cells generated after Vax 3 are expanded.

Although memory B cells participating in secondary GCs can help protect against closely-related variants, our results show that these memory B cells can limit epitope diversification and adversely impact the ability to protect against variants that differ more significantly from the WT strain. This is because the affinity advantage of memory cells can allow them to dominate GCs. We note also that higher antigen availability and epitope masking may underlie recent observations in mice showing that memory B cells are not highly represented in secondary GCs.[27,72]

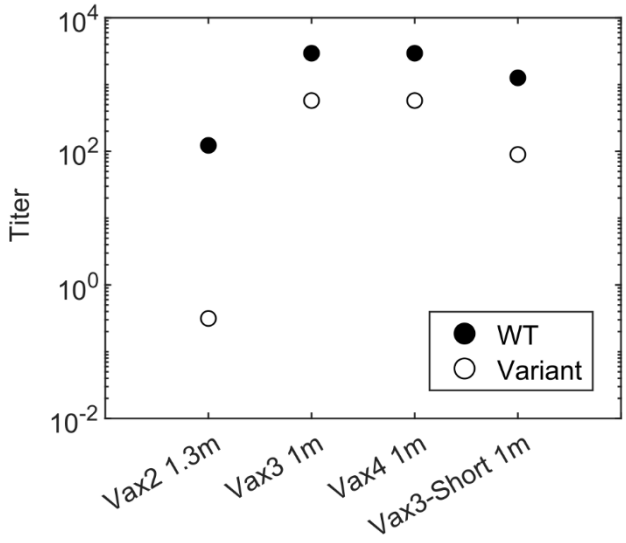

Figure 3-6. Comparison of antibody titers for different vaccination regimens. Antibody titer elicited by different vaccination regimens. "Vax4" refers to the case when a second booster dose was given 5m after Vax3. "Vax3-Short" refers to the case when Vax 3 was given 1.3m after Vax 2 instead of the standard 5m interval. To study how epitope masking may affect the second booster (Vax 4), all cases were simulated with epitope masking and 30 % epitope overlap. Titers are calculated as the antibody concentrations divided by K_d.

Our results provide mechanistic insights into the effects of the timing of booster shots on the ability to develop variant-neutralizing antibodies. A group of subunit vaccine ZF2001 recipients who received Vax 3 only 1 month after Vax 2 were less likely to develop Omicron neutralizing antibodies than the group with a 4 month interval (56% vs. 100%).[31] Our model predicts (**Fig. 3-6**) that when

Vax 3 is given 1.3 month after the second dose ("Vax3-Short"), the subdominant epitope-targeting antibody titer is low. Most of the memory cells that have high affinities 1.3 month after Vax 2 are EGC-derived and thus target the dominant epitope (**Fig. 3-2H**). Also, even subdominant GC-derived memory B cells have a relatively low affinity towards the variant due to limited time for affinity maturation (**Fig. 3-2G**). As a result, receiving Vax 3 1.3 month after Vax 2 will mostly expand B cells with low cross-reactivity. But 4 months after Vax 2, more affinity maturation allows B cells with higher affinity for subdominant epitopes to develop, which is consistent with the observation that the number of mutations increases significantly between 1.3 months and 5 months after Vax 2.[8] The memory B cells available 4 months after Vax 2 can be expanded in EGCs after Vax 3 to result in better Omicron neutralizing capability.

Our results may also have implications for efforts to elicit broadly neutralizing antibodies (bnAbs) against HIV by sequential immunization with variant antigens.[24,84,85] This approach aims to focus the B cell response on a conserved target epitope. Higher antigen availability and masking of the conserved epitope after booster shots will likely promote the evolution of off-target responses in secondary GCs, consistent with observations in macaques.[85] These effects may be especially significant when the conserved target epitope is quite distinct from the diverse variable regions, as is the case for some epitopes targeted by bnAbs against HIV and the conserved epitope in the stem of influenza's spike.[86,87]

The purpose of our *in silico* study is not detailed quantitative fitting of experimental data, but rather obtaining new mechanistic insights which we tested against clinical data. To achieve this, we adopted a simplified model that focuses on the most important aspects of the humoral immune response but omitted details that are unlikely to affect qualitative outcomes. The simplification is necessary because adding these details would increase the number of parameters and associated uncertainties without enhancing mechanistic understanding. Nonetheless, the congruence between our predictions and existing and new clinical data reported in this paper suggest that our model captures much of the relevant biology.

One interesting question is whether the different peptide epitopes presented by people with different HLA haplotypes may influence T helper cell responses, and thus affect B cell immunodominance. BCRs with different binding specificities bind to different surface epitopes on the spike protein, but if binding is sufficiently strong, regardless of B cell epitope specificity, the whole spike protein is internalized. Thus, diverse peptides derived from the entire spike protein are available for presentation by individuals with any given haplotype. The main difference between the

B cells with different specificities is the amounts of antigen they internalize. Therefore, we used the amount of antigen internalized to model the competition between B cells for T cell help without considering the individual helper T cell epitopes. Consistent with this view, the B cell immunodominance observed after receiving COVID vaccines is similar among diverse individuals in the population,[10,13] despite the variability of HLA subtypes and helper T cell epitope immunodominance.[88] In addition, better Omicron responses are consistently observed after the third dose in a diverse group of individuals.[10]

We hope that our results and mechanistic insights will motivate other fundamental studies into how the humoral immune response is influenced by antigen presentation dynamics. For example, it will be interesting to explore whether strategies to modulate antigen availability such as slow antigen delivery and immunization with immune complexes or particulate immunogens may help mitigate unwanted immunodominance hierarchies.[22,89,90]

3.5. Method Details

Simulation details for antigen dynamics

Table 3-S1 describes the reactions that govern antigen dynamics and the differential-algebraic equations derived from the reactions that are solved in the simulations. The values of initial conditions and parameters are also shown, with notes on how they were selected. The following species are involved in the dynamics: soluble antigen (Ag), soluble antibody (Ig), soluble immune complex (IC), immune complex on follicular dendritic cell (IC-FDC), and plasma cell (PC).

The simulation progresses in time steps of 0.01 day, and the concentrations are updated at each step. Since the on-rate for antigen and antibody binding is very fast (order of $k_a = 10^{11}\ \mathrm{M}^{-1}\mathrm{day}^{-1}$),[37] we assume that fast equilibrium is maintained between Ag, Ab, and IC. Thus, the equilibrium concentrations [Ag], [Ig], and [IC] can be calculated. Then, the concentrations of all species except for the PCs are updated to account for Ag decay, IC deposition on FDC, Ig production by plasma cells, IC-FDC consumption, and Ig decay, based on the differential equations described in **Table 3-S1**. The PC concentration is updated based on their stochastic production and apoptosis from B cell dynamics involving GCs and EGCs. Each simulation models 200 GCs and 1 EGC simultaneously, and all the PCs derived from them contribute to the Ig kinetics. After all of the concentrations are updated at each step, the mean antibody association constant K_a for the WT and the variant are updated. The governing equation is derived using the product rule as follows:

$$\frac{dK_a}{dt} = \frac{1}{[Ig]+[IC]}\left[\frac{d(K_a([Ig]+[IC]))}{dt} - K_a\frac{d([Ig]+[IC])}{dt}\right]$$
$$= \frac{1}{[Ig]+[IC]}\left[\{K_a(-d_{Ig}[Ig] - k_{deposit}[IC]) + K_a^{PC}(k_{Ig}[PC])\}\right.$$
$$\left. - K_a(-d_{Ig}[Ig] - k_{deposit}[IC] + k_{Ig}[PC])\right]$$
$$= \frac{(K_a^{PC} - K_a)k_{Ig}[PC]}{[Ig]+[IC]} \qquad \textit{Eq. (1)}$$

K_a and K_a^{PC} are the mean association constants of the existing antibodies and PCs, respectively, and k_{Ig} is the rate of antibody production per plasma cell. The other parameters are described in **Table 3-S1**. The derivation makes use of the fact that the change in total antibody titer, $K_d([Ig] + [IC])$, can be obtained from the consumption and production of the antibody species.

For Vax 1, the initial concentrations for IC, IC-FDC, and PC are set to zeros and the initial concentration for Ag is set to 10 nM to represent a bolus injection of antigen. There will be only a small number of weakly-binding antibodies to the new immunogen, so $[Ig]$ and $K_a = 1/K_d$ are initially set to small values. These values and other parameters in **Table 3-S1** are picked from reasonable physiological ranges based on the literature.[33,63,78,79] While there are uncertainties about the true underlying biological values, the physical significances of these initial values and parameters are in determining the level of antigen availability in the lymph node. In our model, the antigen availability depends on the reference antigen concentration C_0 because antigen capture by B cells depends on the normalized antigen availability $\frac{C}{C_0}$, where C is the amount of antigen in the lymph node. Thus, by changing C_0, we can study the effect of changing antigen availability in the system. As mentioned in the main figures and shown in Fig S4A, we tested the robustness of the results on varying C_0.

For Vax 2, Vax 3, and Vax 4, the initial concentrations of the species are set to the values determined by response to the previous vaccination.

Simulation details for B cells and 2-epitope model

As described in the main text, the dynamics of B cells are simulated with an agent-based model. Each B cell is an agent that has the following properties: type, lineage, target epitope, mutational state, and binding affinities. At each time point, the B cells stochastically undergo different actions based on their properties and the conditions of the simulation. The details of the model are described below,

and the simulation algorithm is summarized in **Table 3-S3**. **Table 3-S2** summarizes the parameters used in the simulations. It shows which equations the parameters appear in, their descriptions, values, and notes about how those values were selected.

Each simulation models 200 GCs simultaneously. Each GC is associated with a pool of naïve B cells that have not yet entered the GC. The number of total naïve B cells in humans is estimated [91,92] to be about 1×10^{10}, and the frequency of SARS-CoV-2 RBD-specific naïve B cells[39] is about 1 in 3×10^4. Thus, we assume that the number of naïve B cells for each GC is $N_{naive} = (1 \times 10^{10})/(3 \times 10^4)$ / $200 \cong 2000$ cells. These naïve B cells have germline-endowed WT-binding affinities, whose possible values are $E_k = 6 + 0.2k$ ($k = 0 \ldots 10$). These affinities correspond to $-\log_{10} K_d$. The distribution of the naïve B cells over the possible values is determined by three parameters: E_1^h, dE_{12}, p. Higher-affinity B cells should be rarer, so the frequency of B cells is determined analogously to a truncated geometric distribution (see Figure 3-S1A for the schematics). The frequency of naïve B cells that target the dominant and subdominant epitopes are as follows:

$$f_{dominant}(E_k) = N_{naive}(1-p)\frac{e^{-r_1(E_k-E_0)}}{\sum_k e^{-r_1(E_k-E_0)}} \qquad \textit{Eq. (2)}$$

$$f_{subdominant}(E_k) = N_{naive}p\frac{e^{-r_2(E_k-E_0)}}{\sum_k e^{-r_2(E_k-E_0)}} \qquad \textit{Eq. (3)}$$

p is the fraction of naïve B cells that target the subdominant epitope, and r_1, r_2 in the exponents are specified by the parameters E_1^h and dE_{12} from the following relationships.

$$f_{dominant}\left(E_1^h\right)/(1-p) = 1 \qquad \textit{Eq. (4)}$$

$$f_{subdominant}\left(E_1^h - dE_{12}\right)/p = 1 \qquad \textit{Eq. (5)}$$

That is, E_1^h and $E_1^h - dE_{12}$ are the affinities at which the frequency of naïve B cells that target the dominant and subdominant epitopes respectively would be 1 cell per GC, before adjusting for the total frequency (**Figure 3-S1A**). For each GC, the exact number of naïve B cells that have germline affinity equal to E_k is determined by stochastically rounding up or rounding down $f_{dominant}(E_k)$ and $f_{subdominant}(E_k)$ to the nearest integer, using the fractional part as the probability of rounding up. Very high-affinity naïve B cells have precursor frequencies of less than 1 per GC (**Figure 3-S1A**), so they will exist only for some of the GCs.

Each naïve B cell also has a germline-endowed binding affinity against the variant strain. Immunization with the WT strain will recruit naïve B cells with high WT-binding affinities; even the naïve B cells with the lowest WT-binding affinity in the pool ($E_0 = 6$) still represents the top 1 in $\sim 3 \times 10^4$ of all naïve B cells in the human repertoire. The binding affinity of these naïve B cells against

the variant will likely be lower. Thus, we assume that all naïve B cells have germline binding affinity of $-\log_{10} K_d = 6$ against the variant, equal to the lowest value of binding affinity against the WT, and that required for GC entry.[37]

During affinity maturation, the affinities of B cells change as they accumulate mutations. To account for mutations, each naïve B cell is represented as a string of 0's with length n_{res}, and an affinity-affecting mutation to a GC B cell changes the value of one randomly selected residue from 0 to 1 or from 1 to 0. Each residue that has a value of 1 changes the binding affinity towards the WT and the variant by pre-determined amounts. These amounts, which are analogous to the fitness landscape of the B cell, are drawn from a correlated probability distribution. **Fig. 3-S1B** schematically shows how the affinities are determined for GC B cell, i. The binding affinities against the WT and the variant are determined as

$$E_i^{wt} = E_i^{0,wt} + \sum_{j=1}^{n_{res}} \delta_{i,j} s_{i,j}^{wt} \qquad \textit{Eq. (6)}$$

$$E_i^{var} = E_i^{0,var} + \sum_{j=1}^{n_{res}} \delta_{i,j} s_{i,j}^{var} \qquad \textit{Eq. (7)}$$

where $E_i^{0,wt}$ and $E_i^{0,var}$ are the germline affinities towards the WT and the variant, respectively; $\delta_{i,j} \in \{0,1\}$ is the mutational state of residue j; and $s_{i,j}^{wt}$ and $s_{i,j}^{var}$ are the effects of the mutation at residue j on the binding affinities against the WT and the variant, respectively. $s_{i,j}^{wt}$ and $s_{i,j}^{var}$ are sampled from the following shifted log-normal distribution, independently for each residue j, at the initiation of the simulation.

$$[s_{i,j}^{wt}, s_{i,j}^{var}] \sim e^{N(\mu,\sigma^2\Sigma)} - \epsilon \qquad \textit{Eq. (8)}$$

The parameters μ, σ, ϵ are chosen to fit experimentally determined distribution, where ~5 % of affinity-affecting mutations are beneficial while most of the mutations are strongly deleterious (**Fig. S1C**).[42,43] The covariance has the form

$$\Sigma = \begin{bmatrix} 1 & \rho \\ \rho & 1 \end{bmatrix} \qquad \textit{Eq. (9)}$$

where ρ represents the level of conservation of an epitope between the WT and variant. As ρ increases, mutations that are beneficial for binding both strains become more common (**Fig. S1D**). We choose $\rho = 0.95$ for the subdominant epitope and $\rho = 0.4$ for the dominant epitope. For B cells that target the subdominant and dominant epitope, respectively 72% and 19% of mutations that are beneficial for binding the WT are also beneficial for binding the variant, and vice versa. Since B cells

are selected in GCs based on their WT-binding affinities, an increase in variant-binding affinities mainly occurs through the accumulation of mutations that increase affinities against both strains. Hence, B cells that target the subdominant epitope are more likely to develop high cross-reactivity for the variant than those that target the dominant epitope.

Simulation details for germinal center entry of naïve B cells

At each time step, the amount of antigen captured by naive B cells is determined based on their WT-binding affinities and the effective antigen concentration in the lymph node, C. For B cell i, this amount, A_i, is determined as follows:

$$A_i = \left(\frac{C}{C_0} 10^{(\min\,(E_i^{WT}, 10) - E_0)}\right)^K \qquad \textit{Eq. (10)}$$

E_i^{WT} is the WT-binding affinity of B cell i. The amount of antigen captured increases with E_i^{WT}, but saturates at affinities higher than $E_i^{WT} = 10$ because of the affinity ceiling.[93] A similar model of antigen capture has been used in several previous studies.[20,24,56,94] B cells can see both the soluble antigen and the antigen presented on FDCs, but the latter is known to be about 2 orders of magnitude more potent at activating B cells due to multivalent presentation [95]. Therefore, the effective antigen concentration C is calculated as $C = 0.01([Ag] + [IC]) + [IC - FDC]$. The parameter K determines how much a given difference in concentration or affinity changes the amount of antigen internalized by a B cell. If K is large, then even a small difference in concentration or affinity results in large difference in the amount of antigen internalized, which in turn affects the probability of activation and positive selection by T helper cells. Thus, K represents the stringency of selection. We studied varying K to test the robustness of the results, since stringency of selection is known to affect the diversity of B cells that develop in GCs[50] (**Fig S3D**).

Naïve B cells that capture enough antigen can be activated.[37] In our simulation, whether B cell i is activated at each time step is determined probabilistically as follows:

$$\Pr(\text{B cell } i \text{ is activated}) = \min\,(A_i, 1) \qquad \textit{Eq. (11)}$$

The entry of activated naïve B cells to GCs is limited by competition for positive selection by helper T cells, and B cells that have internalized greater amounts of antigen have better chances of successfully entering GCs.[48,49] Thus, the rate of entry for an activated B cell i, λ_i, and the probability that it enters GC during a time step are given as follows:

$$\lambda_i = \frac{\frac{N_{max}}{N_{activated}}\frac{A_i}{\langle A \rangle}}{1 + \frac{N_{max}}{N_{activated}}\frac{A_i}{\langle A \rangle}} \qquad \textit{Eq. (12)}$$

$$\Pr(\text{B cell } i \text{ enters GC}) = 1 - e^{-\lambda_i dt} \qquad \textit{Eq. (13)}$$

$N_{activated}$ is the total number of activated B cells, $\langle A \rangle$ is the average amount of antigen captured by all activated B cells, and N_{max} is the capacity for entry that represents the limited amount of T cell help. N_{max} is selected so that about ten distinct naïve B cells will enter the GC per day, consistent with the literature.[64] The assumption that N_{max} is fixed is conservative because higher antigen availability is known to increase naïve B cell recruitment to GCs,[23] which would only further strengthen our finding that secondary GCs produce more diversity. When a naïve B cell enters GC, it simultaneously proliferates twice, so that a total of 4 identical B cells are added to the GC.

Alternative model for antigen capture

According to Eq. 10, the amount of antigen captured by B cells continues to increase with antigen concentration and B cell affinity. However, it is possible that the amount of antigen captured plateaus when antigen concentration and B cell affinity are very high.[46] Therefore, we studied how using an alternative model where antigen capture saturates at high affinities and antigen concentrations affects our findings. Under this model, the amount of antigen captured is determined as:

$$A_i = \frac{(H+1)\frac{C}{C_0}10^{(\min(E_i^{WT},10)-E_0)}}{H + \frac{C}{C_0}10^{(\min(E_i^{WT},10)-E_0)}} \qquad \textit{Eq. (14)}$$

When $H \to \infty$, this formulation becomes equivalent to Eq. 10 with K=1. For a finite value of H, A_i saturates to $H+1$ when $\frac{C}{C_0}10^{(\min(E_i^{WT},10)-E_0)} \gg H$. When H is smaller and antigen availability is higher, the affinity at which saturation will occur will be lower, making the selection of B cells permissive. We studied the effect of varying H on our findings (**Fig. 3-S4E**).

Simulation details for GCs

Each simulation models 200 GCs simultaneously. Plasma cells generated from all GCs collectively determine antibody production, which affects antigen transport and epitope masking, and memory B cells generated from all GCs seed the EGC upon subsequent vaccination. The birth, death, mutation,

and differentiation of GC B cells occur stochastically at each time step. The model implicitly treats migration between GC light zone and dark zone, but such a model has been shown to recapitulate qualitative GC dynamics well.[20,56,96,97]

GC B cells capture antigen and become stochastically activated in the same way as the naïve B cells. Activated GC B cells compete for positive selection signals from helper T cells. The rate of positive selection for a GC B cell i, β_i, and the probability that it gets positively selected during a time step are given as:

$$\beta_i = \beta_{max} \frac{\frac{N_T}{N_{activated}} \frac{A_i}{\langle A \rangle}}{1 + \frac{N_T}{N_{activated}} \frac{A_i}{\langle A \rangle}} \qquad \textit{Eq. (15)}$$

$$\Pr(\text{GC B cell } i \text{ is positively selected}) = 1 - e^{-\beta_i dt} \qquad \textit{Eq. (16)}$$

where β_{max} is the maximum rate of positive selection, $N_{activated}$ is the number of activated GC B cells, and N_T is the number of helper T cells. Thus, $\frac{N_T}{N_{activated}}$ represents the physical availability of helper T cells to GC B cells, and $\frac{A_i}{\langle A \rangle}$ represents the competitive advantage of B cell i compared to other activated GC B cells. B cells internalize the whole spike protein despite binding to potentially different surface epitopes. Thus, each B cell that internalize antigen present diverse peptides derived from the protein to helper T cells. The main difference between the B cells is the amount of antigen they present. Therefore, we model the competition based on the amount of antigen without considering individual T cell epitopes, similar to previous models of affinity maturation.[20,24,57,94]

Clinical data from SARS-CoV-2 vaccinated subjects showed that the number of $CD4^+$ T cells peaked about 2 weeks after vaccination and decayed with a half-life of ~47 days [54]. For simplicity, we model N_T as simple linear growth up to $t_0 = 14\ days$, followed by first-order decay afterwards with rate d_T as follows:

$$N_T(t) = \begin{cases} \dfrac{t}{t_0} N_{T0} \ (t < t_0) \\ N_{T0} e^{-d_T (t - t_0)} \ (t > t_0) \end{cases} \qquad \textit{Eq. (17)}$$

N_{T0} is the peak level of non-dimensionalized T cell availability, and is chosen to give a mean peak GC size of ~1000 cells/GC.

A positively selected B cell exits a GC with a probability p_1, and then differentiates into a PC with a probability p_2 or into a memory cell with a probability $1 - p_2$. The remaining selected B cells proliferate once and one of the daughter cells mutates, as described in the main text.

At the end of the time step, all GC B cells are subject to stochastic apoptosis with a rate α. The probability of apoptosis is given as:

$$\Pr(\text{GC B cell } i \text{ undergoes apoptosis}) = 1 - e^{-\alpha\, dt} \qquad \textit{Eq. (18)}$$

Similarly, plasma cells from both GCs and EGCs also undergo stochastic apoptosis at a rate d_{PC}, so that the probability of apoptosis is given as:

$$\Pr(\text{PC } i \text{ undergoes apoptosis}) = 1 - e^{-d_{PC}\, dt} \qquad \textit{Eq. (19)}$$

Clinical sample collection and analysis methods

Data used in **Fig. 3-4** are derived from B cell sequences reported in Supplemental Table 2 of Muecksch et al., which contains sequences of B cells isolated from SARS-CoV-2 mRNA-vaccinated subjects.[8] Phylogenetic trees were generated from these B cell clonal families using MATLAB's seqlinkage function. EGC-derived B cells were identified by applying the classification method described in the main text and in the next section. Then, using the monoclonal antibodies that correspond to these B cells based on the protein sequences (reported in Supplemental Table 3 of Muecksch et al.), the WT and Omicron-neutralizing activity (IC_{50}) of these sequences were measured, except for three antibodies for which both values were already reported in the Supplemental Table 4 and 5 of Muecksch et al. The measurements were performed as previously described.[8,74,75] We additionally measured the neutralization activity of 26 randomly-selected singlets that were found 5 months after Vax 2, to compare with the EGC-derived antibodies. Table S4 describes the neutralization activities of the EGC-derived antibodies used in this study.

The statistical analyses to compare the neutralization activity of EGC- and GC-derived antibodies were performed based on the logarithm of IC_{50} data. We used the two-sample t-test to calculate the statistical significance (p-value) of the difference in the mean values between the two groups. The degrees of freedom were conservatively estimated using the smaller sample size of the two samples, so that it was given as one less than the number of sequences in the smaller group. The analysis was performed to compare Vax 2 EGC-derived cells with Vax 2 GC-derived cells, and to compare Vax 2 EGC-derived cells with Vax 3 EGC-derived cells.

Sensitivity and precision of the inference of EGC-derived memory cells

A B cell was identified as EGC-derived if it satisfied at least one of the two conditions below.

(1) Criteria 1: At least one other identical sequence was sampled at the same time
(2) Criteria 2: At least one identical sequence was sampled at an earlier time

Assume that after secondary immunization, the sets of unique memory B cell sequences derived from GC and EGC are $\mathbb{S}_{GC} = \{s_1^{GC}, \dots, s_K^{GC}\}$ and $\mathbb{S}_{EGC} = \{s_1^{EGC}, \dots s_K^{EGC}\}$, respectively. Without the loss of generality, let the number of GC-derived memory B cells that have sequences $s_1^{GC}, \dots, s_K^{GC}$ to be $m_1 > \dots > m_K$ for GC-derived cells. Similarly, let the number of EGC-derived memory B cells that have sequences $s_1^{EGC}, \dots s_K^{EGC}$ to be $n_1 > \cdots > n_K$ for EGC-derived cells. K is a sufficiently large number. If the actual number of GC-derived unique sequences is smaller than K, then n_i will be zero for some large values of i. The same is true for EGC-derived sequences.

The sequences $s_1^{EGC}, \dots s_K^{EGC}$ must be identical to the sequences derived from the GC of the primary immunization. Let the numbers of B cells from the prime GC that correspond to these sequences be $l_1, \dots, l_K$.

Suppose that total of S sequences are sampled each after the secondary immunization and the primary immunization. Let these sequences be $\mathbb{S} = \{s_1, \dots s_S\}$ and $\mathbb{S}_p = \{s_{1,p}, \dots s_{S,p}\}$, respectively. Based on the two criteria, a B cell i sampled after secondary immunization is labeled as EGC-derived if and only if

$$s_i \in \mathbb{S}_{\setminus i} \cup \mathbb{S}_p$$

where $\mathbb{S}_{\setminus i} = \{s_1, .., s_{i-1}, s_{i+1}, \dots, s_S\}$ is defined as the set of sequences in $\mathbb{S}$ excluding s_i.

The sensitivity, or true positive rate, of the classification is defined as the following expected value:

$$TPR = \mathrm{E}\left[\frac{n_{TP}}{n_{TP} + n_{FN}}\right]$$

where n_{TP} and n_{FN} are the number of true positives and false negative in the labeled samples. A true positive sample is an EGC-derived sequence labeled as EGC-derived, and false positive is an EGC-derived sequence labeled as GC-derived.

An equivalent definition for sensitivity is the probability that an EGC-derived sequence will be labeled correctly as EGC-derived. That is,

$$\mathrm{TPR} = \Pr\left(s_i \in \mathbb{S}_{\setminus i} \cup \mathbb{S}_p | s_i \in \mathbb{S}_{EGC}\right) \qquad \textit{Eq. (20)}$$

Let $\sum_{j=1}^{K} n_j = N, \sum_{j=1}^{K} m_j = M, \sum_{j=1}^{K} l_j = L$. Then, the sensitivity can be calculated as

$$\begin{aligned}
TPR &= 1 - \Pr\left(s_i \notin \mathbb{S}_{\setminus i} \cup \mathbb{S}_p | s_i \in \mathbb{S}_{EGC}\right) \\
&= 1 - \sum_{j=1}^{K} \Pr\left(s_j^{EGC} \notin \mathbb{S}_{\setminus i} \cup \mathbb{S}_p \middle| s_i = s_j^{EGC}\right) \Pr\left(s_i = s_j^{EGC} \middle| s_i \in \mathbb{S}_{EGC}\right) \\
&= 1 \\
&- \sum_{j=1}^{K} \Pr\left(s_j^{EGC} \notin \mathbb{S}_{\setminus i} \cup \mathbb{S}_p \middle| s_i = s_j^{EGC}\right) \Pr\left(s_j^{EGC} \notin \mathbb{S}_p \middle| s_i = s_j^{EGC}\right) \Pr\left(s_i = s_j^{EGC} \middle| s_i \in \mathbb{S}_{EGC}\right) \\
&= 1 - \sum_{j=1}^{K} \frac{\mathcal{C}_{S-1}^{N+M-n_j}}{\mathcal{C}_{S-1}^{N+M}} \frac{\mathcal{C}_S^{L-l_j}}{\mathcal{C}_S^{L}} \frac{n_j}{N} \\
&\triangleq 1 - \sum_{j=1}^{K} \frac{n_j}{N} Q(n_j, S)\, Q'(l_j, S)
\end{aligned} \qquad \textit{Eq. (21)}$$

where $Q\left(n_j, S\right) = \frac{(N+M-S+1)}{(N+M)} \frac{(N+M-S)}{(N+M-1)} \ldots \frac{\left(N+M-n_j-S+2\right)}{\left(N+M-n_j+1\right)}$, $Q'\left(l_j, S\right) = \frac{(L-S)}{L} \frac{(L-S-1)}{(L-1)} \ldots \frac{\left(L-S-l_j+1\right)}{\left(L-l_j+1\right)}$

$Q(n_j, S)$ decreases with n_j and S. Thus, the sensitivity will be high if most B cells belong to largely expanded sequences, and if the sampling number is large. $Q'\left(l_j, S\right)$ decreases with l_j and S. Thus, the sensitivity will be high if for the values of j such that n_j is large, l_j is also large.

The precision, or positive predictive value, of the classification is defined as

$$PPV = \mathrm{E}\left[\frac{n_{TP}}{n_{TP} + n_{FP}}\right]$$

where n_{FN} is the number of false positives, or GC-derived B cells labeled as EGC-derived. An equivalent definition for precision is the probability that an EGC-labeled B cell is a true EGC-derived B cell.

$$PPV = \Pr\left(s_i \in \mathbb{S}_{EGC} \middle| s_i \in \left(\mathbb{S}_{prev} \cup \mathbb{S}_{\setminus i}\right)\right) \qquad \textit{Eq. (22)}$$

Using Bayes' rule,

$$PPV = \frac{\Pr\left(s_i \in \left(\mathbb{S}_{prev} \cup \mathbb{S}_{\backslash i}\right) \middle| s_i \in \mathbb{S}_{EGC}\right)\Pr\left(s_i \in \mathbb{S}_{EGC}\right)}{\Pr\left(s_i \in \left(\mathbb{S}_{prev} \cup \mathbb{S}_{\backslash i}\right)\right)}$$

$$= \frac{\Pr\left(s_i \in \left(\mathbb{S}_{prev} \cup \mathbb{S}_{\backslash i}\right) \middle| s_i \in \mathbb{S}_{EGC}\right)\Pr\left(s_i \in \mathbb{S}_{EGC}\right)}{\Pr\left(\left(s_i \in \left(\mathbb{S}_{prev} \cup \mathbb{S}_{\backslash i}\right) \middle| s_i \in \mathbb{S}_{EGC}\right)\right)\Pr\left(s_i \in \mathbb{S}_{EGC}\right) + \Pr\left(\left(s_i \in \left(\mathbb{S}_{prev} \cup \mathbb{S}_{\backslash i}\right) \middle| s_i \in \mathbb{S}_{GC}\right)\right)\Pr\left(s_i \in \mathbb{S}_{GC}\right)}$$

$$= \frac{TPR\left(\frac{N}{N+M}\right)}{TPR\left(\frac{N}{N+M}\right) + \left(1 - \sum_{j=1}^{K} \frac{m_j}{N} Q(m_j, S)\right)\left(\frac{M}{N+M}\right)} \qquad \textit{Eq. (23)}$$

Assuming that N and M are similar, high precision is reached if the values of $Q(m_j, S)$ are large for the GC-derived B cells. Since $Q(m_j, S)$ increases with decreasing m_j, precision is high if many GC-derived sequences have similar sizes.

We applied this analysis to the data from simulations to find the sensitivity and precision of the method. We also tested the analysis against Monte-Carlo sampling of sequences from the simulations. For this, we sampled equal numbers of memory B cells from 1 month after Vax 1 and 5 months after Vax 2. Then we applied the labeling method and calculated the number of true positives, false negatives, and false positives. This was repeated 1000 times to calculate the mean sensitivity and precision.

Epitope masking

When epitope masking is considered in the simulations, B cells can only see free antigen. The total amount of antigen in a lymph node is $[Ag] + [IC] + [IC - FDC] = [Ag]_{tot}$. Let us use subscripts 1 and 2 to denote antibodies that target the dominant and subdominant epitopes, respectively, and let q be the epitope overlap. The effective concentration and mean binding affinity of the antibodies that cover the dominant epitope are $[Ig_1]_{eff} = [Ig_1] + q[Ig_2]$ and $\frac{1}{K_{d1,eff}} = (\frac{[Ig_1]}{K_{d,1}} + \frac{q[Ig_2]}{K_{d,2}})/[Ig_1]_{eff}$, respectively. Using these values, the free antigen concentration for the dominant epitope, $[Ag]_{tot,1}$, can be calculated from the following equilibrium.

$$K_{d1,eff} = \frac{[Ag]_{tot,1}[Ig_1]_{eff}}{[Ag]_{tot} - [Ag]_{tot,1}} \qquad \textit{Eq. (24)}$$

Here, we used the fact that typically $[Ig_1]_{eff} \gg [Ag]_{tot}$ to approximate the free antibody concentration. Finally, to calculate the effective free antigen concentration for the dominant epitope, $C_{eff,1}$, we must adjust for the fractions of the free antigen that are soluble or on FDC as follows:

$$C_{eff,1} = [Ag]_{tot,1}\left\{0.01\frac{[Ag]+[IC]}{[Ag]_{tot}} + \frac{[IC-FDC]}{[Ag]_{tot}}\right\} \qquad \textit{Eq. (25)}$$

The effective free antigen concentration for the subdominant epitope can be calculated similarly. Note that although ICs are tethered to FDC, we treat them as free antigen unless it is additionally covered by serum antibody, similar to the computational model from a previous study.[80] In the experimental part of this study, mice were immunized with 4-hydroxy-nitrophenyl coupled to chicken gamma globulin (NP-CGG) along with NP-specific antibodies so that the ICs were deposited on FDCs. These ICs on FDCs elicited NP-specific serum response, suggesting that the NP epitope was not blocked by the tethering of IC to FDC.

3.6. Supplemental Figures and Tables

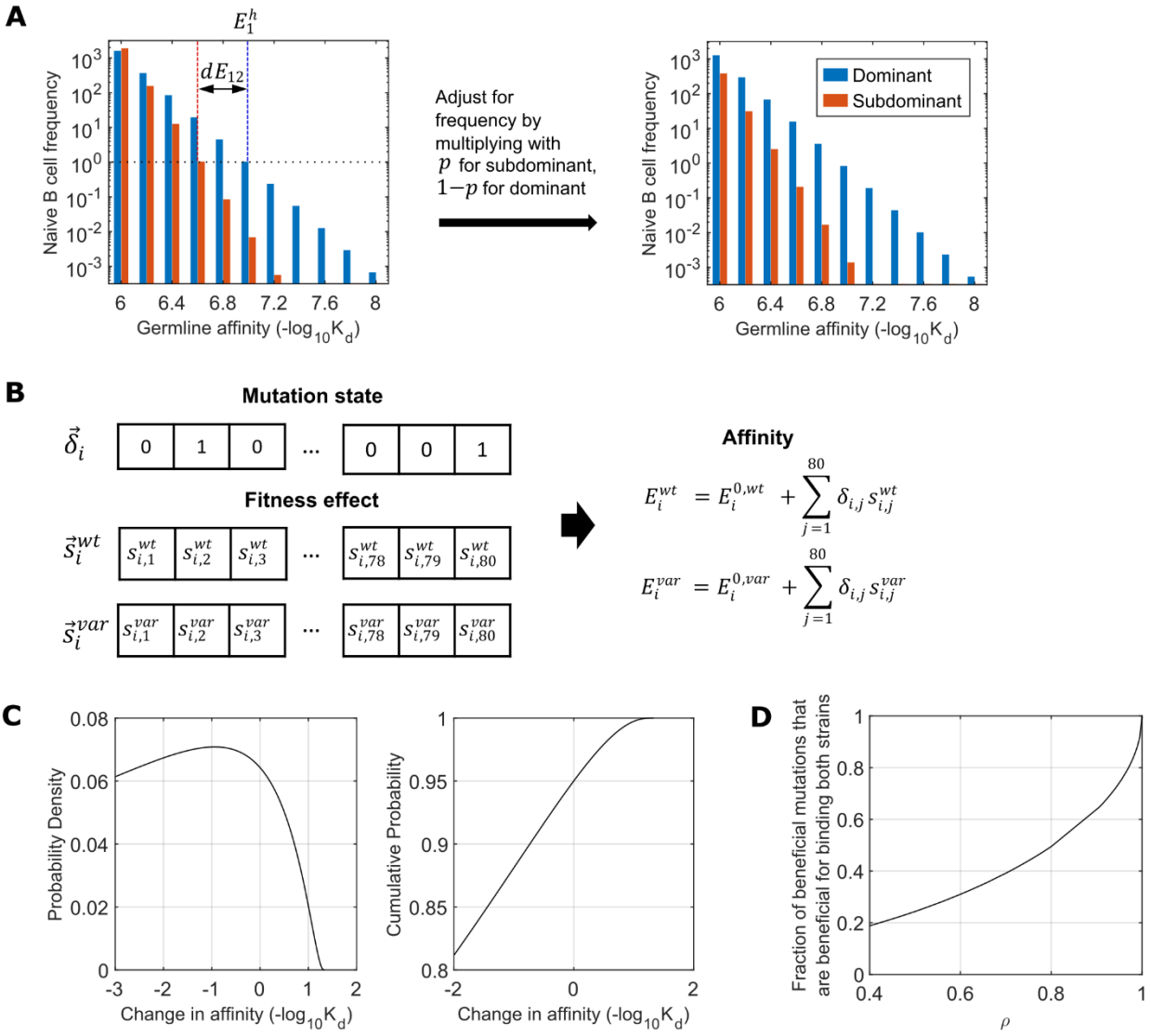

Figure 3-S1. Simulation Details for B cells and 2-epitope model. (**A**) Distribution of germline-endowed affinities of naïve B cells, parameterized by E_1^h, dE_{12}, and p. Left panel) E_1^h and dE_{12} specifies the slopes of the distributions. The naïve B cells can have germline affinities between 6 and 8 at intervals of 0.2. E_1^h is the affinity at which the frequency of naïve B cell that target the dominant epitope would be 1 per GC, assuming there are 2000 B cells distributed according to geometric distribution. It thus specifies the slope of the distribution for the B cells that target the dominant epitope. Analogously, $E_1^h - dE_{12}$ specifies the slope for the B cells that target the subdominant epitope. Right panel) The distributions are adjusted based on the parameter p. The fraction of all naïve B cells that target the dominant and subdominant epitopes are $1-p$ and p, respectively. The distributions from the left panel are multiplied by these values to obtain the actual naïve B cell frequencies. (**B**) Schematics showing how the binding affinities against the WT and the variant strains are determined for a given B cell, i. The mutation state vector, $\vec{\delta_i}$, is initially a string of zeros and some residues are mutated to ones during the affinity maturation. The effects of a mutation of each residue on the WT and variant affinities ($s_{i,j}^{wt}$, $s_{i,j}^{var}$ for residue j) are drawn from a correlated probability distribution. The binding affinities (E_i^{WT}, E_i^{var}) are

sums of the initial affinities ($E_i^{0,wt}$, $E_i^{0,var}$) and the effects of mutated residues. (**C**) Marginal probability density function and cumulative distribution function for both the random variables $s_{i,j}^{wt}$ and $s_{i,j}^{var}$. That is, they show probabilities of how a mutation of one residue from 0 to 1 will change the binding affinities. Although a single mutation will contribute differently to the WT and variant affinities, statistically for both variants ~5% of the all mutations increase affinity, and the best beneficial mutations increase the affinity by ~10 fold. (**D**) Fraction of the mutations that increase the affinity against the WT which also increase the affinity against the variant. $s_{i,j}^{wt}$ and $s_{i,j}^{var}$ are drawn from correlated distributions parameterized by ρ, so that as ρ increases, mutations that are beneficial for binding both strains become more common. Thus, ρ represents the level of conservation of the epitope between the WT and the variant.

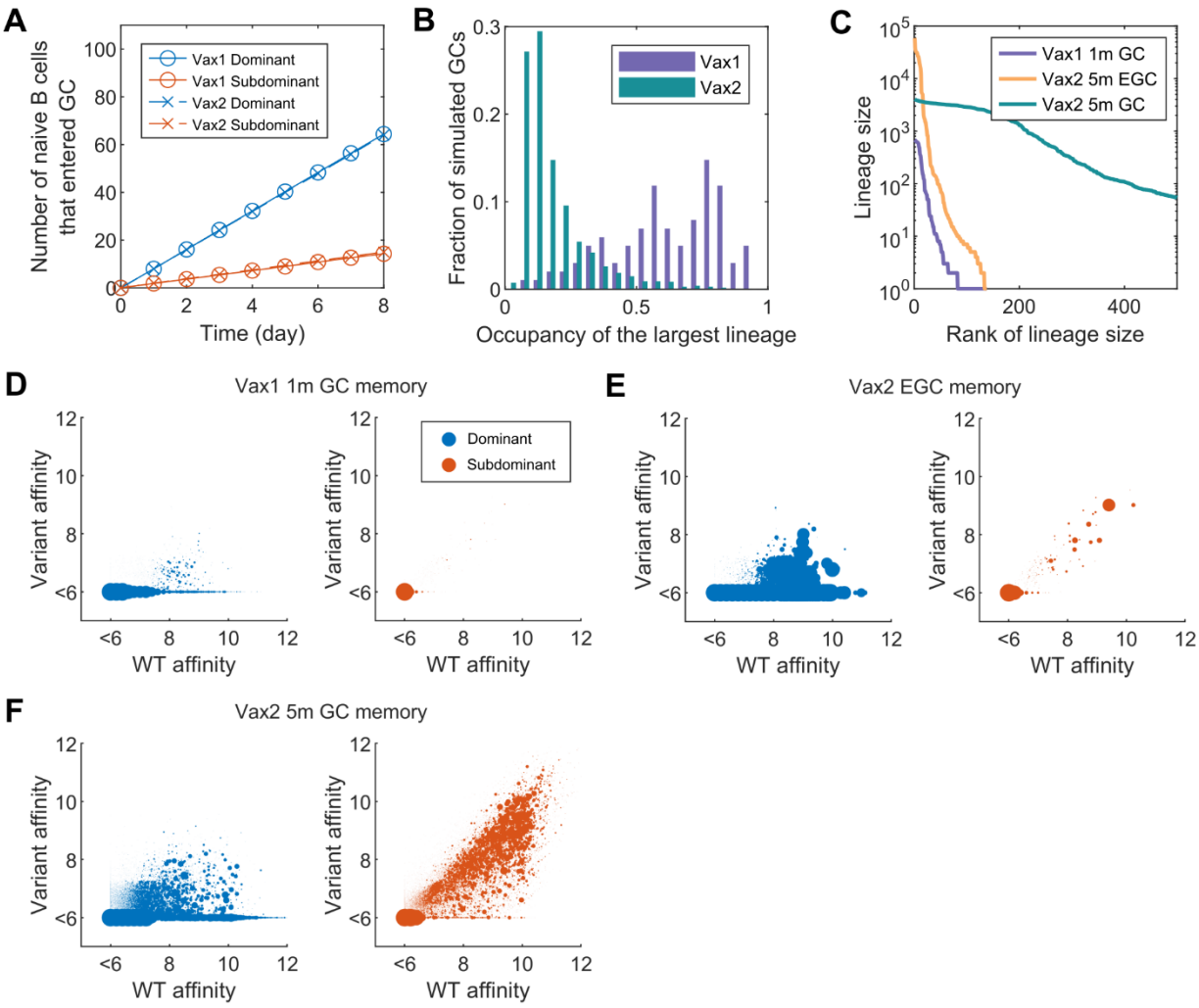

Figure 3-S2. Details of Vax1 and Vax2 B cell response. (**A**) Mean number of naïve B cells that enter a GC over time. The model allows similar number of naive B cells to enter GC after Vax 1 and Vax 2. This model is conservative because higher antigen availability after Vax 2 could increase the number of naïve B cell entry, which would strengthen the finding of greater B cell diversity from Vax 2 response. (**B**) Histogram showing the distribution of the fraction of GC B cells that belong to the single largest lineage at 14 days after Vax 1 and Vax 2. Most of the Vax 1 GCs are already dominated by a single lineage at this time, in contrast to the Vax 2 GCs. (**C**) Number of memory cells from the same lineages, shown in the order of largest to smallest lineages. A few largest lineages dominate the Vax 2 EGC response, like Vax 1 GC response. In contrast, diverse lineages of similar sizes make up the Vax 2 GC response. Result from a single simulation of 200 GCs. (**D-F**) Cross-reactivity of memory B cells derived from GCs and EGCs. The area of the circles scale with the number of cells that have the identical affinities. (D) GC at 1m after Vax 1, (E) EGC after Vax 2, (F) GC at 5m after Vax 2. Only a very small number of subdominant memory cells are generated after Vax 1, and they undergo limited expansion in EGC after Vax 2. In contrast, diverse subdominant B cells are produced in Vax 2 GCs, some of which have very high affinities towards the variant.

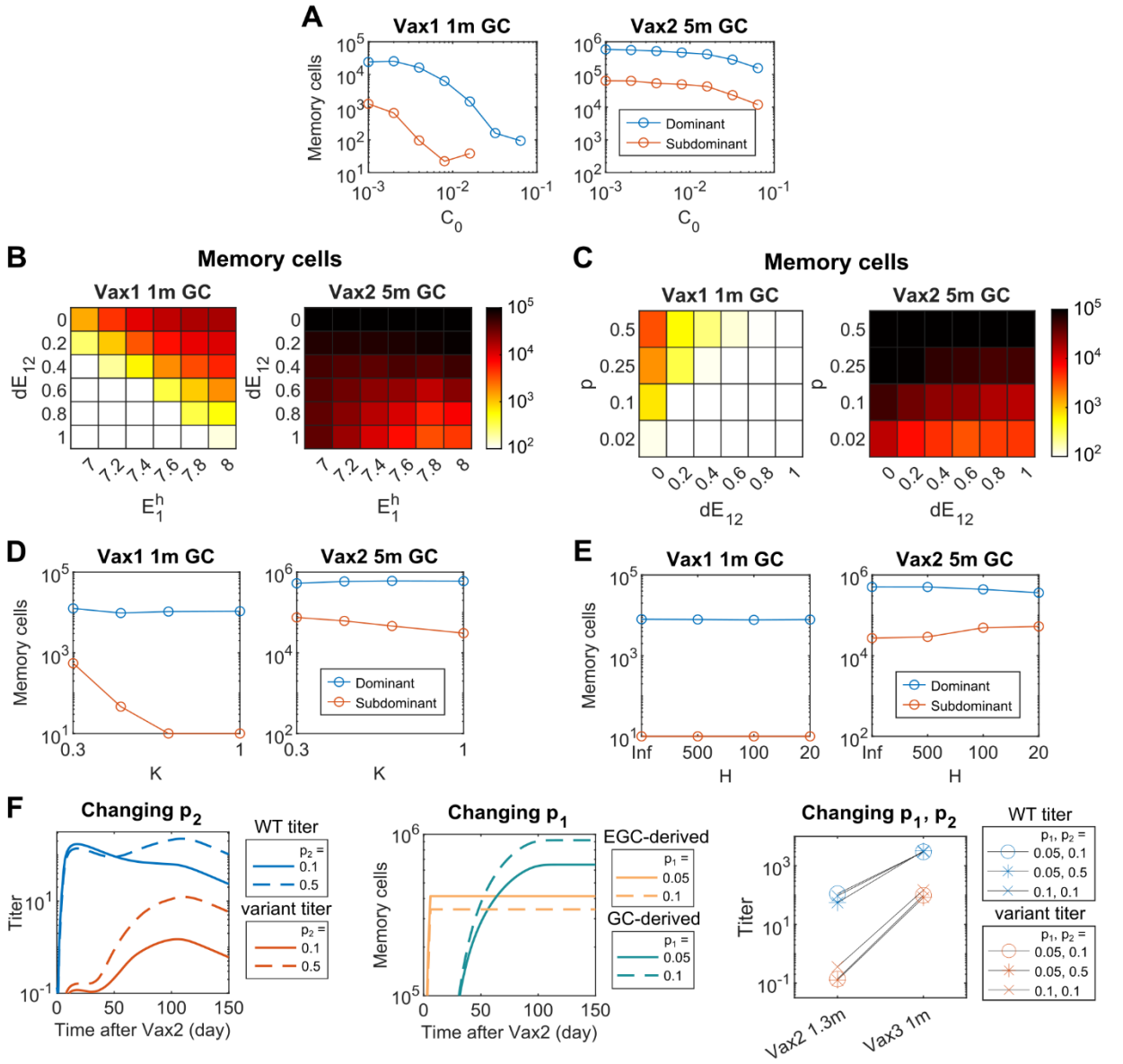

Figure 3-S3. Parameter sensitivity analysis. Number of memory B cells derived from GCs at 1 month after Vax 1 and 5 months after Vax 2 that target dominant and subdominant epitopes, when various simulations parameters are changed. (**A**) The reference antigen concentration, C_0, is varied. Decreasing C_0 makes B cells easily activated even when the antigen concentration is small. The quantitative difference between the number of subdominant memory cells after Vax 2 and Vax 1 is largest when C_0 is large; that is, when the importance of antigen concentration is high. However, the qualitative trend that more subdominant B cells are generated after Vax 2 is robust across ~2 orders of magnitude variation in C_0. (**B-C**) Parameters that characterize the affinity distribution of naïve B cells are varied. E_1^h and dE_{12} are varied in (B), p and dE_{12} are varied in (C). For some parameter values, especially small dE_{12} and large p, some subdominant memory cells develop after Vax 1. However, for all parameter values, the number of subdominant B cells greatly increases after Vax 2, showing the robustness of our findings. (**D**) Parameter K, which controls the stringency of selection, is varied. Both after Vax 1 and Vax 2, more subdominant B cells develop when selection is permissive (small value of K). For all values of K tested, the number of subdominant B cells greatly increase after Vax 2 compared to Vax 1. (**E**) An alternative model of antigen capture is used, and the parameter H is varied. With this model, the amount of

antigen captured by B cells saturates if the product of B cell affinity and antigen concentration is much greater than H. The original model is equivalent to infinite H. The qualitative finding is robust. Quantitatively, slightly more subdominant B cells develop after Vax 2 but not after Vax 1 when H is small, because selection becomes permissive when antigen concentration is high. (**F**) p_1, the fraction of positively selected GC B cells that exits GC, and p_2, the fraction of such cells that become plasma cells are varied. Left panel) If p_2 increases, GC-derived B cells contribute more to the antibody titer at long times after Vax 2. This makes the antibody dynamics not consistent with clinically observed behavior where the antibody titers decay over time after Vax 2. Middle panel) If p_1 increases, the ratio between GC-derived memory cells and EGC-derived memory cells change, and the total number of memory cells increase over time. Right panel) The qualitative finding of the study is highly robust to changes in p_1 and p_2. Only relatively narrow range of p_1 and p_2 values will be consistent with clinically observed dynamics of antibody titer and memory cell numbers, and these uncertainties will not affect the general findings of the study.

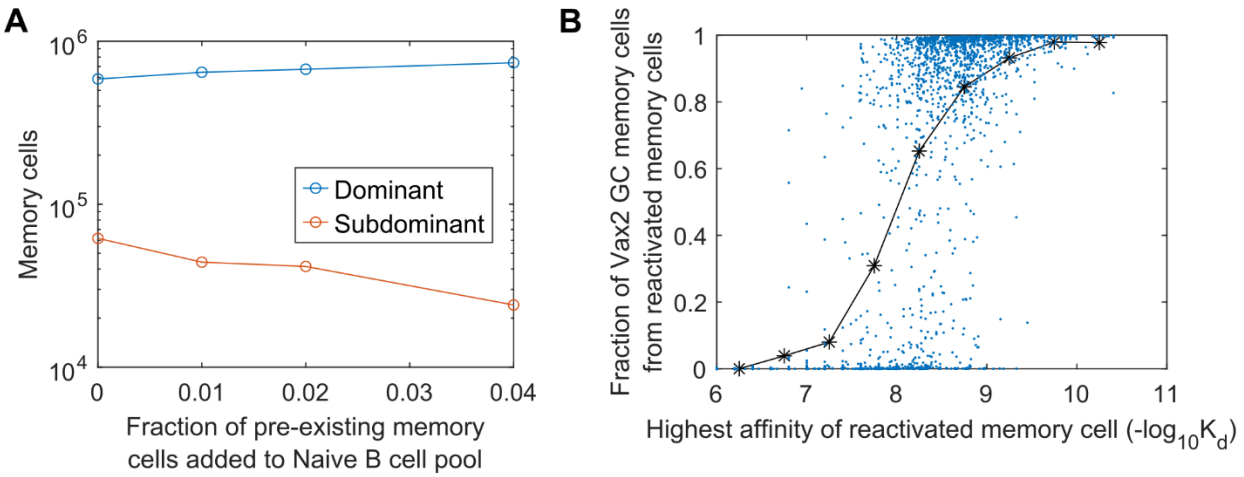

Figure 3-S4. Effect of memory B cell re-entry in secondary GCs. (**A**) Number of memory B cells derived from GCs at 5 months after Vax 2 that target dominant and subdominant epitopes, when different fractions of pre-existing memory cells generated from Vax 1 GCs were allowed to re-enter Vax 2 GCs. (**B**) Fraction of memory cells derived from Vax 2 GC that are descendants of memory cells generated from Vax 1 and re-entered Vax 2 GC, as a function of the highest affinity of such re-activated memory cells. Each GC is represented by a blue dot (n=2000). The black curve shows the mean values. The fraction of pre-existing memory cells allowed to re-enter the secondary GCs is 0.04.

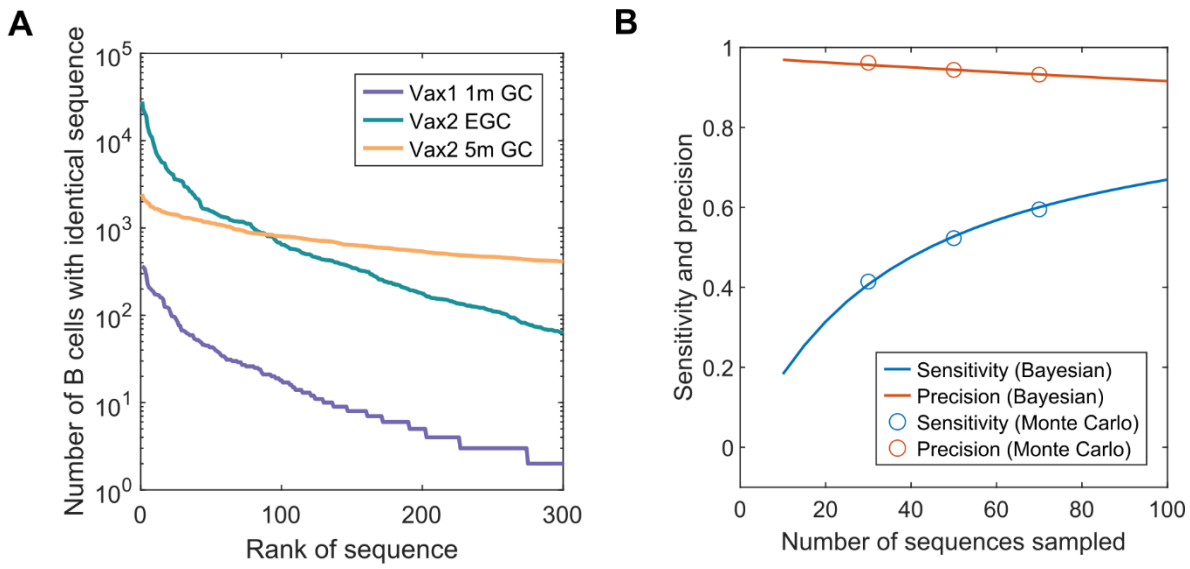

Figure 3-S5. Performance of the EGC B cell labeling method. (**A**) Number of memory B cells from simulated data that have identical sequences, shown in the order of most to least expanded sequences. A few sequences dominate the Vax 2 EGC-derived memory cells. In contrast, diverse sequences of similar sizes make up the Vax 2 GC-derived memory cells. Result is from a single simulation of 200 GCs. (**B**) Sensitivity and precision of our method for finding EGC-derived B cells tested on simulated data while assuming varying numbers of sequences were sampled. The statistics calculated with Bayesian inference and with Monte Carlo method agree well. When only small number of sequences are sampled, the sensitivity will be low, but the precision will be high. This is likely the case for the clinical data; however, since the actual number of memory B cells in vaccinated humans will be different from the simulated data, the quantitative numbers can be different. Sensitivity is defined as (TP/TP+FN), and precision is defined as (TP/TP+FP). TP: True Positive (EGC B cell labeled as EGC), FN: False Negative (EGC B cell labeled as GC), FP: False Positive (GC B cell labeled as EGC).

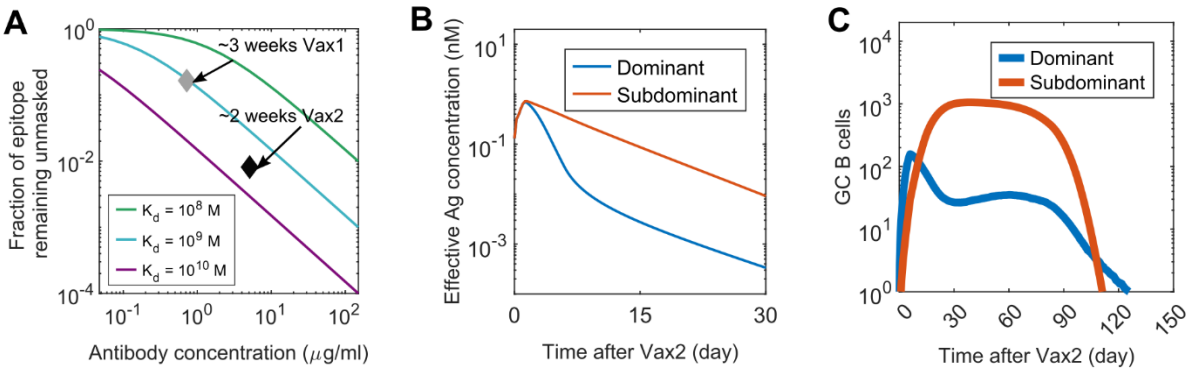

Figure 3-S6. Epitope masking. (**A**) Fraction of antigen molecules that will remain unmasked at ~3 weeks after Vax 1 and ~2 weeks after Vax 2, calculated using the concentration and affinity of serum antibody from mRNA-vaccinated subjects (Demonbreun et al., 2021; Macdonald et al., 2022). (**B**) Effective antigen concentrations for B cells that target dominant and subdominant epitopes after Vax 2, when epitope masking is completely epitope specific with no overlap. (**C**) Number of GC B cells that target dominant and subdominant epitopes after Vax 2, when epitope masking is completely epitope specific with no overlap.

Table 3-S1. Equations and parameters for antigen dynamics. Reactions that govern antigen dynamics and the differential-algebraic equations that describe the changes in concentrations of species. Initial values and parameter values are also shown. Abbreviations: soluble antigen (Ag), soluble antibody (Ig), soluble immune complex (IC), immune complex on follicular dendritic cell (IC-FDC), plasma cell (PC).

Reaction	Description	
$Ag \rightarrow \emptyset$	Decay of free soluble antigen	
$Ag + Ig \rightleftharpoons IC$	Fast equilibrium between free soluble antigen and antibody	
$IC \rightarrow IC - FDC$	Immune complex transport to follicular dendritic cells	
$PC \rightarrow PC + Ig$	Antibody production by plasma cells	
$IC - FDC \rightarrow \emptyset$	Consumption and decay of immune complexes on follicular dendritic cells	
$Ig \rightarrow \emptyset$	Decay of free soluble antibody	
Governing Equation	**Initial Condition / parameters**	**Note**
$\frac{[Ag][Ig]}{[IC]} = K_d$	$[Ag]_0 = 10$ nM	Values were picked within reasonable physiological ranges [63,78]
	$[Ig]_0 = 10^{-2}$ nM	
	$[IC]_0 = 0$ nM	Initially no IC exists
	$K_{d0} = 10^{-6}$ M	Initial value for low affinity; Changes over simulation
$\frac{d[Ag]}{dt} = -d_{Ag}[Ag]$	$d_{Ag} = 3\ \text{day}^{-1}$	Picked to be fast[33,63,98]
$\frac{d[IC]}{dt} = -k_{deposit}[IC]$	$k_{deposit} = 1\ \text{hour}^{-1}$	Picked to be fast[63,98]
$\frac{d[IC-FDC]}{dt} = k_{deposit}[IC] - d_{IC}[IC-FDC]$	$[IC-FDC]_0 = 0$	Initially no IC-FDC exists
	$d_{IC} = 0.15\ \text{day}^{-1}$	Represents the consumption and decay of antigen on FDC. Picked so that secondary GCs last ~3 months
$\frac{d[Ig]}{dt} = k_{Ig}[PC] - d_{Ig}[Ig]$	$k_{Ig} = 0.8 \times 10^{-2}\ \text{nM day}^{-1}\ \text{PC}^{-1}$	Picked to match the antibody titers at the peak of Vax2 response to the values described in the literature[8,54]
	$d_{Ig} = 0.025\ \text{day}^{-1}$	Picked to give antibody half-life of ~28 days[54]
$\frac{dK_d}{dt} = \frac{(K_d^{PC} - K_d)k_{Ig}[PC]}{[Ig]+[IC]}$	K_d^{PC} is the mean affinity of PCs	See **METHODS** Eq. 1 for derivation

Table 3-S2. Simulation parameters. Description of the parameters used in the simulation. Entries highlighted with color denote the parameters whose values are varied for robustness test in the supplemental figures. For the other parameters, the values were chosen to be consistent with experimental observations as described. However, they were not explicitly fitted to data because our model considers new phenomena that has not been studied before and it is therefore not possible to quantitatively fit every past experimental data.

Parameter	Equation	Description	Value	Note
B cells				
N_{naive}	**METHODS** Eqs. 2-3	Number of naïve B cells / GC	2000 cells/GC	About 1×10^{10} total naïve B cells[91,92] multiplied by the frequency of RBD-specific naïve B cells in humans,[39] about 1 in 3×10^4, and divided by 200 GCs
p	**METHODS** Eqs. 2-3	Fraction of germline B cells that are subdominant	0.2 for main panels; varied between 0.02 and 0.5 for robustness test	Varied in simulation
E_1^h	**METHODS** Eqs. 4-5	Affinity at which there is one dominant naive B cell available for each GC on average	7 for main panels; varied between 7 and 8 for robustness test	Varied in simulation
dE_{12}	**METHODS** Eq. 5	$E_1^h - dE_{12}$ is the affinity at which there is one subdominant naïve B cell available for each GC on average	0.4 for main panels; varied between 0 and 1 for robustness test	Varied in simulation
n_{res}	**METHODS** Eqs. 6-7	Length of the string representation of B cell residues	80	Upper range of the sum of CDR lengths in heavy and light chain[99]
μ, σ, ϵ	**METHODS** Eq. 8	Parameters for the shifted log-normal distribution that represent the effects of mutations on B cell binding affinities	3.1, 1.2, 3.08	Based empirical distribution of protein mutations, which suggests 5% of mutations increase binding affinity[43]
ρ	**METHODS** Eq. 9	Level of conservation of an epitope on WT and variant	0.95 for subdominant, 0.4 for dominant	Picked from several values tested; no changes in qualitative findings when varied within reasonable range
GC and EGC				
C_0	**METHODS** Eq. 10	Reference antigen concentration	8×10^{-3} nM for main panels; varied between 1×10^{-3} and 6.4×10^{-2} nM for robustness test	Varied in simulation
E_0	**METHODS** Eq. 10	Reference binding affinity	6	Corresponds to $-\log_{10} K_d = 6$, which is a typical threshold for naïve B cell activation[37]
K	**METHODS** Eq. 10	Stringency of selection of naïve and GC B cells by helper T cells based on the amounts of antigen internalized	0.5 for main panels; varied between 0.3 and 1 for robustness test	Varied in simulation

N_{max}	**METHODS** Eq. 12	Approximately the maximum number of naïve B cells that can enter GC per day	$10\ \mathrm{day}^{-1}$	Picked to match experimental observation in mice[64]
H	**METHODS** Eq. 14	Parameter that controls the saturation point when alternative definition for antigen internalization is used	20, 100, 500	Varied in simulation
β_{max}	**METHODS** Eq. 15	Maximum rate of positive selection for GC and EGC B cells	$2.5\ \mathrm{day}^{-1}$	Maximum proliferation is about ~4 times / day[53]
N_{T0}	**METHODS** Eq. 17	Maximum number of helper T cells	1200	Picked to give peak GC size of ~1000 B cells
t_0	**METHODS** Eq. 17	Time at which the number of helper T cells reaches maximum	$14\ \mathrm{day}$	Matches the dynamics in mRNA-vaccinated humans[54]
d_T	**METHODS** Eq. 17	Rate of decay for helper T cells	$0.015\ \mathrm{day}^{-1}$	Matches the dynamics in mRNA-vaccinated humans[54]
α	**METHODS** Eq. 18	Death rate of GC B cells	$0.5\ \mathrm{day}^{-1}$	Picked to allow B cells to survive ~2 days before death if they don't get selected
Memory and Plasma Cell Dynamics				
p_1	-	Probability that a positively selected GC B cell exits by differentiation	0.05 for main panels; varied between 0.03 and 0.1 for robustness test	Varied in simulation
p_2	-	Probability that a differentiating GC B cell becomes a plasma cell	0.1 for main panels; varied between 0.1 and 0.5 for robustness test	Varied in simulation
p_2^{EGC}	-	Probability that a proliferating memory cell in EGC differentiates into a plasma cell	0.6	Based on observation in mice that ~60% of reactivated B memory cells become short-lived plasma cells[62]
d_{PC}	**METHODS** Eq. 19	Death rate of plasma cells	$0.17\ \mathrm{day}^{-1}$	Short-lived plasma cells have half life of ~4 days[100]

Table 3-S3. Summary of the simulation algorithm. Pseudocode that summarizes the simulation algorithm implemented in MATLAB. It describes a single run of the simulation that models 200 GCs and an EGC.

Inputs: Parameters defining the following simulation conditions: vaccine dose number; germline affinity distribution of naïve B cells (E_1^h, dE_{12}, p); whether epitope masking is considered and epitope overlap; selection model and stringency of selection (H, K); fractions of selected GC B cells that become memory or plasma cells (p_1, p_2); reference antigen concentration (C_0); fraction of pre-existing memory cells that can re-enter GCs; simulation number index

Outputs: Arrays that have following information about the simulation: antigen and antibody concentrations over time; GC entry time of naive B cells; numbers, lineages, target epitopes, affinities, and mutation states of GC B cells; similar information for memory and plasma cells derived from GCs and EGCs

Initializations

Initialize the random number generator with simulation number index.
For each of the 200 GCs, initialize the pool of naïve B cells with their lineages, target epitopes, initial WT- and variant-binding affinities.
For each naïve B cell, initialize the effects of the mutations of its residues on the WT- and variant-binding affinities, by sampling them from appropriate probability distributions.
Initialize the antigen concentrations, antibody concentrations, and antibody binding affinities.
Initialize the arrays of GC B cells, GC-derived memory and plasma cells, EGC-derived memory and plasma cells.
Initialize the array of GC B cell mutation states with zeros.
If dose number is 2 or greater, **do**
    Initialize the antigen concentrations, antibody concentrations, antibody binding affinities, and plasma cells number and affinities to pre-existing values.
    If memory B cell entry to GCs is allowed, **do**
        Randomly choose a defined fraction of pre-existing memory B cells and add to the pool of naive B cells.
    End If
    Add pre-existing memory B cells to EGC.
Else If dose number is 1
    Initialize the antigen concentrations, antibody concentrations, antibody binding affinities, and plasma cells number and affinities to prime values.
End If

Simulation of immune response

For time from 0 to maximum time defined for each immunization in increment of 0.01 day, **do**

Update Concentrations

Antibody:
From the number and affinities of plasma cells, calculate the amount and WT- and variant-binding affinities of newly produced antibodies, separately for the dominant and subdominant epitope targeting antibodies.
Update the antibody concentrations and mean binding affinities after decay and production.
Stochastically determine the plasma cells that will undergo apoptosis based on the death rates.

Antigen:
From the soluble antigen concentration, antibody concentrations, and antibody affinities, determine the concentrations of soluble free antigen and IC.
Update the soluble free antigen concentration after decay.
Update the soluble IC concentration after transport to FDC.
Update the IC concentration on FDC after new deposition and decay.
If epitope masking is imposed, **do**
    Based on the degree of overlapping between the dominant and subdominant epitopes, calculate the effective concentration and binding affinities of the antibodies for masking of each epitope.

Calculate the free antigen concentration based on equilibrium.

End If

GC

Determine the amounts of antigen internalized by naïve B cells that have not yet entered GCs.
Determine the naïve B cells that are activated and positively selected.
Update the time of GC entry for positively selected naïve B cells and add them to the array of GC B cells.
Determine the amounts of antigen internalized by GC B cells.
Determine the GC B cells that are activated and positively selected.
Choose fraction of positively selected GC B cells and differentiate into plasma or memory cells.
Duplicate the remaining positively selected GC B cells and determine whether silent, apoptosis-incurring, or affinity-changing mutations will be introduced to each of the daughter cells.
Update the binding affinities of the new daughter cells and their mutation states accordingly.
Stochastically determine the GC B cells that will undergo apoptosis based on the death rates.

EGC

Determine the amounts of antigen internalized by memory cells.
Determine the memory cells that are activated and positively selected.
Duplicate the remaining positively selected memory B cells.

End for

Save the results of the simulation.

Table 3-S4. Neutralization activities of the recombinant antibodies derived from the memory B cells identified as EGC-derived. Related to Figure 3-4.

IC50 against Omicron were measured against Omicron(R683G) pseudovirus using HT1080/Ace2 cl14 cells. IC50 against WT were measured against WT(R683G) pseudovirus using HT1080/Ace2 cl14 cells unless otherwise noted. The IC50 against Omicron and WT were measured newly for this study except for C3136, C3050, and C2593, whose IC50 values are taken from previously reported values in Muecksch et al.[8] More information about the antibodies including their sequences, germline gene usage, and somatic mutations can be found in the supplemental tables of Muecksch et al. based on their IDs.

Antibody ID	Found In	IC50 Omicron	IC50 WT	Counted As EGC Clone in
C2107	Vax1/Vax2 1.3m	1000.0	1000.0	Vax2
C2173	Vax2 1.3m	1000.0	20.4	Vax2
C4002	Vax2 1.3m	1000.0	1000.0	Vax2
C2175	Vax2 1.3m	918.9	11.6	Vax2
C2174	Vax2 1.3m	920.4	347.2	Vax2
C2478	Vax2 1.3m/5m	948.5	1000.0	Vax2
C3137	Vax2 5m	694.8	1000.0	Vax2
C3136*	Vax2 5m	896.7	28.5**	Vax2
C3050*	Vax2 5m/Vax3	931.3	1000**	Vax2 and Vax3***
C3138	Vax2 5m/Vax3	522.5	8.0	Vax3
C2593*	Vax3	0.9	3.9**	Vax3
C4001	Vax3	7.4	0.9	Vax3
C4003	Vax3	300.6	21.6	Vax3
C3109	Vax3	271.0	77.8	Vax3
C3112	Vax3	44.7	27.3	Vax3
C3117	Vax3	36.4	9.8	Vax3

*The neutralizing activities of C3136, C3050, C2593 are taken from Muecksch et al.
**IC50 values for these antibodies were measured against the WT pseudovirus using 293TAce2 cells, as reported in Muecksch et al.[6]
***Multiple identical sequences were found at each timepoint.

3.7. Chapter 3 References

1. Cele, S., Jackson, L., Khoury, D.S., Khan, K., Moyo-Gwete, T., Tegally, H., San, J.E., Cromer, D., Scheepers, C., Amoako, D.G., et al. (2022). Omicron extensively but incompletely escapes Pfizer BNT162b2 neutralization. Nature 602, 654–656. 10.1038/s41586-021-04387-1.

2. Cao, Y., Wang, J., Jian, F., Xiao, T., Song, W., Yisimayi, A., Huang, W., Li, Q., Wang, P., An, R., et al. (2022). Omicron escapes the majority of existing SARS-CoV-2 neutralizing antibodies. Nature 602, 657–663. 10.1038/s41586-021-04385-3.

3. Planas, D., Saunders, N., Maes, P., Guivel-Benhassine, F., Planchais, C., Buchrieser, J., Bolland, W.H., Porrot, F., Staropoli, I., Lemoine, F., et al. (2022). Considerable escape of SARS-CoV-2 Omicron to antibody neutralization. Nature 602, 671–675. 10.1038/s41586-021-04389-z.

4. Thompson, M.G., Natarajan, K., Irving, S.A., Rowley, E.A., Griggs, E.P., Gaglani, M., Klein, N.P., Grannis, S.J., DeSilva, M.B., Stenehjem, E., et al. (2022). Effectiveness of a Third Dose of mRNA Vaccines Against COVID-19–Associated Emergency Department and Urgent Care Encounters and Hospitalizations Among Adults During Periods of Delta and Omicron Variant Predominance — VISION Network, 10 States, August 2021–January 2022. MMWR Morb Mortal Wkly Rep 71, 139–145. 10.15585/mmwr.mm7104e3.

5. Accorsi, E.K., Britton, A., Fleming-Dutra, K.E., Smith, Z.R., Shang, N., Derado, G., Miller, J., Schrag, S.J., and Verani, J.R. (2022). Association between 3 Doses of mRNA COVID-19 Vaccine and Symptomatic Infection Caused by the SARS-CoV-2 Omicron and Delta Variants. JAMA - Journal of the American Medical Association 327, 639–651. 10.1001/jama.2022.0470.

6. Lauring, A.S., Tenforde, M.W., Chappell, J.D., Gaglani, M., Ginde, A.A., Mcneal, T., Ghamande, S., Douin, D.J., Talbot, H.K., Casey, J.D., et al. (2022). Clinical severity of, and effectiveness of mRNA vaccines against, covid-19 from omicron, delta, and alpha SARS-CoV-2 variants in the United States: Prospective observational study. The BMJ 376. 10.1136/bmj-2021-069761.

7. Canaday, D.H., Oyebanji, O.A., White, E., Keresztesy, D., Payne, M., Wilk, D., Carias, L., Aung, H., St. Denis, K., Sheehan, M.L., et al. (2022). COVID-19 vaccine booster dose needed to achieve Omicron-specific neutralisation in nursing home residents. EBioMedicine 80, 104066. 10.1016/j.ebiom.2022.104066.

8. Muecksch, F., Wang, Z., Cho, A., Gaebler, C., Ben Tanfous, T., DaSilva, J., Bednarski, E., Ramos, V., Zong, S., Johnson, B., et al. (2022). Increased Memory B Cell Potency and Breadth After a SARS-CoV-2 mRNA Boost. Nature 607, 1–6. 10.1038/s41586-022-04778-y.

9. Garcia-Beltran, W.F., St. Denis, K.J., Hoelzemer, A., Lam, E.C., Nitido, A.D., Sheehan, M.L., Berrios, C., Ofoman, O., Chang, C.C., Hauser, B.M., et al. (2022). mRNA-based COVID-19 vaccine boosters induce neutralizing immunity against SARS-CoV-2 Omicron variant. Cell 185, 457-466.e4. 10.1016/j.cell.2021.12.033.

10. Schmidt, F., Muecksch, F., Weisblum, Y., da Silva, J., Bednarski, E., Cho, A., Wang, Z., Gaebler, C., Caskey, M., Nussenzweig, M.C., et al. (2022). Plasma Neutralization of the SARS-CoV-2 Omicron Variant. New England Journal of Medicine 386, 599–601. 10.1056/NEJMc2119641.

11. Corbett, K.S., Gagne, M., Wagner, D.A., Connell, S.O., Narpala, S.R., Flebbe, D.R., Andrew, S.F., Davis, R.L., Flynn, B., Johnston, T.S., et al. (2021). Protection against SARS-CoV-2 Beta variant in mRNA-1273 vaccine–boosted nonhuman primates. Science 374, 1343–1353. 10.1126/science.abl8912.

12. Dejnirattisai, W., Huo, J., Zhou, D., Zahradník, J., Supasa, P., Liu, C., Duyvesteyn, H.M.E., Ginn, H.M., Mentzer, A.J., Tuekprakhon, A., et al. (2022). SARS-CoV-2 Omicron-B.1.1.529 leads to widespread escape from neutralizing antibody responses. Cell 185, 467-484.e15. 10.1016/j.cell.2021.12.046.

13. Greaney, A.J., Starr, T.N., Barnes, C.O., Weisblum, Y., Schmidt, F., Caskey, M., Gaebler, C., Cho, A., Agudelo, M., Finkin, S., et al. (2021). Mapping mutations to the SARS-CoV-2 RBD that escape binding by different classes of antibodies. Nat Commun 12, 1–14. 10.1038/s41467-021-24435-8.

14. Greaney, A.J., Loes, A.N., Gentles, L.E., Crawford, K.H.D., Starr, T.N., Malone, K.D., Chu, H.Y., and Bloom, J.D. (2021). Antibodies elicited by mRNA-1273 vaccination bind more broadly to the receptor binding domain than do those from SARS-CoV-2 infection. Sci Transl Med 13. 10.1126/scitranslmed.abi9915.

15. Yuan, M., Liu, H., Wu, N.C., Lee, C.C.D., Zhu, X., Zhao, F., Huang, D., Yu, W., Hua, Y., Tien, H., et al. (2020). Structural basis of a shared antibody response to SARS-CoV-2. Science 369, 1119–1123. 10.1126/science.abd2321.

16. Robbiani, D.F., Gaebler, C., Muecksch, F., Lorenzi, J.C.C., Wang, Z., Cho, A., Agudelo, M., Barnes, C.O., Gazumyan, A., Finkin, S., et al. (2020). Convergent antibody responses to SARS-CoV-2 in convalescent individuals. Nature 584, 437–442. 10.1038/s41586-020-2456-9.

17. Cho, A., Muecksch, F., Schaefer-Babajew, D., Wang, Z., Finkin, S., Gaebler, C., Ramos, V., Cipolla, M., Mendoza, P., Agudelo, M., et al. (2021). Anti-SARS-CoV-2 receptor-binding domain antibody evolution after mRNA vaccination. Nature 600, 517–522. 10.1038/s41586-021-04060-7.

18. Abbott, R.K., Lee, J.H., Menis, S., Skog, P., Rossi, M., Ota, T., Kulp, D.W., Bhullar, D., Kalyuzhniy, O., Havenar-Daughton, C., et al. (2018). Precursor Frequency and Affinity Determine B Cell Competitive Fitness in Germinal Centers, Tested with Germline-Targeting HIV Vaccine Immunogens. Immunity 48, 133-146.e6. 10.1016/j.immuni.2017.11.023.

19. Sangesland, M., Ronsard, L., Kazer, S.W., Bals, J., Boyoglu-Barnum, S., Yousif, A.S., Barnes, R., Feldman, J., Quirindongo-Crespo, M., McTamney, P.M., et al. (2019). Germline-Encoded Affinity for Cognate Antigen Enables Vaccine Amplification of a Human Broadly Neutralizing Response against Influenza Virus. Immunity 51, 735-749.e8. 10.1016/j.immuni.2019.09.001.

20. Amitai, A., Sangesland, M., Barnes, R.M., Rohrer, D., Lonberg, N., Lingwood, D., and Chakraborty, A.K. (2020). Defining and Manipulating B Cell Immunodominance Hierarchies to Elicit Broadly Neutralizing Antibody Responses against Influenza Virus. Cell Syst 11, 573-588.e9. 10.1016/j.cels.2020.09.005.

21. Havenar-Daughton, C., Abbott, R.K., Schief, W.R., and Crotty, S. (2018). When designing vaccines, consider the starting material: the human B cell repertoire. Curr Opin Immunol 53, 209–216. 10.1016/j.coi.2018.08.002.

22. Cirelli, K.M., Carnathan, D.G., Nogal, B., Martin, J.T., Rodriguez, O.L., Upadhyay, A.A., Enemuo, C.A., Gebru, E.H., Choe, Y., Viviano, F., et al. (2019). Slow Delivery Immunization Enhances HIV Neutralizing Antibody and Germinal Center Responses via Modulation of Immunodominance. Cell 177, 1153-1171.e28. 10.1016/j.cell.2019.04.012.

23. Angeletti, D., Kosik, I., Santos, J.J.S., Yewdell, W.T., Boudreau, C.M., Mallajosyula, V.V.A., Mankowski, M.C., Chambers, M., Prabhakaran, M., Hickman, H.D., et al. (2019). Outflanking

immunodominance to target subdominant broadly neutralizing epitopes. Proc Natl Acad Sci U S A 116, 13474–13479. 10.1073/pnas.1816300116.

24. Wang, S., Mata-Fink, J., Kriegsman, B., Hanson, M., Irvine, D.J., Eisen, H.N., Burton, D.R., Wittrup, K.D., Kardar, M., and Chakraborty, A.K. (2015). Manipulating the selection forces during affinity maturation to generate cross-reactive HIV antibodies. Cell 160, 785–797. 10.1016/j.cell.2015.01.027.

25. Bergström, J.J.E., Xu, H., and Heyman, B. (2017). Epitope-specific suppression of IgG responses by passively administered specific IgG: Evidence of epitope masking. Front Immunol 8. 10.3389/fimmu.2017.00238.

26. McNamara, H.A., Idris, A.H., Sutton, H.J., Vistein, R., Flynn, B.J., Cai, Y., Wiehe, K., Lyke, K.E., Chatterjee, D., KC, N., et al. (2020). Antibody Feedback Limits the Expansion of B Cell Responses to Malaria Vaccination but Drives Diversification of the Humoral Response. Cell Host Microbe 28, 572-585.e7. 10.1016/j.chom.2020.07.001.

27. Tas, J.M.J., Koo, J.-H., Lin, Y.-C., Xie, Z., Steichen, J.M., Jackson, A.M., Hauser, B.M., Wang, X., Cottrell, C.A., Torres, J.L., et al. (2022). Antibodies from primary humoral responses modulate recruitment of naive B cells during secondary responses. Immunity. 10.1016/j.immuni.2022.07.020.

28. Angeletti, D., Gibbs, J.S., Angel, M., Kosik, I., Hickman, H.D., Frank, G.M., Das, S.R., Wheatley, A.K., Prabhakaran, M., Leggat, D.J., et al. (2017). Defining B cell immunodominance to viruses. 18. 10.1038/ni.3680.

29. Schaefer-Babajew, D., Wang, Z., Muecksch, F., Cho, A., Raspe, R., Johnson, B., Canis, M., DaSilva, J., Ramos, V., Turroja, M., et al. (2022). Antibody feedback regulation of memory B cell development in SARS-CoV-2 mRNA vaccination. medRxiv, 2022.08.05.22278483. 10.1101/2022.08.05.22278483.

30. Zarnitsyna, V.I., Lavine, J., Ellebedy, A., Ahmed, R., and Antia, R. (2016). Multi-epitope Models Explain How Pre-existing Antibodies Affect the Generation of Broadly Protective Responses to Influenza. PLoS Pathog 12, 1–22. 10.1371/journal.ppat.1005692.

31. Zhao, X., Li, D., Ruan, W., Chen, Z., Zhang, R., Zheng, A., Qiao, S., Zheng, X., Zhao, Y., Dai, L., et al. (2022). Effects of a Prolonged Booster Interval on Neutralization of Omicron Variant. New England Journal of Medicine 386, 894–896. 10.1056/NEJMc2119426.

32. Regev-Yochay, G., Gonen, T., Gilboa, M., Mandelboim, M., Indenbaum, V., Amit, S., Meltzer, L., Asraf, K., Cohen, C., Fluss, R., et al. (2022). Efficacy of a Fourth Dose of Covid-19 mRNA Vaccine against Omicron. New England Journal of Medicine 386, 1377–1380. 10.1056/nejmc2202542.

33. Tam, H.H., Melo, M.B., Kang, M., Pelet, J.M., Ruda, V.M., and Foley, M.H. (2016). Sustained antigen availability during germinal center initiation enhances antibody responses to vaccination. PNAS 113, 6639–6648. 10.1073/pnas.1606050113.

34. van Beek, M., Nussenzweig, M.C., and Chakraborty, A.K. (2022). Two complementary features of humoral immune memory confer protection against the same or variant antigens. Proc Natl Acad Sci U S A 119, e2205598119. 10.1073/pnas.2205598119.

35. Jacob, J., Kassir, R., and Kelsoe, G. (1991). In situ studies of the primary immune response to (4-hydroxy-3-nitrophenyl)acetyl. I. The architecture and dynamics of responding cell populations. Journal of Experimental Medicine 173, 1165–1175. 10.1084/jem.173.5.1165.

36. Pardi, N., Tuyishime, S., Muramatsu, H., Kariko, K., Mui, B.L., Tam, Y.K., Madden, T.D., Hope, M.J., and Weissman, D. (2015). Expression kinetics of nucleoside-modified mRNA delivered in lipid nanoparticles to mice by various routes. Journal of Controlled Release 217, 345–351. 10.1016/j.jconrel.2015.08.007.

37. Batista, F.D., and Neuberger, M.S. (1998). Affinity dependence of the B cell response to antigen: A threshold, a ceiling, and the importance of off-rate. Immunity 8, 751–759. 10.1016/S1074-7613(00)80580-4.

38. Kuraoka, M., Schmidt, A.G., Nojima, T., Feng, F., Watanabe, A., Kitamura, D., Harrison, S.C., Kepler, T.B., and Kelsoe, G. (2016). Complex Antigens Drive Permissive Clonal Selection in Germinal Centers. Immunity 44, 542–552. 10.1016/j.immuni.2016.02.010.

39. Feldman, J., Bals, J., Altomare, C.G., Denis, K.S., Lam, E.C., Hauser, B.M., Ronsard, L., Sangesland, M., Moreno, T.B., Okonkwo, V., et al. (2021). Naive human B cells engage the receptor binding domain of SARS-CoV-2, variants of concern, and related sarbecoviruses. Sci Immunol 6. 10.1126/sciimmunol.abl5842.

40. Wang, L., Fu, W., Bao, L., Jia, Z., Zhang, Y., Zhou, Y., Wu, W., Wu, J., Zhang, Q., Gao, Y., et al. (2022). Selection and structural bases of potent broadly neutralizing antibodies from 3-dose vaccinees that are highly effective against diverse SARS-CoV-2 variants, including Omicron sublineages. Cell Res 32, 691–694. 10.1038/s41422-022-00677-z.

41. Tan, C.W., Chia, W.N., Zhu, F., Young, B.E., Chantasrisawad, N., Hwa, S.-H., Yeoh, A.Y.-Y., Lim, B.L., Yap, W.C., Pada, S.K.M.S., et al. (2022). SARS-CoV-2 Omicron variant emerged under immune selection. Nat Microbiol 7, 1756–1761. 10.1038/s41564-022-01246-1.

42. Kumar, M.D.S., and Gromiha, M.M. (2006). PINT : Protein – protein Interactions Thermodynamic Database. 34, 195–198. 10.1093/nar/gkj017.

43. Zhang, J., and Shakhnovich, E.I. (2010). Optimality of mutation and selection in germinal centers. PLoS Comput Biol 6, 1–9. 10.1371/journal.pcbi.1000800.

44. Turner, J.S., Benet, Z.L., and Grigorova, I.L. (2017). Antigen Acquisition Enables Newly Arriving B Cells To Enter Ongoing Immunization-Induced Germinal Centers. The Journal of Immunology 199, 1301–1307. 10.4049/jimmunol.1700267.

45. Schwickert, T.A., Lindquist, R.L., Shakhar, G., Livshits, G., Skokos, D., Kosco-Vilbois, M.H., Dustin, M.L., and Nussenzweig, M.C. (2007). In vivo imaging of germinal centres reveals a dynamic open structure. Nature 446, 83–87. 10.1038/nature05573.

46. Fleire, S.J., Goldman, J.P., Carrasco, Y.R., Weber, M., Bray, D., and Batista, F.D. (2006). B cell ligand discrimination through a spreading and contraction response. Science 312, 738–741. 10.1126/science.1123940.

47. Okada, T., Miller, M.J., Parker, I., Krummel, M.F., Neighbors, M., Hartley, S.B., O'Garra, A., Cahalan, M.D., and Cyster, J.G. (2005). Antigen-engaged B cells undergo chemotaxis toward the T zone and form motile conjugates with helper T cells. PLoS Biol 3, 1047–1061. 10.1371/journal.pbio.0030150.

48. Schwickert, T.A., Victora, G.D., Fooksman, D.R., Kamphorst, A.O., Mugnier, M.R., Gitlin, A.D., and Nussenzweig, M.L.D. (2011). A dynamic T cell-limited checkpoint regulates affinity-dependent B cell entry into the germinal center. Journal of Experimental Medicine 208, 1243–1252. 10.1084/jem.20102477.

49. Lee, J.H., Hu, J.K., Georgeson, E., Nakao, C., Groschel, B., Dileepan, T., Jenkins, M.K., Seumois, G., Vijayanand, P., Schief, W.R., et al. (2021). Modulating the quantity of HIV Env-specific CD4 T cell help promotes rare B cell responses in germinal centers. Journal of Experimental Medicine 218. 10.1084/jem.20201254.

50. Victora, G.D., and Wilson, P.C. (2015). Germinal Center Selection and the Antibody Response to Influenza. Cell 163, 545–548. 10.1016/j.cell.2015.10.004.

51. Luo, W., Weisel, F., and Shlomchik, M.J. (2018). B Cell Receptor and CD40 Signaling Are Rewired for Synergistic Induction of the c-Myc Transcription Factor in Germinal Center B Cells. Immunity 48, 313-326.e5. 10.1016/j.immuni.2018.01.008.

52. Shlomchik, M.J., Luo, W., and Weisel, F. (2019). Linking signaling and selection in the germinal center. Immunol Rev 288, 49–63. 10.1111/imr.12744.

53. Victora, G.D., Schwickert, T.A., Fooksman, D.R., Kamphorst, A.O., Meyer-Hermann, M., Dustin, M.L., and Nussenzweig, M.C. (2010). Germinal center dynamics revealed by multiphoton microscopy with a photoactivatable fluorescent reporter. Cell 143, 592–605. 10.1016/j.cell.2010.10.032.

54. Goel, R.R., Painter, M.M., Apostolidis, S.A., Mathew, D., Meng, W., Rosenfeld, A.M., Lundgreen, K.A., Reynaldi, A., Khoury, D.S., Pattekar, A., et al. (2021). mRNA vaccines induce durable immune memory to SARS-CoV-2 and variants of concern. Science 374. 10.1126/science.abm0829.

55. Mayer, C.T., Gazumyan, A., Kara, E.E., Gitlin, A.D., Golijanin, J., Viant, C., Pai, J., Oliveira, T.Y., Wang, Q., Escolano, A., et al. (2017). The microanatomic segregation of selection by apoptosis in the germinal center. Science 358, 0–9. 10.1126/science.aao2602.

56. Amitai, A., Mesin, L., Victora, G.D., Kardar, M., and Chakraborty, A.K. (2017). A population dynamics model for clonal diversity in a germinal center. Front Microbiol 8, 1–9. 10.3389/fmicb.2017.01693.

57. Amitai, A., Chakraborty, A.K., and Kardar, M. (2018). The low spike density of HIV may have evolved because of the effects of T helper cell depletion on affinity maturation. PLoS Comput Biol 14, e1006408. 10.1371/journal.pcbi.1006408.

58. Ganti, R.S., and Chakraborty, A.K. (2021). Mechanisms underlying vaccination protocols that may optimally elicit broadly neutralizing antibodies against highly mutable pathogens. Phys Rev E 103, 1–17. 10.1103/physreve.103.052408.

59. Gitlin, A.D., Shulman, Z., and Nussenzweig, M.C. (2014). Clonal selection in the germinal centre by regulated proliferation and hypermutation. Nature 509, 637–640. 10.1038/nature13300.

60. Michael, N., Martin, T.E., Nicolae, D., Kim, N., Padjen, K., Zhan, P., Nguyen, H., Pinkert, C., and Storb, U. (2002). Effects of sequence and structure on the hypermutability of immunoglobulin genes. Immunity 16, 123–134. 10.1016/S1074-7613(02)00261-3.

61. Moran, I., Grootveld, A.K., Nguyen, A., and Phan, T.G. (2019). Subcapsular Sinus Macrophages: The Seat of Innate and Adaptive Memory in Murine Lymph Nodes. Trends Immunol 40, 35–48. 10.1016/j.it.2018.11.004.

62. Moran, I., Nguyen, A., Khoo, W.H., Butt, D., Bourne, K., Young, C., Hermes, J.R., Biro, M., Gracie, G., Ma, C.S., et al. (2018). Memory B cells are reactivated in subcapsular proliferative foci of lymph nodes. Nat Commun 9, 1–14. 10.1038/s41467-018-05772-7.

63. Martin, J.T., Hartwell, B.L., Kumarapperuma, S.C., Melo, M.B., Carnathan, D.G., Cossette, B.J., Adams, J., Gong, S., Zhang, W., Tokatlian, T., et al. (2021). Combined PET and whole-tissue imaging of lymphatic-targeting vaccines in non-human primates. Biomaterials 275. 10.1016/j.biomaterials.2021.120868.

64. Tas, J.M.J., Mesin, L., Pasqual, G., Targ, S., Jacobsen, J.T., Mano, Y.M., Chen, C.S., Weill, J.C., Reynaud, C.A., Browne, E.P., et al. (2016). Visualizing antibody affinity maturation in germinal centers. Science 351, 1048–1054. 10.1126/science.aad3439.

65. Escarmís, C., Lázaro, E., and Manrubia, S.C. (2006). Population Bottlenecks in Quasispecies Dynamics. In Quasispecies: Concept and Implications for Virology, E. Domingo, ed. (Springer Berlin Heidelberg), pp. 141–170. 10.1007/3-540-26397-7_5.

66. Li, H., and Roossinck, M.J. (2004). Genetic Bottlenecks Reduce Population Variation in an Experimental RNA Virus Population. J Virol 78, 10582–10587. 10.1128/jvi.78.19.10582-10587.2004.

67. Kreer, C., Zehner, M., Weber, T., Ercanoglu, M.S., Gieselmann, L., Rohde, C., Halwe, S., Korenkov, M., Schommers, P., Vanshylla, K., et al. (2020). Longitudinal Isolation of Potent Near-Germline SARS-CoV-2-Neutralizing Antibodies from COVID-19 Patients. Cell 182, 843-854.e12. 10.1016/j.cell.2020.06.044.

68. Brouwer, P.J.M., Caniels, T.G., van der Straten, K., Snitselaar, J.L., Aldon, Y., Bangaru, S., Torres, J.L., Okba, N.M.A., Claireaux, M., Kerster, G., et al. (2020). Potent neutralizing antibodies from COVID-19 patients define multiple targets of vulnerability. Science 369, 643–650. 10.1126/science.abc5902.

69. Barnes, C.O., West, A.P., Huey-Tubman, K.E., Hoffmann, M.A.G., Sharaf, N.G., Hoffman, P.R., Koranda, N., Gristick, H.B., Gaebler, C., Muecksch, F., et al. (2020). Structures of Human Antibodies Bound to SARS-CoV-2 Spike Reveal Common Epitopes and Recurrent Features of Antibodies. Cell 182, 828-842.e16. 10.1016/j.cell.2020.06.025.

70. Turner, J.S., O'Halloran, J.A., Kalaidina, E., Kim, W., Schmitz, A.J., Zhou, J.Q., Lei, T., Thapa, M., Chen, R.E., Case, J.B., et al. (2021). SARS-CoV-2 mRNA vaccines induce persistent human germinal centre responses. Nature 596, 109–113. 10.1038/s41586-021-03738-2.

71. Francis, T. (1960). On the Doctrine of Original Antigenic Sin. Proc Am Philos Soc 104, 572–578.

72. Mesin, L., Schiepers, A., Ersching, J., Barbulescu, A., Cavazzoni, C.B., Angelini, A., Okada, T., Kurosaki, T., and Victora, G.D. (2019). Restricted Clonality and Limited Germinal Center Reentry Characterize Memory B Cell Reactivation by Boosting. Cell. 10.1016/j.cell.2019.11.032.

73. Viant, C., Weymar, G.H.J., Escolano, A., Chen, S., Hartweger, H., Cipolla, M., Gazumyan, A., and Nussenzweig, M.C. (2020). Antibody Affinity Shapes the Choice between Memory and Germinal Center B Cell Fates. Cell 183, 1298-1311.e11. 10.1016/j.cell.2020.09.063.

74. Wang, Z., Muecksch, F., Schaefer-Babajew, D., Finkin, S., Viant, C., Gaebler, C., Hoffmann, H.H., Barnes, C.O., Cipolla, M., Ramos, V., et al. (2021). Naturally enhanced neutralizing breadth against SARS-CoV-2 one year after infection. Nature 595, 426–431. 10.1038/s41586-021-03696-9.

75. Schmidt, F., Weisblum, Y., Muecksch, F., Hoffmann, H.-H., Michailidis, E., Lorenzi, J.C.C., Mendoza, P., Rutkowska, M., Bednarski, E., Gaebler, C., et al. (2020). Measuring SARS-CoV-2

neutralizing antibody activity using pseudotyped and chimeric viruses. Journal of Experimental Medicine 217, e20201181. 10.1084/jem.20201181.

76. Cameroni, E., Bowen, J.E., Rosen, L.E., Saliba, C., Zepeda, S.K., Culap, K., Pinto, D., VanBlargan, L.A., De Marco, A., di Iulio, J., et al. (2022). Broadly neutralizing antibodies overcome SARS-CoV-2 Omicron antigenic shift. Nature 602, 664–670. 10.1038/s41586-021-04386-2.

77. Kotaki, R., Adachi, Y., Moriyama, S., Onodera, T., Fukushi, S., Nagakura, T., Tonouchi, K., Terahara, K., Sun, L., Takano, T., et al. (2022). SARS-CoV-2 Omicron-neutralizing memory B cells are elicited by two doses of BNT162b2 mRNA vaccine. Sci Immunol 7. 10.1126/sciimmunol.abn8590.

78. Demonbreun, A.R., Sancilio, A., Velez, M.P., Ryan, D.T., Saber, R., Vaught, L.A., Reiser, N.L., Hsieh, R.R., D'Aquila, R.T., Mustanski, B., et al. (2021). Comparison of IgG and neutralizing antibody responses after one or two doses of COVID-19 mRNA vaccine in previously infected and uninfected individuals. EClinicalMedicine 38. 10.1016/j.eclinm.2021.101018.

79. Macdonald, P.J., Ruan, Q., Grieshaber, J.L., Swift, K.M., Taylor, R.E., Prostko, J.C., and Tetin, S.Y. (2022). Affinity of anti-spike antibodies in SARS-CoV-2 patient plasma and its effect on COVID-19 antibody assays. EBioMedicine 75. 10.1016/j.ebiom.2021.103796.

80. Zhang, Y., Meyer-Hermann, M., George, L.A., Figge, M.T., Khan, M., Goodall, M., Young, S.P., Reynolds, A., Falciani, F., Waisman, A., et al. (2013). Germinal center B cells govern their own fate via antibody feedback. J Exp Med 210, 457–464. 10.1084/jem.20120150.

81. Barnes, C.O., Jette, C.A., Abernathy, M.E., Dam, K.M.A., Esswein, S.R., Gristick, H.B., Malyutin, A.G., Sharaf, N.G., Huey-Tubman, K.E., Lee, Y.E., et al. (2020). SARS-CoV-2 neutralizing antibody structures inform therapeutic strategies. Nature 588, 682–687. 10.1038/s41586-020-2852-1.

82. Lan, J., Ge, J., Yu, J., Shan, S., Zhou, H., Fan, S., Zhang, Q., Shi, X., Wang, Q., Zhang, L., et al. (2020). Structure of the SARS-CoV-2 spike receptor-binding domain bound to the ACE2 receptor. Nature 581, 215–220. 10.1038/s41586-020-2180-5.

83. Andreano, E., Paciello, I., Pierleoni, G., Piccini, G., Abbiento, V., Antonelli, G., Pileri, P., Manganaro, N., Pantano, E., Maccari, G., et al. (2022). COVID-19 mRNA third dose induces a unique hybrid immunity-like antibody response. bioRxiv, 2022.05.09.491201. 10.1101/2022.05.09.491201.

84. Escolano, A., Steichen, J.M., Dosenovic, P., Kulp, D.W., Golijanin, J., Sok, D., Freund, N.T., Gitlin, A.D., Oliveira, T., Araki, T., et al. (2016). Sequential Immunization Elicits Broadly Neutralizing Anti-HIV-1 Antibodies in Ig Knockin Mice. Cell 166, 1445-1458.e12. 10.1016/j.cell.2016.07.030.

85. Escolano, A., Gristick, H.B., Gautam, R., DeLaitsch, A.T., Abernathy, M.E., Yang, Z., Wang, H., Hoffmann, M.A.G., Nishimura, Y., Wang, Z., et al. (2021). Sequential immunization of macaques elicits heterologous neutralizing antibodies targeting the V3-glycan patch of HIV-1 Env. Sci Transl Med 13. 10.1126/scitranslmed.abk1533.

86. Klein, F., Mouquet, H., Dosenovic, P., Scheid, J.F., Scharf, L., and Nussenzweig, M.C. (2013). Antibodies in HIV-1 vaccine development and therapy. Science 341, 1199–1204. 10.1126/science.1241144.

87. Wu, N.C., and Wilson, I.A. (2020). Influenza hemagglutinin structures and antibody recognition. Cold Spring Harb Perspect Med 10, 1–20. 10.1101/cshperspect.a038778.

88. Tarke, A., Sidney, J., Kidd, C.K., Dan, J.M., Ramirez, S.I., Yu, E.D., Mateus, J., da Silva Antunes, R., Moore, E., Rubiro, P., et al. (2021). Comprehensive analysis of T cell immunodominance and immunoprevalence of SARS-CoV-2 epitopes in COVID-19 cases. Cell Rep Med 2, 100204. 10.1016/J.XCRM.2021.100204.

89. Pauthner, M., Havenar-Daughton, C., Sok, D., Nkolola, J.P., Bastidas, R., Boopathy, A. v., Carnathan, D.G., Chandrashekar, A., Cirelli, K.M., Cottrell, C.A., et al. (2017). Elicitation of Robust Tier 2 Neutralizing Antibody Responses in Nonhuman Primates by HIV Envelope Trimer Immunization Using Optimized Approaches. Immunity 46, 1073-1088.e6. 10.1016/j.immuni.2017.05.007.

90. Moyer, T.J., Kato, Y., Abraham, W., Chang, J.Y.H., Kulp, D.W., Watson, N., Turner, H.L., Menis, S., Abbott, R.K., Bhiman, J.N., et al. (2020). Engineered immunogen binding to alum adjuvant enhances humoral immunity. Nat Med 26, 430–440. 10.1038/s41591-020-0753-3.

91. Rees, A.R. (2020). Understanding the human antibody repertoire. MAbs 12. 10.1080/19420862.2020.1729683.

92. Boyd, S.D., and Joshi, S.A. (2014). High-Throughput DNA Sequencing Analysis of Antibody Repertoires. Microbiol Spectr. 10.1128/MICROBIOLSPEC.AID-0017-2014.

93. Foote, J., and Eisen, H.N. (1995). Kinetic and affinity limits on antibodies produced during immune responses. Proc Natl Acad Sci U S A 92, 1254 LP – 1256. 10.1073/pnas.92.5.1254.

94. Molari, M., Eyer, K., Baudry, J., Cocco, S., and Monasson, R. (2020). Quantitative modeling of the effect of antigen dosage on b-cell affinity distributions in maturating germinal centers. Elife 9, 1–49. 10.7554/eLife.55678.

95. Kim, Y.M., Pan, J.Y.J., Korbel, G.A., Peperzak, V., Boes, M., and Ploegh, H.L. (2006). Monovalent ligation of the B cell receptor induces receptor activation but fails to promote antigen presentation. Proc Natl Acad Sci U S A 103, 3327–3332. 10.1073/pnas.0511315103.

96. Oprea, M., and Perelson, A. (1997). Somatic mutation leads to efficient affinity maturation when centrocytes recycle back to centroblasts. Journal of Immunology 158, 5155–5162. 10.1016/s0165-2478(97)87000-9.

97. Kepler, T.B., and Perelson, A.S. (1993). Cyclic re-entry of germinal center B cells and the efficiency of affinity maturation. Immunol Today 14, 412–415. https://doi.org/10.1016/0167-5699(93)90145-B.

98. Aung, A., Cui, A., Maiorino, L., Amini, A.P., Gregory, J.R., Bukenya, M., Zhang, Y., Lee, H., Cottrell, C.A., Morgan, D.M., et al. (2023). Low protease activity in B cell follicles promotes retention of intact antigens after immunization. Science 379, eabn8934. 10.1126/science.abn8934.

99. Nowak, J., Baker, T., Georges, G., Kelm, S., Klostermann, S., Shi, J., Sridharan, S., and Deane, C.M. (2016). Length-independent structural similarities enrich the antibody CDR canonical class model. MAbs 8, 751–760. 10.1080/19420862.2016.1158370.

100. Khodadadi, L., Cheng, Q., Radbruch, A., and Hiepe, F. (2019). The Maintenance of Memory Plasma Cells. Front Immunol 10, 721. 10.3389/fimmu.2019.00721.

Chapter 4.

Two-dose “extended priming” immunization amplifies humoral immune responses by synchronizing vaccine delivery with the germinal center response

4.1. Summary

“Extended priming” immunization regimens that prolong exposure of the immune system to vaccines during the primary immune response have shown promise in enhancing humoral immune responses to a variety of subunit vaccines in preclinical models. We previously showed that escalating-dosing immunization (EDI), where a vaccine is dosed every other day in an increasing pattern over 2 weeks dramatically amplifies humoral immune responses. But such a dosing regimen is impractical for prophylactic vaccines. We hypothesized that simpler dosing regimens might replicate key elements of the immune response triggered by EDI. Here we explored "reduced ED" immunization regimens, assessing the impact of varying the number of injections, dose levels, and dosing intervals during EDI. Using a stabilized HIV Env trimer as a model antigen combined with a potent saponin adjuvant, we found that a two-shot extended-prime regimen consisting of immunization with 20% of a given vaccine dose followed by a second shot with the remaining 80% of the dose 7 days later resulted in increased total GC B cells, 5-10-fold increased frequencies of antigen-specific GC B cells, and 10-fold increases in serum antibody titers compared to single bolus immunization. Computational modeling of the GC response suggested that this enhanced response is mediated by antigen delivered in the second dose being captured more efficiently as immune complexes in follicles, predictions we verified experimentally. Our computational and experimental results also highlight how properly designed reduced ED protocols enhance activation and antigen loading of dendritic cells and activation of T helper cells to amplify humoral responses. These results suggest that a two-shot priming approach can be used to substantially enhance responses to subunit vaccines.

4.2. Introduction

Vaccines are a critical public health tool for the control of infectious diseases and, most recently, their efficacy in mitigating severe outcomes during the COVID-19 pandemic has further highlighted their importance[1]. However, despite significant advances, there remain a number of pathogens, including the human immunodeficiency virus (HIV), for which effective vaccines are unavailable,

owing to challenges such as high mutation rates, immune evasion mechanisms, and unfavorable immunodominance patterns[2,3]. HIV continues to pose a persistent global health threat, and the development of an effective vaccine against the virus remains an urgent priority[4]. Broadly neutralizing antibodies that can neutralize diverse strains have been isolated from naturally infected people [5] and they target relatively conserved regions of the HIV ENV spike. Based on non-human primate and human studies of antibody passive transfer, a vaccine capable of eliciting broadly neutralizing antibodies (bnAbs) against the HIV envelope trimer (Env) should be protective against HIV infection[6–8]. However, generation of antibodies capable of broad and potent native HIV neutralization via vaccination has proven challenging due to multiple factors including immunodominance of non-neutralizing epitopes, high sequence variability of the trimer, and difficult structural accessibility of highly conserved epitopes[3,9,10]. Similar challenges have hindered the development of universal influenza vaccines that target the relatively conserved receptor binding site of hemagglutinin (HA)[11,12].

Following vaccination, germinal centers (GCs) play a pivotal role in the evolution of the clonality and affinity of the antibody response, and influence the composition of the memory B cell and long-lived plasma cell compartments following immunization[13,14]. The provision of antigen to GC B cells by follicular dendritic cells (FDCs), which efficiently capture complement- or antibody-decorated antigen, and support from follicular helper T cells (Tfh), which control GC B cell survival, are crucial factors in this process[15,16]. Notably, the size of the early GC response correlates with the magnitude of neutralizing antibodies (Abs) generated by immunization with HIV Env trimers in rhesus macaques[17]. Furthermore, for difficult-to-neutralize pathogens such as HIV, increasing the number of clones entering the GC increases the likelihood that a rare germline B cell that targets a neutralizing epitope undergoes affinity maturation[9,18].

One effective approach to enhance the GC response during vaccination is via the use of “extended prime” dosing regimens for administering HIV immunogens[19–22]. In this approach, a given dose of antigen and adjuvant are provided over a prolonged window of time compared to traditional bolus vaccine injection, through methods such as repeated injections[19,20,22], implanted drug delivery devices[19,20], or through slow-release biomaterials[23–25]. Among these approaches, a simple strategy that elicits profound changes to humoral immunity is escalating-dose immunization (EDI), where a given dose of vaccine is administered as a series of repeated injections over a period of 2 weeks. For stabilized HIV Env trimer immunogens, EDI using seven injections in an exponentially-increasing dosing pattern has been shown to increases the magnitude of the GC and Tfh response, increase the number of B cell clones entering the GC, increase the size of the memory B cell response, increase

autologous tier 2 neutralizing antibody titers, and initiate a GC response that can persist for at least 6 months in non-human primates[19,20,22].

Although this extended-prime regimen is highly effective, it is not practical for mass vaccination. Slow-delivery technologies aiming to mimic the effects of extended dosing regimens following a single injection are in development[23,26–28], but it remains to be seen if these approaches can fully replicate the potency of EDI and they must meet a high bar of safety for wide implementation in vaccine development. Our early computational modeling work seeking to understand the mechanics of ED vaccine immune responses suggested that the key elements driving strong GC responses following ED immunization are the initiation of B cell priming and GC formation by small amounts of antigen early in the dosing course, followed by later (~1-2 weeks) arrival of larger quantities of antigen that can be captured in immune complexes formed by newly-produced affinity-matured antibody in the lymph node [19]. This late-arriving antigen becomes deposited on FDCs at high levels, providing a reservoir of antigen to drive the GC response.

Based on these mechanisms, we hypothesized that a "reduced escalating-dose" immunization could be possible, where we simplify the ED dosing regimen to just 2 injections: a first dose to initiate B cell priming, followed by a second shot 1-2 weeks later that would provide antigen for capture on FDCs. Here, we explored the parameter space of EDI and carried out systematic studies varying the number of doses, dose ratio, and dose intervals using a model HIV Env stabilized trimer immunogen and potent saponin adjuvant in mice. We found that a reduced 2-shot extended-prime approach is able to retain much of the benefit of the 7-dose EDI regimen in amplifying the humoral response against Env trimers. Guided by computational modeling of mechanistic steps required for T cell and B cell priming following bolus or multi-shot immunization, we show that even a two-shot priming approach is capable of greatly augmenting antigen deposition on FDCs to drive the GC response compared to a bolus priming immunization. Together these data suggest that a simple extended-prime immunization approach for subunit vaccines could provide substantial enhancements to humoral immunity, and provide new insights into how the modulation of vaccine kinetics can be leveraged to augment the germinal center response of broad relevance to vaccines for diverse infectious diseases.

4.3. Results

4.3.1. A two-dose priming regimen greatly augments responses to HIV Env trimer protein immunization over traditional bolus immunization

Using a stabilized HIV Env SOSIP trimer immunogen engineered to promote priming of N332-supersite-directed B cells (N332-GT2[29]) and a potent saponin nanoparticle adjuvant (saponin/MPLA nanoparticles, SMNP[30,31]), we conducted an evaluation of simplified dosing regimens in mice. Given the large parameter space to explore, we opted to focus on analysis of GC responses at day 14 for all groups, as we previously found that GC responses in mice peaked at this timepoint for immunization patterns as disparate as bolus and the full 7-dose ED regimen[19]. First, we tested the effect of number of doses, starting from the previously defined optimal 7-ED regimen, and reducing the number of doses systematically, while keeping the escalation-over-time pattern, the total time interval (12 days), and amount of total vaccine administered (summing all the doses for a given regimen) constant (**Fig. 4-1A**). Here we found that the total size of the GC and Tfh responses steadily dropped as the number of doses was reduced (**Fig. 4-1B-C**). However, staining with fluorescent trimer probes to identify antigen-specific cells, we found the number of trimer-binding GC B cells dropped only ~5-fold moving from 7 doses down to 3 doses, while a 2-dose ED pattern elicited an antigen-specific GC B cell response not statistically different from bolus (**Fig. 4-1D**). This poor response to the two-dose ED immunization was not due to the choice of time point for GC analysis, as the GC response for this regimen was still low when measured 7 days after the second dose (**Fig. 4-S1A-C**). Trimer-specific serum IgG titers measured one month after dosing were similar for 7, 6, 4, and 3-dose ED, but 2-dose and bolus immunization antibody responses were ~1 and ~2 logs lower, respectively (**Fig. 4-1E**). Thus, even a 3-dose escalating immunization pattern can substantially enhance many elements of the humoral immune response relative to traditional bolus immunization.

We hypothesized that the poor response to 2-dose escalating immunization could reflect that a 12-day interval between doses is too wide a gap to optimally feed antigen to the GC response, and thus we next tested two-dose escalating patterns administered at intervals ranging from 4 to 12 days, fixing the initial dose at 20% of the total, and the remaining 80% of the vaccine dose administered at the second injection (**Fig. 4-1F**). In this series, a two-dose escalating prime immunization with an interval of 7 days elicited an optimal response, eliciting 4-fold more total GC B cells and 5-fold more Tfh than bolus immunization (**Fig. 4-1G-H**). Remarkably, the 7-day 2-dose pattern elicited 10-fold more trimer-binding GC B cells than bolus immunization, only 3-fold fewer than the previously-optimized 7-dose two-week escalating dosing pattern (**Fig. 4-1I**).

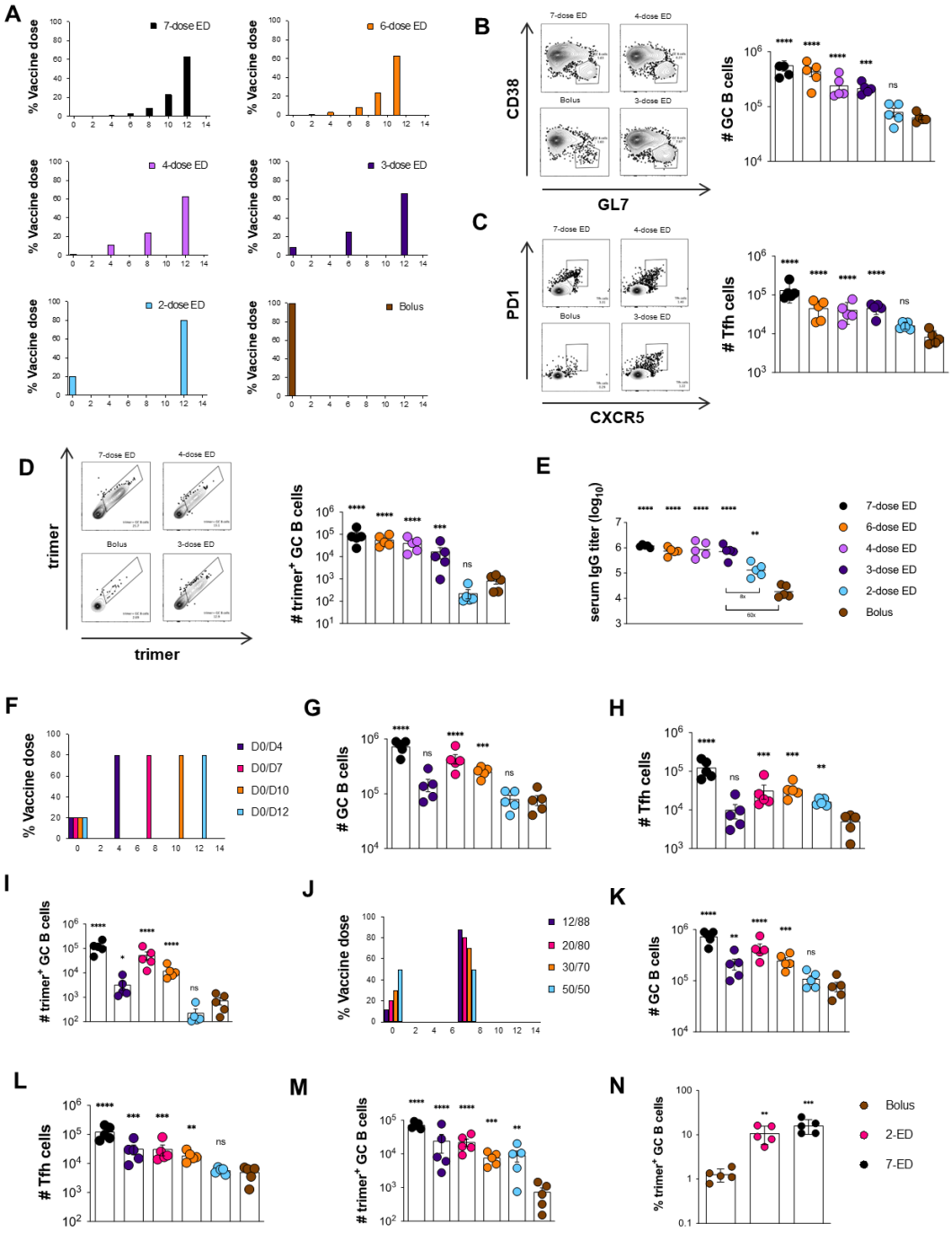

Figure 4-1. An optimally designed two-shot extended-prime vaccination substantially enhances GC responses to subunit vaccines compared to bolus immunization.

(A) Schematic of escalating dose vaccination regimens with varying dose number. (**B-E**) C57BL/6J mice (*n*=5 animals/group) were immunized with 10 μg N332-GT2 trimer and 5 μg SMNP adjuvant according to the dosing schemes in (**A**). GC responses were evaluated on day 14 by flow cytometry and antibody responses by ELISA on day 28. Shown are representative flow cytometry histograms and cell counts for total GC B cells (**B**), Tfh (**C**), and trimer-specific GC B cells (**D**) at day 14, and trimer-specific serum IgG titers at day 28 (**E**). (**F**) Schematic of dosing schedules tested for two-shot ED regimens. (**G-I**) C57BL/6J mice (*n*=5 animals/group) were immunized with 10 μg N332-GT2 trimer and 5 μg SMNP adjuvant according to the dosing schemes in (**F**), and total GC B cells (**G**), Tfh cells (**H**), and trimer-specific GC B cells (**I**) were analyzed by flow cytometry on day 14. Note: Bolus

and 7-dose ED comparisons are also shown with black and brown colors respectively. (**J**) Schematic of dosing ratios evaluted for for 2-shot ED immunization. (**I-M**) C57BL/6J mice (*n*=5 animals/group) were immunized with 10 μg N332-GT2 trimer and 5 μg SMNP adjuvant according to the dosing schemes in (**J**), and total GC B cells (**K**), Tfh cells (**L**), and trimer-specific GC B cells (**M**) were analyzed by flow cytometry on day 14. (**N**) Frequencies of GC B cells recognizing intact trimer antigen for bolus, optimized 2-ED, and 7-ED regimens. Points represent responses of individual animals while bars indicate mean± s.e.m. Shown are data from one representative of two independent experiments for each immunization series. ****, $p < 0.0001$; ***, $p < 0.001$; **, $p < 0.01$; *, $p < 0.05$; ns, not significant; by one-way ANOVA with Dunnett's multiple comparison post test compared to bolus immunization.

Motivated by these findings, we next evaluated the impact of the dosing ratio (the proportion of total vaccine administered at dose 1 vs. dose 2, **Fig. 4-1J**). Administration of 12 or 20% of the vaccine in the first dose led to similar total GC, trimer-binding GC B cells, and Tfh responses, while increasing the initial immunization to 30 or 50% of the total dose led to decaying responses (**Fig. 4-1K-M**). Notably, this optimized 2-dose regimen administering 20% of the vaccine at day 0 and 80% at day 7 (hereafter, 2-ED) induced similar responses as administration of 2 full vaccine doses a week apart, suggesting that additional antigen at the first dose cannot further augment the GC response (**Fig. 4-S1D-H**). The enhanced elicitation of antigen-binding GC B cells elicited by two-dose ED priming reflects a combination of increased size of the GC as well as an increased proportion of GC B cells recognizing intact antigen (**Fig. 4-1N**). Altogether, these data demonstrate that even a minimal two-dose extended priming immunization augments multiple facets of the humoral response to vaccination.

4.3.2. Optimized 2-dose ED priming amplifies the magnitude but does not alter overall lifetime of the GC response compared to bolus immunization

We next assessed the evolution of the B cell response over time for the optimized 2-ED regimen compared to bolus immunization to evaluate potential differences in the temporal dynamics or lifetime of the GC in each case (**Fig. 4-2A**). Trimer-binding B cells were detectable in both groups at day 7 and peaked at day 14, but total antigen-binding B cells were 5-fold greater in the 2-ED group compared to bolus (**Fig. 4-2B**). Interestingly, despite the difference in initial vaccine dose administered, GC responses for bolus and 2-dose ED are similar at day 7, but diverged at day 14 (**Fig. 4-2C**). At this timepoint, the GC response for the 2-ED group continued to expand and followed a temporal trajectory distinct from the bolus immunization. The number of Tfh cells in the 2-ED group also sharply expanded between day 10 and 14 (**Fig. 4-2D**). At the peak of the response at day 14, 2-dose ED vaccination elicited ~6-fold greater numbers of Tfh cells compared to bolus immunization. Trimer-binding GC B cell numbers peaked for both immunization conditions at day 14, and the 2-ED

regimen maintained higher levels of antigen-specific GC cells compared to bolus immunization through day 21 (**Fig. 4-2E**). These data demonstrate that a two-dose escalating prime immunization alters the magnitude but not the lifetime of the GC response.

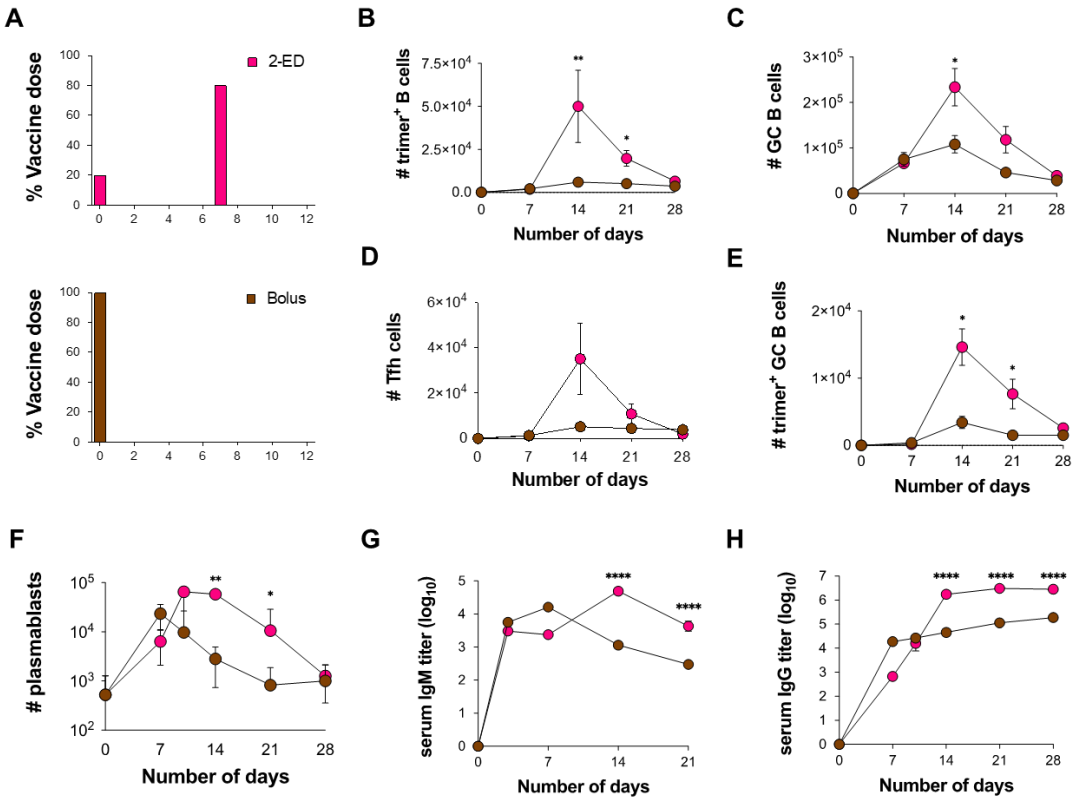

Figure 4-2. Optimized 2-shot prime immunization amplifies the GC response and trimer-specific serum antibody titers over time compared to bolus immunization.
(**A**) Schematic of dosing schemes. (**B-H**) C57BL/6J mice (*n*=9 animals/group) were immunized with 10 μg N332-GT2 trimer and 5 μg SMNP adjuvant according to the dosing schemes in (**A**)**.** GC responses were evaluated on days 7, 14, 21, and 28 by flow cytometry and antibody responses by ELISA on days 3, 7, 14, 21, and 28. Shown are trimer-specific B cell counts (**B**)**,** GC B cell counts (**C**)**,** Tfh cell counts (**D**)**,** trimer-specific GC B cell counts (**E**)**,** plasmablast counts (**F**)**,** trimer-specific IgM titers (**G**)**,** and trimer-specifc IgG titers (**H**)**,** plotted over time for bolus and 2-ED regimens. Shown are data from one independent experiment for each immunization series. ****, $p < 0.0001$; ***, $p < 0.001$; **, $p < 0.01$; *, $p < 0.05$; ns, not significant; by two-way ANOVA with Dunnett's multiple comparison post test compared to bolus immunization.

Lymph node plasmablasts were expanded by day 7 for both the bolus and 2-ED immunizations; these responses peaked at day 7 and day 10, respectively, then steadily decayed (**Fig. 4-2F**). ED immunizations also impacted the evolution of serum antibody responses. IgM responses primed by bolus immunization peaked at day 7 then decayed steadily, while the 2-ED group elicited IgM responses that peaked later, at day 14 (**Fig. 4-2G**). Bolus immunization elicited substantial serum IgG titers by day 7 which rose only slightly over the subsequent 3 weeks (**Fig. 4-2F**). By contrast, IgG

responses for the 2-ED regimen increased sharply between day 7 and day 14, reaching levels ~10-fold greater than the bolus group by day 28 (**Fig. 4-2H**). Hence, the simplified 2-dose ED regimen elicited changes in the humoral response that persisted over many weeks and primed strong, stable serum antibody responses greatly increased over traditional bolus immunization.

4.3.3. Extended-prime dosing regimens boost innate inflammation in lymph nodes and allow for improved T cell responses

We next sought to understand the mechanisms underlying the substantial amplification of the humoral immune response obtained by 2-ED prime relative to traditional bolus immunization. A strong correlation between the number of Tfh and GC B cells has been observed in prior studies [32,33], and is consistent with selection by Tfh cells serving as a key bottleneck controlling proliferation of GC B cells[13,14,34,35]. We hypothesized that the relative kinetics of antigen and adjuvant availability during ED vs. bolus immunization could substantially impact steps in the priming of Tfh cells. To test this idea, we developed a coarse-grained kinetic computational model of the innate immune response and T cell priming following vaccine administration (**Fig. 4-3A, Fig. 4-S2A**). Briefly, in this simple model, both antigen (Ag) and adjuvant (Adj) appear as a bolus at an initial administered concentration and clear from the tissue at a constant rate. The adjuvant activates tissue cells at the immunization site and/or draining lymph node, which release cytokines and chemokines that recruit dendritic cells (DCs). Adjuvant also plays an important role in activating DCs and promoting antigen uptake by these cells[36]. As a proxy for these effects, we assume that the adjuvant increases the rate of antigen uptake by DCs and induces DC activation in an Adj and Ag concentration-dependent manner. Activated, antigen-loaded DCs (aDC^{Ag+}) then prime T cells in the draining lymph node. The proliferation of T cells induced by the Ag^+ DCs is described according to a previously reported model[37], and we assume proliferating T cells differentiate into Tfh cells at a constant rate. This minimal model is easily interpretable and has a small number of parameters, most of which can be estimated from previous experimental studies (See **Methods** and **Table 4-S2** for the details on parameter estimation)[38].

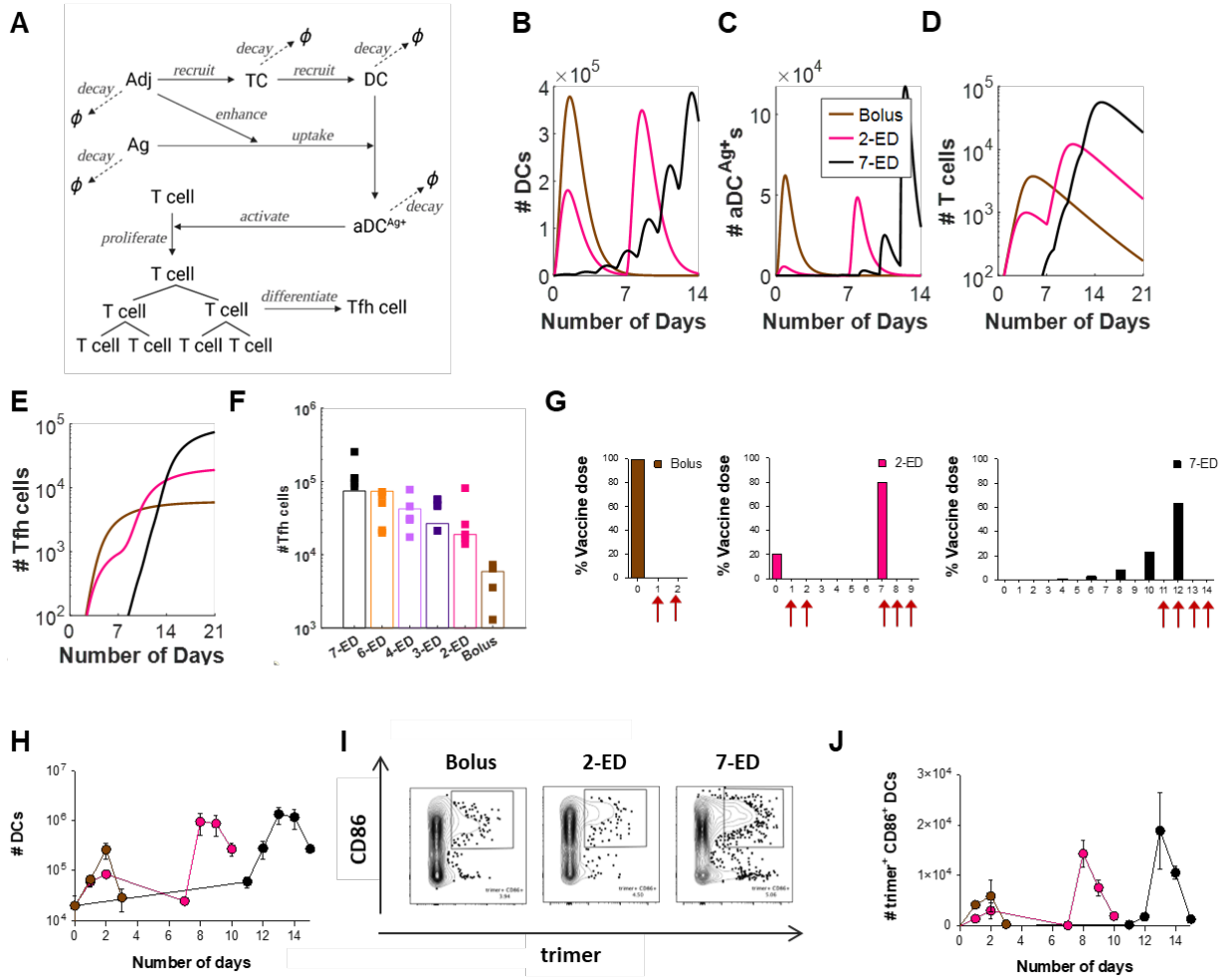

Figure 4-3. In Silico modeling predicts enhanced T cell priming with extended-prime immunization, consistent with experimental measurements of DC antigen acquisition and activation in draining lymph nodes.

(**A-F**) Computational model of vaccine uptake by dendritic cells and helper T cell priming. (**A**) Schematic outlining elements of the kinetic model. (**B-E**) Modeling predictions of the number of (**B**) total DCs (**B**), Ag^+Adj^+ DCs (**C**), Ag-specific T cells (**D**), and Tfh cells (**E**) for bolus, 2-ED, or 7-ED immunization regimens. (**F**) Comparing Tfh cell count predicted by the model with the experimental data at day 14. (**G-J**) Experimental analysis of lymph node DC antigen uptake and activation. C57BL/6J mice (n=3 animals/group) were immunized with 10 μg Cy5 dye-labled-N332-GT2 trimer and 5 μg SMNP adjuvant according to the dosing schemes shown in (**G**), and DCs in draining lymph nodes were analyzed by flow cytometry on days indicated by arrows. Shown are number of DCs (**H**), representative histograms of trimer antigen fluorescence and CD86 expression by $CD11c^+$ DCs (**I**), and number of $trimer^+CD86^+$ DC counts over time for bolus, 2-ED, and 7-ED immunization regimens (**J**).

We first examined model predictions of the number of total DCs, Ag^+ activated DCs, antigen-specific proliferating T cells, and Tfh cells following bolus, optimal 2-ED, and 7-dose ED immunization schemes (**Fig. 4-3B-E**). This analysis revealed that for bolus immunization, levels of total DCs and activated, antigen-loaded DCs peak within ~1 day and rapidly decay due to rapid adjuvant and antigen clearance (**Fig. 4-3B-C**). By contrast, with 7-ED dosing, waves of DC recruitment induced by

the sequential doses leads to DC accumulation in lymph nodes from day ~10 onwards (**Fig. 4-3B**). A significant number of DCs are already present when the final dose of standard ED is given at day 12, which leads to very efficient generation of aDC^{Ag+} toward the end of the dosing course (**Fig. 4-3C**). Because T cells proliferate exponentially, extended stimulation by Ag^+ DCs during the 7-ED regimen contributes to the substantially greater peak antigen-specific T cell expansion and Tfh production compared to the bolus (**Fig. 4-3D-E**), consistent with previous studies[37,39]. The model suggests that the 7-ED regimen also benefits from efficient generation of aDC^{Ag+}. Unlike bolus immunization, where antigen decays before most DCs are recruited, a substantial number of DCs are already present in the lymph node when the final dose of 7-ED regimen is given on day 12. This leads to a predicted prominent increase in the number of aDC^{Ag+}s (**Fig. 4-3B-C**). For the 2-ED regimen, the model predicts T cells proliferate after the 1st dose, and remain at elevated numbers at the time of the second dose (**Fig. 4-3D**). This expanded pool of antigen-specific T cells will then continue to expand on stimulation with the second dose of vaccine. However, with realistic biological parameters, this simple model predicts that DC numbers elevated after the first dose returns to baseline before the second dose (**Fig. 4-3B**).

We next modeled each of the escalating-dose regimens tested in **Fig. 4-1C**, and found that the model indeed captured the pattern of Tfh responses observed experimentally (**Fig. 4-3F**). Further, the model correctly predicts the enhanced Tfh response elicited by a day 0/day 7 two-dose vaccination (**Fig. 4-3F**). Because of the relationship between adjuvant and DC recruitment/activation, the model also predicts that optimal ED immunization requires co-administration of antigen and adjuvant across the time course- if antigen is administered in an escalating-dose pattern but adjuvant is administered as a bolus, poor synchronization of DC recruitment and antigen availability is predicted, and thus weak Tfh priming despite escalating dose antigen administration (**Fig. 4-S2B-C**). In agreement with this prediction, vaccination of mice with a bolus adjuvant/7-ED antigen dosing schedule elicited much weaker GC and Tfh responses than escalating dosing of antigen and adjuvant together (**Fig. 4-S2D-E**). Thus, this very simple model captures the relative magnitudes of increased Tfh expansion observed for the two ED regimens compared to traditional bolus immunization.

In order to further interrogate the predictions of the kinetic model, we immunized mice with fluorescently-labeled N332-GT2 trimer and SMNP adjuvant using ED or bolus dosing schemes, and analyzed DCs in the draining lymph node at key time points post immunization (**Fig. 4-3G, Fig. 4-S3**). After bolus immunization, both the total number of DCs and activated ($CD86^+$) $trimer^+$ DCs in LNs increased over 2 days (**Fig. 4-3H-J**). The initial dose of 2-ED also expanded activated antigen-loaded DCs over the first two days, though at a lower level, and returned to baseline by day 7 when the

second dose was administered, as predicted by the model (**Fig. 4-3H,J**). Interestingly for the 2-dose regimen, although the number of DCs in LNs return to the baseline as predicted by the model, the kinetics of DC influx after the 2nd dose are much faster than after the 2nd shot of the regimen, with antigen-bearing activated DCs numbers notably increased as early as 24h post injection (**Fig. 4-3I, J**). For the 7-ED regimen, lymph node DCs did not show substantial accumulation until day 12– when the final dose was administered– and continued to sharply accumulate to peak levels of trimer-specific CD86+ DCs at day 13 more than double that achieved in the bolus immunization and more than 2 dose ED, as predicted by the model (**Fig. 4-3I-J,** also compare **Figs. 4-3J** and **4-3C**). We note that while the accumulation of antigen-loaded DCs is not substantially measurable before day 12, even a small number of antigen-loaded DCs may initiate T cell proliferation from the baseline, as suggested by the model (**Fig. 4-3C-D**). Given the exponential nature of T cell proliferation, such early proliferation can have considerable importance.

4.3.4. Computational modeling of the GC response predicts improved native antigen capture following extended-prime immunizations

Using a computational model of the germinal center reaction, we previously predicted that ED immunization can increase the size of the GC response via capture of antigen on follicular dendritic cells (FDCs)[19]: initial vaccine doses in the ED regimen trigger initial B cell priming, and 7-10 days after the start of dosing, affinity-matured antigen-specific antibodies will begin to be produced. During ED immunization, antigen is still being delivered to the lymph node at this time point, and these newly produced antibodies form immune complexes with incoming antigen and facilitate its transport to FDCs, where it can promote expansion of the GC response. However, in the present studies we found that ED dosing also dramatically enhances the proportion of GC B cells that bind to the intact immunogen (10-fold and 5-fold vs. bolus for standard ED and 2-dose ED, respectively, **Fig. 4-1N**). In other work, we recently showed that extracellular protease activity in lymph nodes can play an important role in modifying B cell responses, as extracellular antigen accumulated in lymph nodes following bolus vaccination undergoes rapid proteolytic degradation over a period of a few days[40]. This antigen breakdown occurring in sinuses and extrafollicular regions of the node limits the quantity of intact antigen available to B cells and creates immunogen breakdown products that can prime competitive off-target B cell responses. However, protease activity was found to be low in B cell follicles, and antigen captured by FDCs during ED immunization led to a much greater accumulation of intact antigen in follicles for escalating dose vs. traditional bolus immunization[40].

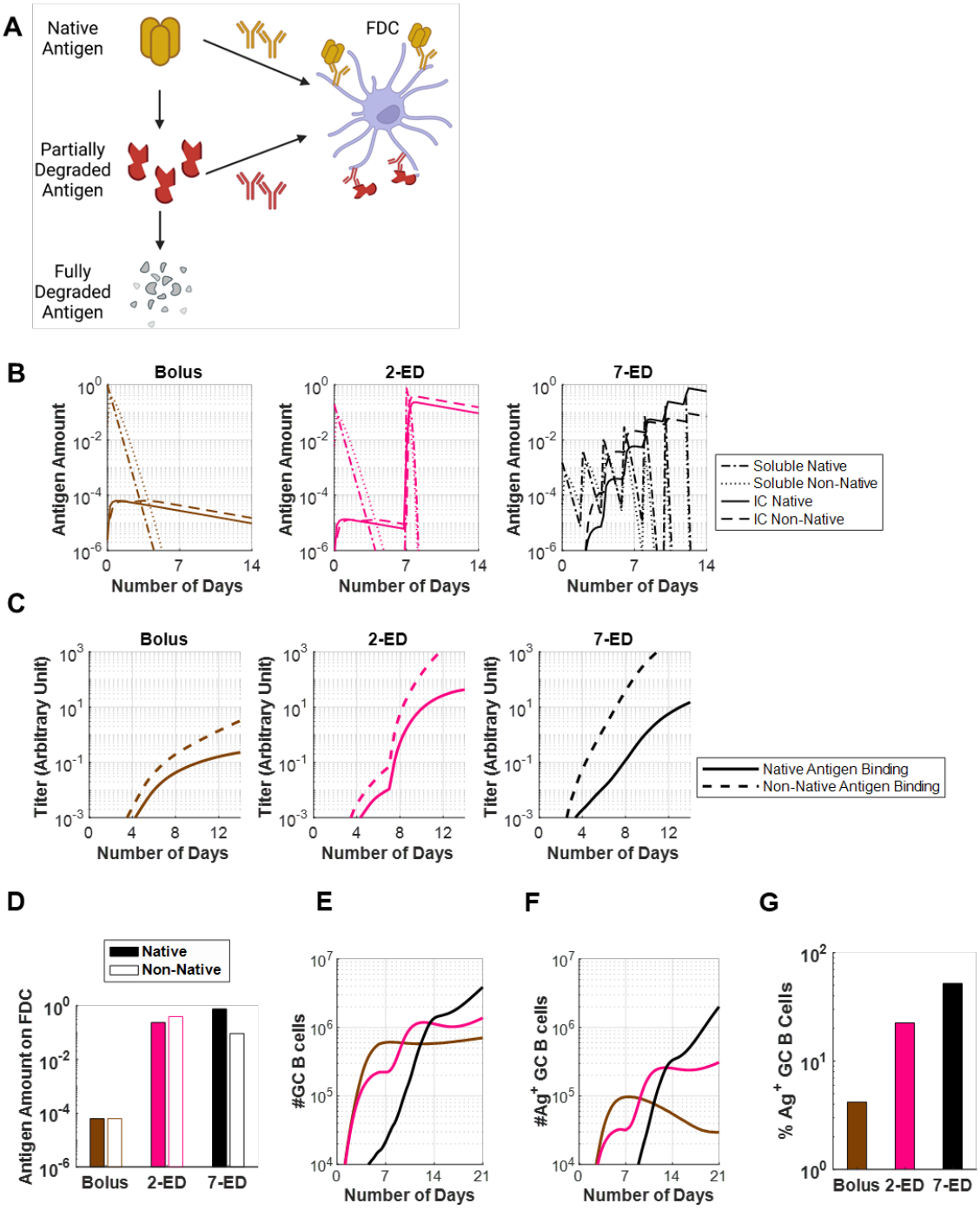

Figure 4-4. *In Silico* modeling predicts increased intact antigen accumulation on FDCs for extended dosing compared to bolus immunization.

(**A**) Schematic showing antigen fates considered in the computational model. (**B**) *In silico* prediction of the levels of free antigen in lymph nodes over time in an intact ("soluble native") or degraded ("soluble non-native") state, and amounts of native and non-native antigen captured on FDCs in the form of immune complexes ("IC") over time. The antigen amounts are normalized to the total antigen dose in immunization. (**C**) Antibody titers predicted by the *in silico* model for bolus, 2-ED, and 7-ED immunization regimens. In the simulation, antibody

titers are defined as the concentration of antibodies weighted by their affinities, reflecting their capabilities to bind to the antigen. (**D**) Comparison of predicted antigen amounts accumulated on FDCs after the final shot from each dosing scheme, normalized to the total antigen dose in immunization. (**E**) Model prediction for the number of GC B cells over time. (**F, G**) Model prediction for the number of native antigen-binding (i.e. trimer$^+$) GC B cells over time (**F**) and frequency of trimer$^+$ GC B cells at day 21 (**G**) from bolus, 2-ED, and 7-ED immunization schemes. The results reported are mean values from 10 independent stochastic simulations of the lymph node. ****, $p < 0.0001$; by one-way ANOVA with Tukey's multiple comparison post test.

To determine if greater levels of intact antigen captured in follicles could explain the greatly increased proportion of trimer-specific GC B cells detected for ED immunization, we modified our recently developed computational model of the B cell and antibody response[35] (which combines the cellular dynamics of B cell proliferation and GC B affinity maturation with the kinetics of antibody production and antigen capture), to incorporate effects of antigen degradation (see **Methods**). Briefly, we assume that B cells can target either native or partially degraded antigen, as schematically shown in **Fig. 4-4A**. Both types of antigens can be transported to FDCs by the corresponding antibodies that bind to them, where they are protected from further degradation. Additionally, to model the antibody response to HIV Env immunogens, we assume that the non-native antigen is more immunodominant– as HIV Env trimers are heavily glycosylated and present few sites for high affinity antibody binding in the intact state, but are expected to expose more proteinaceous surfaces as they degrade[9].

This revised GC model shows that very small overall amounts of antigen are captured by FDCs following bolus immunization because most of the antigen decays before antigen-specific antibody responses are induced, and very low levels of immune complexes (IC) are formed (**Fig. 4-4B-D**). As a result, highly stringent conditions are maintained for GC B cell survival, resulting in a GC response that is dominated by the immunodominant non-native epitope-targeting B cells, and the frequency of B cells able to bind to native antigen (Ag$^+$ GC B cells) is very low (**Fig. 4-4E-G**). With the 2-dose regimen, a weak antibody response against both the native and non-native epitopes are generated after the first dose (**Fig. 4-4C**). However, upon the second dose, this modest level of antibody is predicted to efficiently form ICs with incoming antigen leading to a dramatic increase in the amount of antigen deposited on FDCs (**Fig. 4-4B,D**). The increased antigen availability weakens the immunodominance hierarchy between the two antigens and leads to a much greater native trimer-binding GC B cell response that expands post-second-dose (**Fig. 4-4E-G**)[35]. Finally, with 7-ED dosing, the antibody titer is already high when the final dose (63% of vaccine dose) is administered on day 12 (**Fig. 4-4B**). Although titer for both types of antigen is high, antigen can be rapidly captured by the high titer of antibodies and move to the follicles where it is protected (**Fig. 4-4C**). Therefore, the ratio of native and non-native antigen presented on FDC is modestly shifted in favor of the former (**Fig. 4-4D**), allowing even better trimer-specific response compared to the 2-dose scheme (**Fig. 4-4E-G**).

Note that native antigen-binding antibody titer at the time of final dose for 7-ED (on day 12) is greater than that for 2-ED at the time of the final dose (on day 7) (**Fig. 4-4C**). These predictions of the GC model align well with the experimentally-measured frequencies of intact trimer-binding GC B cells at day 14 (compare **Fig. 4-4G** and **Fig. 4-1N**).

4.3.5. A two-dose escalating prime increases antigen capture in follicles compared to bolus immunization

A key prediction of the GC computational model is that a sufficient quantity of antibody specific for intact antigen can be produced by day 7 to enable substantial antigen capture on FDCs using the 2-dose escalating prime immunization. As shown in **Fig. 4-2G-H**, antigen-specific IgM and IgG were both detectable in serum by day 7 in the 2-ED regimen. To test the model prediction, we immunized mice with fluorescently-labeled N332-GT2 HIV Env trimer by each of the three dosing schedules, and analyzed the biodistribution of the antigen in lymph nodes via confocal imaging of lymph node histological sections and cleared whole lymph node tissues following bolus or ED immunizations. As seen in prior studies [19,20], both cleared whole LN (**Fig. 4-5A, Fig. 4-S4A-C**) and traditional thin section imaging (**Fig. 4-5B, Fig. 4-S4D**) revealed the presence of substantial amounts of antigen co-localized with FDCs 2 days following the last dose of the full ED regimen, while little if any antigen could be detected 2 days after bolus vaccination. Strikingly, substantial amounts of FDC-localized antigen were also found in draining lymph nodes two days following the second dose of the 2-dose ED immunization (**Fig. 4-5A-B, Fig. 4-S4).** High magnification imaging of the follicles of the ED groups suggested this follicle-localized antigen was associated with FDC dendrites (**Fig. 4-5B**).

Flow cytometry analysis of FDCs recovered from pooled LNs from multiple mice immunized with the different dosing regimens revealed that 2-dose or standard ED immunizations increased the amount of FDC-trapped antigen by 20-fold and 60-fold over bolus immunization, respectively (**Fig. 4-5C-E**). Thus, consistent with the computational model of GC dynamics, even a two-dose escalating prime vaccination is capable of achieving antigen targeting to FDCs and increasing the level of antigen retained within the LN.

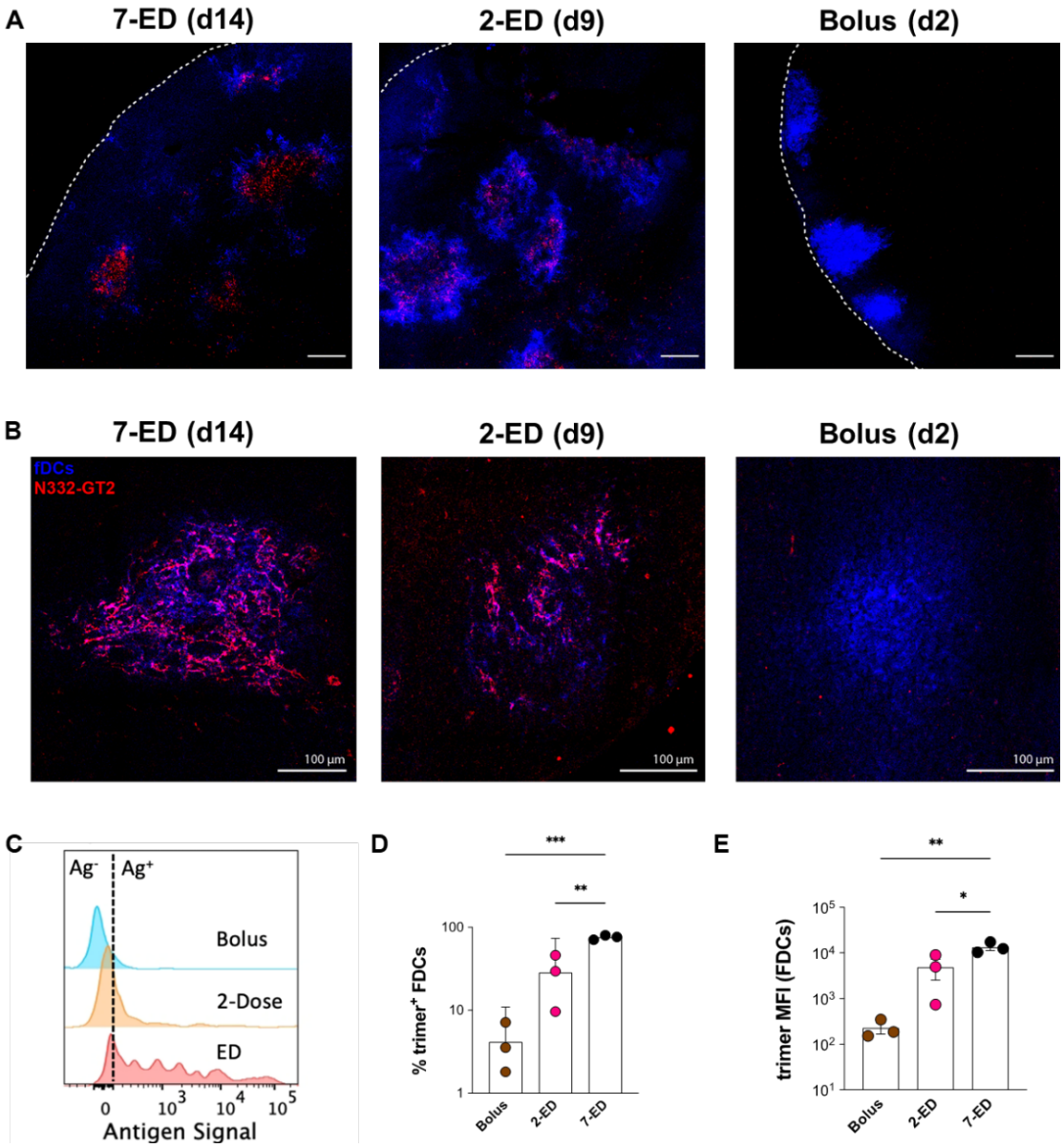

Figure 4-5. Two-dose extended prime immunization enables antigen capture of the second shot on FDCs (**A-B**) Groups of C57Bl/6 mice (n=3 animals/group) were immunized by bolus, 2-ED, or 7-ED regimens as in Fig. 3G followed by collection of lymph nodes for imaging at 48 h after bolus or after the last injection of 2-ED and 7-ED regimens. FDC networks were labeled *in situ* by s.c. injection of anti-CD35 antibody 16h before tissue collection. Collected tissues were clarified and imaged intact by confocal microscopy; shown are maximum intensity projections from z-stacks through FDC clusters (Scale bars, 150 µm), (**A**). Alternatively**,** lymph node sections were stained for FDCs (CD35; blue) and then analyzed by confocal microscopy (Scale bars, 300 µm) to detect co-localization with Cy5-labeled N332-GT2 (pink), (**B**). (**C-E**) Flow cytometry analysis of LN cells (*n*=3 pools/group, with each pool containing six LNs from 3 mice) isolated 48 hr after the final injection following immunization with fluorescently labeled N332-GT2 (10 ug) and SMNP (5 ug) using either bolus, 2-ED, or 7-ED dosing regimens. Shown are representative histograms of antigen intensities among LN cells (**C**)**,** frequencies of trimer+ FDCs (**D**)**,** and the mean trimer fluorescence intensity among trimer⁺ FDCs (**E**) for the indicated immunization conditions. Shown are data from one independent experiment for each immunization series. ****, $p < 0.0001$; ***, $p < 0.001$; **, $p < 0.01$; *, $p < 0.05$; ns, not significant; by one-way ANOVA with Dunnett's multiple comparison post test compared to bolus immunization.

4.3.6. Extending antigen availability on the second immunization further boosts humoral responses as a consequence of innate immune activation and Tfh help

Given that the computational model of the GC reaction is able to provide qualitatively accurate predictions of the observed GC size and proportion of antigen-specific GC B cells, we next used the model to explore a much wider parameter space of dosing patterns than would be possible experimentally, to gain further insight into how humoral responses might be further bolstered using extended priming. The modeling and experimental data suggest that having a high trimer-binding antibody titer present before the majority of the antigen dose is cleared is an important factor governing the magnitude of the "on target" GC response. In the 2-dose extended prime immunization, antibody titers increase steadily after the 2nd injection (**Fig. 4-2H**). However, because intact antigen in the lymph node decays rapidly (estimated half-life ~6.2 hours, **Table S1**), most of the antigen arriving after the second immunization decays before high titers of antibody are reached, limiting immune complex formation and subsequent antigen capture by FDCs. Thus, we hypothesized that extending antigen availability over a longer time period at the second dose might substantially enhance GC responses. We thus simulated a 2-dose ED regimen where antigen was released from the injection site at a constant rate over 10 days after the second injection (**Fig. 4-6A**). In this case, a significant fraction of the antigen dose arrives at the dLN after high titer levels of trimer-specific antibody are generated and is thus captured in immune complexes in an intact state (**Fig. 4-6B-C**). Compared to 2-ED dosing using bolus injections, the fraction of intact antigen among ICs increases from ~38% to 92% with the slow-release second dose (**Fig. 4-6D**). Thus, the model predicted that such a scheme may lead to a superior trimer-specific GC B cell response compared to the 2-dose immunization (**Fig. 4-6E-F**). Varying the duration of antigen delivery after the second dose shows that a longer release duration leads to higher fraction of native antigen on FDCs (**Fig. 4-6G**) and better trimer-specific GC B cell response (**Fig. 4-6H-I**), highlighting the importance of dosing kinetics.

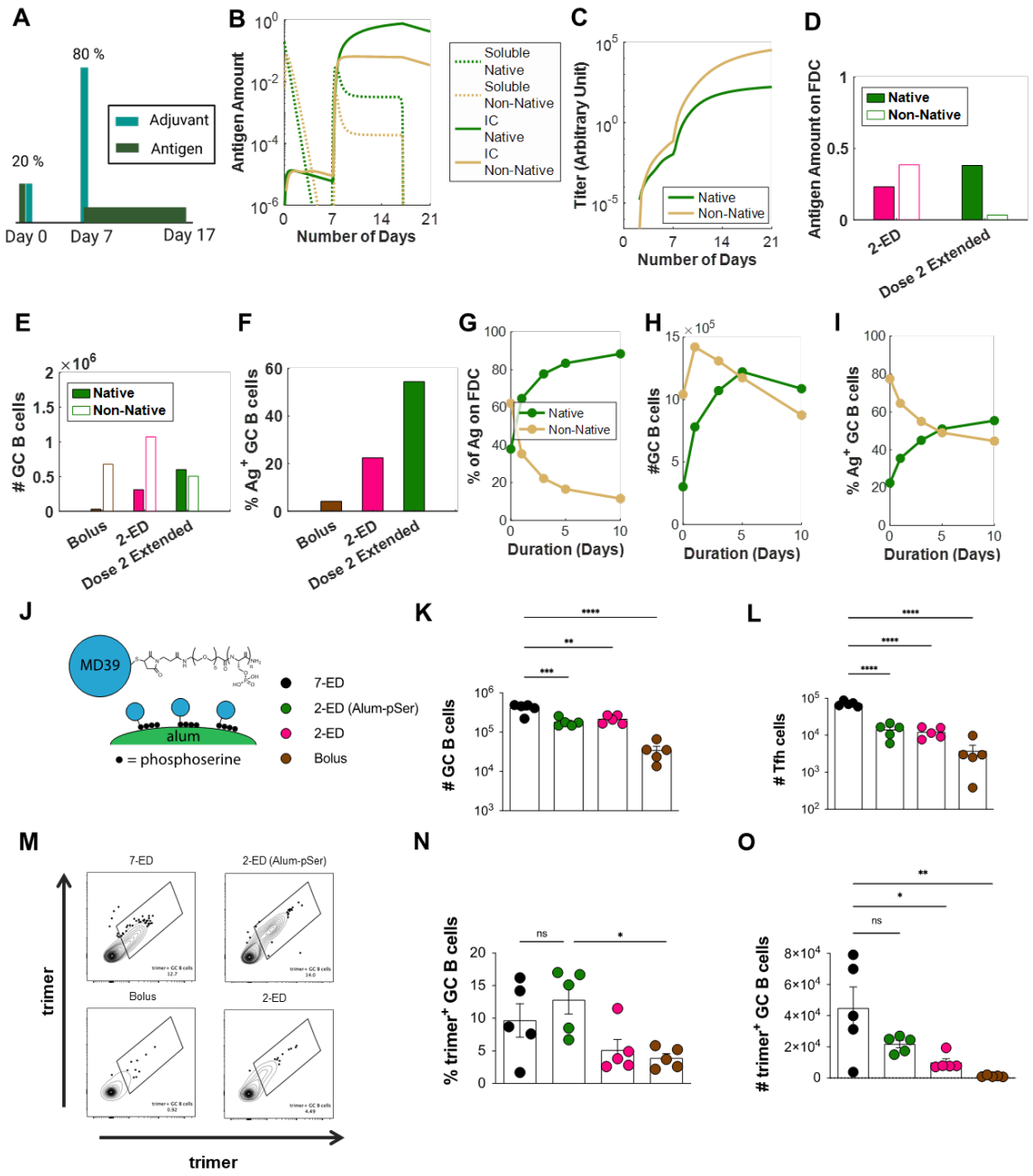

Figure 4-6. Extending the duration of antigen delivery during the second dose of 2-ED vaccination increases native antigen capture on FDCs and antigen-specific GC responses

(**A-I**) Computational modeling of GC responses elicited by 2-ED dosing administered as two bolus doses vs. a bolus on day 0 and a prolonged antigen delivery at day 7 ("dose 2 extended"). (**A**) Schematic of 2-ED vs. "dose 2 extended" vaccination regimens. (**B, C**) Amounts of free and immune-complexed native or degraded ("non-native") antigen in the LN over time (**B**) and serum antibody titers recognizing native vs. non-native antigen (**C**) for the "dose 2 extended" regimen. (**D-F**) *In silico* prediction of antigen captured on FDCs (**D**), total GC B cells at day 21 (**E**), and frequency of trimer-binding GC B cells at day 21 (**F**) for bolus, 2-ED, and "dose 2 extended" vaccination regimens. (**G-I**) *In silico* prediction of proportions of intact vs. degraded antigen captured by FDCs (**G**), total number of GC B cells (**H**), and the fraction of GC B cells that are native vs. non-native antigen-binding (**I**) at day 21 as a function of the duration of antigen release used in "dose 2 extended" vaccination. (**J-O**) Experimental testing of "dose 2 extended" immunizations using alum-anchored immunogens. (**J**) Schematic demonstrating anchoring trimer immunogen onto alum via phosphoserine linkers (Alum-pSer). (**K-O**)

C57Bl/6J mice (*n*=5 animals/group) were immunized with 10 μg MD39 trimer (either soluble bound to 50 μg alum) and 5 μg SMNP adjuvant as in Fig. 3G. Shown are the numbers of GC B cells (**K**) and Tfh cells (**L**), representative histograms of trimer staining of GC B cells (**M**), frequencies of trimer-binding GC B cells (**N**), and the number of trimer-binding GC B cells (**O),** for the different dosing regimens determined by flow cytometry at day 14. Shown are data from one representative of two independent experiments for each immunization series. ****, $p < 0.0001$; ***, $p < 0.001$; **, $p < 0.01$; *, $p < 0.05$; ns, not significant; by one-way ANOVA with Dunnett's multiple comparison post test compared to bolus immunization.

To experimentally test this idea, we employed an approach we previously developed[27] to achieve slow-delivery effects in a manner readily translatable to clinical use: a stabilized HIV Env trimer termed MD39[41] (very similar in sequence to the N332-GT2 trimer) was conjugated with short phosphoserine (pSer) peptide affinity tags (one tag per protomer at the C-termini located at the base of the trimer). Phosphate groups in the affinity tags undergo a ligand exchange reaction with the surface of alum particles, enabling oriented high-avidity binding of the trimer to aluminum hydroxide adjuvant (**Fig. 4-6J**). By stably anchoring the antigen to alum particles, on injection, the antigen is slowly released from the injection site as alum particles slowly disaggregate over time[27,31]. Using this simple approach, alum-adsorbed MD39 trimers that normally clear from the injection site within a few days instead clear much more slowly, over ~10 days[27]. We thus tested a two-dose ED immunization giving 20% of the vaccine dose on day 0 as a bolus and 80% of the dose as an alum/pSer-trimer formulation on day 7. Total GC B cells and Tfh cells elicited were similar between the 2-ED and 2-ED (alum-pSer) groups (**Fig. 4-6K-L**). However, relative to the bolus 2-ED immunization, extended antigen delivery provided by alum particle anchoring of the second shot in the 2-ED (alum-pSer) group elicited a 2.4-fold increase in the frequency of intact trimer-binding GC B cells and a 2-fold increase in the absolute number of these antigen-specific cells (**Fig. 4-6M-O**). These observations are consistent with model predictions (**Fig. 6E-F**). Interestingly, using the pSer-alum anchoring approach for both shots of the 2-dose regimen showed no improvement in trimer-specific GC responses over using it on the 2nd shot (**Fig. 4-S5A-C**) indicating that the benefit of constant release of antigen is more relevant once high antibody levels are present to enable capture of the native antigen. *In silico* simulation of this scenario agrees with this experimental observation (**Fig. 4-S5D-E**). Thus, an engineered 2-dose immunization, providing an initial "priming" dose followed by a larger extended-release vaccine dose retains much of the benefit to the GC response and fully amplifies the serum antibody response, substantially greater than bolus immunization.

4.4. Discussions

Germinal center responses are critical to the evolution of diverse and high affinity antibody responses, and the size of the early GC response has been shown to predict the magnitude of neutralizing antibodies generated by HIV Env trimer immunization in rhesus macaques[17]. In previous studies, we discovered that prolonging vaccine availability through extended dosing strategies such as implantable osmotic pumps or repeated injections of a given dose of vaccine over time alters multiple facets of the immune response– increasing the number of B cells entering GCs, the number of antigen-specific Tfh cells generated, and the number of unique clones in the GC, accompanied by increased total antibody titers, memory B cells, and neutralizing antibody production[17,19,20]. In particular, an escalating-dose immunization of 7 shots administered in an exponentially-increasing dose pattern over two weeks was particularly effective in both mice and non-human primates for promoting humoral responses to HIV Env immunogens[19,20,22]. However, administering seven doses is not practical for mass vaccination. Here we sought to better understand the critical elements of this potent dosing strategy, and based on our understanding of the mechanisms of ED-induced B cell responses, we hypothesized that a two-dose immunization, with an initial small dose of antigen to initiate B cell priming followed by a larger second dose that could be given to promote antigen deposition in follicles, might still offer substantial enhancements in humoral responses over traditional bolus vaccination. Such a scenario- two shots administered 1-2 weeks apart, would not be out of the realms of practicality (e.g., compare to current COVID-19 mRNA vaccines, administered twice at a 3- or 4-week interval).

Through systematic studies varying the number of doses, dose ratio, and dose intervals in mice, we found that a two-shot reduced ED regimen, administering 20% of the vaccine dose on day 0 and 80% vaccine dose on day 7 elicited 10-fold increases in peak antigen-binding total B cells and GC B cells, respectively, and increased serum antibody responses 100-fold relative to bolus immunization. Informed by computational modeling of the GC response, we further optimized an extended-release formulation on the 2nd shot by anchoring the antigen onto alum via a phosphoserine linker resulting in even better antigen-specific GC responses over the reduced 2-shot regimen.

Our combined computational modeling and experimental studies revealed that our motivating initial hypothesis was correct, that 2-ED priming promotes substantial antigen capture on FDCs, which is very limited to undetectable following bolus immunization. However, this is not the only effect of the extended-prime dosing. 2-ED immunization also increased Tfh responses (by 6-fold over bolus at the peak of the response), T follicular helper (Tfh) cells are essential for the germinal center

(GC) reaction, providing support to B cells to generate long-lived plasma cells and memory B cells[42–44]. In particular, the 2-shot regimen benefits from the fact that T cells begin to concentrate in GCs 5-8 days post immunization[45,46]. Thus, giving the 2nd shot of greater antigen after the GC has matured has a potent effect on improving the T cell response as compared to giving it at an earlier time point. The 2-shot and standard ED regimens show an increasing number of Tfh cells, supporting this observation. Tfh cell development relies on initial antigen priming of naïve T cells by dendritic cells (DCs)[44], maintenance of Tfh cell phenotype requires sustained antigenic stimulation[33]. The 2-shot immunization leads to a rapid increase in MHC-II$^+$ DCs after the 2nd dose, priming previously activated T cells and allowing pre-GC Tfh cells to develop into GC-Tfh cells, resulting in the improved Tfh response we observed. This approach overcomes the requirement for antigen/adjuvant during the effector phase to achieve optimum Tfh responses since Tfh cells are heavily regulated in the early GC phase [47,48].

We observed that the amplification of GC/Tfh occurs towards the end of the dosing schedule, corresponding to the capture of native antigen on FDCs. Our study results show that an important mechanism underlying the efficacy of extended dosing regimens is the improved capture of native antigen on FDCs. In a reduced 2-shot immunization, administering a majority of the antigen on the 2nd shot allows for exploitation of pre-existing antibody responses from the lower 1st dose to form FDC-targeted immune complexes *in vivo* since the larger dose of immunogen is provided during a window of time when antigen-specific antibody is available for immune complex formation. Extended 2nd shot dosing further takes advantage of the increasing concentration of antibody to improve native antigen capture & consequently boost trimer-specific GC responses since prolonging antigen availability allows the affinity-matured antibodies being produced to bind to native antigen. This leads to even greater capture and retention of intact antigen on FDCs within follicles.

Our synergistic deployment of computational and experimental studies has led to new insights into the fundamental dynamics of antibody development & antigen capture that can have broad implications designing vaccine dosing regimens. With extended dosing, availability of intact antigen in the lymph node is synchronized with the developing GC response. We observed that for the 7-ED regimen, amplification of GC and Tfh cells occurs towards the end of the dosing schedule, corresponding to the timing when antigen capture on FDCs is most prominent. The computational model suggests that an important mechanism underlying the efficacy of extended dosing regimens is the improved capture of native antigen on FDCs. In a simplified 2-shot immunization, administering a majority of the antigen on the 2nd shot allows for exploitation of pre-existing antibody responses induced by the lower 1st dose, maximizing the quantity of the immunogen dose captured in immune

complexes. The computational model further predicts that if antigen is slowly released at 2nd dose, increased representation of antigen in native form on FDC can further promote intact antigen-specific GC responses. This is in contrast to bolus immunization where only a small amount of antigen is presented on FDC to GC B cells, much of which is non-native protein and breakdown products that can be immunodominant and distract the GC response from relevant targets[49,50]. These predictions were positively tested by our experiments. More antigen on FDCs during later stages of a GC likely increases GC B cell clonotypic diversity, allowing for significantly more BCR sequence space to be explored for high affinity BCR mutations.

Several technologies are being developed to recapitulate the effects of the 7-dose ED regimen. Our findings provide a strong rationale for utilizing reduced dosing immunization strategies that promote native antigen capture in the FDC network and enhance humoral responses. Developing a single-shot system that could mimic the effects of extended dosing would greatly improve compliance and increase vaccine coverage in developing countries. We have demonstrated the potential of a 2-shot regimen, but several single-shot approaches, such as microfabrication-based PLGA particles or atomic layer deposition-based technologies, could also achieve this goal. The particles contain vaccine-infused core that can release its cargo at various timepoints based on chemical modifications to the PLGA polymer [51]. Similarly utilizing a slow-dissolving alum coating to unmask and release the vaccine over tunable time periods can alter vaccine kinetics to mimic extended dosing effects [28]. These technologies could be particularly important for generating protective antibody responses against challenging pathogens such as HIV and for generating broadly neutralizing antibody responses against other variable pathogens. However, it is crucial to consider potential toxicities associated with these regimens, as multiple immunizations of potent adjuvants with the standard ED regimen could result in undesirable side effects. Similarly, extended delivery technologies must avoid injection site reactogenicity and chronic inflammation. Collectively, these efforts will establish effective strategies that can be broadly applied in vaccine design to achieve the benefits of extended dosing in real-world vaccines.

To summarize, we have designed an optimized extended two-dose priming approach that improves humoral immune responses to HIV trimers in an attempt to recapitulate responses achieved by the standard escalating dose regimen comprised of 7 doses. Our findings demonstrate our ability to: (i) augment GC and Tfh responses to HIV immunogens; (ii) increase trimer-specific serum antibody titers over bolus immunization; and (iii) highlight the critical role of antigen capture dynamics and priming of DCs in driving the enhanced immune responses.

4.5. Method Details

4.5.1. Experimental Details

Study design

The primary aim of this research was to assess the feasibility of decreasing the number of doses in the standard 7-dose escalating immunization regimen and compare it to bolus immunization in mouse models, while also investigating the underlying mechanisms involved. To achieve this goal, we immunized mice with clinically relevant subunit protein immunogens in combination with saponin adjuvants, and evaluated early (antigen uptake and induction of TFH and GC) and late (lymph node and serum antibody) responses over a period of time. The mechanistic studies conducted focused on examining antigen acquisition and activation of antigen-specific B and T cells, as well as computational analyses of the germinal center response to parse out differences in the dosing regimens.

Immunogens

N332-GT2 trimers were expressed in FreeStyle 293F cells (Invitrogen, Cat no. R79007) and purified in two steps by affinity chromatography using a GE HisTrap column and size-exclusion chromatography using a GE S200 Increase column as described previously [29,52]. MD39 HIV Env trimer was generated as previously described [52]. Both trimers were administered at a dose of 10 ug per animal.

pSer-conjugation

Immunogens were expressed with a free terminal cysteine and reduced by incubation with 10 molar equivalents of tris(2-carboxyethyl)phosphine (TCEP, ThermoFisher) at a concentration of 1 mg/ml, followed by incubation at 25°C for 10 minutes. The reduced protein solutions were then processed using Amicon Ultra Centrifugal Filters (10 kDa MWCO, Millipore Sigma) to remove TCEP, and the resulting protein was mixed with 5 molar equivalents of pSer-maleimide linkers at a concentration of 1 mg/ml for 16 hours at 4°C in tris-buffered saline (TBS, Sigma Aldrich) at pH 7.2-7.4. After the reaction, unreacted pSer linker was removed using centrifugal filters in TBS, and pSer-antigen was buffer exchanged to PBS.

Adjuvant preparation

The saponin adjuvant used in this study was an ISCOM-like self-assembled nanoparticle consisting of Quillaja saponin, cholesterol, DPPC, and MPLA [30]. Briefly, solutions of cholesterol (20mg/ml final concentration, Avanti Polar Lipids Cat# 700000), DPPC (20mg/ml final concentration, Avanti Polar Lipids Cat# 850355), and MPLA (10mg/ml final concentration, PHAD) were prepared in Milli-Q water containing 20% w/vol MEGA-10 (Sigma D6277) detergent. Quil-A saponin (InvivoGen; vac-quil) was dissolved in Milli-Q water at a final concentration of 100 mg/ml. All components were mixed at a molar ratio of 10:10:2.5:1 (Quil-A:chol:DPPC:MPLA) followed by dilution with PBS to a final concentration of 1 mg/ml cholesterol. The solution was allowed to equilibrate overnight at room temperature, followed by dialysis against PBS using a 10k MWCO membrane. The adjuvant solution was then sterile filtered, concentrated using 50k MWCO centricon spin filters, and further purified by FPLC using a Sephacryl S-500 HR size exclusion column. Doses are reported in terms of the amount of saponin administered, calculated by measuring the concentration of cholesterol (Cholesterol Quantitation kit; Millipore Sigma; Cat# MAK043) in the preparation and assuming quantitative incorporation of the saponin during synthesis.

Antigen labeling and characterization

1 mg/mL solution of protein antigen (N332-GT2) in PBS was mixed with an equal volume of 0.2 M sodium bicarbonate buffer (pH 8.4) on ice. A fresh stock solution of Sulfo-Cyanine 5 NHS ester was prepared at a concentration of 1 mg/mL in 0.2 M sodium bicarbonate buffer (pH 8.4) and added to the antigen solution. The mixture was incubated at 4°C for 16 hours, and then desalted twice using a Zeba Spin Desalting column equilibrated in PBS. The labeled antigen was filtered through 0.22 μm pore size Spin-X centrifuge tube filters and stored at 4°C until use. The degree of labeling of the antigen was determined by measuring the absorbance at 280 and 646 nm wavelengths for total protein and Cy5 dye, respectively. The extinction coefficient values of 113215 and 271000 $M^{-1}cm^{-1}$ were used to calculate the concentration of one subunit of N332-GT2 Trimer and sulfo-cy5 NHS ester, respectively. The degree of labeling for soluble antigen was determined by calculating the ratio of antigen concentration to Cy5 concentration.

Mice

All *in vivo* experiments were performed in 8-week-old female C57BL/6J mice (Jackson Laboratory). Experiments were performed in specific pathogen-free animal facilities at the MIT Koch Institute for Integrative Cancer Research. Mice were housed under standard 12-hour light - 12-hour dark conditions with ad libitum access to water and chow. All mouse studies were performed according to institutional and National Institutes of Health (NIH) guidelines for humane animal use and in accordance with the Association for Assessment and Accreditation of Laboratory Animal Care. Protocols were approved by the Institutional Animal Care and Use Committee (IACUC) at MIT.

Immunizations and sample collections

8-week-old female C57BL/6 mice were anesthetized and immunized with 10 μg of indicated antigens (N332-GT2 trimer or MD39 trimer) in the presence of 5 μg saponin adjuvant (SMNP) subcutaneously at the left and right sides of the tail base. In the case of the pSer-conjugated MD39 trimer antigen, immunizations were prepared by mixing 10 μg of antigen and 100 μg of alum in 100 μl of sterile TBS (Sigma-Aldrich, catalog no. T5912) per mouse unless otherwise specified. Antigen was loaded onto alum for 30 min on a tube rotator after which 5 μg of SMNP was added into the immunization and incubated with antigen-alum formulations for 30 min before immunization. This dose of SMNP corresponds to 5 μg of Quil-A and 0.5 μg of MPLA. Blood (from submandibular; 100 μL) was collected at indicated time-points into serum separator tubes (BD Corporation) and centrifuged at 4,000 × g for 10 min at 4 °C. Sera extracted from blood samples were stored at −80 °C until ready for analysis. Inguinal LNs were harvested and added to Eppendorf tubes containing Protease inhibitor buffer (containing protease inhibitor cocktail and EDTA in PBS with 2% FBS). LNs were processed using a pestle and centrifuged at 16,000g for 5 min at 4 °C to pellet the cell/tissue debris. Supernatant was transferred to Spin-X tubes (Corning™ Costar™) and centrifuged again for 5 min with the flow through being transferred to final collection tubes, flash frozen and stored at −80 °C until ready for analysis.

ELISA

To analyze on-target antibody response, high-binding ELISA plates (07-200-37, Fisher Scientific) were coated with 1 mg/ml trimer and blocked with 2% BSA in PBS overnight. To detect antigen-specific IgG responses, dilutions of serum or lymph node aspirate were added to the wells and incubated for 1.5 hours at 25°C. Plates were washed three times in PBS containing 0.2% Tween-20,

and then anti-mouse IgG secondary antibody conjugated to HRP (172-1011, Bio-Rad Laboratories), diluted 1:5000 in blocking buffer as per manufacturer instructions, was added to the wells. After 1 hour of incubation, plates were again washed, developed with TMB, and the reaction was stopped with sulfuric acid. The optical density of the mixture was read out at 450 nm minus the absorbance at 540 nm according to the manufacturer's instructions.

Immunofluorescence staining

Inguinal lymph nodes (LNs) extracted from euthanized mice were submerged into cryomolds containing O.C.T. (23-730-571, Fisher Scientific) compound and dipped into 2-methylbutane (M32631, Millipore Sigma) pre-chilled in liquid nitrogen. All frozen tissues were cryosectioned on a Leica CM1950 at 10 μm thickness, adhered to Superfrost Plus microscope slides (12-550-15, Fisher Scientific), and stored in -80°C until use. Frozen sections were retrieved from -80°C, quickly thawed, and incubated in 4% paraformaldehyde for 10 minutes at 25°C. The sections were washed 3 times in PBS with 10-minute incubation time between each wash. Excess PBS was removed after the final wash before incubating the slides in blocking buffer, comprised of 2% BSA and 2% Triton X-100 in PBS. After 30 minutes, the blocking buffer was aspirated and the slides were stained in 1:75 anti-CD35 (740029, BD Biosciences) primary antibody solution also made in blocking buffer for ~16 hours at 4°C. These slides were washed in PBS 3 times for 10 min, stained with 1:200 diluted secondary antibodies solution in blocking buffer (ab150063 Abcam, ab150061, Abcam) for 4 hours at room temperature, and washed again in PBS. To mount the slides, one drop of ProLong Diamond Antifade Mountant (Thermo) was added directly onto the stained tissues prior to gently placing a 20x20 mm coverslip on top of the droplet to sandwich the section. The coverslip was sealed using CoverGrip coverslip sealant (23005, Biotium) and imaged immediately.. For all experiments, imaging was performed on a Leica SP8 confocal microscope equipped with a white light laser and spectral emission filter to detect emission wavelengths between 470 and 670 nm with a minimum bandwidth of 10 nm. All images were recorded with a 25X water immersion lens and a 63X oil immersion lens for assessing antigen drainage in the LNs, laser settings were kept constant across different time points for each immunogen.

Whole tissue imaging

For whole tissue imaging, mice were injected with anti-CD35 BV421 antibody (clone 8C12) and lymph nodes were isolated after 16 hours and fixed overnight in 4% paraformaldehyde. Lymph nodes were then processed with a modified DISCO protocol as previously described [53]. Briefly, the nodes were washed twice in PBS and excess fat and connective tissue was removed. Nodes were then gradually moved into solutions containing successively high concentrations (20, 50, 80%) of methanol for 30 mins, until they were incubated for half an hour in pure methanol. Nodes were then bleached for 2 minutes in hydrogen peroxide and returned to methanol for half an hour. They were then gradually moved into solutions containing increasing concentrations of tertiary-butanol (20, 50, 80%) before eventually being incubated in pure tertiary-butanol for one hour at 37° C. All solutions used after bleaching contained an additional 0.4% α-tocopherol (vitamin E). Nodes were then removed from solution and allowed to dry completely before being placed in dichloromethane for delipidation. After the 8 lymph nodes dropped to the bottom of tubes following swirling (indicating removal of remaining tertiary-butanol), they were stored in dibenzyl ether with 0.4% α-tocopherol, which was used as a refractive index matching solution. Cleared lymph nodes were imaged using an Olympus FV1200 Laser Scanning Confocal Microscope at 10x magnification. Lasers were set to minimize pixel saturation in the brightest samples. All laser and channel settings were then kept constant across groups for direct comparison between different samples. Each lymph node was imaged over a depth of 300 μm with line average of 3. FDC occupancy calculations were performed with a MATLAB script, where images for each channel were smoothed with a 3-D Gaussian filter (sigma = 0.5), then binarized into a mask to identify follicle or antigen area. The fraction of FDC area occupied by antigen was achieved by calculating overlapping pixels in the two binary masks. This calculation was performed for each individual image in the z-stack (9 per image), as well as for the z-projection (sum of slices).

Flow Cytometry Analysis of Lymph Nodes.

Inguinal lymph nodes were harvested and single-cell suspensions were obtained by passage of the lymph nodes through a 70-μm filter (BD Biosciences). The isolated cells were stained with Live/Dead fixable aqua stain (L34957, Thermo Fisher Scientific) for 10 min at 25°C before washing twice in flow cytometry buffer. Cells were then incubated with Fc block for 10 min at 4°C before staining with antibodies listed (see the supplementary materials) for 20 additional min at 4°C. For trimer specific GC B cell analysis, cells stained with antibodies were distributed evenly and exposed to biotinylated trimer preincubated with streptavidin (30 min at molar ratio of 1:4 at 25°C)

conjugated to phycoerythrin (405203, BioLegend) and/or BV421 (405226, BioLegend). Flow cytometry was carried out on a BD LSR Fortessa or LSR II. Plasmablasts were gated as live/single, B220 int, $CD138^+$.

Statistical analysis

Statistical analysis and graphing were done with GraphPad Prism. The two-tailed Student's *t* test was used to compare two experimental groups and one-way Anova with Tukey's post hoc analysis was used for comparing more than two groups. Details of the statistical test and number of replicates are indicated in the figure legends. A value of $P<0.05$ was considered statistically significant.

4.5.2. Computational Details

The coarse-grained model of T cell priming by antigen and adjuvant was formulated by integrating insights from experimental literature [54–60] with a model of T cell proliferation previously published [61]. The system of ordinary differential equations is summarized in Fig. 4-S2A, and a detailed description of the model and parameters is provided in Supplementary Materials. The model of the GC B cell response was adapted with minor modifications from chapter 2, also published in Yang et al. [62]. Though some details overlap with Chapter 2, we still present a comprehensive overview of the model, including the equations and parameters, that is sufficient for independent understanding and reproducibility of the enable self-sufficient understanding and reproduction.

Model of T cell priming

We constructed our model based on the biological observations of the mechanism of action of adjuvants [54–60]. Upon administration of adjuvants, local tissue-resident cells such as neutrophils and macrophages are recruited to the site of vaccine administration and draining lymph nodes. These cells release cytokines and chemokines, which serve as chemotactic agents for dendritic cells (DCs). As a result, DCs migrate to the sites and take up antigen. The presence of adjuvant significantly enhances this process. Adjuvant facilitates the maturation of DCs, ensuring a more efficient antigen [59], and aids in the delivery of antigen to the DCs [54]. Following the antigen uptake, the activated DCs present peptide-major histocompatibility complex (pMHC) molecules to CD4 T cells in lymph nodes. This interaction leads to the proliferation of CD4 T cells and initiates their differentiation into Tfh cells [63].

In the model, the concentrations of antigen and adjuvant rise upon administration and subsequently decay according to first-order kinetics, consistent with previous models [61,62,64]. If the dosing scheme involves n doses given at times $t_1, \ldots t_n$ and the amount of antigen and adjuvant given with each dose is $f_1, \ldots f_n$, the differential equations that govern their concentrations are as follows:

$$\frac{d[Ag]}{dt} = \sum_{i=1}^{n} f_i \delta(t - t_i) - d_{Ag}[Ag] \qquad \text{(Equation 1)}$$

$$\frac{d[Adj]}{dt} = \sum_{i=1}^{n} f_i \delta(t - t_i) - d_{Adj}[Adj] \qquad \text{(Equation 2)}$$

where $\delta(t - t_i)$ is the Dirac delta function, whose value is zero everywhere except at $t = t_i$, and whose integral over the domain that includes $t = t_i$ is equal to one.

The recruitment of tissues cells (TCs) and their decay are modeled as:

$$\frac{d[TC]}{dt} = \frac{[Adj]}{S_{Adj} + [Adj]} - \mu[TC] \qquad \text{(Equation 3)}$$

where the first term stands for the activity of the adjuvant with S_{Adj} being the half-max adjuvant concentration. The activity increases with adjuvant concentration when $S_{Adj} > [Adj]$ but saturate when $S_{Adj} \ll [Adj]$. Employing a saturation function to represent biological activity is widely adopted [61,62,65]. We pick a small value for S_{Adj} based on the observation that there is not a big difference between the numbers of DCs recruited after full dose and 20 % of the dose (Fig. 4-S3H). μ is the decay rate, assumed to be identical for all innate immune cells for simplicity. Its value is taken from Mayer et al. [61]

The recruitment of DCs by the TCs and their activation and antigen uptake are modeled as:

$$\frac{d[DC]}{dt} = D_0[TC] - \left(1 + k\frac{[Adj]}{S_{Adj} + [Adj]}\right)[DC][Ag] - \mu[DC] \qquad \text{(Equation 4)}$$

$$\frac{d\left[aDC^{Ag^+}\right]}{dt} = \left(1 + k\frac{[Adj]}{S_{Adj} + [Adj]}\right)[DC][Ag] - \mu\left[aDC^{Ag^+}\right] \qquad \text{(Equation 5)}$$

where aDC^{Ag^+} represent activated antigen-primed DCs. Here, D_0 acts as a scaling factor and its value is derived from the best fit of model prediction to experimental data in Fig. 4-3F. The parameter k quantifies the extent to which the adjuvant's activity expedite antigen uptake by the DCs. Given the recognized role of adjuvants in promoting antigen uptake, we set k to be large.

The activated antigen-primed DCs induce the proliferation of CD4 T cells, which we assume to differentiate into Tfh cells according to first-order kinetics:

$$\frac{d[T]}{dt} = \alpha \frac{[aDC^{Ag^+}][T]}{[T] + [aDC^{Ag^+}]} - \eta([T] - T_0) \quad \text{(Equation 6)}$$

$$\frac{d[T_{FH}]}{dt} = \eta([T] - T_0) \quad \text{(Equation 7)}$$

where α is the maximum proliferation of the T cells, and η is the rate at which proliferating T cells differentiate into Tfh cells. The model of T cell proliferation, including its parameter values, is derived from Mayer et al. [61], which encompasses T cell proliferation and death. In this study, rather than accounting for death, we model the process as T cells migrating for differentiation [66].

See Table S2 for the summary of model parameters and their values.

Model of B cell response

Overview of the Model

We adapted and refined the B cell response model from a study previously published [62], where an in-depth description of the rationale for model development, alternative model structure exploration, and parameter sensitivity analysis can be found. Here, we present a concise overview of the model as applied in our study, including the equations and parameters necessary for reproducing the results. Additionally, we have outlined the changes made to the original model to aid readers interested in understanding the modifications. See Table S3 for the summary of parameters and their values.

The model incorporates four key components of B cell and antibody dynamics: (i) display of antigens on follicular dendritic cells (FDCs), (ii) activation of naïve B cells and entrance into GCs, (iii) the process of affinity maturation in GCs, leading to the production of memory and plasma cells, and (iv) the process of memory B cell expansion and differentiation outside of GCs upon antigen encounter. To capture the dynamics of antigen administration, breakdown, immune complex formation, and transport to FDCs, we employ a system of differential equations. Immune complex formation depends on the concentration and affinity of antigen-specific antibodies, which is determined by the model of B cells.

For simulating the various stages of B cell activation, proliferation, mutation, and differentiation, we utilize stochastic agent-based model. We categorize B cells into four overarching classes: naive B cells, GC B cells, memory B cells, and plasma cells. The simulation progresses in time steps of 0.01 day, and antigen and antibody concentrations are updated at each step. Simultaneously, in each step, action probabilities for events like activation, selection, cell division, somatic hypermutation, differentiation, and apoptosis are computed for the B cells and subsequently executed. To emulate the conditions of a secondary lymphoid organ, the simulation simultaneously models up to 200 distinct GCs. The number of Tfh cells obtained from the model of T cell priming is used to determine the number of active GCs and the number of Tfh cells available in each GC. Each simulation is iterated 10 times. The averaged outcomes can be interpreted as representative of a population-level immune response.

In this study, we consider the partial degradation of antigen as schematically depicted in Fig. 4-4A. We postulate there are two distinct antibodies: one targeting the native antigen (nAg) and the other targeting the partially degraded, non-native antigen (pAg). We further postulate that the partially degraded antigen is immunodominant. Drawing parallel to the original model - which distinguished immunodominant and subdominant epitopes on the SARS-CoV-2 receptor binding site - we employ a two-epitope model. In this approach, epitopes on the nAg are aggregated into a singular subdominant epitope while the epitopes on the pAg are aggregated into a singular immunodominant epitope. Each B cell targets either the nAg or the pAg. In this model, the germline affinity distribution of naïve B cells displays an extended tail for the immunodominant non-native antigen.

Equations for the antigen dynamics

First, we describe the processes that are included in the model for antigen dynamics. We use the following abbreviations: native soluble antigen (nAg), partially degraded soluble antigen (pAg), either type of soluble antigen (Ag), soluble antibody (Ig), soluble immune complex (IC), immune complex on follicular dendritic cell (IC-FDC), plasma cell (PC).

The partial and full decay of the soluble antigen are described as:

$nAg \rightarrow pAg$	Decay of free native soluble antigen into partially degraded antigen
$pAg \rightarrow \emptyset$	Decay of partially degraded antigen

The production and decay of antibodies, which apply to both the nAg and pAg-targeting antibodies are described as:

$PC \rightarrow PC + Ig$	Antibody production by plasma cells
$Ig \rightarrow \emptyset$	Decay of free soluble antibody

The formation of immune complexes, deposition on FDC, and decay on FDC, which apply to both the nAg and pAg, are described as:

$Ag + Ig \rightleftharpoons IC$	Fast equilibrium between free soluble antigen and antibody
$IC \rightarrow IC - FDC$	Immune complex transport to follicular dendritic cells
$IC - FDC \rightarrow \emptyset$	Consumption and decay of immune complexes on follicular dendritic cells

The above processes lead to the following differential-algebraic equations:

$$\frac{[Ag][Ig]}{[IC]} = K_d \quad \text{(Equation 8)}$$

$$\frac{d[nAg]}{dt} = -d_{Ag}[Ag] \quad \text{(Equation 9)}$$

$$\frac{d[pAg]}{dt} = d_{Ag}[nAg] - d_{Ag}[pAg] \quad \text{(Equation 10)}$$

$$\frac{d[IC]}{dt} = -k_{deposit}[IC] \quad \text{(Equation 11)}$$

$$\frac{d[IC - FDC]}{dt} = k_{deposit}[IC] \; - d_{IC}[IC - FDC] \quad \text{(Equation 12)}$$

$$\frac{d[Ig]}{dt} = k_{Ig}[PC] - d_{Ig}[Ig] \quad \text{(Equation 13)}$$

$$\frac{dK_d}{dt} = \frac{(K_d^{PC} - K_d)k_{Ig}[PC]}{[Ig] + [IC]} \quad \text{(Equation 14)}$$

Here, K_d and K_d^{PC} represent the dissociation constants of the serum antibodies and the BCRs of plasma cells, respectively.

Initiation of GCs

In Yang et al. [62], which solely focused on bolus injections, the assumption was made that 200 GCs are simultaneously initiated post each injection, with a separate pool of naïve B cells tied to each GC. This simplified model is not best suited for depicting dosing schemes with gradual administration of antigen and adjuvant. Therefore, contrary to the previous model, we consider a single pool of naïve B cells collectively shared across all GCs. We then postulate that GCs are sequentially initiated,

influenced by the increasing number of Tfh cells. The number of Tfh cells is determined by the model of T cell priming (Eqs. 1-7) and is affected by the dosing scheme.

The number of active GCs at time *t*, $N_{GC}(t)$, is determined from the number of Tfh cells, $N_{Tfh}(t)$, as follows:

$$N_{GC}(t) = \min\left(\left[\frac{N_{Tfh}(t)}{N_{T0}}, 200\right]\right) \quad \text{(Equation 15)}$$

Here, N_{T0} is the peak number of Tfh cells in each GC when the number of GCs have not reached the maximum value of 200.

Naïve B cell germline affinities

The model of germline-endowed binding affinities of naïve B cells follows the approach from the previous study We parametrize the distribution of the binding affinity, denoted as $E = -\log_{10}(K_d)$, with a geometric distribution. The distribution takes discrete values between 6 and 8, expressed as $E_k = 6 + 0.2k$ for $k = 0 \ldots 10$. Note that higher E value indicates stronger binding.

We differentiate between two groups of naïve B cells: one group binding to the native antigen and the other to the partially degraded antigen. We assume the partially degraded antigen is more immunodominant. The frequencies of naïve B cells binding to either antigen type with affinity E_k are formulated as follows:

$$f_{pAg}(E_k) = N_{naive}(1-p)\frac{e^{-r_1 E_k}}{\sum_{k=0}^{10} e^{-r_1 E_k}} \quad \text{(Equation 16)}$$

$$f_{nAg}(E_k) = N_{naive}p\frac{e^{-r_2 E_k}}{\sum_{k=0}^{10} e^{-r_2 E_k}} \quad \text{(Equation 17)}$$

where N_{naive} is the number of naïve B cells and p is the fraction of B cells that target the native antigen. The exponents r_1, r_2 determine the slope of the distribution. They are derived from the parameters E_1^h and dE_{12} which we directly specify. The following relationships are satisfied:

$$f_{pAg}\left(E_1^h\right) = 1 - p \quad \text{(Equation 18)}$$

$$f_{nAg}\left(E_1^h - dE_{12}\right) = p \quad \text{(Equation 19)}$$

Given $dE_{12} > 1$, this parameterization results in an extended tail of germline-endowed affinities for the naïve B cells targeting the partially degraded antigen, reflecting their immunodominance.

The above model was initially developed to represent a pool of naïve B cells associated with an individual GC. For this study, we adjust the model by amplifying the frequencies by a factor of 200, thereby consolidating a shared pool of naïve B cells across all GCs.

Activation of naïve B cells, differentiation into plasmablasts, and entry into GCs

We model the quantity of antigen captured by a B cell, denoted as *i,* using the following equation:

$$A_i = \left(\frac{C}{C_0} 10^{(\min(E_i, 10) - E_0)}\right)^K \quad \text{(Equation 20)}$$

where $\frac{C}{C_0}$ signifies antigen availability, $E_0 = 6$ serves as the reference affinity, and K represents the selection stringency. The *min* function accounts for the effect of affinity ceiling. The term $C = 0.01([Ag] + [IC]) + [IC - FDC]$ represents the effective antigen concentration, accounting for the predominant influence of surface-presented immune complexes. C_0 is the reference concentration. For B cells targeting the native or partially degraded antigen, the appropriate antigen concentration is applied respectively.

The probability of B cell activation at each step is determined as:

$$\Pr(\text{B cell } i \text{ is activated}) = \min(A_i, 1) \quad \text{(Equation 21)}$$

The entry of activated naïve B cells to GCs is limited by competition for positive selection from helper T cells. The selection rate for an activated naive B cell i, denoted as λ_i, is given by:

$$\lambda_i = \frac{\frac{N_T}{N_{activated}} \frac{A_i}{\langle A \rangle}}{1 + \frac{N_T}{N_{activated}} \frac{A_i}{\langle A \rangle}} \quad \text{(Equation 22)}$$

Here, $N_{activated}$ stands for the total count of activated B cells, $\langle A \rangle$ denotes the average quantity of antigen captured by all activated B cells, and N_T represents the limited number of helper T cells that B cells compete for. Activated naïve B cells migrate to the T-B border and interact with antigen-

primed T cells before they migrate back to the B cell zone and enter GCs [66]. Thus, we choose the value of N_T as the number of T cells from the model of T cell priming (Eq. 6).

Upon positive selection, a naïve B cell has three potential fates: it can differentiate into a memory cell, a plasmablast, or a GC B cell [67]. In our model, a B cell differentiates into either a memory cell or a plasmablast with a probability of p_1, and otherwise enters a GC. Upon entering a GC, a naïve B cell is randomly allocated to one of the active GCs. If it does not enter a GC, the B cell has probability p_2 of becoming a plasma cell, and otherwise becomes a memory cell. When the B cell becomes a plasmablast, it undergoes five division cycles [68].

Proliferation, mutation, and death of GC B cells

GC B cells must be activated by antigen and then receive help from Tfh cells to proliferate. The activation step for GC B cells is identical to that of naïve B cells. The rate of positive selection, β_i, of a GC B cell, i, is modeled based on competition for limited number of Tfh cells:

$$\beta_i = \beta_{max} \frac{\frac{N_{Tfh}/N_{GC}}{N_{activated}} \frac{A_i}{\langle A \rangle}}{1 + \frac{N_{Tfh}/N_{GC}}{N_{activated}} \frac{A_i}{\langle A \rangle}} \qquad \text{(Equation 23)}$$

where β_{max} is the maximum rate of positive selection, and the number of Tfh cells in each active GC is calculated as N_{Tfh}/N_{GC}.

Upon positive selection, a B cell exits the GC with a probability of p_1 and proliferates inside the GC with a probability of 1-p_1. When it exits the GC, it becomes a plasma cell with a probability of p_2 or a memory cell with a probability of 1- p_2. When it proliferates, one offspring undergoes mutation. This mutation can result in apoptosis (probability 0.3), no affinity change (probability 0.5), or a change in the mutation state of a randomly selected residue (probability 0.2).

The affinities of GC B cells change with mutations. Each B cell is represented as a string of 0's and 1's with a total length of n_{res}. The residues are all 0's for a naïve B cell. Each time an affinity-affecting mutation occurs, one of the residues is randomly chosen and its value is flipped. The affinity of a B cell is determined by the sum of its germline-endowed affinity and the contributions of the mutations, as follows:

$$E_i = E_i^{germline} + \sum_{j=1}^{n_{res}} \delta_{i,j} s_{i,j} \quad \text{(Equation 24)}$$

where $\delta_{i,j} \in \{0,1\}$ is the mutational state of residue j, and $s_{i,j}$ is the effect of the mutation at residue j on the binding affinity. The values of $s_{i,j}$ $(j = 1 \dots n_{res})$ are independent and identically distributed as follows:

$$s_{i,j} \sim e^{N(\mu,\sigma)} - \epsilon \quad \text{(Equation 25)}$$

This shifted log-normal distribution with μ, σ, ϵ chosen to fit experimentally determined distribution leads to ~5 % of affinity-affecting mutations increasing the binding affinity.

Expansion and differentiation of B cells in Extra Germinal Center

In schemes involving multiple injections, we model the expansion of memory cells and their differentiation into plasma cells outside of germinal centers, termed extra germinal centers (EGCs). The process of affinity-based positive selection, which results in either differentiation or proliferation, is identical to that in the GCs. However, proliferating cells in EGC differentiates into plasma cells with higher probability. Moreover, to reflect the fast kinetics in the EGC, the number of Tfh cells is maintained at its peak value, N_{T0}.

Modifications from the model in Chapter 2

In our study, we have introduced several changes from the model in Chapter 2 and in Yang et al. [62], which are described in detail in the relevant sections. We summarize these changes here to aid readers interested in understanding the modifications.

(1) T cell priming: We developed a detailed T cell priming model that is suitable for gradual dosing schemes.
(2) Antigen decay and targeting: We introduced partial decay of antigen and B cells targeting the partially degraded antigen.
(3) Initiation of GCs: We introduced asynchronous initiation of GCs, which is suitable for gradual dosing schemes.

(4) Cell differentiation: We consider differentiation of memory cells and plasmablasts from a positively selected naïve B cell. This was not considered for simplicity in the previous model, but the shorter timescale in this study makes these early dynamics important.

(5) Parameter adjustment: We adjusted a small number of model parameters to match the timescales of experimental observations in the current study. The previous model was built for vaccine responses in humans, which can have slower and longer-lasting GC responses than mice. Table S3 provides all the parameter values for the model of B cell responses. Those that take values not tested in Yang et al. are highlighted.

4.6. Supplemental Figures and Tables

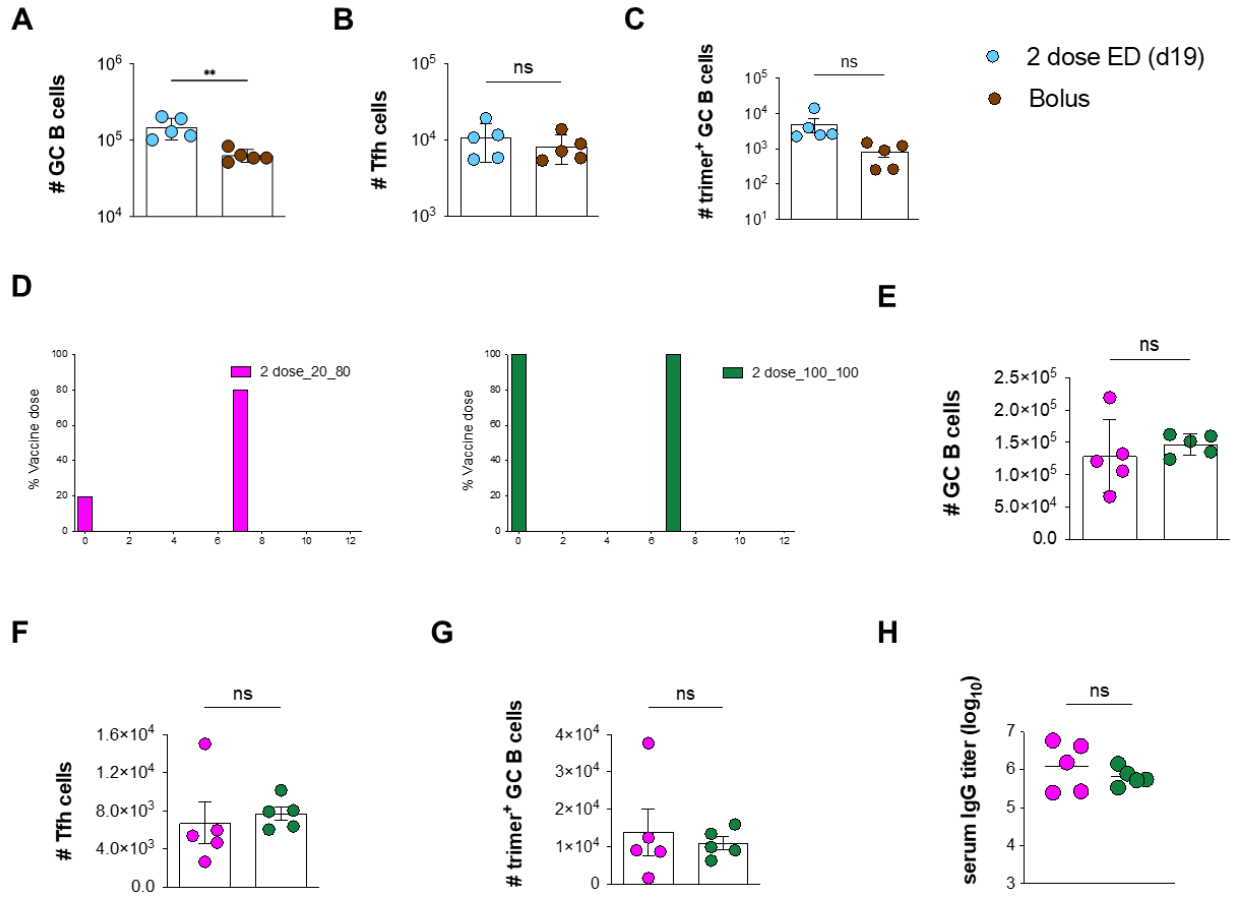

Figure S1: Additional 2-shot prime immunization GC response comparisons.

(A) GC, **(B)** Tfh, and **(C)** trimer-specific GC B cell responses at day 19 for 2-dose regimen compared to bolus immunization. **(D)** Schematic of 2-shot regimens comparing dose 1 (20%) and dose 2 (80%) vs dose 1 (100%) and dose 2 (100%) at day 14. **(E)** GC, **(F)** Tfh, and **(G)** trimer-specific GC B cell responses at day 14. **(H)** trimer-specific IgG titer at day 28 for the two groups.

A

$$\frac{d[Adj]}{dt} = -d_{Adj}[Adj]$$
$$\frac{d[TC]}{dt} = \frac{[Adj]}{S_{Adj} + [Adj]} - \mu[TC]$$
$$\frac{d[DC]}{dt} = D_0[TC] - \left(1 + k\frac{[Adj]}{S_{Adj} + [Adj]}\right)[DC][Ag] - \mu[DC]$$
$$\frac{d[Ag]}{dt} = -d_{Ag}[Ag]$$
$$\frac{d[aDC^{Ag^+}]}{dt} = \left(1 + k\frac{[Adj]}{S_{Adj} + [Adj]}\right)[DC][Ag] - \mu[aDC^{Ag^+}]$$
$$\frac{d[T]}{dt} = \alpha\frac{[aDC^{Ag^+}][T]}{[T] + [aDC^{Ag^+}]} - \eta([T] - T_0)$$
$$\frac{d[T_{FH}]}{dt} = \eta([T] - T_0)$$

d_{Ag}	Antigen decay rate
d_{Adj}	Adjuvant decay rate
S_{Adj}	Half-max adjuvant activity concentration
k	Max increase in antigen uptake rate
α	Max T cell proliferation rate
η	T cell differentiation rate
μ	Innate immune cell death rate
D_0	Scaling factor for DCs
T_0	Scaling factor for Tfh cells

Adj – Adjuvant, TC – Tissue cells, DC – Dendritic cells, Ag – Antigen
DC^{Ag^+} - Antigen-primed dendritic cells, T – Proliferating T cells, T_{FH} - Follicular helper T cells

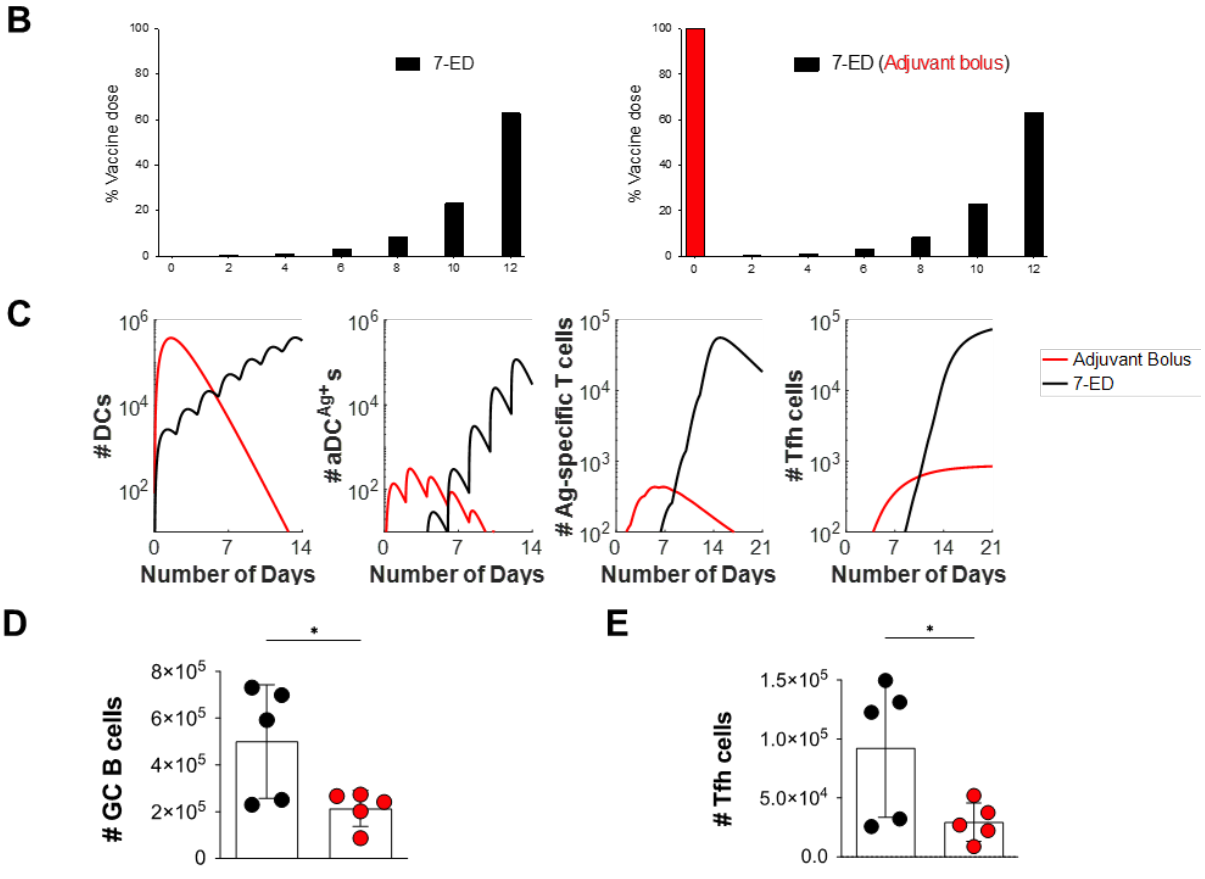

Figure S2. Analysis of 7-ED (adjuvant bolus) regimen.

(A) Equations governing the kinetic model for innate immune responses and T cell priming. **(B)** Dosing scheme for 7-ED and 7-ED (adjuvant bolus) immunization regimens. **(C)** Model predictions for DC, aDC^{Ag+}, T cells, and Tfh cell responses under the standard 7-ED and 7-ED (adjuvant bolus) immunization schemes. **(D-E)** Experimentally observed numbers on day 14 for (D) GC B cells and (E) Tfh cells.

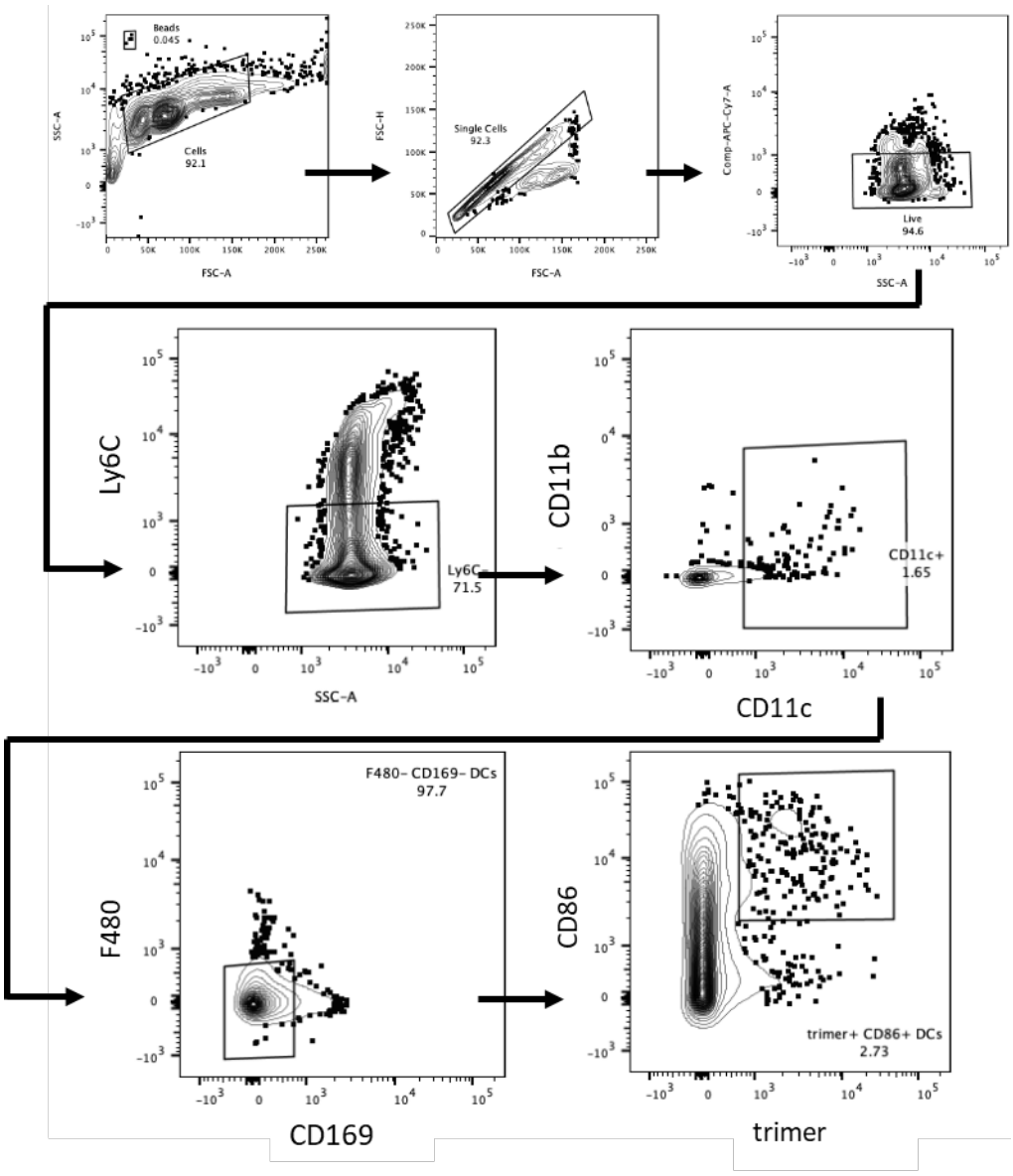

Figure S3. Gating strategy for DC kinetic analysis of different immunization regimens.

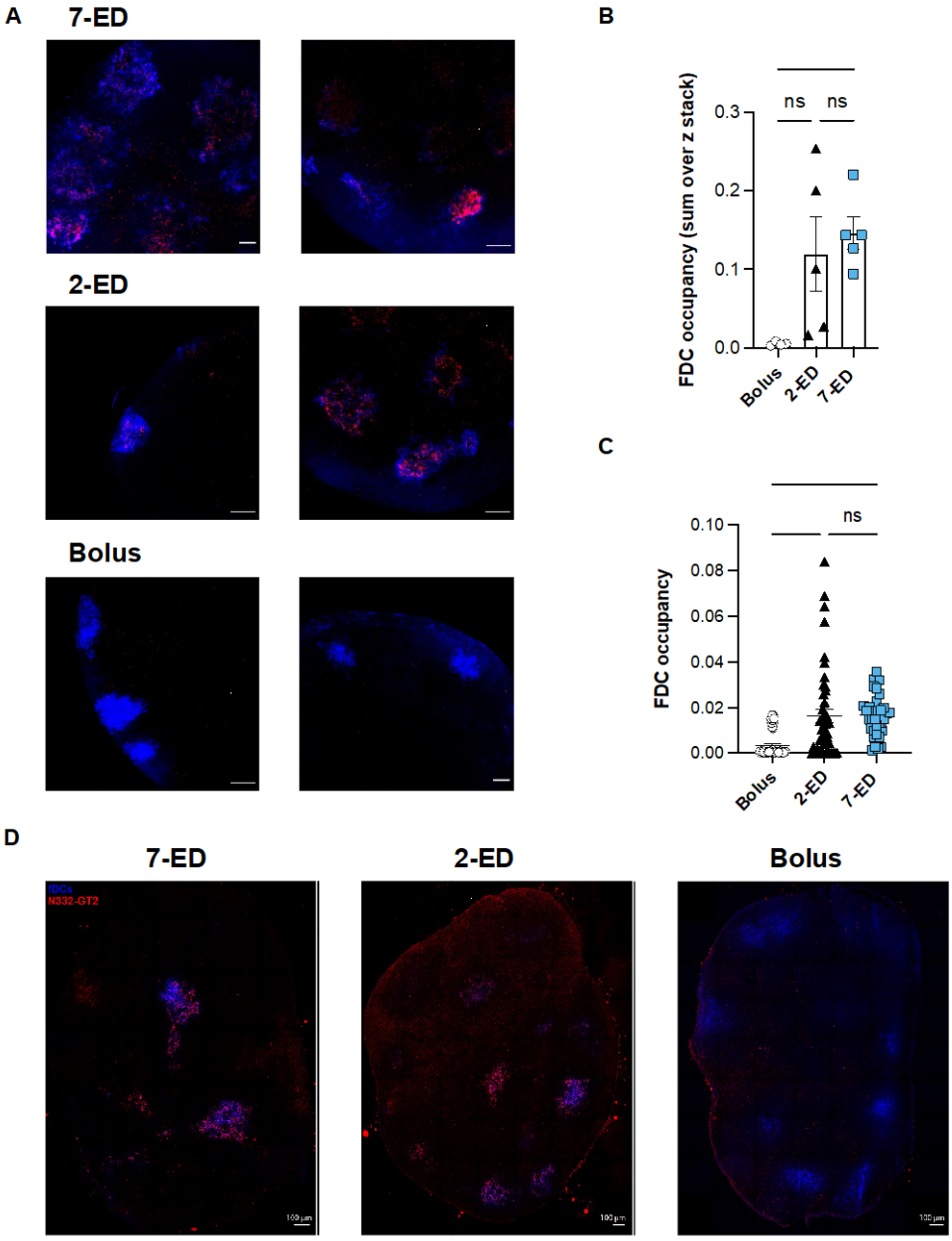

figure S4. Additional antigen capture on FDCs data. (A-D)

Groups of C57Bl/6 mice (*n* = 3 animals/group) were immunized by bolus, 2-ED, or 7-ED regimens as shown in Fig. 3G, followed by collection of lymph nodes for imaging at 48 h after bolus or after the last injection of the 2-ED and 7-ED regimens. Shown are additional cleared whole LN images for bolus, 2-ED, and 7-ED regimens **(A)**, fraction of FDC area occupied by antigen for each individual image in the z-stack (9 per image) **(B)**, and for the z-projection (sum of slices) **(C)** and additional representative histological LN slices for 7-ED, 2-ED, and bolus dosing regimens **(D)**. Shown are data from one independent experiment for each immunization series. ****, $p < 0.0001$; ***, $p < 0.001$; **, $p < 0.01$; *, $p < 0.05$; ns, not significant; by one-way ANOVA with Dunnett's multiple comparison post test compared to bolus immunization.

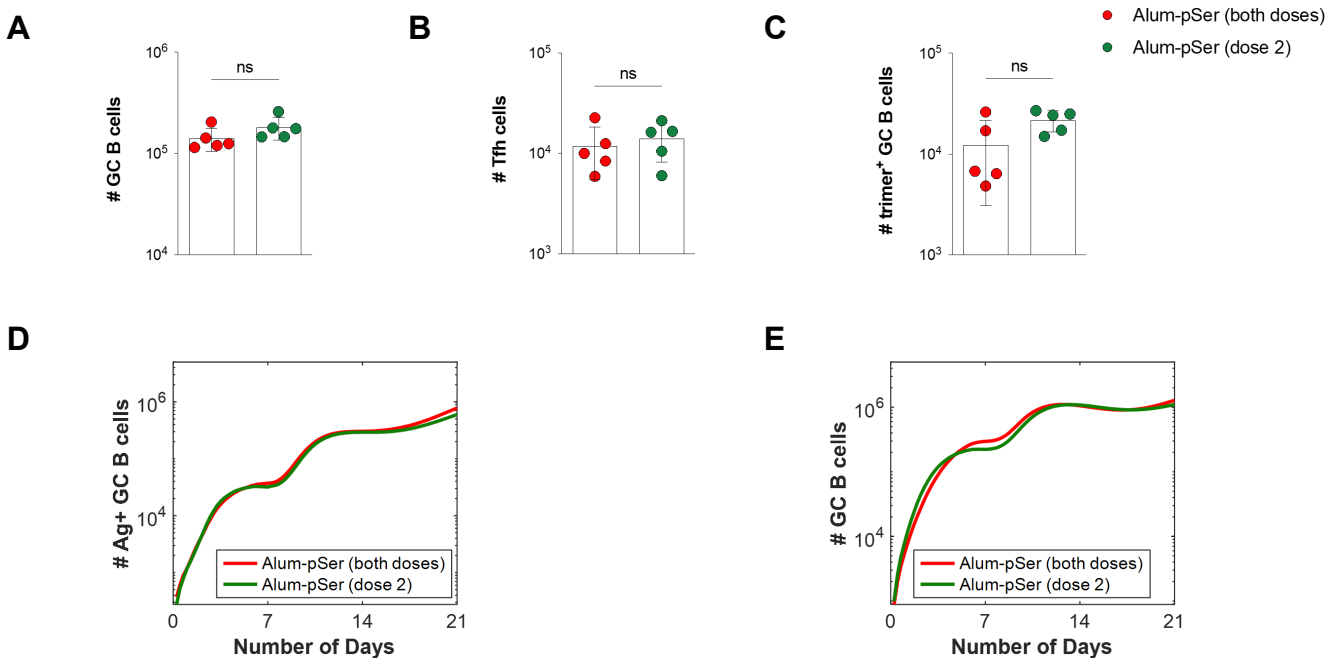

figure S5: Additional data on Alum-pSer immunizations.

(A-C) C57Bl/6J mice (*n*=5 animals/group) were immunized with 10 μg MD39 trimer anchored onto 50 ug Alum combined with 5 μg SMNP adjuvant (20% vaccine on day 0, 80% on day 7, red) or with alum anchoring only used for the second dose (green). Shown are experimentally measured responses on day 14 for GC B cells **(A),** Tfh cells **(B),** and trimer-specific GC B cells **(C). (D-E)** *In silico* predictions modeling the same experiment as in (A-C), showing numbers of native antigen-binding GC B cells **(D),** and total GC B cells **(E)** over time. Shown are data from one independent experiment for each immunization series. ****, $p < 0.0001$; ***, $p < 0.001$; **, $p < 0.01$; *, $p < 0.05$; ns, not significant; by one-way ANOVA with Dunnett's multiple comparison post test compared to bolus immunization.

Table S1. Antigen decay kinetics data.

Measured antigen trimer mass per lymph node after immunization. Maximum likelihood estimate of the antigen decay rate assuming first-order kinetics is ~2.7 / day, corresponding to half-life of ~6.2 hrs.

	Extracellular Ag (ng)		
6 Hrs	52.11	38.29	48.32
Day 1	5.60	6.85	6.82
Day 2	0.64	0.12	0.83

Table S2. Simulation parameters for the model of T cell priming

Parameter	Value	Description	Equation	Note
T cell priming				
d_{Ag}	$3\ \mathrm{day}^{-1}$	Antigen decay rate	1	Our data (Table S1)
d_{Adj}	$3\ \mathrm{day}^{-1}$	Adjuvant decay rate	2	Taken to be identical to d_{Ag}
S_{Adj}	0.1	Half-max adjuvant activity concentration	3	See text for Eq. 3
k	10	Max increase in antigen uptake rate	4, 5	See text for Eqs. 4-5
μ	1.2	Innate immune cell death rate	3, 4, 5	From ref. [61]
α	1.5	Max T cell proliferation rate	6	
η	0.22	T cell differentiation rate	7	
D_0	1.8×10^6	Scaling factor for DCs	4	Fitted to data
T_0	33	Scaling factor for Tfh cells	6,7	Fitted to data
$[Ag]_0, [Adj]_0, [TC]_0, [DC]_0, [aDC^{Ag+}]_0, [T_{FH}]_0$	0	Initial conditions	1-7	
$[T]_0$	T_0			

Table S3. Simulation parameters for the model of B cell responses

Description of the parameters used in the simulation. Highlighted parameters have values changed from the model in Chapter 2.

Parameter	Value	Description	Equation	Note
Antigen and antibody dynamics				
k_{Ig}	10^{-1} nM day^{-1} PC^{-1}	Rate of antibody production per plasma cell per day, in terms of change in serum concentration	13, 14	Increased from ref. [62] to match the faster kinetics observed in mice
d_{Ig}	0.17 day^{-1}	Antibody decay rate	13	
d_{Ag}	3 day^{-1}	Antigen decay rate	9,10	From ref. [62]
$k_{deposit}$	1 hour^{-1}	Rate of immune complex transport to FDC	11, 12	
d_{IC}	0.15 day^{-1}	Rate of decay of immune complex on FDC	12	
$[Ag]_0$	0 nM	Initial Conditions	8-14	
$[Ig]_0$	10^{-2} nM			
$[IC]_0$, $[IC-FDC]_0$	0 nM			
B cell affinities				
N_{naive}	2000 cells/GC	Number of naïve B cells / GC	16, 17	From ref. [62]
p	0.5	Fraction of naïve B cells that target the naitve antigen	18, 19	
E_1^h	7.2	Affinity at which there is one dominant naive B cell available for each GC on average	18, 19	
dE_{12}	0.6	$E_1^h - dE_{12}$ is the affinity at which there is one subdominant naïve B cell available for each GC on average	18, 19	
n_{res}	80	Length of the string representation of B cell residues	24	
μ, σ, ϵ	3.1, 1.2, 3.08	Parameters for the shifted log-normal distribution that represent the effects of mutations on B cell binding affinities	25	
GC and EGC				
C_0	0.2 nM	Reference antigen concentration	20	Increased from ref. [62] to match the faster kinetics observed in mice
β_{max}	4 day^{-1}	Maximum rate of positive selection for GC and EGC B cells	23	
E_0	6	Reference binding affinity	20	From ref. [62]
K	0.5	Stringency of selection of naïve and GC B cells by helper T cells based on the amounts of antigen internalized	20	
N_{T0}	1200	Maximum number of helper T cells	15	
α	0.5 day^{-1}	Death rate of GC B cells	6	
Memory and Plasma Cell Dynamics				
p_1	0.1	Probability that a positively selected GC B cell exits by differentiation	Text	From ref. [62]
p_2	0.1	Probability that a differentiating GC B cell becomes a plasma cell		
p_2^{EGC}	0.6	Probability that a proliferating memory cell in EGC differentiates into a plasma cell		
d_{PC}	0.17 day^{-1}	Death rate of plasma cells		

4.7. Chapter 4 References

1. Barouch, D.H. (2022). Covid-19 Vaccines — Immunity, Variants, Boosters. New Engl J Med *387*, 1011–1020. 10.1056/nejmra2206573.

2. Lee, J.H., and Crotty, S. (2021). HIV vaccinology: 2021 update. Semin Immunol *51*, 101470. 10.1016/j.smim.2021.101470.

3. Haynes, B.F., Wiehe, K., Borrow, P., Saunders, K.O., Korber, B., Wagh, K., McMichael, A.J., Kelsoe, G., Hahn, B.H., Alt, F., et al. (2023). Strategies for HIV-1 vaccines that induce broadly neutralizing antibodies. Nat Rev Immunol *23*, 142–158. 10.1038/s41577-022-00753-w.

4. Feinberg, M.B. (2021). Uhambo — Twists and Turns on the Journey to an Efficacious HIV-1 Vaccine. New Engl J Med *384*, 1157–1159. 10.1056/nejme2102358.

5. Burton, D.R., and Hangartner, L. (2016). Broadly Neutralizing Antibodies to HIV and Their Role in Vaccine Design. Annu. Rev. Immunol. *34*, 635–659. 10.1146/annurev-immunol-041015-055515.

6. Burton, D.R. (2019). Advancing an HIV vaccine; advancing vaccinology. Nat Rev Immunol *19*, 77–78. 10.1038/s41577-018-0103-6.

7. Gilbert, P.B., Huang, Y., deCamp, A.C., Karuna, S., Zhang, Y., Magaret, C.A., Giorgi, E.E., Korber, B., Edlefsen, P.T., Rossenkhan, R., et al. (2022). Neutralization titer biomarker for antibody-mediated prevention of HIV-1 acquisition. Nat Med *28*, 1924–1932. 10.1038/s41591-022-01953-6.

8. Corey, L., Gilbert, P.B., Juraska, M., Montefiori, D.C., Morris, L., Karuna, S.T., Edupuganti, S., Mgodi, N.M., deCamp, A.C., Rudnicki, E., et al. (2021). Two Randomized Trials of Neutralizing Antibodies to Prevent HIV-1 Acquisition. New Engl J Med *384*, 1003–1014. 10.1056/nejmoa2031738.

9. Havenar-Daughton, C., Lee, J.H., and Crotty, S. (2017). Tfh cells and HIV bnAbs, an immunodominance model of the HIV neutralizing antibody generation problem. Immunol Rev *275*, 49–61. 10.1111/imr.12512.

10. Klasse, P.J., Ozorowski, G., Sanders, R.W., and Moore, J.P. (2020). Env Exceptionalism: Why Are HIV-1 Env Glycoproteins Atypical Immunogens? Cell Host Microbe *27*, 507–518. 10.1016/j.chom.2020.03.018.

11. Krammer, F., and Palese, P. (2015). Advances in the development of influenza virus vaccines. Nat. Rev. Drug Discov. *14*, 167–182. 10.1038/nrd4529.

12. Krammer, F., and Palese, P. (2019). Universal Influenza Virus Vaccines That Target the Conserved Hemagglutinin Stalk and Conserved Sites in the Head Domain. J. Infect. Dis. *219*, S62–S67. 10.1093/infdis/jiy711.

13. Victora, G.D., and Nussenzweig, M.C. (2022). Germinal Centers. Annu Rev Immunol *40*, 1–30. 10.1146/annurev-immunol-120419-022408.

14. Victora, G.D., and Nussenzweig, M.C. (2012). Germinal Centers. Immunology *30*, 429–457. 10.1146/annurev-immunol-020711-075032.

15. Shulman, Z., Gitlin, A.D., Weinstein, J.S., Lainez, B., Esplugues, E., Flavell, R.A., Craft, J.E., and Nussenzweig, M.C. (2014). Dynamic signaling by T follicular helper cells during germinal center B cell selection. Science *345*, 1058–1062. 10.1126/science.1257861.

16. Gitlin, A.D., Mayer, C.T., Oliveira, T.Y., Shulman, Z., Jones, M.J.K., Koren, A., and Nussenzweig, M.C. (2015). T cell help controls the speed of the cell cycle in germinal center B cells. Science *349*, 643–646. 10.1126/science.aac4919.

17. Pauthner, M., Havenar-Daughton, C., Sok, D., Nkolola, J.P., Bastidas, R., Boopathy, A.V., Carnathan, D.G., Chandrashekar, A., Cirelli, K.M., Cottrell, C.A., et al. (2017). Elicitation of Robust Tier 2 Neutralizing Antibody Responses in Nonhuman Primates by HIV Envelope Trimer Immunization Using Optimized Approaches. Immunity *46*, 1073-1088.e6. 10.1016/j.immuni.2017.05.007.

18. Abbott, R.K., Lee, J.H., Menis, S., Skog, P., Rossi, M., Ota, T., Kulp, D.W., Bhullar, D., Kalyuzhniy, O., Havenar-Daughton, C., et al. (2018). Precursor Frequency and Affinity Determine B Cell Competitive Fitness in Germinal Centers, Tested with Germline-Targeting HIV Vaccine Immunogens. Immunity *48*, 133-146.e6. 10.1016/j.immuni.2017.11.023.

19. Tam, H.H., Melo, M.B., Kang, M., Pelet, J.M., Ruda, V.M., Foley, M.H., Hu, J.K., Kumari, S., Crampton, J., Baldeon, A.D., et al. (2016). Sustained antigen availability during germinal center initiation enhances antibody responses to vaccination. Proc National Acad Sci *113*, E6639–E6648. 10.1073/pnas.1606050113.

20. Cirelli, K.M., Carnathan, D.G., Nogal, B., Martin, J.T., Rodriguez, O.L., Upadhyay, A.A., Enemuo, C.A., Gebru, E.H., Choe, Y., Viviano, F., et al. (2019). Slow Delivery Immunization Enhances HIV Neutralizing Antibody and Germinal Center Responses via Modulation of Immunodominance. Cell *177*, 1153-1171.e28. 10.1016/j.cell.2019.04.012.

21. Irvine, D.J., Aung, A., and Silva, M. (2020). Controlling timing and location in vaccines. Adv Drug Deliver Rev. 10.1016/j.addr.2020.06.019.

22. Lee, J.H., Sutton, H.J., Cottrell, C.A., Phung, I., Ozorowski, G., Sewall, L.M., Nedellec, R., Nakao, C., Silva, M., Richey, S.T., et al. (2022). Long-primed germinal centres with enduring affinity maturation and clonal migration. Nature *609*, 998–1004. 10.1038/s41586-022-05216-9.

23. Boopathy, A.V., Mandal, A., Kulp, D.W., Menis, S., Bennett, N.R., Watkins, H.C., Wang, W., Martin, J.T., Thai, N.T., He, Y., et al. (2019). Enhancing humoral immunity via sustained-release implantable microneedle patch vaccination. Proc National Acad Sci *116*, 16473–16478. 10.1073/pnas.1902179116.

24. Roth, G.A., Gale, E.C., Alcántara-Hernández, M., Luo, W., Axpe, E., Verma, R., Yin, Q., Yu, A.C., Hernandez, H.L., Maikawa, C.L., et al. (2020). Injectable Hydrogels for Sustained Codelivery of Subunit Vaccines Enhance Humoral Immunity. Acs Central Sci *6*, 1800–1812. 10.1021/acscentsci.0c00732.

25. Gale, E.C., Powell, A.E., Roth, G.A., Meany, E.L., Yan, J., Ou, B.S., Grosskopf, A.K., Adamska, J., Picece, V.C.T.M., d'Aquino, A.I., et al. (2021). Hydrogel-Based Slow Release of a Receptor-Binding Domain Subunit Vaccine Elicits Neutralizing Antibody Responses Against SARS-CoV-2. Adv. Mater. *33*, 2104362. 10.1002/adma.202104362.

26. Roth, G.A., Picece, V.C.T.M., Ou, B.S., Luo, W., Pulendran, B., and Appel, E.A. (2021). Designing spatial and temporal control of vaccine responses. Nat Rev Mater, 1–22. 10.1038/s41578-021-00372-2.

27. Moyer, T.J., Kato, Y., Abraham, W., Chang, J.Y.H., Kulp, D.W., Watson, N., Turner, H.L., Menis, S., Abbott, R.K., Bhiman, J.N., et al. (2020). Engineered immunogen binding to alum adjuvant enhances humoral immunity. Nat Med *26*, 430–440. 10.1038/s41591-020-0753-3.

28. Garcea, R.L., Meinerz, N.M., Dong, M., Funke, H., Ghazvini, S., and Randolph, T.W. (2020). Single-administration, thermostable human papillomavirus vaccines prepared with atomic layer deposition technology. Npj Vaccines *5*, 45. 10.1038/s41541-020-0195-4.

29. Steichen, J.M., Lin, Y.-C., Havenar-Daughton, C., Pecetta, S., Ozorowski, G., Willis, J.R., Toy, L., Sok, D., Liguori, A., Kratochvil, S., et al. (2019). A generalized HIV vaccine design strategy for priming of broadly neutralizing antibody responses. Science *366*, eaax4380. 10.1126/science.aax4380.

30. Silva, M., Kato, Y., Melo, M.B., Phung, I., Freeman, B.L., Li, Z., Roh, K., Wijnbergen, J.W.V., Watkins, H., Enemuo, C.A., et al. (2021). A particulate saponin/TLR agonist vaccine adjuvant alters lymph flow and modulates adaptive immunity. Sci Immunol *6*, eabf1152. 10.1126/sciimmunol.abf1152.

31. Rodrigues, K.A., Rodriguez-Aponte, S.A., Dalvie, N.C., Lee, J.H., Abraham, W., Carnathan, D.G., Jimenez, L.E., Ngo, J.T., Chang, J.Y.H., Zhang, Z., et al. (2021). Phosphate-mediated coanchoring of RBD immunogens and molecular adjuvants to alum potentiates humoral immunity against SARS-CoV-2. Sci Adv *7*, eabj6538. 10.1126/sciadv.abj6538.

32. Havenar-Daughton, C., Carnathan, D.G., Peña, A.T. de la, Pauthner, M., Briney, B., Reiss, S.M., Wood, J.S., Kaushik, K., Gils, M.J. van, Rosales, S.L., et al. (2016). Direct Probing of Germinal Center Responses Reveals Immunological Features and Bottlenecks for Neutralizing Antibody Responses to HIV Env Trimer. Cell Reports *17*, 2195–2209. 10.1016/j.celrep.2016.10.085.

33. Baumjohann, D., Preite, S., Reboldi, A., Ronchi, F., Ansel, K.M., Lanzavecchia, A., and Sallusto, F. (2013). Persistent Antigen and Germinal Center B Cells Sustain T Follicular Helper Cell Responses and Phenotype. Immunity *38*, 596–605. 10.1016/j.immuni.2012.11.020.

34. Mintz, M.A., and Cyster, J.G. (2020). T follicular helper cells in germinal center B cell selection and lymphomagenesis. Immunol Rev *296*, 48–61. 10.1111/imr.12860.

35. Yang, L., Beek, M.V., Wang, Z., Muecksch, F., Canis, M., Hatziioannou, T., Bieniasz, P.D., Nussenzweig, M.C., and Chakraborty, A.K. (2023). Antigen presentation dynamics shape the antibody response to variants like SARS-CoV-2 Omicron after multiple vaccinations with the original strain. Cell Reports *42*, 112256. 10.1016/j.celrep.2023.112256.

36. Pulendran, B., Arunachalam, P.S., and O'Hagan, D.T. (2021). Emerging concepts in the science of vaccine adjuvants. Nat Rev Drug Discov, 1–22. 10.1038/s41573-021-00163-y.

37. Mayer, A., Zhang, Y., Perelson, A.S., and Wingreen, N.S. (2019). Regulation of T cell expansion by antigen presentation dynamics. Proc National Acad Sci *116*, 5914–5919. 10.1073/pnas.1812800116.

38. Johansen, P., Storni, T., Rettig, L., Qiu, Z., Der-Sarkissian, A., Smith, K.A., Manolova, V., Lang, K.S., Senti, G., Müllhaupt, B., et al. (2008). Antigen kinetics determines immune reactivity. Proc National Acad Sci *105*, 5189–5194. 10.1073/pnas.0706296105.

39. Quiel, J., Caucheteux, S., Laurence, A., Singh, N.J., Bocharov, G., Ben-Sasson, S.Z., Grossman, Z., and Paul, W.E. (2011). Antigen-stimulated CD4 T-cell expansion is inversely and log-linearly related to precursor number. Proc National Acad Sci *108*, 3312–3317. 10.1073/pnas.1018525108.

40. Aung, A., Cui, A., Maiorino, L., Amini, A.P., Gregory, J.R., Bukenya, M., Zhang, Y., Lee, H., Cottrell, C.A., Morgan, D.M., et al. (2023). Low protease activity in B cell follicles promotes retention of intact antigens after immunization. Science *379*, eabn8934. 10.1126/science.abn8934.

41. Kulp, D.W., Steichen, J.M., Pauthner, M., Hu, X., Schiffner, T., Liguori, A., Cottrell, C.A., Havenar-Daughton, C., Ozorowski, G., Georgeson, E., et al. (2017). Structure-based design of native-like HIV-1 envelope trimers to silence non-neutralizing epitopes and eliminate CD4 binding. Nat Commun *8*, 1655. 10.1038/s41467-017-01549-6.

42. Qi, H. (2016). T follicular helper cells in space-time. Nat Rev Immunol *16*, 612–625. 10.1038/nri.2016.94.

43. Crotty, S. (2014). T Follicular Helper Cell Differentiation, Function, and Roles in Disease. Immunity *41*, 529–542. 10.1016/j.immuni.2014.10.004.

44. Crotty, S. (2019). T Follicular Helper Cell Biology: A Decade of Discovery and Diseases. Immunity *50*, 1132–1148. 10.1016/j.immuni.2019.04.011.

45. Dominguez-Sola, D., Victora, G.D., Ying, C.Y., Phan, R.T., Saito, M., Nussenzweig, M.C., and Dalla-Favera, R. (2012). The proto-oncogene MYC is required for selection in the germinal center and cyclic reentry. Nat Immunol *13*, 1083–1091. 10.1038/ni.2428.

46. Shulman, Z., Gitlin, A.D., Targ, S., Jankovic, M., Pasqual, G., Nussenzweig, M.C., and Victora, G.D. (2013). T Follicular Helper Cell Dynamics in Germinal Centers. Science *341*, 673–677. 10.1126/science.1241680.

47. Devarajan, P., Vong, A.M., Castonguay, C.H., Kugler-Umana, O., Bautista, B.L., Jones, M.C., Kelly, K.A., Xia, J., and Swain, S.L. (2022). Strong influenza-induced TFH generation requires CD4 effectors to recognize antigen locally and receive signals from continuing infection. Proc National Acad Sci *119*, e2111064119. 10.1073/pnas.2111064119.

48. Deenick, E.K., Chan, A., Ma, C.S., Gatto, D., Schwartzberg, P.L., Brink, R., and Tangye, S.G. (2010). Follicular Helper T Cell Differentiation Requires Continuous Antigen Presentation that Is Independent of Unique B Cell Signaling. Immunity *33*, 241–253. 10.1016/j.immuni.2010.07.015.

49. Cirelli, K.M., and Crotty, S. (2017). Germinal center enhancement by extended antigen availability. Curr Opin Immunol *47*, 64–69. 10.1016/j.coi.2017.06.008.

50. Hu, J.K., Crampton, J.C., Cupo, A., Ketas, T., Gils, M.J. van, Sliepen, K., Taeye, S.W. de, Sok, D., Ozorowski, G., Deresa, I., et al. (2015). Murine Antibody Responses to Cleaved Soluble HIV-1

Envelope Trimers Are Highly Restricted in Specificity. J Virol *89*, 10383–10398. 10.1128/jvi.01653-15.

51. McHugh, K.J., Nguyen, T.D., Linehan, A.R., Yang, D., Behrens, A.M., Rose, S., Tochka, Z.L., Tzeng, S.Y., Norman, J.J., Anselmo, A.C., et al. (2017). Fabrication of fillable microparticles and other complex 3D microstructures. Science *357*, 1138–1142. 10.1126/science.aaf7447.

52. Steichen, J.M., Kulp, D.W., Tokatlian, T., Escolano, A., Dosenovic, P., Stanfield, R.L., McCoy, L.E., Ozorowski, G., Hu, X., Kalyuzhniy, O., et al. (2016). HIV Vaccine Design to Target Germline Precursors of Glycan-Dependent Broadly Neutralizing Antibodies. Immunity *45*, 483–496. 10.1016/j.immuni.2016.08.016.

53. Tokatlian, T., Read, B.J., Jones, C.A., Kulp, D.W., Menis, S., Chang, J.Y.H., Steichen, J.M., Kumari, S., Allen, J.D., Dane, E.L., et al. (2019). Innate immune recognition of glycans targets HIV nanoparticle immunogens to germinal centers. Science *363*, 649–654. 10.1126/science.aat9120.

54. Silva, M., Kato, Y., Melo, M.B., Phung, I., Freeman, B.L., Li, Z., Roh, K., Wijnbergen, J.W.V., Watkins, H., Enemuo, C.A., et al. (2021). A particulate saponin/TLR agonist vaccine adjuvant alters lymph flow and modulates adaptive immunity. Sci. Immunol. *6*, eabf1152. 10.1126/sciimmunol.abf1152.

55. Didierlaurent, A.M., Morel, S., Lockman, L., Giannini, S.L., Bisteau, M., Carlsen, H., Kielland, A., Vosters, O., Vanderheyde, N., Schiavetti, F., et al. (2009). AS04, an aluminum salt- and TLR4 agonist-based adjuvant system, induces a transient localized innate immune response leading to enhanced adaptive immunity. J. Immunol. (Baltim., Md : 1950) *183*, 6186–6197. 10.4049/jimmunol.0901474.

56. Dupuis, M., McDonald, D.M., and Ott, G. (1999). Distribution of adjuvant MF59 and antigen gD2 after intramuscular injection in mice. Vaccine *18*, 434–439. 10.1016/s0264-410x(99)00263-7.

57. Murphy, K., and Weaver, C. (2016). Janeway's Immunobiology. 10.1201/9781315533247.

58. Awate, S., Babiuk, L.A., and Mutwiri, G. (2013). Mechanisms of Action of Adjuvants. Front. Immunol. *4*, 114. 10.3389/fimmu.2013.00114.

59. Liang, F., Lindgren, G., Sandgren, K.J., Thompson, E.A., Francica, J.R., Seubert, A., Gregorio, E.D., Barnett, S., O'Hagan, D.T., Sullivan, N.J., et al. (2017). Vaccine priming is restricted to draining lymph nodes and controlled by adjuvant-mediated antigen uptake. Sci. Transl. Med. *9*. 10.1126/scitranslmed.aal2094.

60. Calabro, S., Tortoli, M., Baudner, B.C., Pacitto, A., Cortese, M., O'Hagan, D.T., Gregorio, E.D., Seubert, A., and Wack, A. (2011). Vaccine adjuvants alum and MF59 induce rapid recruitment of neutrophils and monocytes that participate in antigen transport to draining lymph nodes. Vaccine *29*, 1812–1823. 10.1016/j.vaccine.2010.12.090.

61. Mayer, A., Zhang, Y., Perelson, A.S., and Wingreen, N.S. (2019). Regulation of T cell expansion by antigen presentation dynamics. Proc. Natl. Acad. Sci. *116*, 5914–5919. 10.1073/pnas.1812800116.

62. Yang, L., Beek, M.V., Wang, Z., Muecksch, F., Canis, M., Hatziioannou, T., Bieniasz, P.D., Nussenzweig, M.C., and Chakraborty, A.K. (2022). Antigen presentation dynamics shape the

antibody response to variants like SARS-CoV-2 Omicron after multiple vaccinations with the original strain. Cell Rep. *42*, 112256. 10.1016/j.celrep.2023.112256.

63. Crotty, S. (2014). T Follicular Helper Cell Differentiation, Function, and Roles in Disease. Immunity *41*, 529–542. 10.1016/j.immuni.2014.10.004.

64. Tam, H.H., Melo, M.B., Kang, M., Pelet, J.M., Ruda, V.M., Foley, M.H., Hu, J.K., Kumari, S., Crampton, J., Baldeon, A.D., et al. (2016). Sustained antigen availability during germinal center initiation enhances antibody responses to vaccination. Proc. Natl. Acad. Sci. *113*, E6639–E6648. 10.1073/pnas.1606050113.

65. Altan-Bonnet, G., Mora, T., and Walczak, A.M. (2020). Quantitative immunology for physicists. Phys. Rep. *849*, 1–83. 10.1016/j.physrep.2020.01.001.

66. Okada, T., Miller, M.J., Parker, I., Krummel, M.F., Neighbors, M., Hartley, S.B., O'Garra, A., Cahalan, M.D., and Cyster, J.G. (2005). Antigen-Engaged B Cells Undergo Chemotaxis toward the T Zone and Form Motile Conjugates with Helper T Cells. PLoS Biol. *3*, e150. 10.1371/journal.pbio.0030150.

67. Taylor, J.J., Pape, K.A., Steach, H.R., and Jenkins, M.K. (2015). Apoptosis and antigen affinity limit effector cell differentiation of a single naïve B cell. Science *347*, 784–787. 10.1126/science.aaa1342.

68. Sze, D.M.-Y., Toellner, K.-M., Vinuesa, C.G. de, Taylor, D.R., and MacLennan, I.C.M. (2000). Intrinsic Constraint on Plasmablast Growth and Extrinsic Limits of Plasma Cell Survival. J. Exp. Med. *192*, 813–822. 10.1084/jem.192.6.813.

Chapter 5.
Conclusion and Perspectives

In this thesis, we presented three projects on how immunodominance affects vaccination outcomes, and how different vaccination strategies can be used to change immunodominance. Understanding the dynamics of this hierarchy is crucial for effective vaccine development and predicting immune responses to various pathogens. Each of the three projects sheds light on a different aspect of immunodominance.

In Chapter 2, we studied ways to manipulate B cell immunodominance in the context of eliciting RBS-directed bnAbs against influenza virus. The pursuit of a universal influenza vaccine hinges on eliciting bnAbs against evolving seasonal and pandemic strains. The first step towards this goal is to amplify the subdominant B cells that target the RBS with cross-reactivity. We investigated the use of heterotrimeric RBS-enriched chimeras and a cocktail of homotrimeric rsHAs. Computational model was developed to derive mechanistic insights into the process of affinity maturation. It highlighted the importance of interplay among different factors: the antigen's binding valency to B cells, the variety of antigens B cells capture, and the stringency of selection by T cells. Moreover, comparing the model prediction with experimental observation provided evidence of stringent selection by helper T cells during affinity maturation.

In Chapter 3, we provided mechanistic explanation of how repeated doses of SARS-CoV-2 vaccine change the B cell and antibody immunodominance. B cell response after initial dose is focused on immunodominant epitopes that are highly mutated in the variant Omicron strain. After the second dose, these memory B cells expand and differentiate into plasma cells, producing antibodies that have low neutralization capacity for Omicron. However, simultaneously, germinal centers after the second dose benefit from increased antigen presentation and epitope masking, producing memory B cells targeting subdominant and more conserved epitopes. After the third dose, expansion of these cells lead to production of neutralizing antibodies against Omicron. The study's in-silico results, validated with clinical data, underscore the significance of the sequential immunizations and timing between doses for optimizing the antibody response. Antigen availability and epitope masking dynamics were found to play pivotal roles in shaping the immune response, and strategies that modulate these factors may be promising.

In Chapter 4, we studied the impact of extended priming dosing strategies on the immune response after vaccination with HIV Env trimer. The native trimer-binding B cells are subdominant and corresponding antibody responses are minimal upon conventional bolus immunization. While a seven-dose escalating regimen was previously found effective in stimulating strong humoral responses, such a strategy is not practical. We investigated several reduced two-dose strategies, and identified 2-ED regimen, administering 20% of the vaccine initially and 80% a week later, which achieves a significant enhancement in humoral responses compared to bolus. Computational models and experimental studies revealed that this strategy improves the capture of native antigens on follicular dendritic cells (FDCs), essential for germinal center (GC) reactions and T follicular helper (Tfh) cell development. The success of this two-dose regimen indicates the importance of antigen capture dynamics and priming of dendritic cells in boosting the immune response. We then identified a slow-releasing alum depot as an effective platform, which extended antigen availability and optimized its presentation. This optimized two-dose approach offers promise in designing more efficient vaccines, especially for challenging pathogens like HIV.

The projects included in this thesis show the multitude of the scale and scope that immunodominance matters. We hope the works presented in this thesis provide foundations for future efforts in developing vaccines against highly mutable viruses. The following are two of the interesting outstanding questions:

(1) Modulating T cell selection to focus B cell responses

Can we harness T cell selection to direct B-cell responses towards a conserved epitope? Chapter 2 demonstrates the impact of helper T cell selection stringency on epitope immunodominance. A cocktail of antigens, each containing distinct helper T cell epitopes, can enable B cells targeting the conserved epitope to interact with more diverse helper T cells than off-target B cells. This mechanism is uniquely enabled by the large mutational distances between the individual antigens in the cocktail. If the selection stringency of helper T cells in germinal centers is low, this difference could promote the immunodominance of the conserved epitope. In contrast, stringent T cell selection promotes the immunodominance of the conserved epitope after immunization with the chimera antigen. A promising avenue for future exploration is investigating whether selection stringency can be modulated. This could involve manipulating the number and immunogenicity of T cell epitopes in antigens, using adjuvants that influence the activation of innate immune cells and T cells, or upregulating adhesion molecules on T cell surfaces.

(2) Designing immunogen and delivery scheme to elicit longer-lasting protection

Chapter 3 and 4 highlight the interplay between pre-existing humoral immunity (antibodies, memory cells, and plasma cells) and design of vaccine (choice of antigen sequence, delivery kinetics) in determining epitope immunodominance. This in turn affects the diversity of B cell responses and degree of protection against evolving viral mutants. Current vaccination strategy against mutable viruses like influenza and SARS-CoV-2 is to vaccinate with strains that are already prevalent or are anticipated to become prevalent in near future. While this focuses on neutralizing immediate threats, it overlooks how vaccine-induced immunity might resist the escapes of viral mutations. If the goal is to produce longer-lasting protection by producing diverse B cell responses, what would be the optimal choice of antigen or antigens, and in what temporal kinetics should they be delivered? The various mechanistic principles that we have revealed in Chapter 3 and 4 may serve as foundations for designing such vaccines.